UNIVERSITY OF LIVERPOOL

BIOAVAILABILITY-BASED APPROACH TO UNDERSTAND THE EFFECTS OF METALS AS TOXICANTS AND NUTRIENTS: IMPLICATIONS FOR ENVIRONMENTAL MANAGEMENT

Thesis submitted in accordance with the requirements of the University of Liverpool for the degree of Doctor in Philosophy

by

Boling Li

April, 2022

ABSTRACT

Environmental Management is a framing concept for the specific research topics in this thesis, and within that the work focuses on metals in the environment. Some of the work focuses on metals as toxicants, some on metal micronutrients, and some on metals that may be either, depending upon conditions. This thesis begins with work in which I developed a "two-in-one" whole-cell bioreporter approach to assess harmful effects of cadmium and lead. With the lights-on bioreporter's unique two-in-one ability for speciation and toxicity measurement, in conjunction with the validated biotic ligand model, the bioreporter can predict toxicity endpoints over the range of the lowest Water Quality Criterion to the 50th rank-percentile of aquatic organisms sensitivity.

In the context of dramatic environmental/biogeochemical change from metal pollution, relatively little work has been done on the role of micronutrients in influencing the development and progression of harmful algal blooms. In this thesis, I report results from mesocosm experiments with *Microcystis* and *Desmodesmus* spp., in mono- and mixed-cultures, to probe questions of how copper, iron, and copper-iron amendments affect the growth, short-term assemblage progression, and production of siderophore, chalkophore, and microcystin in lake water. The findings from this study are summarized: 1) copper-iron impacts on growth and community progression do not agree with lab-based findings. 2) Interplay between chalkophore/siderophore production supports a concept model wherein *Microcystis* spp. varies behavior to manage copper/iron requirements in a phased manner. In being able to specifically screen for chalkophores, I observed a previously unreported link between chalkophore and microcystin production that may relate to iron-limitation. 3) the lake water itself influences mesocosm changes; differentiated effects for iron regarding growth indicators and/or reduction of iron-limitation stress were found at a harmful algal bloom-free field station, likely a consequence of low bioavailability of iron in this station.

My findings that *Microcystis* spp. varies behavior to manage copper/iron through the interplay between chalkophore/siderophore production and the previously unreported link between chalkophore and microcystin production addressed an important gap in furthering research on the effects of micronutrients bioavailability in natural water. Follow-up research with revised copper/iron amendments and increased level of algal acclimation was achieved. Similar to the initial work, I again saw a very similar dynamical phased behavior between chalkophore/siderophore production for *Microcystis* spp. that exhibited significant differences in trajectories according to specific differences in copper and iron amendments. The most interesting finding was that I observed a strong microcystin-chalkophore relationship again. Based on this research, I can say that chalkophore is a predictor of this cyanobacterial toxin production. While I discuss possible reasons for this new finding, it is previously undocumented, and I outline follow-up work that I believe would be fruitful to further elucidate the biological mechanisms underlying this behavior and why *Microcystis* spp. produce the toxin, microcystin.

ACKNOWLEDGMENTS

I will never forget. It was a nice sunny afternoon in the early summer of 2017 when Dr. Mona Wells offered me the candidate's position for Doctor in Philosophy in Environmental Science. More than happy at that moment, I had no idea about what I would "suffer" in the coming years. The "suffer" came in every direction of my Doctor in Philosophy study life: from the departure before dawn for my field experiments at Taihu; from the thousands of exchanges on manuscript writing, and seventeen exchanges even when it was just an experimental rationale; from the week plans, which required detail taking two hours; from the lively explanation of scientific principles to the stories about when she was young; from the nice beers and from her beautiful songs. Dr. Mona Wells kept mentoring me and gave me strength from overseas, even she had already left my department 3 years. I thereby do not think any words or language can fully express my sincere acknowledgments, but to say, she is my knight under the darkness!

The "suffer" also came from Dr. Boris Tefsen, with unbelievably detailed guidance and patience to fill the gap between Environmental Science and Microbiology for me. The way he insisted for himself to be on the road to the "real science" set a very good example to me and touched my soul. I do not know where I came into such luck that I can know my supervisors, Dr.s Mona Wells and Boris Tefsen, and I could not never achieve my current level of success without their continuous support.

I would also like to say thanks to my colleague Dr. Xiaokai Zhang, with his patient guidance and help for experimental training and field work. Without his help I might still be suffering with cell culturing and pipette adjusting.

My sincere thanks also goes to Professor Boqiang Qin and Professor Jianming Deng at the Nanjing Institute of Geography and Limnology, Chinese Academy of Sciences, for their support with water quality data and their extensive expertise and assistance with all aspects of work on Taihu. The extremely tidy and good order of their lab pointed the way for me to execute experiments well.

Thanks to my friend Qingxin He who taught me fishing and to know that it is not always that important how many fish we catch, but how much peace we can find in the soft wind from the lake, how much we can dive into hobbies like the way we do science, and how we accept loss when we almost caught them.

I like the saying that babies are up high in the sky and busy selecting their best mom when the mom is about to give birth. I regard that the best decision I made so far must be the mom I selected, by saying so I would like to express my great and deep gratitude to my parents for their continuous support in my life and deep understanding of my feelings.

Finally, I would like to express my respect and also say thanks to all the scientific researchers working hard and lonely under the current society. Thanks for the ideas that you shared, the adventures that you took and the discoveries that you made. It is all because of your exploration of science that made the civilization of humankind.

PREFACE

The study leading to the award of a Doctor in Philosophy begins for all kinds of reasons, but when all is said and done, looking back on the adventures I had over the past four years, they have one thing in common: they are shooting stars, a spectacular moment of light in the universe, a fleeting glimpse of eternity, and in a flash, set deeply into my memory.

I did not begin for the reason of a strong interest in the way of science, nor did I begin to consider how much this degree might increase life quality. I begin for the reason to win this title, as the best proof to show “smart”. Deeper into the study toward the Doctor in Philosophy changed my arrogant way of thinking myself to know a lot. The more I read, the more I tried to explore, the more I found how little I know, how little we know, as the limitation of knowledge for science. The inner flame then burns gradually, encouraging me to uncover what lies in the darkness.

The elements, the organisms, wind and sun, space and water, what are the relationships and the profound mysteries behind all those? How do we understand those responses and what will we learn in the way of Biology, and in the way of Environmental Science? Bringing those macroscopic minds into microscopic researches, I focused my study on the topic of toxic metals, micronutrients, whole-cell biosenors, biomolecules and algal blooms from the lab into the field, trying to uncover the deeper relationships among those, and trying to improve the knowledge of Environmental Management.

TABLE OF CONTENTS

LIST OF TABLES

LIST OF FIGURES

List of Abbreviations and Symbols

2-D	Two-dimensional
3-D	Three-dimensional
Δ	Delta, difference between two quantities
Δ_{avg}	Average delta
λ_{max}	Emission maximum
$\lambda_{max,\ PI}$	Emission maximum for propidium iodide
$\lambda_{max,\ SYTO\ 9}$	Emission maximum for SYTO 9
µeq	Micro-equivalent
$\sum_{BLspecies}$	Sum of all biotic ligand species
a	Activity
$a_{BL^{-1}}$	Activity of free biotic ligand sites
$a^{Ca}_{Mg^{2+}}$	Activity of Mg^{2+} in the Ca-set (or other variants of major cations)
$a_{Cd^{2+}}$	Activity of Cd^{2+}
$a_{Pb^{2+}}$	Activity of Pb^{2+}
$a_{MBL^{n-1}}$	Activity of the MBL complex
$a_{M^{n+}}$	Activity of metal free-ion
a_{TBL}	Total activity of biotic ligand sites
Alg_{is}	*in situ* algae
AUC	Area under curve
b	Intercept of line
BG	Blue-green algae
BL	Biotic ligand
BLM	Biotic ligand model
B_{meso}	1:1 mixture of *Microcystis* spp. and non-nuisance green algae by OD
C	Total concentration, subscript indicates component or species
$C^{TDM}_{spike,\ t0}$	Concentration of total dissolved metal resulting from spiking a blank (ultra-pure water) mesocosm
$C^{TDM}_{water,\ t0}$	Concentration of total dissolved metal in filtered freshwater sample used for mesocosms

$C^{TM}_{algae,\ t0}$	Concentration of total metal in algae used for mesocosms initially
C^{TM}_{meas}	Measured concentration of total metal
C^{TM}_{pred}	Predicted concentration of total metal
Ca	Calcium
CAS	Chrome azurol sulfonate
Cd	Cadmium
Chl-a	Chlorophyll-a
Cl	Chloride
CMC	Criterion maximum concentration
CRM	Certified reference material
CTA	Community trajectory analysis
Ctl	Control
Cts.ef	Counts determined by electric-field exclusion
Cts.m	Counts determined by microscope
Cu	Copper
CueR	Copper-dependent regulator
d.avg	Average diameter
Des	Desmids
Dia	Diatoms
D_{meso}	Mesocosm dosed with *Desmodesmus* spp.
DOC	Dissolved organic carbon
DOM	Dissolved organic matter
DON	Dissolved organic nitrogen
DOP	Dissolved organic phosphorus
DTW	Dynamic time warping
EC_{50}	Effective concentration causing 50% toxic effect
$\mathbf{EC}_{\mathbf{50}}^{a_{\mathbf{Cd^{2+}}}}$	Effective activity of cadmium causing 50% toxic effect
$\mathbf{EC}_{\mathbf{50}}^{C_{\mathbf{Cd}}}$	Effective total concentration of cadmium causing 50% toxic effect
$\mathbf{EC}_{\mathbf{50}}^{a_{\mathbf{Pb^{2+}}}}$	Effective activity of lead causing 50% toxic effect
$\mathbf{EC}_{\mathbf{50}}^{C_{\mathbf{Pb}}}$	Effective total concentration of lead causing 50% toxic effect
EDTA	Ethylene diamine tetra-acetic acid
EM	Environmental management
EQS	Environmental quality standards

ESV	Effective spherical volume
f	Fraction of biotic ligand sites occupied by toxic metal
f_{crit}	Critical fraction of biotic ligand sites occupied by toxic metal at which EC_{50} occurs
FAV	Final acute value
FD	Fréchet distance
Fe	Iron
Fur	Iron-uptake regulator
GMAV	Genus Mean Acute Value
G_{meso}	1:1 mixture of *Desmodesmus* and *Chlorella* spp. by OD
HA	Humic acid
HABs	Harmful algal blooms
H_0	Null hypothesis
HSD	Honest Significant Difference (Tukey's)
ICP-MS	Inductively Coupled Plasma-Mass Spectrometry
K	Potassium
$K_{CationBL}$	Binding constant of cation-biotic ligand
K_{CdHA}	Binding constant of cadmium-humic acid
K_{MBL}	Binding constant of metal-biotic ligand
K_{PbHA}	Binding constant of lead-humic acid
LB	Lysogeny broth
LOD	Limit of detection
LOQ	Limit of quantitation
LT	Lake Tai
m	Slope of line
M	Metal (toxic)
M_{meso}	Mesocosm dosed with *Microcystis* spp.
M^{n+}	Metal free-ion of valence n
MBL^{n-1}	Complex of metal-biotic ligand
Mg	Magnesium
MM	Minimal medium
MN	Micronutrient
MOPS	3-[*N*-morpholino] propane sulfonic acid
MRR	Maximum response ratio
MRR_{0i}	Maximum response with zero inhibition

MRR_{Ci}	Maximum response at concentration, C_i, at which bioluminescence is inhibited
N	Nitrogen
Na	Sodium
NH4	Ammoniacal nitrogen
NIGLAS	Nanjing Institute of Geography and Limnology, Chinese Academy of Sciences
NLB	Nutrient limitation bioassay
NO2	Nitrite
NO3	Nitrate
NP	Nitrogen and phosphorus
NTP	National Toxicology Prgram of the United States
OD	Optical density (at 600 nm for bacteria and 750 nm for algae)
OD_{600}	Optical density at 600 nm
OD_{750}	Optical density at 750 nm
P	Phosphorus
$P_{5\%}$	5^{th} rank percentile
$P_{n\%}$	n^{th} rank percentile
Pb	Lead
PCA	Principal component analysis
ρ	Spearman's ρ
p	Slope at the steepest part of dose-response curve (Hill slope)
PI	Propidium iodide
PO4	Orthophosphate
POM	Particulate organic matter
Q_{sample}	Q-value of the sample
Q_{crit}	Critical Q-value
QA/QC	Quality assurance/quality control
R_{cation}	Ratio of slope to intercept for EC_{50}-cation linear relationship
Rest	Designation for algae not classified into specific groups
$R_{L/D}$	Ratio of live-to-dead cells (LIVE/DEAD assay)

R_{Lum}	Ratio of bioluminescence inhibition to maximum bioluminescene without inhibition (bioluminescence inhibition assay)
$R_{toxic\ effect}$	Ratio of LIVE/DEAD or bioluminescence inhibition assay
RLU	Relative luminescence units
$RLU_{0,\ max}$	Maximum response, in RLU, of the blank
$RLU_{C_M,\ max}$	Maximum response, in RLU, for metal concentration C_M
RPD	Relative percent difference
RSD	Relative standard deviation
SHM	Stockholm Humic Model
SO4	Sulfate
St	Sample station
SV	Speciation validation
SYTO 9	Designation for green fluorescent nucleic acid stain (“live”) in LIVE/DEAD kit
t	Abbreviation for sampling time
t	Time, variable
TCu	Total copper
TDCu	Total dissolved copper
TDFe	Total dissolved iron
TDM	Total dissolved metal
TDN	Total dissolved nitrogen
TDP	Total dissolved phosphorus
TFe	Total iron
TLLER	Taihu Laboratory for Lake Ecosystem Research
TM	Total metal
TOC	Total organic carbon
TotG	Sum of green algae
TV-C	Toxicity validation-cations
TV HA-C	Toxicity validation with humic acid and cations
UG	Dominant unicellular green algae
UPW	Ultrapure water
VM	Visual MINTEQ speciation/biotic ligand model software
WQC	Water quality criteria
xN	Variable *x,* after normalization
s_{xN}	Propagated error of *x*N

s_x	Standard deviation of *x* (or other variable as subscript)
zntA	*Escherichia coli* PHL268 strain zntA
zntA	*zntA* gene
zntR	Responsive MerR-like transcriptional regulator of zntA in *Escherichia coli*

1 Introduction

1.1 BACKGROUND

This thesis focuses on different aspects of progressing the fundamental understanding of trace metal bioavailability in the context of dramatic environmental/biogeochemical change from trace metal pollution. As I had diverse topics in my thesis, and some of the work evolved in a manner that led me to include background about the research and literature review, existing research gaps, and specific research objectives in individual chapters. In doing so, the thesis also deals with development of new approaches to using this understanding in Environmental Management (EM) of priority metal pollutants. The interplay between chemical speciation, bioavailability, and toxicity are key issues in pollution assessment (US EPA, 2002) and are also central to a proper understanding of biogeochemical cycles, hence this interplay is a common theme for the different research work presented here.

Within these central themes, this thesis can be divided into two research areas, one dealing with bioreporters (a type of whole-cell biosensor) and trace metal pollution. The other research area deals with how trace metals affects bloom-forming algae. An overview of the first research area is shown in Figure 1-1. For this research I show how a bioreporter can be used to develop a two-in-one

approach to speciation and toxicity in the context of Water Quality Criteria (WQC). This work concerns cadmium (Cd) and lead (Pb), two of the most toxic and globally prevalent pollutants that also disproportionately impact disadvantaged communities. Anthropogenic release of Cd and Pb to the environment poses a serious ecotoxicological threat to many aquatic organisms.

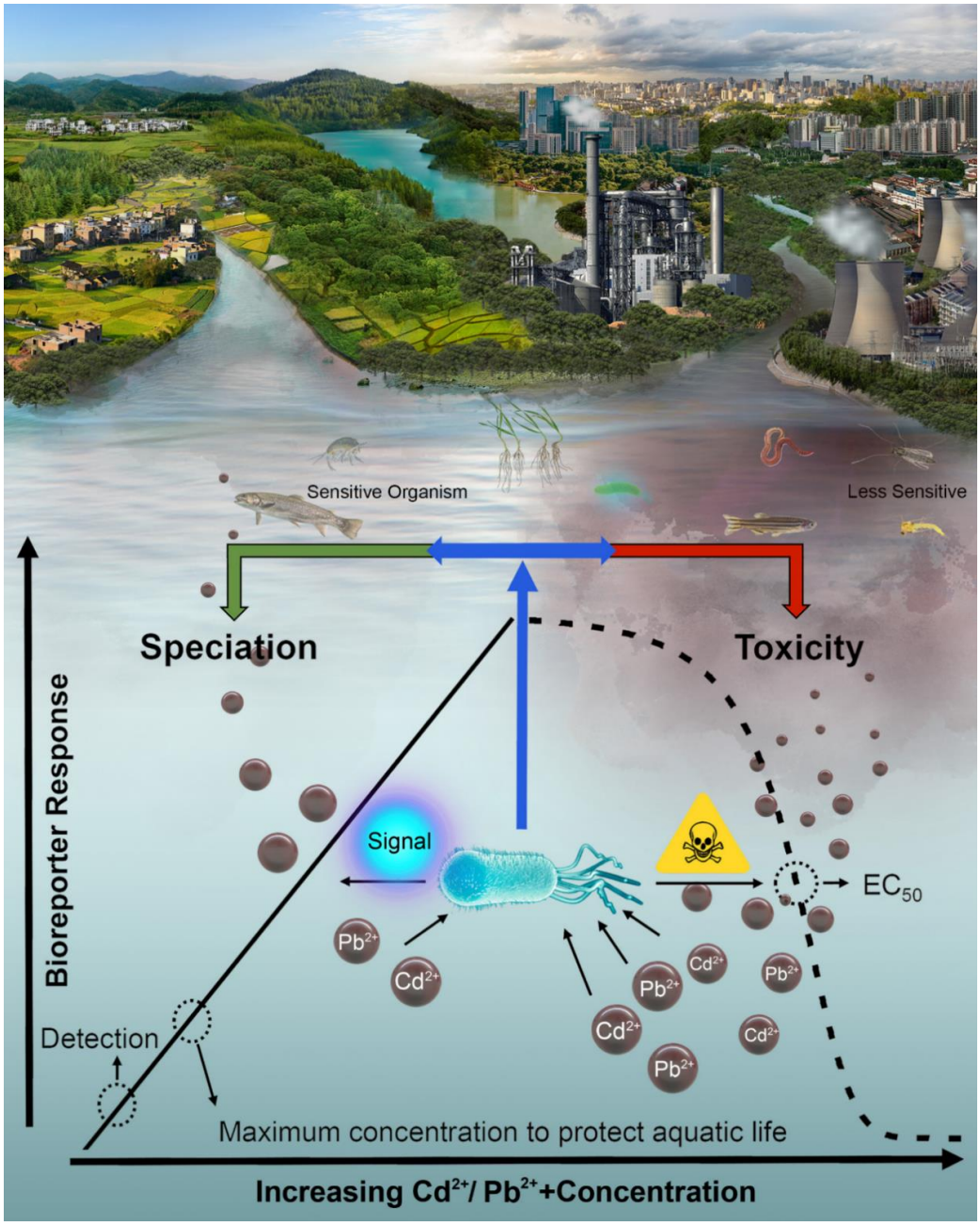

Figure 1-1. Schematic representation of the bioreporter two-in-one approach to speciation and toxicity. Unlike other organisms in use for setting WQC via toxicity testing results, the bioreporter is able to give a response under the maximum concentration to protect aquatic life up to the limit of the bioreporter's toxic response.

To quantify bioavailability for metals, genetically engineered whole-cell bioreporters have become of increasing interest with respect to hazardous materials. Lights-on bioreporters have only been used for measurements of metal speciation and bioavailability, whereas lights-off bioreporters can only be used for metal toxicity measurements. I used bioreporter technology to demonstrate an approach combining the study of speciation and toxicity simultaneously and within the biotic ligand model framework for risk assessment of hazardous materials. I used the LIVE/DEAD toxicity assay for bacteria to measure toxic effects from cadmium and lead and use this as a benchmark to demonstrate how the lights-on reporter can be used for toxicity measurements in addition to speciation. At the outset of my work, I posited, and was later able to demonstrate, that whole-cell biosensor technology based on so-called lights-on bioreporters (depicted as the flagellated rod in the centre of Figure 1-1) could enable an approach for the determination of bioavailability that spans the continuum from speciation to toxicity, and in a manner that permits the unified validation of both within a modeling framework that is commonly used in development of WQC and decision support in EM. The figure illustrates conceptually how this works. Various components in the aqueous-phase affect overall speciation and the amount of toxic free-metal that is bioavailable. The bioreporter is able to give a report, in the form of an optical signal (blue arrow pointing upwards), that is proportional to bioavailable toxicant up to the limit of the bioreporter's toxic response (line with constant slope). Thereafter, toxicity causes inhibition of bioluminescence (dashed curve). The limit of detection (LOD) of the bioreporter is under the maximum concentration to protect aquatic life set by WQC. Toxicity endpoints for other

cadmium and lead biotic ligand models reported in literature average 71st and 44th rank-percentile sensitivity (i.e., insensitive). In comparison, with the lights-on bioreporter's unique two-in-one ability for speciation and toxicity measurement, in conjunction with the validated biotic ligand model, the bioreporter can predict toxicity endpoints over the range of the lowest Water Quality Criterion to the 50th rank-percentile of aquatic organism sensitivity. The approach is generally extensible to a large number of toxic environmental pollutants that increasingly pose environmental challenges globally.

For my research area that deals with how trace metals affect bloom-forming algae, I found that trace metals have a phased effect on biomolecule production, which thus in turn may affect trace metal bioavailability. My approach is an entirely new perspective to understand micronutrients dynamics in aqueous environments as this is the first work to systematically screen for chalkophores and siderophores separately, as a function of copper (Cu)/iron (Fe) amendment, and using community trajectory analysis. I also performed multivariate analysis of the extended dataset of 117 mesocosm results × 28 parameters using principal component analysis to understand differences in mesocosm behavior across the large data set. Figure 1-2 is a conceptual graphic showing the phased trajectory-type behavior of the effects of Cu and Fe on the production of the algal biomolecules that chalkophore, siderophore and microcystin. This figure shows how, for one set of experiments, *Microcystis* spp. increased siderophore production, or molecules strongly complex Fe and are believed to increase the bioavailability of Fe. In a phased manner, chalkophore (molecules that strongly complex Cu) production then increased.

It was of interest to me to restructure the copper amendment in particular to see potentially contrasting effects between different levels, and I also wanted to collect additional evidence on the microcystin-chalkophore link. The follow-up research was methodologically similar, though I revised copper/iron amendments and increased the level of algal acclimation, as well as using more advanced algorithms within the family of techniques used in trajectory analysis. While in follow-up experiments, I found that rates of change and phase-differences vary, in all cases I found a previously undocumented link between chalkophore and microcystin. While it remains unclear why *Microcystis* generates the toxin microcystin, many authors posit that competing algae, green algae in the figure, are adversely affected by microcystin, hence its production conveys a competitive advantage, in this case in nutrient stressed conditions.

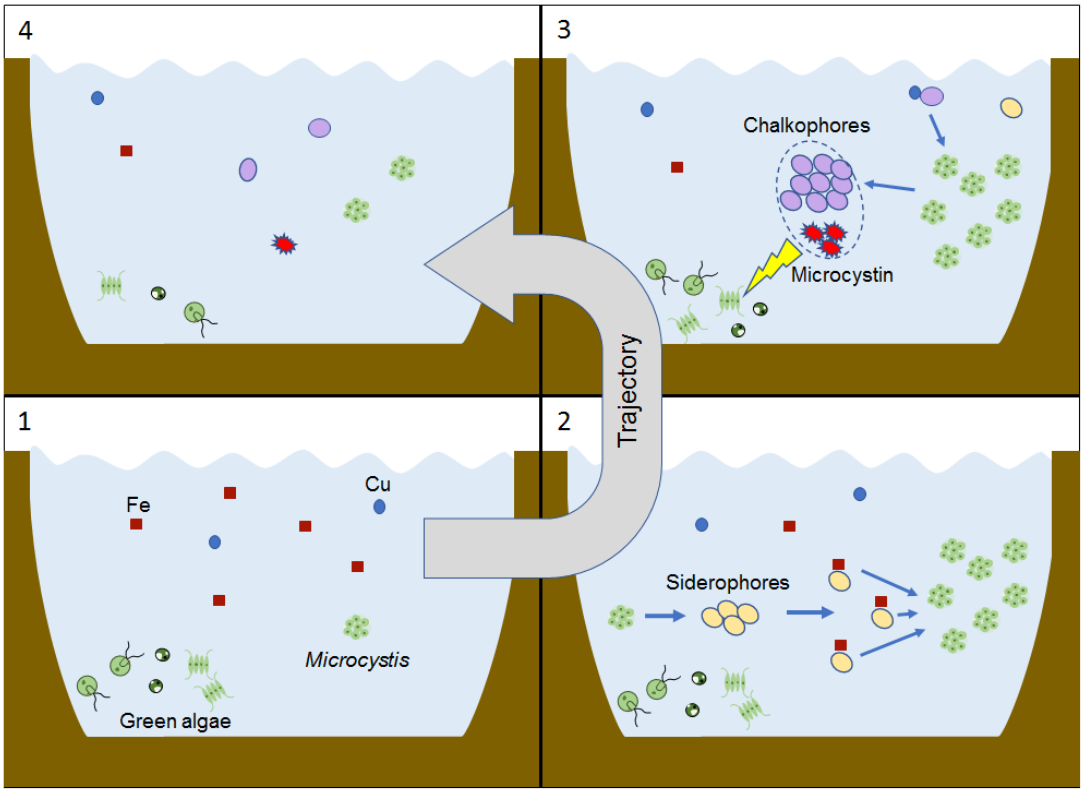

Figure 1-2. Graphic trajectory over time showing Cu and Fe effects on the production of algal biomolecules (chalkophore, siderophore and microcystin).

Both areas of research that I describe herein deal with freshwater environments, however the results might also be relevant to estuarine or even marine settings, as much of the background literature that I cite illustrates. The field components of my work were conducted in a highly impacted lacustrine environment, which is highly relevant to my interest in EM, as these sinks represent an endpoint for catchment-wide effects (pollution, land use and land use change).

1.2 Research Questions and Structure of Thesis

This thesis is structured to contain six chapters and Chapter 1 was arranged as a general overview of this thesis with summarized research questions and statement of my publications in construct this thesis. Three research questions framed around the main thesis, each of which is reported on in detail in Chapters 2–4. I summarize the three research questions as follows:

I) Will "lights-on" whole-cell bioreporters also predict metal toxicity in addition to metal speciation, thus being able to give a report on the status of toxic metals, spanning the continuum of speciation up to the reporter's toxicity endpoint?

II) How do Cu, Fe, and Cu-Fe together affect bloom-forming algae in a highly impacted environment, and are there implications concerning the use of Cu in whole-lake EM of harmful algae blooms?

III) Is the microcystin-chalkophore link that I observed in the course of work on Research Question II above a general phenomenon, and how does this relate to Fe-limitation?"

In Chapter 5, conclusions are made for the work reported in Chapter 2–4 with further work being pointed out. Chapter 6 listed the references cited in this thesis.

1.3 STATUS OF MANUSCRIPTS ARISING FROM WORK

All of the work reported in this thesis is either published or scheduled for publication. The publication status of the work presented here, at the time of submission of this manuscript to the examiner, is listed below.

Work presented in Chapter 2, published in **Water Research:**

Li, B., Zhang, X., Tefsen, B., Wells, M., 2022. From Speciation to Toxicity: Using a "Two-in-One" Whole-cell Bioreporter Approach to Assess Harmful Effects of Cd and Pb. Water Res. 217, 118384.

Work presented in Chapter 3, published in **Water Research:**

Li, B., Zhang, X., Deng, J., Cheng, Y., Chen, Z., Qin, B., Tefsen, B., Wells, M., 2021. A new perspective of copper-iron effects on bloom-forming algae in a highly impacted environment. Water Res. 195, 116889.

Work presented in Chapter 4, manuscript in preparation:

Li, B., Zhang, X., Deng, J., Qin, B., Tefsen, B., Wells, M., 2021. Chalkophore is a predictor of microcystin toxin production by harmful cyanobacteria.

Additionally, in this thesis I cite works that substantively inform my primary research, reported here. The articles below represent work in which I

participated with my colleague, Dr. Zhang, during my PhD study and for which I am second author:

Zhang, X., **Li, B**., Xu, H., Wells, M., Tefsen, B., Qin, B., 2019. Effect of micronutrients on algae in different regions of Taihu, a large, spatially diverse, hypereutrophic lake. Water Res. 151, 500–514.

Zhang, X., **Li, B**., Deng, J., Qin, B., Wells, M., Tefsen, B., 2020a. Advances in freshwater risk assessment: Improved accuracy of dissolved organic matter-metal speciation prediction and rapid biological validation. Ecotox. Environ. Safe. 202, 110848.

Zhang, X., **Li, B**., Deng, J., Qin, B., Wells, M., Tefsen, B., 2020b. Quantitative high-throughput approach to chalkophore screening in freshwaters. Sci. Total Environ. 139476.

Zhang, X., **Li, B**., Deng, J., Qin, B., Wells, M., Tefsen, B., 2020c. Regional-scale investigation of dissolved organic matter and lead binding in a large impacted lake with a focus on environmental risk assessment. Water Res. 115478.

2 From Speciation to Toxicity: Using a "Two-in-One" Whole-cell Bioreporter Approach to Assess Harmful Effects of Cd and Pb

2.1 Background on Whole-cell Bioreporters, the Biotic Ligand Model, and Cadmium and Lead Pollution

Chemical speciation, bioavailability, and toxicity are key issues in hazard assessment, as this assessment are processes occurring at environmental interfaces (including organisms) and/or in different environmental compartments which regulate the rate of formation, stability and prevalence of these metal species. These reactions likewise control the chemical speciation of metals that enhance or restrict their transport in the environment, and to and within organisms (see review of the Metals Action Plan to identify key scientific issues important for assessing the hazards and risks of toxic metal contamination, US EPA, 2002). Toxic effect is a function of bioavailability rather than total concentration (Wells et al., 2004; Harms et al., 2006), as acknowledged, for instance, by the US Environmental Protection Agency's

Framework for Metals Risk Assessment, which states that for hazardous metals risk assessors should "*explicitly incorporate factors that influence the bioavailability of a metal*" (Fairbrother et al., 2007). While the US EPA was early to recognize these inter-relationships, the perspective is now woven into practice in many countries (e.g., see EC, 2013). Because bioavailability is a function of metal chemical speciation (hereafter speciation, Nor and Cheng, 1986; Tessier and Turner, 1995; Machado et al., 2010; Sander et al., 2011; Khan et al., 2017; Zhang et al., 2017 and 2020a), many environmental factors that influence speciation (e.g., pH, organic matter complexation with heavy metals) also influence metal bioavailability. Most environmental studies focus on either speciation/bioavailability (e.g., Sundaray et al., 2010; Bagherifam et al., 2014; Zhang et al., 2017; Yan et al., 2020), or toxicity (based on bioavailability, e.g., An et al., 2012 and 2015; Gong et al., 2021), i.e. one or the other, usually not both. To my knowledge, there is a paucity of work combining the simultaneous study of speciation and toxicity as a holistic approach to understanding biological effects.

To assist with setting defensible WQC, the biotic ligand model (BLM) was developed (US EPA, 2003; US EPA, 2016a), which is a model that is mechanistic and explicitly links speciation to toxicity, albeit for most risk assessment work the BLM is run in toxicity mode since available biological endpoints consist of a single metric, such as EC_{50} (effective concentration causing 50% toxic effect). In the framework of the BLM, a biotic ligand (BL) is a specific receptor within an organism for which complexation by a metal (M) can lead to toxic effects, hence the BLM includes expressions to describe metal complexation with BLs (US EPA, 2007). Complexation of nontoxic-metal cations with the BL is also specified in

the model, and the competition of major cations in environmental samples, that is cations of calcium, magnesium, potassium and sodium (Ca, Mg, K, Na, respectively), for binding with BL reduces toxic M-BL complexation, and therefore toxic effects. Parameters describing the reactions of M with other solution constituents are required for BLM models run in speciation mode. For BLM toxicity mode, there needs to be further parameterization for calculation of a toxicity endpoint such as EC_{50} (e.g., Di Toro et al., 2001; Crémazy et al., 2016). The BLM model is mechanistic in nature, and model inputs are simple and inexpensive to obtain. BLM results have been demonstrated to be an accurate predictor of environmental risk for several toxic heavy metals and to be fit-for-purpose tool for decisions regarding WQC (Niyogi and Wood, 2004). Though developed in the US, the BLM has also been adopted as the basis of some environmental quality standards (EQS) in Europe to enable site-specific EQS values to be derived (EC, 2010). While copper and nickel BLMs have been thoroughly studied and are used in the United States, in Europe, and increasingly in other places (EC, 2010; US EPA, 2016a), as An et al. (2012) have pointed out, fewer BL-based models are available for Cd and Pb. Considering the toxicity of Cd and Pb, increasing the focus on these environmental contaminants within the BLM framework is timely.

Cd and Pb are considered to be two of the most hazardous substances globally (Tellez-Plaza et al., 2013; Pure Earth/Green Cross, 2015; Alengebawy et al., 2021), and also contribute to alarming environmental issues in China and India, which together account for about 37% of the entire global population (Tong et al., 2000; Cheng, 2003; Kan, 2009; Kumar et al., 2019; Hu et al., 2020). Cd ranks seventh on one list referred to as the "*Top 20 Hazardous Substance*" (CERCLA,

2005). Additionally, "*Cadmium and cadmium compounds*", i.e. *anything* that contains Cd, is on the two most well-known lists of carcinogens as classified by the International Agency for Research on Cancer and the National Toxicology Program (NTP) of the United States, the latter of which only contains 69 line items as compared to the tens of thousands of agents that are probable or possible carcinogens (McGuire, 2016; NTP, 2016; Oldani et al., 2020). Cd is notably affected by pH in soils, which is exacerbated by anthropogenic increases in acid rain, and this contributes to Cd's being accumulated in important foodstuffs such as rice (Liu et al., 2007; Song et al., 2015). Due to the carcinogenicity of Cd and its increasing presence in food items, Cd contamination represents a global hazard to both food security and human health (Khan et al., 2021). With regard to Pb, its increasing environmental prevalence might arguably be described as an impending crisis inasmuch as there is no safe level of Pb exposure (Grandjean, 2010), and Pb is differentially neurotoxic to children, compromising cognitive development (Grandjean and Landrigan, 2014). The global annual costs of childhood Pb exposure from cognitive defects alone are estimated to be 1.15 trillion US dollars, most of which is borne by low- and middle-income countries (Grandjean and Bellange, 2017). Due to activities such as coal burning that release Pb (and Cd), and the continued increasing global production of Pb (Mudd, 2013; Marx et al., 2016) for use in various applications, including increasing use in "sustainable" solar photovoltaic energy systems (Gottesfeld and Cherry, 2011), a continued stark increase in environmental Pb levels is virtually assured. The increasing prevalence and extremely hazardous nature of Cd and Pb ensures that exposure

to these contaminants is an intergenerational issue, predicating my choice to study Cd and Pb in this work.

Many different methods have been and are being developed to quantify bioavailability for metals (Florence, 1986; Batley et al., 2004; US EPA, 2007a; Fairbrother et al., 2007), among which whole-cell bioreporters have become of increasing interest with respect to pollutants in environmental matrices such as water, soil, sediments and other geomaterials (Belkin, 2003; Al-Anizi et al., 2014; Wells, 2012; Xu et al., 2014; Zhang et al, 2017; Jiang et al., 2021). Bioreporters are living microbial cells that have been genetically engineered to produce a measurable signal (typically optical, measured as bioluminescence, fluorescence, or absorbance) in response to a specific chemical or physical agent in their environment (van der Meer and Belkin, 2010). Whole-cell bioreporters have been described as falling into two mechanistic response categories: lights-off and lights-on (Belkin, 2003; Xu et al., 2014). Lights-off bioreporters are used for metal toxicity measurements, as they constitutively emit a continuous signal in the absence of bioavailable metal, and only after dosing with toxic levels of metals is signal inhibited (Belkin, 2003; An et al., 2012; Abbas et al., 2018). As diminishing signal accompanies toxicity, the process is referred to as lights-off, and the effect is non-specific—any toxin could cause signal diminution. Lights-on bioreporters are notably used in speciation measurements as they have the capacity to emit a dose-dependent bioluminescence in response to bioavailable metals (Belkin, 2003; Magrisso et al., 2008; Senevirathna et al., 2009; Shemer et al., 2015; Kauffer et al., 2017), i.e., signal increases (lights-on), typically linearly, with the metal free-ion species concentration. Lights-on bioreporters are notably selective, or sometimes even specific, to a single analyte. For example, I

used a lights-on bioreporter in this work for which resistance to Cd and Pb toxicity is mediated, at least in part, by the presence of the *zntA* gene (Riether et al., 2001). This gene endows the bioreporter with the capacity to emit a positive (nontoxic) dose-dependent bioluminescence response to available Cd and Pb within environmentally relevant Cd and Pb concentration ranges (Kessler et al., 2012). While lights-on bioreporters have demonstrated success for speciation measurements of metal free-ion, to my knowledge they have not been used to quantify toxic effects.

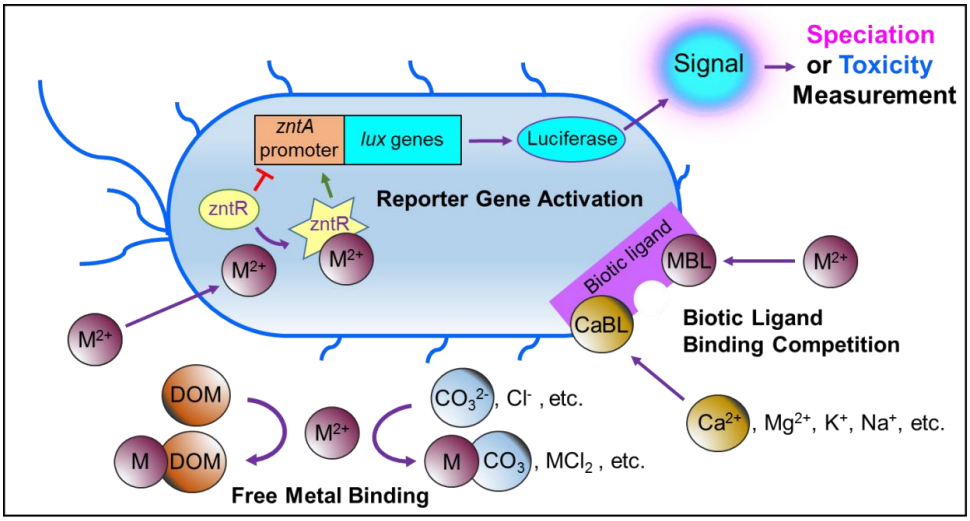

Figure 2-1. Schematic diagram illustrating two-in-one study concept. Interactions between inorganic and organic solution constituents, free metal, and the bioreporter, affect bioreporter signal production. For speciation or toxicity measurement, a bioreporter bacteria is first exposed to environmental free metal (M^{2+}). The *zntA* promoter will only be activated when M^{2+} binds with zntR (a transcriptional regulator), which controls expression of a reporter gene (*lux* genes). Luciferase is then formed and provides an optical signal or report. For M^{2+} binding, environmental constituents dissolved organic matter (DOM) and inorganic anions bind with M^{2+}, reducing metal bioavailability. Cations compete with M^{2+}, for binding with BL, and thus reduce the bioavailability and toxicity of the M^{2+}.

Here I use bioreporter technology to demonstrate an approach to combining the study of speciation and toxicity simultaneously and within the BLM framework

for risk assessment of hazardous materials. The general approach is graphically summarized in Figure 2-1. I used the standard LIVE/DEAD toxicity assay for bacteria to measure toxic effects, which furnishes a benchmark to demonstrate how the lights-on reporter can be used for toxicity measurements in addition to speciation. Results are used to construct BLM models, and I perform additional experiments to validate BLM predictions for Cd and Pb in BLM speciation and toxicity modes.

2.2 BIOREPORTER EXPERIMENTS

Bioreporter strain and growth media

Escherichia coli PHL268 strain zntA (hereafter zntA, in contrast to the gene *zntA*), was used as the lights-on bioreporter for this study. The strain was stored at 4 °C on Lysogeny Broth (LB) agar (Bertani, 2004) amended with 40 $\mu g \cdot mL^{-1}$ ampicillin. Overnight cultures were grown at 30 °C with shaking at 90 rpm for 16 hours. The overnight culture was diluted 100-fold in fresh LB without ampicillin and re-grown at 26 °C, shaking at 200 rpm. At an optical density at 600 nm (OD_{600}) of 0.10, cells were harvested by centrifugation (13,200 *g*). The supernatant was discarded, and the cells were resuspended in optimized minimal medium (MM) to an OD_{600} of 0.20. The MM contained 6.06 g of 3-[*N*-morpholino] propane sulfonic acid (MOPS), 2 g of sodium gluconate, 0.23 g β-glycero-phosphate, 4.68 g of NaCl, 1.07 g of NH_4Cl, 0.43 g of Na_2SO_4, 0.2 g of $MgCl_2 \cdot 6H_2O$ and 0.03 g of $CaCl_2 \cdot 2H_2O$, dissolved in 1000 mL of distilled water and adjusted to pH 7.0 ± 0.1 (Mergeay et al., 1985; Magrisso et al., 2009). All chemicals were reagent grade or better and purchased from Alfa Aesar Co., Ltd

(Shanghai, China).

Bioreporter speciation assays

A common feature of lights-on bioreporters that enables them to be useful in work with contaminated samples is that they are, by design, to some extent resistant to their toxic target analytes. In zntA, resistance to Cd and Pb toxicity is mediated by the *zntA* gene, which encodes a metal efflux pump that enables the reduction of intracellular toxic metals (Riether et al., 2001), and accordingly, many previous studies have used zntA to measure metal free-ion speciation, i.e., the metal species regarded as causing toxic effects (e.g., Magrisso et al., 2009; Zhang et al., 2017; Zhang et al., 2020a). The method that I use here is well-known and relies on the use of a bioavailability calibration curve (Magrisso et al., 2009) calibrated to the activity of metal free-ion, in this case $a_{Cd^{2+}}$ or $a_{Pb^{2+}}$(activity of Cd^{2+} or Pb^{2+}, respectively). The bioavailability/speciation assay (Zhang et al., 2017, and references therein) entails adding 50 µL of bioreporter cell suspension (OD_{600} = 0.2) to a 96-well white microtiter plate (Nunc, Denmark) followed by adding 50 µL of Cd or Pb standard (prepared per Zhang et al., 2017) or sample. Next, the microplate was incubated at 26 °C with a rotation speed of 180 rpm and bioluminescence was measured every 10 minutes for 3 hours using a luminometer (Varioskan LUX, Thermo Fisher Scientific, USA). Since for some experiments I needed to collect both bioluminescence and fluorescence readings in one measurement (discussed below), a single type of white microtiter plate was used for internal consistency. Bioluminescence response was calculated as maximum response ratio (MRR, $MRR = RLU_{C_M,\,max}/RLU_{0,\,max}$, where $RLU_{C_M,\,max}$ is the maximum response, in

relative luminescence units or RLU, for metal concentration C_M, and $RLU_{0,max}$ is the maximum response of the blank, per Zhang et al., 2017). The LOD was calculated as signal greater than three times the standard deviation of the blank, and the limit of quantitation (LOQ) as three times the LOD (Shrivastava, 2011).

Bioreporter toxicity assays

While lights-on bioreporters do typically have characteristics that convey resistance to toxic effects from the chemical species on which they report, for zntA toxic effects from Cd and Pb nonetheless occur given high enough levels (Riether et al., 2001). Since this is the first time that I know of for a lights-on bioreporter to be used for toxicity studies or in a BLM context, and a low bioluminescence signal can equally well result either from low $a_{Cd^{2+}}/a_{Pb^{2+}}$ or bioluminescence inhibition due to toxicity at high $a_{Cd^{2+}}/a_{Pb^{2+}}$, I employed the well-known LIVE/DEAD toxicity bioassay as a benchmark for toxicity studies. Using the LIVE/DEAD® BacLight™ Bacterial Viability Kit (L13152, Thermo Fisher), live and dead cells were differentiated, respectively, by SYTO 9 and propidium iodide (PI) staining (Stocks, 2004).

To perform the LIVE/DEAD assay, a working solution of the LIVE/DEAD staining reagent was made by mixing solubilized SYTO 9 and PI dyes from the kit to achieve a final concentration of 12 μM SYTO 9 and 60 μM PI. To perform LIVE/DEAD experiments, 100 μL of the prepared LIVE/DEAD working solution was added to each well of the microplate 1:1 with cell suspensions to stain live and dead cells, and then mixed thoroughly by pipette. After 15 minutes' incubation in the dark at room temperature, the fluorescence emission at 490–700 nm (emission maxima, λ_{max}, for SYTO 9 and PI being 500 and 635 nm,

respectively) was then measured according to the L13152 kit protocol, with excitation at 470 nm. The LIVE/DEAD fluorescence emission ratio, $\lambda_{\text{max, SYTO 9}}/\lambda_{\text{max, PI}}$, was calculated from spectra. Calibration plots of $\lambda_{\text{max, SYTO 9}}/\lambda_{\text{max, PI}}$ versus the ratio of live-to-dead cells, $R_{\text{L/D}}$, were constructed using mixtures of live and dead zntA prepared according to the L13152 kit protocol. Subsequently, for LIVE/DEAD toxicity assays, 100 µL of working solution was added to each well 1:1 with activated bioreporter solutions (i.e., 50 µL of bioreporter cell suspension + 50 µL of Cd or Pb standard/sample) and mixed, and after incubation the $R_{\text{L/D}}$ metric of toxic effect was determined.

LIVE/DEAD toxicity measurements were always performed immediately after bioreporter bioluminescence measurements to quantify bioluminescence inhibition, per the common approach to toxicity measurements for lights-off bioreporters (An et al., 2012; Qu et al., 2013). Here I test whether such an approach is extensible to lights-on reporter measurements. In my experimental protocol, speciation, as $a_{\text{Cd}^{2+}}$ or $a_{\text{Pb}^{2+}}$, is measured in ranges for which bioreporter bioluminescence increases as a function of increasing activity of metal free-ion, until a transition point is reached wherein bioluminescence decreases in a sigmoidal fashion consistent with toxic effect. While lights-on reporters are not normally used for toxicity work, it is normal to combine cell viability tests with lights-on reporter speciation measurements to ensure that low bioluminescence results from low activity of metal free-ion and not toxicity. For instance, Buffi et al (2011) measured cell viability during lights-on bioreporter studies using the approach that I use here. For the assay to measure toxicity via bioreporter bioluminescence inhibition, toxic effect is expressed as

R_{Lum} = MRR_{Ci}/MRR_{0i}, where MRR_{0i} is the maximum response with zero inhibition and MRR_{Ci} is the MRR at some concentration, C_i, at which bioluminescence is inhibited by Cd or Pb.

Experiments on the effect of inorganic cations and dissolved organic matter on Cd and Pb bioavailability/speciation and toxicity assays

Table 2-1 summarizes the experiments performed in this study in order to build and validate BLM models. Regarding parameterization of BLM models for zntA, no further information was needed for speciation, since the BLM run in speciation mode requires no specific organism-dependent parameters. For BLM run in toxicity mode, parameterization is needed, and it is necessary to first characterize the individual effect of cations Ca, Mg, K and Na (major inorganic constituents) on Cd and Pb toxicity. The Cd and Pb toxicity tests for BLM parameterization contained four sets of major cation concentrations, referred to as Ca-set, Mg-set, K-set and Na-set. Each set was composed of a series of media having different concentrations of one target cation, with the remaining major cation and other component concentrations being fixed (US EPA, 2003). For each specific target cation concentration in each set, toxicity bioassays across a range of Cd or Pb concentrations were conducted, allowing the calculation of the EC_{50} (Sebaugh, 2011) and the subsequent systematic analysis of the effects of inorganic cations on EC_{50}.

Subsequent to construction of the BLM toxicity model for zntA, validation experiments were conducted for BLM performance in speciation- and toxicity-mode calculations. For parameterization of the zntA BLM model, experiments with dissolved organic matter (DOM) were not needed, however, for validation

experiments it was desirable to test effects of varying both cations and DOM. To investigate the effect of DOM on Cd and Pb bioavailability, humic acid (HA) was selected to represent DOM as, in aqueous systems, HA is typically the fraction of DOM that is prevalent and most strongly complexes bivalent metals (Coles and Yong, 2006; Shahid et al., 2012; Schwarzenbach et al., 2016). HA (Alfa Aesar, Tianjin, China) stock solutions were prepared according to the method of Zhang et al. (2017). The concentrations of the prepared HA stock solutions were verified using a total organic carbon (TOC) analyzer (multi N/C®3100, Analytikjena, Germany). Per Zhang et al. (2017), solutions with different HA concentrations were spiked with Cd or Pb standard and stored in the dark overnight at room temperature to allow equilibration of metal complexation with HA before use (Sander et al., 2004).

Bioavailability of Cd or Pb in metal-spiked HA solutions was determined as described above. Measurements were also made to monitor bioreporter response in the presence of HA and absence of Cd or Pb (i.e., to see if the HA alone had any effect on the bioreporter, such as affecting growth), and results from these experiments showed the same (to within experimental precision) very slow and monotonic increase in OD_{600} with time as I observe in the same concentration of MM (without HA). A similar approach was used for organic matter experiments as for cations wherein DOM was varied while all other components were held constant. There were three types of validation experiments, two using lab-prepared samples to mimic the environmental variability of cations and/or HA, and the third type of validation experiment used real complex matrix environmental field samples.

Table 2-1. Chemical composition of the test media for different types of experiments conducted[a].

Components in solution, as prepared[b] or as analyzed[c]:					
	Ca (mM)	Mg (mM)	K (mM)	Na (mM)	DOM[c]
MM ("Control")	0.10	0.50	10.	54	NA
Experiments for parameterization of the zntA BLM toxicity model, by series:					
Ca-set	0.01, 0.10, 0.58, 1.1, 3.0, 5.8, 11	0.50	10.	54	NA
Mg-set	0.10	0.005, 0.05, 0.5, 1.5, 2.8, 4.0, 5.0	10.	54	NA
K-set	0.10	0.50	0.025, 0.25, 1.3, 2.5, 10, 18, 25	54	NA
Na-set	0.10	0.50	10.	14, 20., 23, 28, 43, 54, 83	NA
Speciation-mode calculation validation experiments, by series[d]:					
SV-Ca	0.01, 11	0.50	10.	54	NA
SV-Mg	0.10	0.005, 5.0	10.	54	NA
SV-K	0.10	0.50	0.025, 25.	54	NA
SV-Na	0.10	0.50	10.	14, 80.	NA
SV-HA	0.10	0.50	10.	54	0–19.6 $mg{\cdot}L^{-1}$ [e]
Toxicity mode calculation validation experiments, by series[d]:					
TV-C1	1.0	0.50	2.0	85	NA
TV-C2	9.0	0.50	5.0	59	NA
TV-C3	5.0	1.0	3.0	24	NA
TV-C4	15	3.5	2.5	20.	NA
TV HA-C1	0.10	0.50	10.	27	5.0
TV HA-C2	1.0	1.0	2.0	85	10.
TV HA-C3	15	3.5	2.5	20.	20.
TV LT-St 7[b]	22	7.3	5.0	39	0.75 µM[f]
TV LT-St 26[b]	33	7.7	4.8	36	0.48 µM

[a] Concentrations are reported in units that correspond to BLM software inputs. This is M for cations and dissolved organic matter modeled as aqueous-phase, and $mg{\cdot}L^{-1}$ for HA modeled using the Stockholm Humic Model (Section 2.3). [b] The concentrations of cations in all test media except Lake Tai were as prepared. [c] The concentrations of humic acid (HA) and the cations in Lake Tai were as analyzed. [d] Abbreviations: speciation validation (SV); toxicity validation-cations (TV-C), where C represents a randomly chosen combination of concentrations for Ca, Mg, K, Na; toxicity validation with HA and cations (TV HA-C); Lake Tai (LT), Station (St). [e] The amount of HA in solutions used in speciation validation is 16 in total, arranged as a dilution series with a maximum of 19.6 $mg{\cdot}L^{-1}$, decreasing by a factor of two (16 HA concentrations) plus 1 control without HA). [f] The HA concentrations in LT samples were reported in Zhang et al. (2020c).

The first type of validation involved testing samples containing different concentrations of major cations, according to extrema for speciation

(representative low and high values, SV-cation series, Table 2-1) and varied randomly for toxicity (i.e., randomly chosen variation of cations within the range of extrema, TV-C series, Table 2-1). Solutions were spiked with Cd or Pb, equilibrated and tested. For the second type of validation experiment, a range of HA solutions were prepared, holding cation concentrations constant for speciation (SV-HA, Table 2-1). For toxicity, three different HA solutions with cation concentrations varied randomly (TV HA-C series, Table 2-1) were made. Solutions were subsequently spiked with different concentrations of Cd and Pb, equilibrated and tested. The third exercise for validation involved testing natural water samples from Lake Tai[1] (TV LT-St series, Table 2-1) collected at stations that are routinely monitored by NIGLAS (Nanjing Institute of Geography and Limnology, Chinese Academy of Sciences, Zhang and Chen, 2011). These water samples were chosen as they were characterized as part of an investigation of metal bioavailability-based risk assessment (Zhang et al., 2020a; Zhang et al., 2020c). Table 2-1 summarizes major cation and DOM/HA concentrations of these samples; see Table 2-2 for the detailed results from water quality analysis of those water samples. Water samples were filtered through a pre-combusted 45 mm Whatman GF/F glass fiber filters (nominal pore size 0.7 mm) and then spiked with different concentrations of Cd or Pb standards allowed to equilibrate overnight and tested. Speciation and toxicity measurements for Cd and Pb for all types of validation experiments were measured per Section 2.2.

[1] Taihu, 太湖, in Chinese.

Table 2-2. Chemical and physical properties of water samples from Lake Tai[1].

Parameter	Units	LT-St 7	LT-St26
pH	pH units	7.94	8.21
COD	($mg \cdot L^{-1}$)	4.88	3.91
DO	($mg \cdot L^{-1}$)	6.51	7.83
BOD	($mg \cdot L^{-1}$)	2.09	1.63
NH_4^+	($mg \cdot L^{-1}$)	0.36	0.06
NO_2^-	($mg \cdot L^{-1}$)	0.016	0.002
NO_3^-	($mg \cdot L^{-1}$)	0.090	0.069
TDN	($mg \cdot L^{-1}$)	0.76	0.45
TN	($mg \cdot L^{-1}$)	1.57	1.08
PO_4^{3-}	($mg \cdot L^{-1}$)	0.029	0.007
TDP	($mg \cdot L^{-1}$)	0.06	0.01
TP	($mg \cdot L^{-1}$)	0.14	0.06
Chl-a	($\mu g \cdot L^{-1}$)	22	17
DOC	($mg \cdot L^{-1}$)	4.85	3.25
Ca^{2+}	($mg \cdot L^{-1}$)	5.01	4.76
Mg^{2+}	($mg \cdot L^{-1}$)	39.33	36.40
K^+	($mg \cdot L^{-1}$)	21.81	32.88
Na^+	($mg \cdot L^{-1}$)	7.31	7.70
Cl^-	($mg \cdot L^{-1}$)	44.56	42.96
SO_4^{2-}	($mg \cdot L^{-1}$)	51.86	52.95
Transp	(m)	0.30	0.30
Cond	($\mu S \cdot cm^{-1}$)	440	485

[1]Abbreviations are dissolved oxygen (DO), Biological oxygen demand (BOD), chemical oxygen demand (COD), ammoniacal nitrogen (NH_4^+), nitrate (NO_3^-), nitrite (NO_2^-), total dissolved nitrogen (TDN), total nitrogen (TN), phosphate radical (PO_4^{3-}), total phosphorus (TP), total dissolved phosphorus (TDP), chlorophyll-a (Chl-a), dissolved organic carbon (DOC), chloride (Cl^-), sulfate (SO_4^{2-}) and electrical conductivity (Cond).

2.3 Biotic Ligand Model Parameterization and Associated Data Analysis

Formal derivation of the full set of equations describing BLM parameterization has been well-documented elsewhere (US EPA, 2003). For brevity, here I summarize those expressions and equations that are needed in practice. The affinities of Cd/Pb metal cations for binding to BL sites are represented by complexation/association constants, K_{MBL}, the relevant expressions governing

complexation being written as follows (US EPA, 2003):

$$M^{n+} + BL^{-1} \leftrightarrow MBL^{n-1}, \text{ and} \quad (2\text{-}1a)$$

$$K_{MBL} = \frac{a_{MBL^{n-1}}}{a_{M^{n+}} \cdot a_{BL^{-1}}}, \quad (2\text{-}1b)$$

where the charges and reaction stoichiometry are operationally assumed, $a_{M^{n+}}$ is the activity of the toxic metal (Cd or Pb, bivalent), $a_{BL^{-1}}$ is the BL free site activity, and $a_{MBL^{n-1}}$ is the activity of the MBL^{n-1} complex.

While I use M in the sense of toxic metal, the same expressions in eq. 2-1a and 2-1b would also apply to Ca, Mg, K, Na binding with BL, in which case a system of four major cation equations exist, which can be solved for $K_{cationBL}$ values using a matrix expression if the relationships that specify how major cations affect EC_{50} are known. Linear regression analysis of EC_{50} versus cation free-ion activity expresses these EC_{50}-cation relationships linearly in the form of a slope, *m,* and an intercept, *b*. From *m* and *b* the ratio R_{cation} (m/b) is calculated, and the resulting matrix expression is as follows (US EPA, 2003):

$$\begin{pmatrix} 1 & -R_{Ca} \cdot a^{Ca}_{Mg^{2+}} & -R_{Ca} \cdot a^{Ca}_{K^{+}} & -R_{Ca} \cdot a^{Ca}_{Na^{+}} \\ -R_{Mg} \cdot a^{Mg}_{Ca^{2+}} & 1 & -R_{Mg} \cdot a^{Mg}_{K^{+}} & -R_{Mg} \cdot a^{Mg}_{Na^{+}} \\ -R_{K} \cdot a^{K}_{Ca^{2+}} & -R_{K} \cdot a^{K}_{Mg^{2+}} & 1 & -R_{K} \cdot a^{K}_{Na^{+}} \\ -R_{Na} \cdot a^{Na}_{Ca^{2+}} & -R_{Na} \cdot a^{Na}_{Mg^{2+}} & -R_{Na} \cdot a^{Na}_{K^{+}} & 1 \end{pmatrix} \begin{pmatrix} K_{CaBL} \\ K_{MgBL} \\ K_{KBL} \\ K_{NaBL} \end{pmatrix} = \begin{pmatrix} R_{Ca} \\ R_{Mg} \\ R_{K} \\ R_{Na} \end{pmatrix}, \quad (2\text{-}2)$$

where, for instance, $a^{Ca}_{Mg^{2+}}$ is the activity of Mg^{2+} in the Ca-set (Table 2-1). After solving eq. 2-2 for $K_{cationBL}$, additional parameters are needed to describe the interaction of M with BL. The total activity of BL sites (a_{TBL}) is a sum of all BL species, the expression for which can be rearranged to express the fraction, *f*, of BL sites occupied by M, according to

$$a_{\mathrm{TBL}} = a_{\mathrm{BL}^{-1}}(\sum_{\mathrm{BLspecies}}), \tag{2-3a}$$

and

$$f = \frac{a_{\mathrm{MBL}}}{a_{\mathrm{TBL}}} = K_{\mathrm{MBL}} \cdot a_{\mathrm{M}^{\mathrm{n+}}}/(\sum_{\mathrm{BLspecies}}), \tag{2-3b}$$

where

$$\sum_{\mathrm{BLspecies}} = 1 + K_{\mathrm{CaBL}} \cdot a_{\mathrm{Ca}^{2+}} + K_{\mathrm{MgBL}} \cdot a_{\mathrm{Mg}^{2+}} + K_{\mathrm{KBL}} \cdot a_{\mathrm{K}^{+}} + K_{\mathrm{NaBL}} \cdot a_{\mathrm{Na}^{+}} + K_{\mathrm{MBL}} \cdot a_{\mathrm{M}^{\mathrm{n+}}}.$$

The quantity f is related to the toxicity imposed on an organism by a metal toxicant (Brown and Markich, 2000), and K_{MBL} is obtained as a fitting parameter from the optimized relationship between the logit-transformed toxic effect ($R_{\mathrm{L/D}}$ or R_{Lum}) plotted versus f, (eq. 2-3b). The specific fraction of BL sites occupied by M at the EC_{50}, f_{crit} (critical fraction), is the x-intercept of this plot.

The BLM, and indeed all speciation models in common use, are based on the Tableau method of Morel (1983), which entails using total concentrations (e.g., Table 2-1) as model component inputs, with outputs being speciation in concentration or activity. Since Ks as referred to above are thermodynamic quantities, activity is used. In literature however, particularly toxicity literature, total concentration is more common, for instance as the abscissa in dose-response curves or reported EC_{50}s. In discussing my results, activity was used for BLM parameterization and validation. Total concentration was used when comparing my results to literature findings. I have already introduced the symbol a for activity. Hereafter I use C to refer to total concentration.

Dose-response curves (Ritz, 2010) were used to determine EC_{50}s for both LIVE/DEAD and bioluminescence inhibition toxicity assays via nonlinear fitting

using OriginLab software and the following sigmoidal function:

$$R_{\text{toxic effect}} = \frac{1}{1+10^{(\text{LOGEC}_{50}-a_{\text{M}^{n+}})p}}, \quad (2\text{-}4)$$

where $R_{\text{toxic effect}}$ is either $R_{\text{L/D}}$ or R_{Lum} (for LIVE/DEAD or bioluminescence inhibition assays, respectively) and p is the slope at the steepest part of the curve, also known as the Hill slope for the sigmoidal dose-response curve.

For BLM toxicity model parameterization, values for m and b that are needed to calculate R_{cation}s in eq. 2-2 were obtained by linear regression analysis of EC_{50} versus major cation free-ion activity. A one-tailed t-test was used to confirm $m > 0$, which in turn determines whether data for any given major cation is used in parameterization of BLM models. The K_{cationBL} parameters required for BLM metal toxicity predictions were obtained by solving eq. 2-2 using R (R Core Team, 2020). The 95% confidence limits for K_{cationBL} were calculated by performing 1000 Monte Carlo simulations of R_{cation} based on uncertainty in measured m and b, followed by solution of eq. 2-2. (de Schamphelaere and Janssen, 2002). Subsequently, K_{MBL} and f_{crit} were determined via optimization of the logit toxic response versus f plot.

Speciation and toxicity-mode calculations were performed using Visual MINTEQ 3.1 (VM, Gustafsson, 2014). These calculations involved component inputs, comprised of C_{Cd}, C_{Pb}, C_{Ca}, C_{Mg}, C_{K}, C_{Na}, and $C_{\text{DOM/HA}}$, as well as total concentrations of all other MM constituents (Section 2-2, Table 2-1) and yield species outputs in activity. In both speciation and toxicity calculations, DOM does not directly interact with the BL, however it has a competitive effect via complexing toxic metal. For experiments utilizing commercially purchased HA, the standard parameterization of M-DOM binding in the Stockholm Humic Model (SHM) in

VM was retained (Zhang et al., 2017, 2020a). For toxicity predictions for experiments utilizing Lake Tai natural water samples, DOM-specific values of K_{PbHA} from Zhang et al (2020a) were used, and values of K_{CdHA} were determined according to the approach of Plaza et al (2006) based on relationships between Cd and Pb binding. All BLM toxicity predictions were run with the parameters $K_{cationBL}$, K_{MBL} and $f_{crit,}$ determined as described herein, to obtain predicted EC_{50} for any given sample composition.

2.4 BIOAVAILABILITY AND BLM SPECIATION-MODE RESULTS

For bioreporter measurement of speciation, it is first necessary to construct bioavailability calibration curves (Magrisso et al., 2009). Figure 2-2A–D shows the bioluminescence response of zntA subsequent to activation with Cd and Pb. Figures 2-2A and 2-2B display the kinetics of the bioluminescent response (in RLU) versus time and as a function of C_{Cd} and C_{Pb}, respectively. After the bioreporter is exposed to Cd or Pb, the bioluminescence response increases over time, typically reaching maximum bioluminescence at ~180 minutes. Figures 2-2C and 2-2D show three representative bioavailability calibration curves (independent experiments) (Magrisso et al., 2009), for which response is reported as the MRR versus $a_{Cd^{2+}}$ or $a_{Pb^{2+}}$, respectively. The MRR results of three independent experiments are similar, and the average relative standard deviation (RSD) of replicates for each experiment was lower than 8%, which represents excellent precision for this type of biological measurement. The zntA LOQ for Cd and Pb in MM ("control" or reference), expressed as C_{Cd} and C_{Pb}, is 0.0011 mg·L^{-1} and 0.015 mg·L^{-1}, respectively.

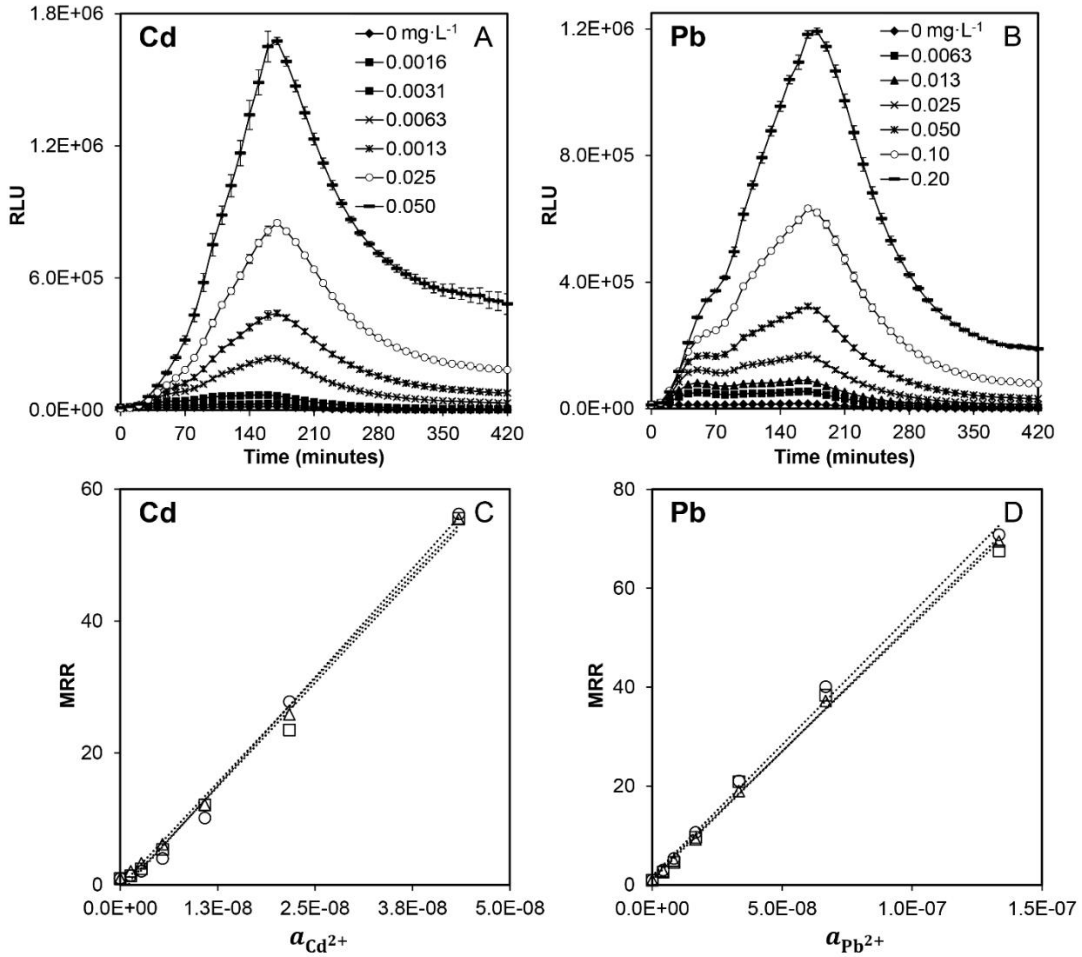

Figure 2-2. Bioreporter bioluminescent response kinetics and bioavailability calibration curves. Response kinetics (in RLU) of bioreporter strain zntA are shown over time and as a function of (A) C_{Cd} and (B) C_{Pb} in standards, and representative examples of the resulting bioavailability calibration curves (three independent experiments represented by circles, triangles, squares to differentiate each experiment three) for MRR versus (C) $a_{Cd^{2+}}$ and (D) $a_{Pb^{2+}}$. Per the expression for MRR given in Section 2.2, the time of maximum intensity is not specified, as these may vary slightly from experiment to experiment and from strain to strain. The Pearson R^2 for all lines in panels C–D is consistently > 0.99.

It has long been recognized that both inorganic and organic constituents of environmental samples can strongly affect the speciation, and thus bioavailability, of metals (Morel and Hering, 1993; Scwarzenbach et al., 2002). To measure how such constituents affect metal free-ion speciation, I designed experiments keeping the C_{Cd} or C_{Pb} constant and varying C_{Cation} (inorganic) or

C_{HA} (organic). As C_{Cd} or C_{Pb} increases, $a_{Cd^{2+}}$ or $a_{Pb^{2+}}$, the bioavailable toxic metal free-ion, will increase to a greater or lesser extent, depending upon the reactions with major cations and/or HA in solution.

Figure 2-3A–B shows the measured and predicted $a_{Cd^{2+}}$ and $a_{Pb^{2+}}$ for the speciation-mode validation experiments listed in Table 2-1. The solid black line indicates exact agreement between measured and predicted, and the dashed lines indicate a factor of twice the average relative percent difference (RPD) between measured and predicted over the range of Cd and Pb response, pooled (all measurements, speciation and toxicity) to provide a common indicative metric. I use average RPD as a nominal guideline; my average RPD of 12% reflects how results I report herein are consistently well below the validation guideline that measured and predicted response should agree within a factor of two (Zhang et al., 2020a; US EPA, 2003).

For major cations, the agreement between predicted and measured $a_{Cd^{2+}}/a_{Pb^{2+}}$ is generally distributed about the black line that represents exact agreement, and free-ion activity increases with increasing total concentration. For DOM, I find that, as HA increases, the bioavailability of Cd and Pb decreases, and results here are in very close agreement with Zhang et al.'s (2017) previous findings for Pb. The average RPD for predicted and measured $a_{Cd^{2+}}/a_{Pb^{2+}}$ for HA speciation was 22%, which is higher than for major cations. The least favorable agreement is for Pb at lower $a_{Pb^{2+}}$, and in Figure 2-3A–B I see that for Cd and Pb, agreement is better at higher $a_{Cd^{2+}}/a_{Pb^{2+}}$, and vice versa, with a slight bias toward overestimation and underestimation of predictions for Cd and Pb, respectively, at lower $a_{Cd^{2+}}/a_{Pb^{2+}}$. This may be due in part to values that are

approaching LOQ, however, published work in which I contributed as an author and the published work of others have previously documented the shortcomings of one-size-fits all models such as the SHM for describing M-HA speciation (Mostofa et al., 2013; Ahmed et al., 2014; Zhang et al., 2020a and 2020c). Working with colleagues in my doctoral research group, while we do use one-size-fits-all models for some work, we have found much better agreement when using M-HA models based on our own parameterization of M-HA binding (Zhang et al., 2020a), however, obtaining bespoke parameters is more experimentally intensive, with models such as the SHM being more convenient.

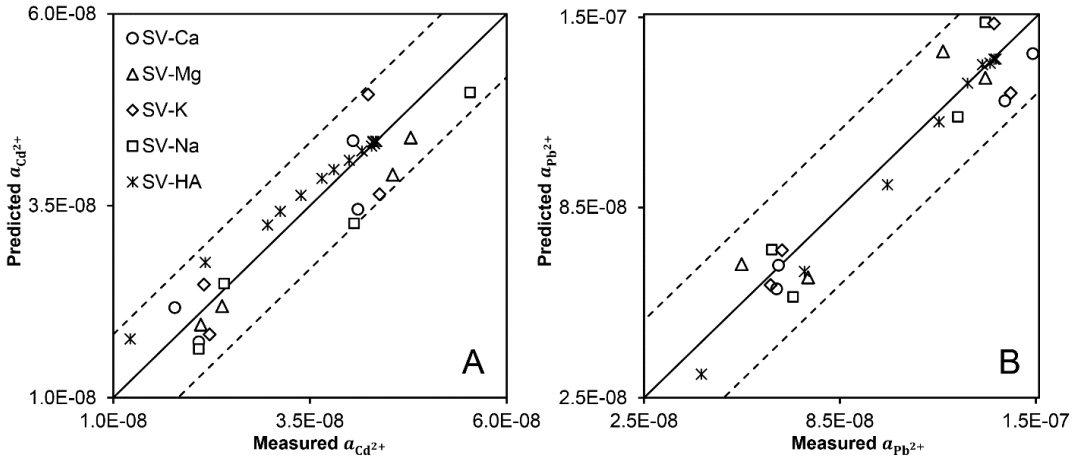

Figure 2-3. Effects of major cations and HA on predicted versus measured Cd and Pb free-ion. (A) $a_{Cd^{2+}}$, and (B) $a_{Pb^{2+}}$. Note that $a_{Cd^{2+}}/a_{Pb^{2+}}$ increase as C_{Cd}/C_{Pb} increase. For panels A and B the solid line indicates an exact match between measured and predicted $a_{Cd^{2+}}/a_{Pb^{2+}}$, and the dashed lines a factor of twice the pooled average RPD between measured and predicted over the range of Cd and Pb response. All of the results I report herein are below the accepted validation guideline that measured and predicted response to agree within a factor of two.

2.5 USING A LIGHTS-ON BIOREPORTER TO MEASURE TOXICITY, TOWARDS TOXICITY PREDICTION

Results from LIVE/DEAD toxicity measurements

The results discussed in Section 2.4 are consistent with other reports (Hynninen and Virta, 2009; Zhang et al, 2017; Hansen et al., 2019) adducing how bioreporter measurements are used in the study of speciation. I have not found reports detailing the use of a lights-on bioreporter to measure toxicity, thus the point of departure in toxicity studies was to use a standard method such as LIVE/DEAD for comparison. According to the manufacturer's protocol for the LIVE/DEAD kit, I first conducted preliminary experiments with different percentages of live and dead zntA cells to optimize dye ratios and experimental conditions, then, I subsequently performed experiments determining the EC_{50}s for Cd and Pb. The experiments performed to parameterize the Cd and Pb BLMs for toxicity are given in Table 2-1, and representative results from these experiments are shown in Figure 2-4. The results in Figure 2-4A show fluorescence spectra for different percentages of live (higher fluorescence signal at 505 nm from SYTO 9) to dead (higher fluorescence signal at 645 nm from PI) zntA cells after dyeing with the LIVE/DEAD working solution, and Figure 2-4B shows a resulting calibration line. The linear relationship between $\lambda_{\text{max, SYTO 9}}/\lambda_{\text{max, PI}}$ plotted versus $R_{\text{L/D}}$ showed good agreement with manufacturer's protocol specifications, confirming that the LIVE/DEAD method was suitable for toxicity experiments with zntA. Figures 2-4C–F show fluorescence spectra (C and E) and dose-response curves (D and F) in the control medium for Cd and Pb LIVE/DEAD toxicity experiments with zntA.

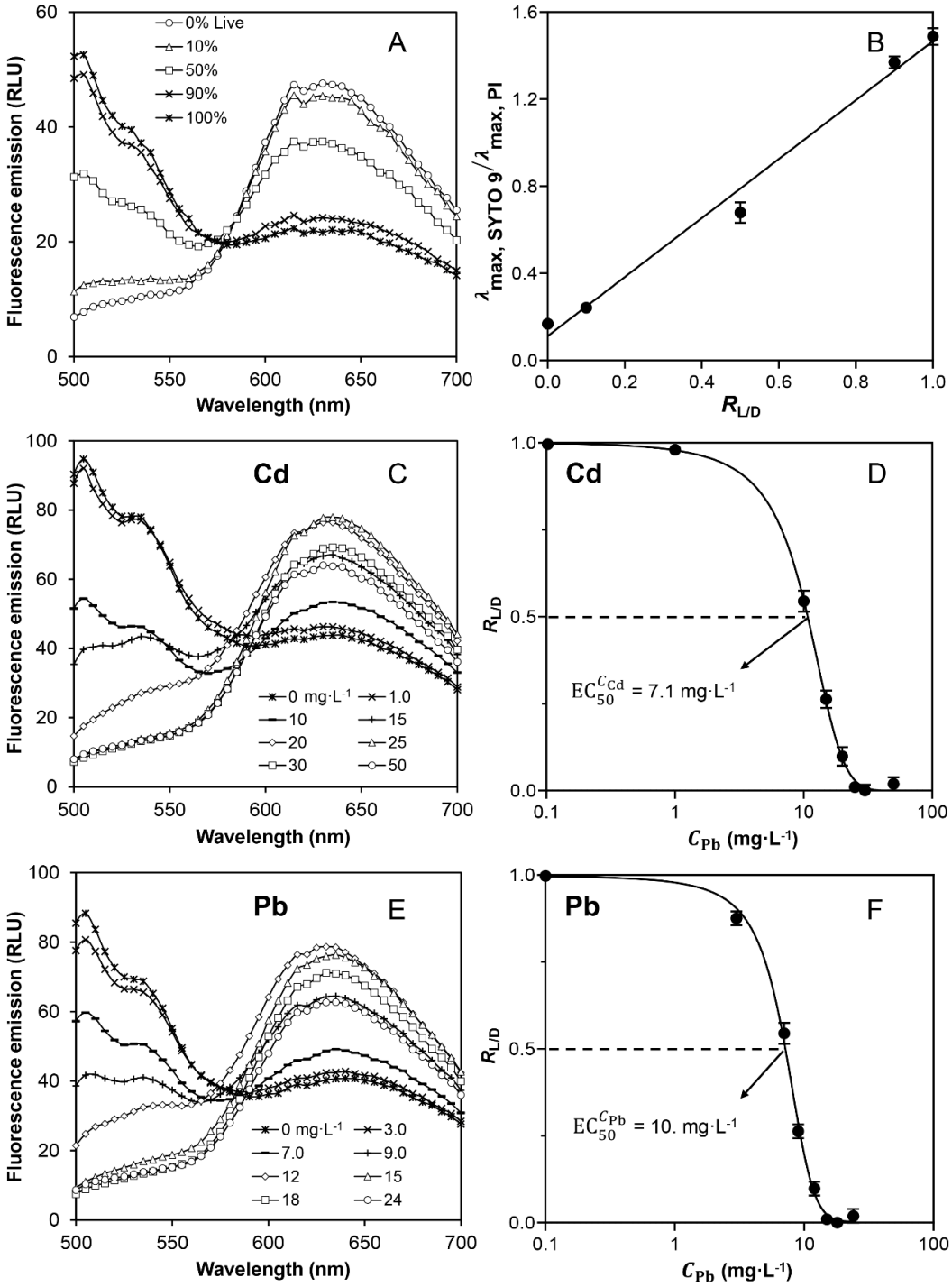

Figure 2-4. Representative fluorescence spectra and dose-response curves for bioreporter LIVE/DEAD experiments. (A) Fluorescence spectra and (B) $\lambda_{\text{max, SYTO 9}}/\lambda_{\text{max, PI}}$ plotted versus $R_{\text{L/D}}$ for experiments varying the percentages of live and dead zntA bioreporter. Panels C–F show representative fluorescence spectra (C and E) and dose-response curves (D and F) for zntA toxicity experiments with Cd (C–D) and Pb (E–F), respectively in the control medium.

For the control, I found an $EC_{50}^{C_{Cd}}$ of 7.1 mg·L^{-1} compared to an $EC_{50}^{C_{Pb}}$ of 10. mg·L^{-1}, indicating that these two metals are similarly toxic to zntA. One recent report for the green algae *Chlamydomonas reinhardtii*, frequently investigated for its resistance to metals, also found less tolerance to Cd ($EC_{50}^{C_{Cd}}$~13 mg·L^{-1}) than to Pb ($EC_{50}^{C_{Pb}}$~30 mg·L^{-1}, Li et al., 2021). Meanwhile, the World Health Organization (WHO, 2013) has set guidance levels for drinking water quality for C_{Cd} and C_{Pb} at 0.001 and 0.005 mg·L^{-1}, respectively. Results from my and Li et al.'s (2021) acute toxicity tests on lower organisms and the WHO exposure metrics for humans indicate that the hazards posed by Cd, in comparison to Pb are of the same order of magnitude in each case, albeit with lower metrics for Cd (i.e., lower levels being associated with greater exposure hazard/acute toxicity).

For BLM parameterization, I used the LIVE/DEAD method to determine $EC_{50}^{a_{Cd^{2+}}}$ and $EC_{50}^{a_{Pb^{2+}}}$ and how these vary as a function of major cation free-ion activities, results for which are shown in Figure 2-5. All four major cations have a protective effect on the toxicity of Cd. The results are different for Pb; only Ca and Mg have a protective effect on the toxicity of Pb, whereas increasing K and Na appear to promote Pb toxicity nonlinearly. Similar results have been found by An et al. (2011) for Cd and Pb effects on the bacterium *Vibrio fischeri*; these authors did not discuss their observations of this effect, and omitted these alkaline metals in their BLM parameterization. Kim et al. (2002) observed that increases in Ca and Mg aqueous free-ion decreased the bioaccumulated Cd and Pb in rice roots, however K did not diminish Cd and Pb bioaccumulation. The effect that I observe for K and Na on Pb in Figure 2-5C–D was also found for copper (Cu) by de Schamphelaere and Janssen (2002) with *Daphnia magna*.

These authors remarked upon the effect, however, gave no explanation of possible reasons behind behind it. Gao et al. (2020), in studying the toxicity of Cu to *Danio rerio*, reported the slope for EC_{50}s versus K and Na activities were not differentiable from zero. Similar to my results, Qu et al. (2013) also observed the non-protect effects of K for Cd toxicity on the bacterium *Photobacterium phosphoreum*; these authors theorized that Cd might inhibit Na^+/K^+-ATPase in a variety of tissues, such that increases in K will promote the excretion of Na by cells, making *P. phosphoreum* more sensitive to Cd. This explanation seems reasonable, but since Qu et al. (2013) did not vary Na in their toxicity tests, their explanation may not be suitable to explain why both K and Na lack the protective effect in the case of my observations and those of other authors cited above. The non-protective effect found in An et al. (2011), Qu et al. (2013), and de Schamphelaere and Janssen (2002) looks very similar to my results here in Figure 2-5 (C and D), exhibiting a behaviour that is fitted better with a decreasing logarithmic function rather than a linear decrease. Since I do not have a suitable explanation for the effect that would also support cogent parameterization, I do as others and omit K and Na from calculations for K_{KBL} and K_{NaBL} for Pb. Since the effect has been observed for multiple metals and is not limited to bacteria, it would seem to warrant more detailed investigation.

Results from bioluminescence inhibition toxicity measurements

Subsequent to characterizing Cd and Pb toxicity using the LIVE/DEAD method, I was interested to see how the results based on bioreporter bioluminescence inhibition might compare, representative results from which using the control medium are shown in Figure 2-6. I generally find that dose-response curves

based on bioluminescence inhibition are quite similar to those obtained with the LIVE/DEAD method. For instance, when comparing toxicity in the same medium measured by the standard toxicity method LIVE/DEAD in Figure 2-4 to the bioluminescence inhibition results in Figure 2-6, I find that the $EC_{50}^{a_{Cd^{2+}}}$ is 5.2 mg·L^{-1} and 7.1 mg·L^{-1} for bioluminescence and LIVE/DEAD, respectively, and for $EC_{50}^{a_{Pb^{2+}}}$ the values are both 10. mg·L^{-1}.

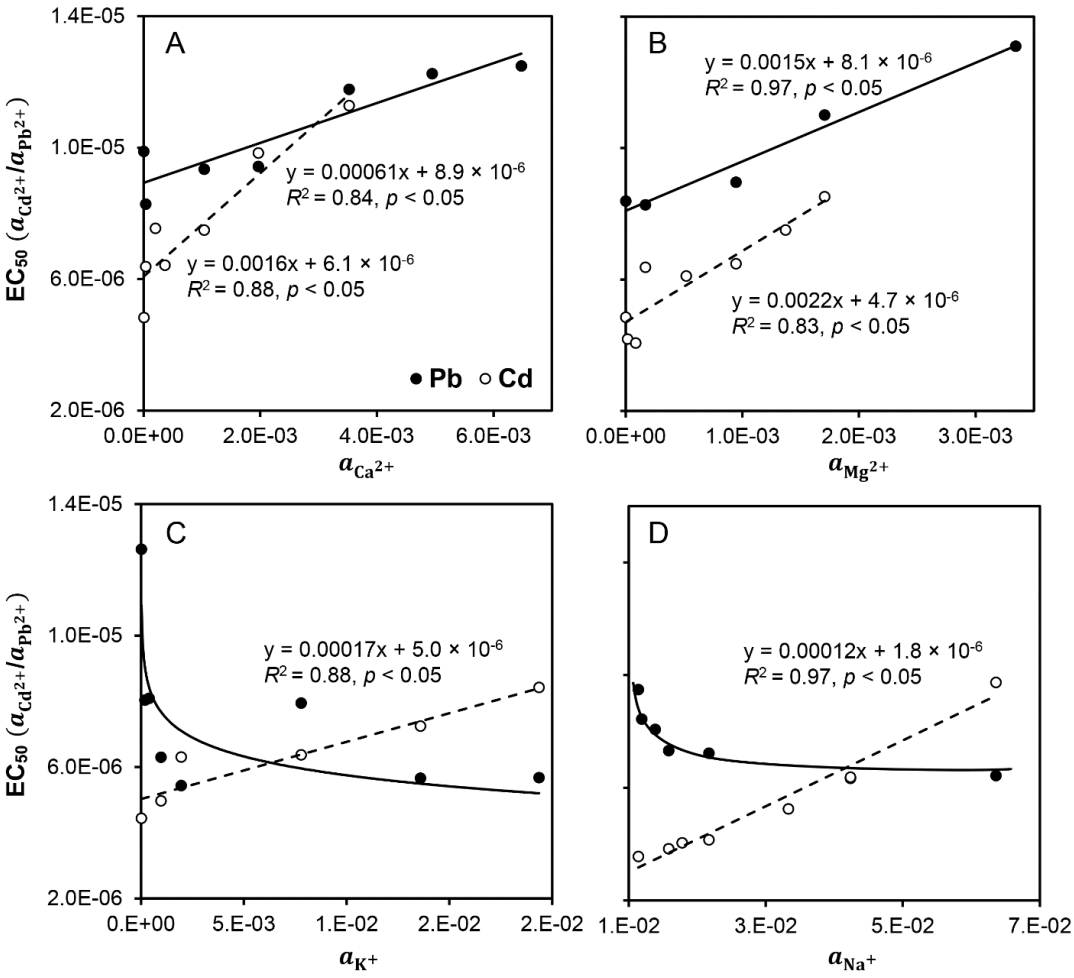

Figure 2-5. EC_{50} versus major cations for LIVE/DEAD toxicity experiments. Effects of competing/major cation free-ion activities on $EC_{50}^{a_{Cd^{2+}}}$ (hollow circles) and $EC_{50}^{a_{Pb^{2+}}}$ (filled circles) are shown in the four panels A–D.

On average, I find that the EC_{50} I obtain from bioluminescence inhibition for Cd and Pb is, respectively, 83% and 89% of the EC_{50} for these toxic metals that I

obtain with the LIVE/DEAD method and that these differences are both significant at $p < 0.001$. This difference might be viewed as reasonable, due to the uncertainties from sigmoidal curve fitting, and also the endpoint of these two types of toxicity measurement methods are different.

Regarding curve fitting, there is uncertainty in measurement regarding the exact concentration at which MRR_{0i} occurs, which will affect the curve fit. With respect to the measurement endpoint, LIVE/DEAD reflects cell membrane integrity, while bioluminescence inhibition measures cellular metabolic status as bioluminescence is directly linked to respiration, through the electron transport chain. The inhibition of bacterial metabolism is manifested by attenuation of light emittance that occurs at the toxicity level of the tested substance (Girotti et al., 2008). Nonetheless, considering that the generally accepted BLM convention holding that predicted versus measured need to agree to within a factor of two was adopted in view of large uncertainties associated with many types of toxicity test, agreement to within 83 or 89% hardly seems a notable difference, even if statistically significant.

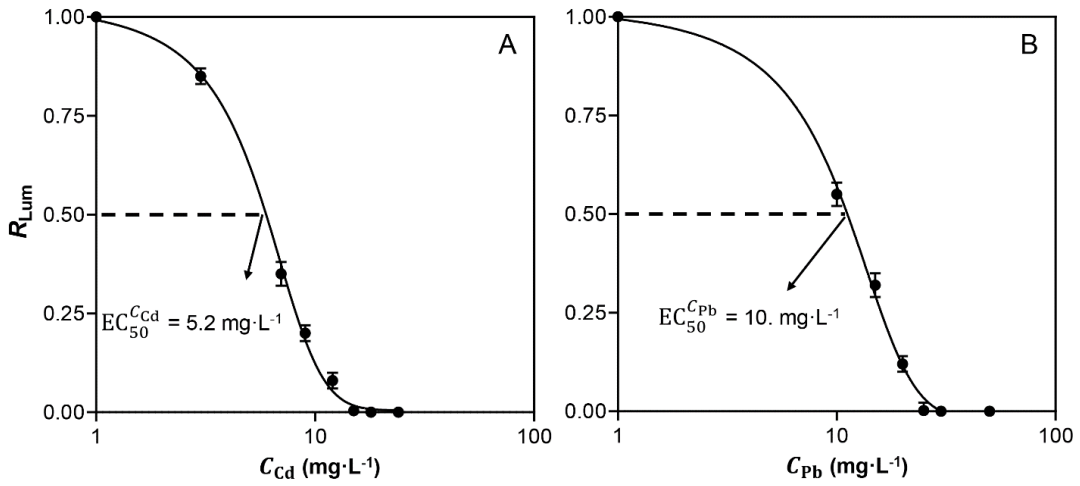

Figure 2-6. Representative dose-response curves for bioluminescence inhibition experiments. Values of R_{Lum} are plotted versus increasing (A) C_{Cd} and (B) C_{Pb} in the control medium.

Figure 2-7 shows $EC_{50}^{a_{Cd^{2+}}}$ and $EC_{50}^{a_{Pb^{2+}}}$ plotted as a function of major cation free-ion activities for toxicity measurements using bioluminescence inhibition. As for the LIVE/DEAD results in Figure 2-5, bioluminescence inhibition experiments also show that K and Na did not have a protective effect with respect to Pb toxicity. Comparing Cd/Pb toxicity measured by LIVE/DEAD (Figure 2-5) to bioluminescence inhibition (Figure 2-7), there is no systematic trend for differences in *m* and *b*, however R_{cation} (described in Section 2.3) is always smaller for LIVE/DEAD compared to the bioluminescence inhibition method.

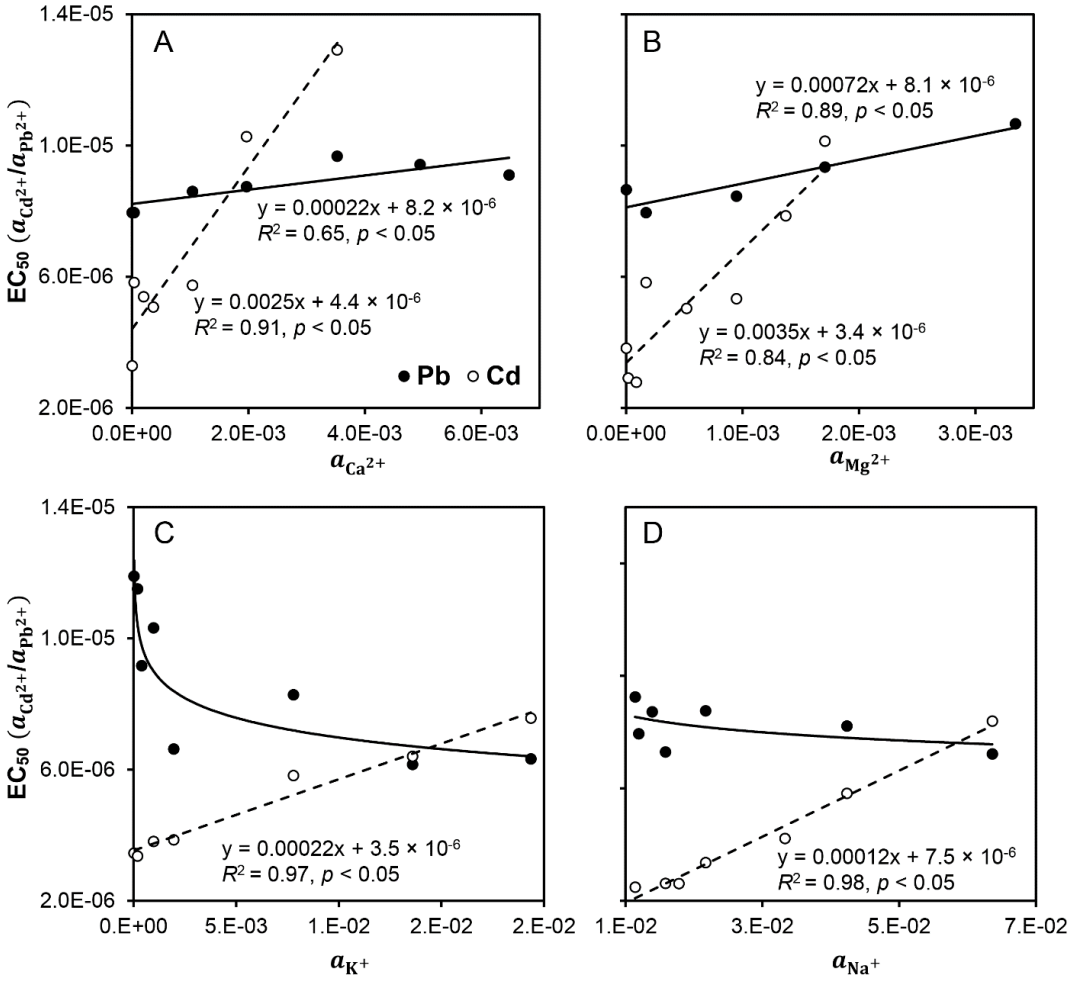

Figure 2-7. EC_{50} versus major cations for bioluminescence inhibition toxicity experiments. Effects of competing/major cation free-ion activities on $EC_{50}^{a_{Cd^{2+}}}$ (hollow circles) and $EC_{50}^{a_{Pb^{2+}}}$ (filled circles) are shown in the four panels A–D.

The value R_{cation} may be thought of as the rate of change of M toxicity as a function of the rate of change of major cation free-ion activity, *m*, normalized to the toxicity of M in the absence of any given major cation, *b*. In physical terms, a smaller R_{cation} indicates that the protective effect of major cations per unit increase in major cation free-ion activity is less as measured by bioluminescence inhibition as compared to LIVE/DEAD. The key issue is how such differences affect model parameterization, which I discuss in the next section.

2.6 Parameterization of Cd and Pb BLM Toxicity-mode Models for Lights-on Bioreporter

As described in Section 2.3, R_{cation} values from the data in Figures 2-5 and 2-7 were calculated and used to solve eq. 2-2 for K_{CaBL}, K_{MgBL}, K_{KBL} and K_{NaBL}. One-tailed *t*-tests were performed to confirm that the *m* values used in calculating R_{cation} were greater than zero. After obtaining values for $K_{CationBL}$, K_{MBL} and f_{crit} were then calculated with those values using eq. 2-3. Figure 2-8 shows the logit of the $R_{L/D}$ and R_{Lum}, for Cd and Pb, respectively, plotted versus *f* for both the LIVE/DEAD (A–B) and bioluminescence inhibition method (C–D), reflecting the fits associated with final values of K_{MBL} and f_{crit}. Results for all parameters used to construct final BLM toxicity models are given in Table 2-3, along with parameters reported for Cd and Pb BLM models developed for other test organisms.

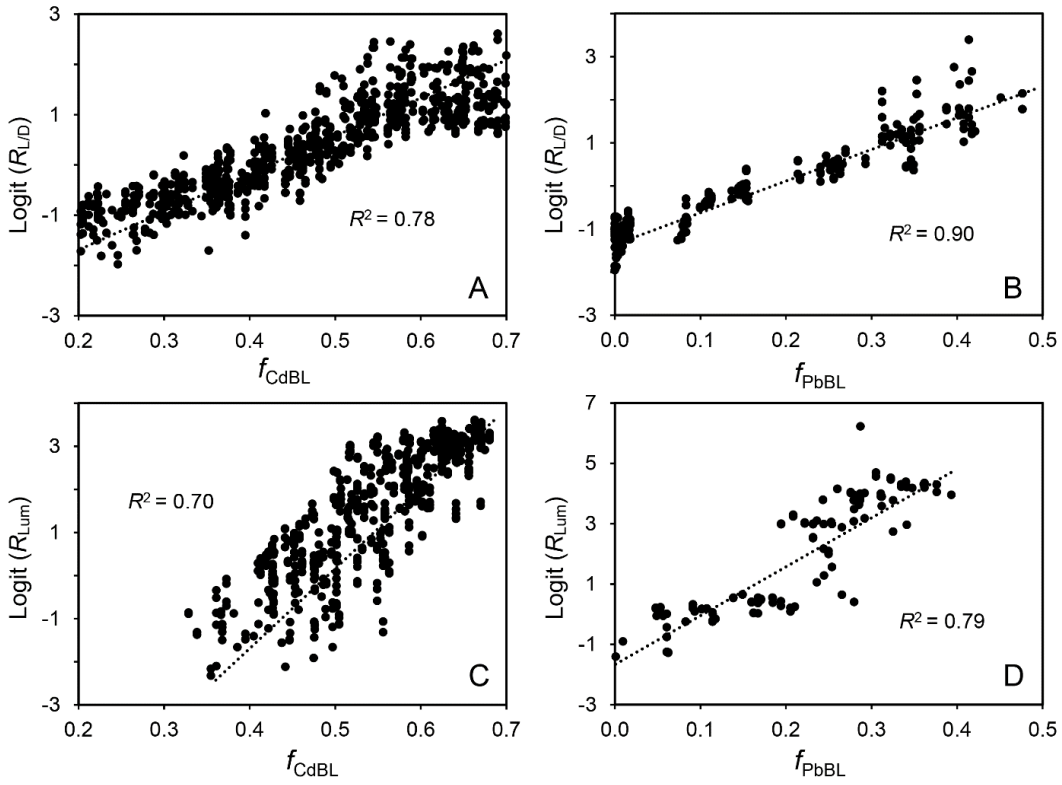

Figure 2-8. Relationships between toxic response and the fraction of BL sites occupied. The logit of the measured toxic response ($R_{L/D}$ and R_{Lum}) is plotted versus values of f calculated for LIVE/DEAD with (A) Cd and (B) Pb, and for bioluminescence inhibition with (C) Cd and D) Pb.

The parameters K_{cation}, K_{MBL} and f_{crit} interactively determine the toxic effect within the framework of the BLM. Higher K_{cation} values indicate that major cations are more competitive with toxic metals for BL binding, thus reducing toxicity. Higher K_{MBL} values indicate that the toxic metal has a higher binding affinity for BL, increasing toxicity. A small f_{crit} indicates that only a small fraction of the BL needs to be occupied to cause a toxic effect, and the bioreporter will reach the toxic effect sooner as compared to an organism that models high f_{crit}. In theory, K_{cation} and K_{MBL} for zntA by LIVE/DEAD and bioluminescence inhibition methods should be the same as the competitive binding ability of any given major cation and M for the BL should be invariant. While my one tailed *t*-tests showed that K_{cation} determined by LIVE/DEAD compared to the bioluminescence inhibition method are not the same, this may result from various experimental uncertainties, some of which I discussed previously.

Table 2-3. Parameters for Cd and Pb BLM models constructed for this work compared to literature values.

Organism	Source	logK_{Ca}	logK_{Mg}	logK_{K}	logK_{Na}	logK_{MBL}	f_{crit}
BLM toxicity-mode parameters for **Cd**:							
zntA	This study, LIVE/DEAD	3.67 (3.39-3.84)[a]	3.82 (3.56-3.98)	2.72 (2.47-2.88)	2.48 (2.23-2.64)	6.40	0.500
	This study, bioluminescence inhibition	3.16 (3.13-3.18)	3.39 (3.36-3.41)	2.08 (2.06-2.10)	1.77 (1.76-1.79)	5.90	0.520
V. fischeri	(An et al., 2012)	2.84	2.19	1.56	NA[b]	5.02	0.435
E. fetida	(Li et al., 2008)	3.35	2.82	2.31	1.57	4.00	0.720
H. vulgare	(Wang et al., 2016)	2.87	2.98	EX[c]	NA	5.19	0.290
D. rerio	(Feng et al., 2018)	4.57 (4.51-4.67)	4.39 (4.33-4.44)	3.05 (3.01-3.09)	EX	5.66	NR[d]
BLM toxicity-mode parameters for **Pb**:							
zntA	This study, LIVE/DEAD	1.90 (1.84-1.95)	2.28 (2.25-2.31)	EX	EX	4.30	0.140
	This study, bioluminescence inhibition	1.28 (0.95-1.46)	1.99 (1.63-2.18)	EX	EX	4.44	0.185
V. fischeri	(An et al., 2012)	2.30	2.13	EX	NA	6.67	0.547
D. rerio	(Feng et al., 2018)	4.17 (4.11-4.23)	3.82 (3.80-3.85)	EX	EX	4.93	NR

[a] 95% confidence limits. [b] NA–not applicable, was not varied. [c] K was excluded (EX) from the calculation (eq. 2-2). [d] f_{crit} was not reported (NR).

Because all of these parameters influence model predictions, it is difficult to draw conclusions from pairwise comparison of like parameters in Table 2-3, however I will return to a discussion of how they affect the overall model result later, in the context of WQC.

2.7 BENCHMARKING AND VALIDATION OF BIOREPORTER BLM TOXICITY-MODE MODELS

Figure 2-9 shows BLM predicted versus measured $EC_{50}^{a_{Cd^{2+}}}$ and $EC_{50}^{a_{Pb^{2+}}}$, including results from back-calculation and validation using LIVE/DEAD (A–B) and bioluminescence inhibition (C–D) methods. Back-calculation is the process of verifying that predicted toxicities from the BLM toxicity-mode parameterization experiments in Table 2-1 (Ca-set, Mg-set, K-set and Na-set) correspond to measurements.

For validation, three types of experiment were performed to verify that the model could predict resulting changes in toxicity: 1) Varying major cation concentrations randomly (changes in inorganic components); 2) Varying HA concentrations (changes in organic components); 3) Testing natural freshwater samples (changes in inorganic and organic components in environmental matrices). As with speciation, agreement between measured and predicted values is quite strong and well within the factor of two guideline for validation. The results in Figure 2-9 demonstrate that the bioluminescence inhibition assay produces similarly well-behaved validation results for both Cd and Pb when compared to the well-known LIVE/DEAD toxicity bioassay, and in practice I find that the bioluminescence inhibition assay is much faster and cheaper when compared to the LIVE/DEAD toxicity measurement.

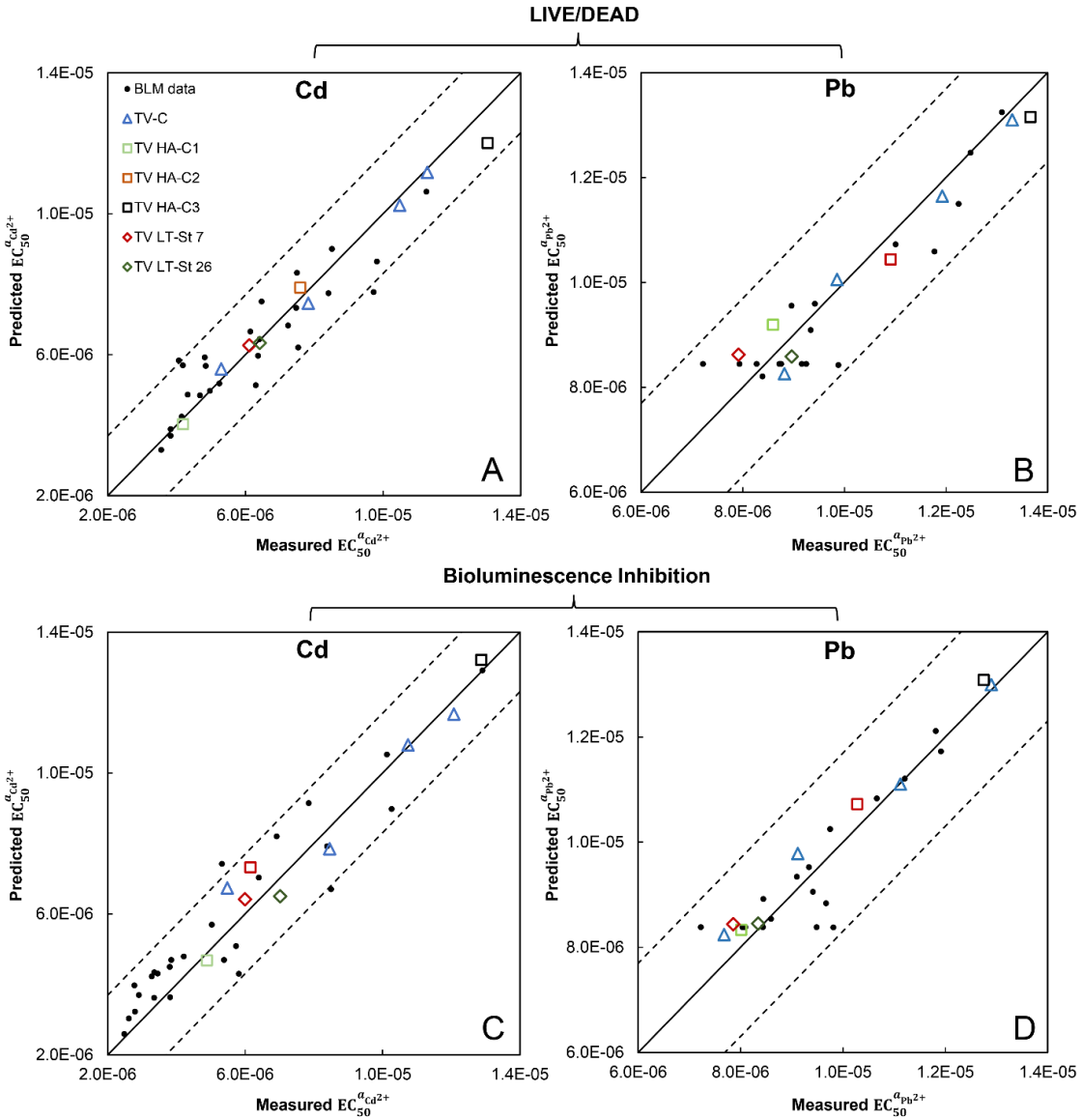

Figure 2-9. Plots of predicted versus measured toxicity. A–B show the linear relationship, respectively, between the predicted and measured $EC_{50}^{a_{Cd^{2+}}}$ and $EC_{50}^{a_{Pb^{2+}}}$ using the LIVE/DEAD toxicity test, and C–D show the comparative results from the bioluminescence inhibition method. The solid line indicates an exact match between measured and predicted $EC_{50}^{a_{Cd^{2+}}}/EC_{50}^{a_{Pb^{2+}}}$, and the dashed lines a factor of twice the pooled average RPD between measured and predicted $EC_{50}^{a_{Cd^{2+}}}/EC_{50}^{a_{Pb^{2+}}}$. All of the results that I report herein are within the accepted validation guideline (measured and predicted response shall agree within a factor of two).

2.8 LIGHTS-ON BIOREPORTER'S TWO-IN-ONE PROPERTIES RELATE TO WATER QUALITY CRITERIA

Returning to the discussion of the BLM toxicity-mode parameters in Table 2-3, I was interested to compare the outcomes, i.e., the predicted $EC_{50}^{C_{Cd}}$ and $EC_{50}^{C_{Pb}}$ from BLM models for different organisms in the context of WQC, as the BLM was developed to assist with setting defensible WQC. The $EC_{50}^{C_{Cd}}$ and $EC_{50}^{C_{Pb}}$ that I predict here are acute criteria, and for illustrative purposes I will consider results relative to the criterion maximum concentration (CMC), which is the highest concentration of a material in ambient water to that an aquatic community can tolerate for brief durations (acute basis) without resulting in an unacceptable adverse effect. The CMC originates from Genus Mean Acute Values (GMAVs) for toxicity.

To calculate a CMC, the typical approach is to rank available data for GMAVs, with the most sensitive genus having the lowest rank, and from this assess the EC_{50} at $P_{5\%}$ (5th percentile according to rank) to obtain a final acute value (FAV). Since the FAV is a mean EC_{50}, i.e., a concentration at which 50% of a population experiences effects, the FAV is divided by two to obtain the CMC. According to the one set of guidance documentation on ambient freshwater WQC, the Cd GMAVs range from 0.00419 mg·L^{-1} for *Salvelinus* (char/trout) to 49.052 mg·L^{-1} for *Chironomus* (midge) (US EPA, 2016b). The Cd freshwater FAV WQC for Cd at a hardness of 100 mg·L^{-1} was reported to be 0.00573 mg·L^{-1}, however, for Cd the CMC was set at C_{Cd} = 0.0018 mg·L^{-1} (US EPA, 2021), lower than the FAV/2, to protect the commercially important Rainbow trout. For Pb, the GMAV ranged from 0.3446, for *Gammarus* (amphipod crustacean) to 570.1 mg·L^{-1}, for the

Tanytarsus (midge) (US EPA, 1984). Relatively fewer data were available for Pb, and the Pb CMC for freshwater was set at C_{Pb} = 0.065 mg·L^{-1} at hardness of 100 mg·L^{-1} (US EPA, 2021), based on inference of the $P_{5\%}$ GMAV. In order to assess how useful BLM models for the organisms listed in Table 2-3 are in light of these WQC/CMC, predicted $\mathrm{EC}_{50}^{C_{\mathrm{Cd}}}$ and $\mathrm{EC}_{50}^{C_{\mathrm{Pb}}}$ were plotted in Figure 2-9, along with the GMAV for the most sensitive organism used in calculating FAV WQCs, the least sensitive organism's GMAV from the same ranking, the CMC and the LOD of zntA, which I discuss in context further below. The *x*-axis in Figure 2-10 places the EC_{50} results for the organisms in Table 2-3 at the $P_{n\%}$ percentile where they fall among all the GMAVs in the WQC guidance documentation. In Figure 2-10 I see immediately that, although the zntA BLM parameters for bioluminescence inhibition are consistently lower than for LIVE/DEAD, the predicted $\mathrm{EC}_{50}^{C_{\mathrm{Cd}}}$ and $\mathrm{EC}_{50}^{C_{\mathrm{Pb}}}$ for the two are similar for both Cd and Pb, and in comparison to variations from other organisms, even though the BLM parameters for zntA from LIVE/DEAD are in some cases statistically different from bioluminescence inhibition, the outcome in terms of toxicity is a result of the interplay of all parameters. Hence, the decreased protective effect of the lower K_{cation} values for zntA bioluminescence inhibition are in whole or part offset by the lower K_{MBL} values found for bioluminescence inhibition.

Comparing the $\mathrm{EC}_{50}^{C_{\mathrm{Cd}}}$ and $\mathrm{EC}_{50}^{C_{\mathrm{Pb}}}$ for zntA from Figure 2-10 to other organisms with reported Cd/Pb BLMs, the predicted EC_{50}s for *D. rerio*, and especially *Eisenia fetida,* are higher. The highest predicted $\mathrm{EC}_{50}^{C_{\mathrm{Cd}}}$ is for *E. fetida*, which, at 1,234 mg·L^{-1}, is over an order of magnitude higher than the highest Cd GMAV for *Chironomus* (thus plotted above $P_{100\%}$). In terms of BLM parameters, the highest

f_{crit} in Table 2-3 is for *E. fetida*, being half again (~50%) higher than the average f_{crit} in Table 2-3. It is logical that *E. fetida* is relatively insensitive; work by Jones et al. (2009) and Li et al. (2009) shows that *E. fetida* can compartmentalize/sequester Cd and Pb, increasing the organism's resistance to Cd and Pb toxicity. *D. rerio*, meanwhile, has documented heavy metal detoxification mechanisms, such as glutathione S-transferase protein expression (Tierbach et al., 2018). The f_{crit} of *Hordeum vulgare* is the lowest compared to all the organisms in Table 2-3, such that only 29% of BL sites need to complex with Cd to cause a toxic effect for barley root elongation. Cd is absorbed and accumulated in plant tissues, and as roots are the primary site of accumulation (Shi et al., 2016 and references therein), they are also a locus of toxic effects, likely explaining the sensitivity and low f_{crit} of *H. vulgare*.

Regarding results for bacteria in Figure 2-10, *V. fischeri* and zntA have similar predicted $EC_{50}^{C_{Cd}}$s (12. mg·L^{-1} for *V. fischeri*; 9.1 mg·L^{-1} for zntA LIVE/DEAD; and 10.1 mg·L^{-1} for zntA bioluminescence inhibition), however the *V. fischeri* $EC_{50}^{C_{Pb}}$ is ~30 times lower, on average, than for zntA (0.4 mg·L^{-1} for *V. fischeri* versus 12.6 mg·L^{-1} for zntA LIVE/DEAD and 12.8 mg·L^{-1} for zntA bioluminescence inhibition). The insensitivity of *V. fischeri* to Cd in comparison to zntA was not expected, inasmuch as *V. fischeri* is a lights-off bioreporter, hence a lower $EC_{50}^{C_{Cd}}$ is consistent with needs for measurement of toxic response, whereas zntA, as a lights-on reporter, should ideally be more resistant to toxic metals in order to measure speciation for environmental samples from contaminated sites. For *V. fischeri*, Ranjitha and Karthy (2011) have reported that heavy metal resistance is highly variable, and Teodorovic et al. (2009) have questioned the applicability

of *V. fischeri* as a useful screening method in assessing various environmental samples due to its low sensitivity to heavy metals. As such, the variability of results, and insensitivitiy with regard to Cd, for *V. fischeri* in Figure 2-10 are consistent with literature reports.

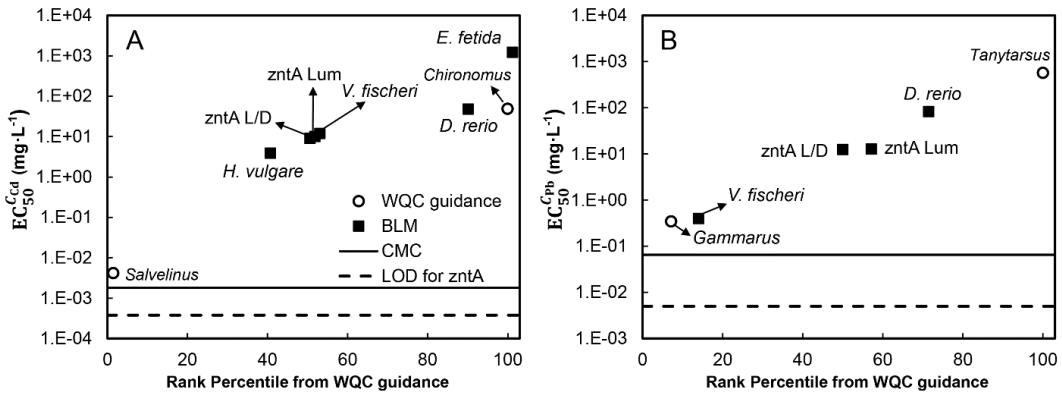

Figure 2-10. BLM-predicted EC_{50} in the context of WQC. (A) $EC_{50}^{C_{Cd}}$ and (B) $EC_{50}^{C_{Pb}}$ for different organisms listed in Table 2-3 (filled squares) by sensitivity from more sensitive (low EC_{50}) to less sensitive (high EC_{50}) plotted according to the comparative $P_{n\%}$ from WQC guidance documentation (see text). Data is also shown for the most sensitive genera used in formulating CMC (*Salvelinus* for Cd, *Gammarus* for Pb) and for the $P_{100\%}$ (*Chironomus* for Cd, *Tanytarsus* for Pb (open circles), along with, for comparison, the CMCs (solid lines) and zntA LOD (dashed lines) for Cd and Pb, respectively. All data reflect a hardness of 100 mg/L. The labels L/D and Lum in the figures indicate BLMs for zntA based on LIVE/DEAD and bioluminescence inhibition assays, respectively. The f_{crit} value for *D. rerio* was assumed to be 0.5 since the authors of that work did not report it.

While some organisms are more sensitive than others, as compared to the FAV for Cd and Pb and the $EC_{50}^{C_{Cd}}$ and $EC_{50}^{C_{Pb}}$ for sensitive species (*Salvelinus* and *Gammarus*, respectively), none of the organisms for which BLMs have been developed could be regarded as fit-for-purpose for toxic metal environmental risk assessment according to existing WQCs, i.e., the metrics that matter. Even *V. fischeri* for Pb is above the $P_{10\%}$, while the CMC is set at $P_{5\%}$. This point has not been addressed in any of the works whose model results I include in Figure 2-

10. It is an important point, and it underscores the essential difference in the approach I take here, namely, that because lights-on reporters are capable of measuring speciation and toxicity, consistent with how the BLM can be run in speciation and toxicity mode, they are much less limited compared to effectively any other organisms in use for BLM studies.

Figure 2-11 graphically illustrates the dual-mode response characteristic for Cd and Pb, whereby at concentrations well below the EC_{50}, the lights-on zntA is able to report levels of toxic Cd and Pb in a linear (data not shown) to log-linear (solid lines in Figure 2-11) response pattern. The relative ranges over which zntA is able to report for Cd and Pb begin below the corresponding CMC for each metal (compare the LODs for these metals to the CMCs in Figure 2-10). At the maximum of the log-linear speciation range, the response smoothly transitions to bioluminescence inhibition/toxicity. Thus, while other organisms used in BLM work report toxicity as a single metric such as EC_{50}, for any given water composition, the lights-on bioreporter is able to render results for an entire concentration range, in the case of Cd and Pb starting from well below the respective FAVs for these metals, up to the EC_{50} for the bioreporter.

While the Cd and Pb BLMs for other organisms listed in Table 2-3 are not able to produce results for Cd and Pb levels that are environmentally relevant in terms of WQC, zntA, and by extension other lights-on reporters, can measure speciation before reaching toxic effect. Consequently, the two-in-one speciation + toxicity capability of lights-on bioreporters, as demonstrated here for zntA, may be used to report at toxicity endpoints for many other organisms whose toxicity endpoints lie in the LOD–EC_{50} range of the bioreporter. In the case of

zntA specifically, I can measure, and with the validated BLM predict, Cd and Pb EC_{50}s for any genus for which the GMAV falls in the range of CMC– $P_{50\%}$ or CMC–$P_{55\%}$, respectively for Cd and Pb, i.e., the most sensitive half of all species for which data has been reported in setting the WQC guidance values used for discussion in Figure 2-10. While this range excludes relatively insensitive species such as *E. fetida*, it includes the majority of sensitive species, and these are precisely the species that are of interest with regard to WQC and environmental risk assessment.

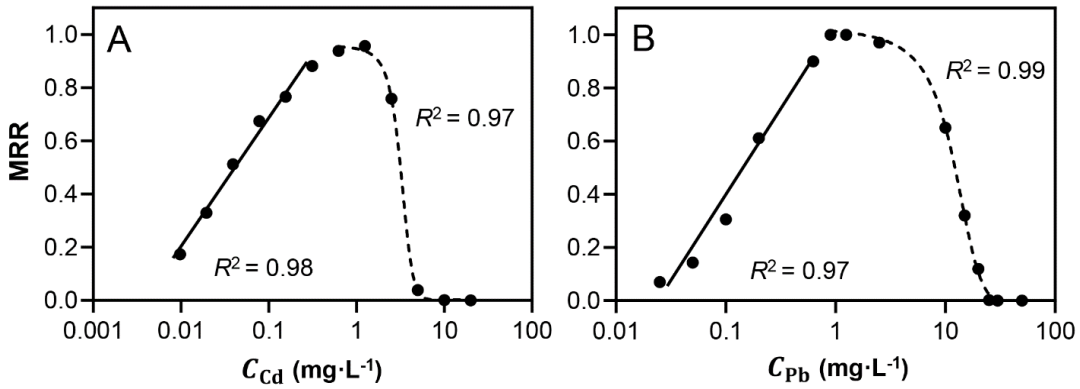

Figure 2-11. Two-in-one bioluminescence response of zntA. Response is plotted for increasing (A) C_{Cd} and (B) C_{Pb}. The solid lines show the log-linear response range for speciation whereas the dashed line corresponds to a dose-response curve for the region of bioluminescence inhibition/toxicity response. This response pattern is unique in the context of other reports on BLM models, which focus on toxicity only and render a single toxicity response metric (EC_{50}). The lights-on bioreporter response is able to represent the entire functionality of the BLM model, speciation *and* toxicity modes. In this way, the lights-on bioreporter can report at toxicity endpoints for any organism for which the toxicity/EC_{50} endpoint lies in the LOD–EC_{50} range of the bioreporter. In the case of zntA Cd and Pb, the reporter can measure and predict EC_{50}s for the most sensitive half of species for which data has been reported in the WQC guidance documentation used for illustrative purposes here.

3 A new perspective of copper-iron effects on bloom-forming algae in a highly impacted environment

3.1 Background on Copper and Iron Micronutrient Effects on Algae

Increasing population, growing demands on water resources and anthropogenically induced environmental change create urgent surface-water management challenges (Best, 2019; Mushtaq et al., 2020). Lakes particularly contribute to ecosystem services/ productivity and are important for fisheries, drinking water and hydrological regulation (Lévêque, 2001; Schallenberg et al., 2013). Ecological problems from lacustrine harmful algal blooms (HABs) have been named as possibly the greatest inland water quality threat, impacting public health and aquatic ecosystems (Brooks et al., 2016; Paerl, 2018). Eutrophication, from excess anthropogenic nitrogen (N) and phosphorous (P), is a major cause of HABs (Heisler et al., 2008; O'Neil et al., 2012), investigated by many studies regarding effects on algal growth (Paerl et al., 2011, 2015;

Quiblier et al., 2013; Gobler et al., 2016). For some notable examples, HABs have not responded as expected to abatement efforts despite significant investments (Posch et al., 2012; Qin et al., 2019).

In addition to N and P (hereafter NP), a wide range of algal cellular processes require micronutrients (MNs, Andersen's definitive text, 2005, nine MNs were discussed), however some MNs become toxic with increasing concentration (Chakraborty et al., 2010). Early research noted the role of MNs on freshwater ecosystem's cycling (Outridge and Noller, 1991; Maier and Knight, 1994), since which other investigators have emphasized that a crucial research frontier is understanding MN-coupled biogeochemical cycles (Finzi et al., 2011; Schlesinger et al., 2011). Complicating matters, trace metal pollution, which has occurred due to industrialization, urbanization, and increases in energy consumption, has brought massive disruption of MN biogeochemical cycles (Andreae et al., 1984; Kaushal et al., 2014). Relative to this dramatic environmental/biogeochemical change, comparatively little work aims to understand the role of MNs in influencing HAB development and progression (Facey et al., 2019; Zhang et al., 2019), which is therefore an important and largely neglected topic. My colleague, Dr. Zhang, and I previously found statistically significant effects of algal growth limitation for B, Co, Cu and Fe (Zhang et al., 2019). Fe is frequently limiting in marine environments (Boyd et al., 2007; Tripathy et al., 2019), and there have been some reports for freshwater (Nagai et al., 2007; Molot et al., 2010). MNs have an interesting role in regard to environmental management, since relatively minor inputs/changes could potentially have pronounced effects. For example, Cu has been suggested at concentrations on the order of 100 $\mu g \cdot L^{-1}$ as an algal biocide for use in HAB

management (Wu et al., 2017). At 20 μg·L^{-1} Cu, however, my colleague Dr. Zhang and I found a tremendous stimulatory effect (Zhang et al., 2019), suggesting that HAB management with Cu may not always be advisable.

The environmental bioavailability of Fe is often low, yet some phytoplankton have relatively high cellular requirements (Brand, 1991; Schoffman et al., 2016). Some studies report Cu-Fe interactions, whereby Cu facilitates Fe uptake (Schoffman et al., 2016), and in previous work in which I was involved in my doctoral group, we were unable to discount that Cu amendment induced increased Fe bioavailability (Zhang et al., 2019). Synergistic NP-MN interactions involving Fe (e.g. phototroph N-metabolism is sensitive to Fe-limitation, Quigg et al., 2008) have contributed to conceptualization of the extended Redfield ratio (Ho et al., 2003). In addition to NP-MN synergies, there are well-known MN-MN interactions for algae. As early as 1987, Stauber and Florence observed that Fe reduced Cu toxicity to different algal species, which they attributed to Cu scavenging by a layer of Fe-hydroxide on algal cell surfaces, thus reducing cellular Cu penetration. Recently, Kochoni and Fortin (2019) also found that Fe ameliorates Cu toxicity to the green algae *Chlamydomonas reinhardtii*, an effect rationalized via the BLM, i.e., Fe competes with Cu for the BL binding sites of *C. reinhardtii*, such that less Cu was binded with the BL site and initiates toxic response caused by Cu. Fe-hydroxide scavenging or BLM theories cannot explain the stimulatory effect observed for Cu in work in which I participated (Zhang et al., 2019), whereby we hypothesized a Cu-Fe link involving bacterial or algal production of strong Fe- and Cu-binding ligands, respectively, called siderophores (Saha et al., 2016) and chalkophores (Solioz, 2018) that have demonstrated importance in aiding organisms to navigate the divide between

MN nutrition and toxicity. In 1980, McKnight and Morel found that Fe-limitation caused *Anabaena* spp. to secrete strong Cu-binding ligands; they speculated that Cu-ligand complexes reduced Cu^{2+}, conveying an advantage to cyanophytes. In another example, Nicolaisen et al. (2010) reported that at low Fe and Cu, *Anabaena* spp. secrete the siderophore schizokinen to complex with Fe and increase its bioavailability to these organisms. At high Cu/low Fe concentrations, Cu-schizokinen complexation lowers Cu intake/toxicity and synthesis of another Fe transporter (IacT) is activated. Similarly, for *P. aeruginosa*, toxic Cu concentrations caused siderophore production that conveyed a Cu-protective effect (Braud et al., 2010).

The literature I found concerning coupled Cu-Fe effects is from laboratory studies on algal monocultures, which is very different from field settings. Also, the environmental half-life of some MN-binding ligands is relatively low (Maldonado et al., 2005). What happens in field settings is actually relevant to MNs and environmental management. "Whole lake" management is much discussed (Carpenter et al., 1987; Nault et al., 2014; Paerl et al., 2016; Hanson et al., 2017), including HABs, and using Cu to control *Microcystis* (Jančula and Maršálek, 2011). If Cu-Fe links affect chalkophore/siderophore production, this affects Cu/Fe bioavailability, and whole-lake management of HABs using Cu may have unanticipated side effects. Certainly, a better understanding is needed, including field settings, before implementing whole-lake Cu application, particularly in geographical settings with highly variable ecosystem dynamics across a regional scale.

Here I examine how Cu and Fe amendments affect small-scale mesocosms initiated with *Microcystis* and *Desmodesmus* spp. in lake water from a large, hypereutrophic lake that has widely varying algal ecology geographically. My field area is Taihu, China's third largest freshwater lake (2,338 km^2 surface area; catchment area 36,900 km^2), located in a rapidly developing region (Yangtze Delta, Qin et al., 2007). Cyanobacterial HABs have impacted Taihu every summer since the mid-1980s due to environmental change/human impacts (Qin et al., 2007; Wang et al., 2009). Hence Taihu has become a locus of field studies to understand HAB management. I monitored mesocosm changes for 25 standard water quality parameters plus the biomolecules chalkophore, siderophore, and microcystin. Chalkophore screening is new (Zhang et al., 2020b), and this is the first work to analyze chalkophore and siderophore separately, and as a function of Cu/Fe. Chalkophore/siderophore results are not well characterized by standard time-series analysis, and I use Community Trajectory Analysis (CTA), a powerful new approach in ecological studies. I also apply multivariate analysis to the full 28-parameter data set. Results offer an entirely new perspective to understanding MN dynamics in aqueous environments. Summarizing, I find 1) Cu-Fe impacts on growth and community progression do not agree with lab-based findings, 2) there is an interplay between chalkophore/siderophore production wherein *Microcystis* spp. varies behavior to manage Cu/Fe requirements, including a link between chalkophore and microcystin, and 3) the lake water itself influences mesocosm changes.

3.2 METHODS USED IN ALGAL MESOCOSM EXPERIMENTS

Study area, collection and treatment of lake water

Taihu is a polymictic lake located ~150 km west of Shanghai (lake center: 31°10'0"N, 120°90'0"E). Water samples were collected during an HAB in August, 2018, at three stations (Figure 3-1) monitored quarterly by NIGLAS. Meiliang Bay, (St 3), receives large amounts of untreated wastewater via the Liang and Zhihu rivers (Paerl et al., 2011). Accordingly, recurring and increasing *Microcystis*-dominated HABs often originate at St 3 (Qin et al., 2007). Xukou Bay (St 28) has a high density of macrophytes and is typically unimpacted by HABs. Gonghu Bay (St 13), located in between St 3 and St 28, is usually less impacted by HABs compared to St 3. These three stations were selected for sampling based on our previous work (Zhang et al., 2019) wherein my colleague Dr. Zhang and I found that water chemistry is different and significant differences were found in MN mesocosm experiments for these stations.

Forty-L water samples from 0.2 m below the surface were collected into acid-cleaned polyethylene carboys. All work was conducted trace-metals clean, using ultrapure water (UPW). Water temperature, pH, turbidity and dissolved oxygen were measured in the field using an YSI 6600 sonde. Water samples from Taihu were filtered immediately after collection using Whatman GF/F glass-fiber filters, nominal pore size 0.7 μm, to remove *in situ* phytoplankton. Due to filter clogging when filtering 40-L, many filters must be used, and small amounts of *in situ* algae (Alg_{is}) are introduced to the filtrate from transfer during filter changes (confirmed to be below the limit of detection/LOD by microscopic counting and automated cell counts).

Algal Cultures

Microcystis was selected as the main HAB-forming species in Taihu (Qin et al., 2007), also reportedly sensitive to Cu (Wu et al., 2017). *Desmodesmus* was selected as a contrasting, non-nuisance green alga with a relative tolerance to Cu (Buayam et al., 2019), also having been used as a model *Microcystis*-competitor in lab studies (Chang et al., 2012; Omidi et al., 2019).

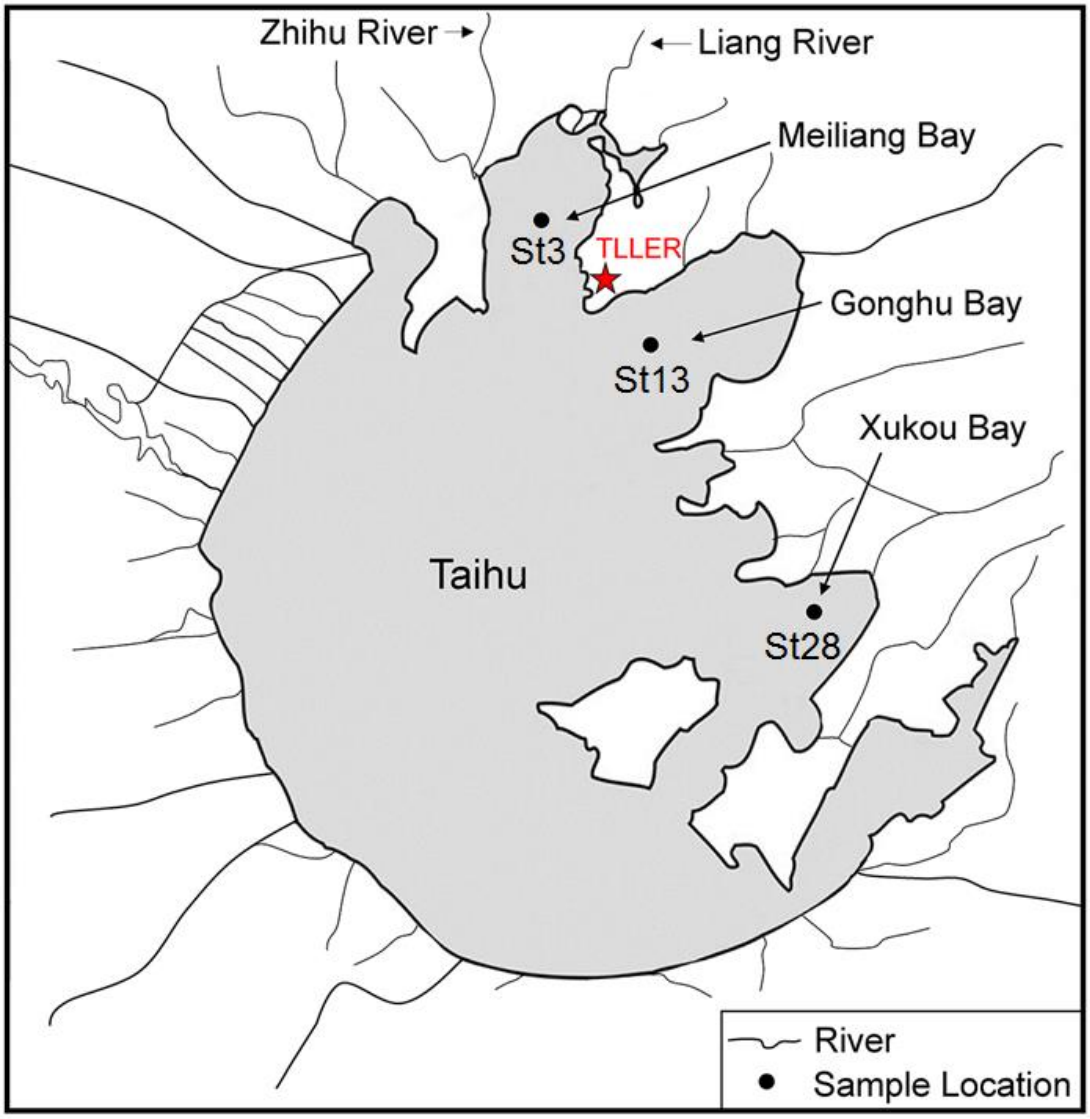

Figure 3-1. Map of Taihu field area and stations sampled for mesocosm work in the year of 2018. The location in Taihu of Sts 3, 13 and 28 where water samples were collected is shown along with the site of mesocosm experiments (Taihu Laboratory for Lake Ecosystem Research, TLLER).

Microcystis (> 99% *Microcystis* spp. from microscopic examination) were collected from a point off the dock at TLLER in August, 2018. *Desmodesmus* was purchased from Aquatic Biology Services (Wuxi Zhongshun Biotechnology Co., Ltd; > 99% *Desmodesmus* from microscopic examination and 18s rRNA sequencing). Algae were passed through a 65 μm zooplankton net, then acclimated in modified COMBO medium (Kilham et al., 1998, with 1 $mg \cdot L^{-1}$ N, 0.1 $mg \cdot L^{-1}$ P, no Cu/Fe, and all other ingredients at 50% of COMBO). Mono-algal status was verified by microscopic examination periodically and on mesocosm establishment. For mesocosm bioassays, algae were collected/concentrated by coarse filtration.

Nutrient Limitation Bioassays (NLBs)

The NLB used here is a small-scale field mesocosm study that possesses an element of control akin to lab experiments (improved reproducibility, isolation of variables, resulting basis for tractable hypotheses), while also offering environmental reality (e.g. diel cycles, temperature conditions) that lab experiments lack (Spivak et al., 2011). Meta-analysis by Elser et al., (2007) and Spivak et al., (2011) on 1060 NLB experiments, spanning a wide range of volumetric (as little as 0.02 L) and temporal (0–7 days) scales, concluded that the approach is applicable to larger-scale processes. Their findings confirm the suitability of NLBs for my large factorial experiment that screens for potential environmental MN effects.

I designed NLB amendments as follows (Table 3-1): 1) no added Cu/Fe (control, Ctl), 2) 50 $\mu g \cdot L^{-1}$ Cu, 3) 200 $\mu g \cdot L^{-1}$ Fe, and 4) Cu and Fe (CuFe) at the dose used for each individually. All had NP to ensure that these are non-limiting and to

focus on the effects of Cu, Fe, and Cu-Fe. Concentrations of NP and Fe were the same used previously (Zhang et al., 2019); Cu concentration was increased 2.5 times over previous work (Zhang et al., 2019) to levels reportedly at or approaching levels toxic to *Microcystis* (Wu et al., 2017) to observe how this affects mesocosm progression. I also varied the chemical form of Fe (Table 3-1). For Fe only I used FeCitrate, a solubilized and exchangeable, more bioavailable[2], form of Fe (Sutak et al., 2012; Quigg, 2016; Mustoe, 2018). I used $FeCl_3 \cdot 6H_2O$ for CuFe, which, as a less bioavailable form due to the formation of insoluble Fe-oxyhydroxides, was to test whether the response of algae to Cu will have an influence on the bioavailability of Fe.

Table 3-1. Amendment schedule used in Taihu NLB in the year of 2018.

	N [a]	P [b]	Fe	Cu [e]
Control	2.0 mg·L^{-1} N	0.2 mg·L^{-1} P	No added Fe	No added Cu
Fe	"	"	200 µg·L^{-1} Fe [c]	No added Cu
Cu	"	"	No added Fe	50 µg·L^{-1} Cu
CuFe	"	"	200 µg·L^{-1} Fe [d]	50 µg·L^{-1} Cu

[a] added as KNO_3; [b] added as $K_2HPO_3 \cdot 3H_2O$; [c] added as FeCitrate; [d] added as $FeCl_3 \cdot 6H_2O$; [e] added as $CuSO_4 \cdot 5H_2O$.

Trials were also conducted to see if MN effects differ for mono- and mixed-cultures. I designate the different groups of mesocosm trials as M_{meso} (dosed with *Microcystis* spp.), D_{meso} (*Desmodesmus* spp.), and B_{meso} (1:1 mixture of *Microcystis* and *Desmodesmus* by OD, or "both"). To perform NLBs, filtered lake water was divided into three portions and dosed with algae to a starting optical density at 750 nm (OD_{750} hereafter OD) of 0.05. Given the difficulty of obtaining

[2] Here I adhere to the terminology of Semple et al. (2004), whereby bioavailability references only the amount of a substance available to an organism at some time, which is distinguished from bioaccessibility, i.e. that which might become or be rendered bioavailable. As an outgrowth of some decades of study, bioavailability and bioaccessibility of micronutrients and other species are generally recognized to be a function of chemical speciation, i.e., per Campbell, 1995, as an example.

large amounts of algae-free water from natural water, it was given that Alg_{is} species might grow in my mesocosms over time. Our prior work from my colleague Dr. Zhang and I found that MNs may mediate changes in algal assemblages (Zhang et al. 2019), which is a possible outcome of interest; my primary criterion of importance for NLB experimental design is that the initial conditions for all mesocosms are controlled. For each NLB permutation (station water used, algae dosed, amendment type), triplicate subsamples were placed into 1-L transparent, chemically inert, cubitainers, which were then spiked to achieve the final concentrations of NP and MN (Table 3-1). The cubitainers were then incubated *in situ* in Taihu near the surface at TLLER. Samples for analysis were collected from initial water, initial algal suspensions (t0), and then each cubitainer was sampled three times, at days 2, 4 and 6 (t2, t4, and t6, respectively) for analysis.

Sample Analysis

Mesocosm subsamples were analyzed for OD, pH, dissolved organic carbon (DOC), total dissolved nitrogen (TDN), ammoniacal nitrogen (NH4), nitrate (NO3), nitrite (NO2), total dissolved phosphorus (TDP), orthophosphate (PO4), total dissolved copper (TDCu), total copper (TCu), total dissolved iron (TDFe), total iron (TFe), cations Na, K, Mg, Ca, chloride and sulfate anions (Cl, SO4), Chlorophyll-a (Chl-a), chalkophore, siderophore and total microcystin. I identified and enumerated algae by microscopic counting (Cts.m) and automated cell counting by electric-field exclusion (Cts.ef). I used flow cytometry measurement to determine average diameter (d.avg). Some analytes were measured at t0 and t6 only due to sample volume or other limitations.

OD was measured in 96-well plates (3599, Costar) using a plate luminometer (Varioskan LUX, Thermo Fisher Scientific, USA). pH was measured with a pH-meter (Seven easy, Mettler Toledo). Chl-a concentrations were determined spectrophotometrically, following extraction in 90% hot ethanol (ISO, 1992). Chalkophore and siderophore were measured operationally using the competitive-ligand exchange assay that I helped to develop (Zhang et al., 2020b). This approach is a competitive ligand exchange (chrome azurol sulfonate, CAS, spectrophotometric assay) based high-throughput chalkophore screening approach. CAS assay conforms to this operational nature of the term; any ligand, in solution that functionally displaces Cu or Fe from Cu-CAS or Fe-CAS is screened as positive for chalkophore or siderophore (Zhang et al., 2020b and references therein). EDTA was used as a model ligand and as calibration, as it is one of the best studied metal chelating ligands, and therefore useful in confirming function of the competitive ligand exchange scheme. Per Zhang et al. (2020), since the definition of chalkophore and siderophore is operational according to association constants, calibration is performed in terms of μequivalents ethylene diamine tetra-acetic acid (μeq EDTA), i.e. an equivalent amount of EDTA that would bind metal. Microcystin was measured by enzyme-linked immunosorbent assay (ELISA) using the Microcystins-ADDA ELISA kit (No.52011) from Abraxis (USA, per US EPA, 2015).

Phytoplankton samples were preserved with 0.25% glutaraldehyde (Medical grade, Macklin; Marie et al., 2014). Cts.ef were obtained using a CASY cell counter and protocol (CASY TT, OLS, Germany). Algal objects were identified using field counting (Woelkerling et al., 1976) from microscopic observation of samples in a Sedgwick-Rafter chamber (SCA, 1990). Samples were surveyed at

1000x prior to counting at 400x; colonies and individuals were counted and Cts.m reported as total individual counts. Genera differentiated t2–t6 and, based on observations, I grouped them as follows: 1) Blue-green algae (BG); 2) Desmids (Des); 3) Dominant unicellular green algae (UG); 4) Diatoms (Dia); and 5) the remainder (Rest), typically dominated by green algae. I designate the sum of green algae as TotG. The d.avg was obtained from analysis of single cells using a FACSCalibur flow cytometer (Becton Dickinson, California, USA, argon solid-state and red diode lasers, excitation at 488 and 635 nm, respectively). The intake speed was set to 12 $\mu L \cdot min^{-1}$; forward scatter and side scatter amplification gain was set at 1 and measured in the linear mode. Acquisition was set to capture 25,000 total events for each sample. Size calibration was achieved using microspheres (Dae Technology, China) of 1, 6 and 15 μm.

DOC was determined using the high-temperature combustion method with a Dohrmann DC-190 TOC analyzer (Rosemont Analytical Inc., Calif., US EPA, 1979). The quantities TDN and TDP were determined using a combined persulfate digestion (Ebina et al., 1983). NH4 was determined using the indophenol blue method and NO3 and NO2 with the cadmium reduction method (APHA, 1995). The PO4 was determined by using the molybdenum blue method (APHA, 1995). Cations and anions were analyzed using ion chromatography following the National Standards of the People's Republic of China (MHPRC, 2016a, b). Samples for TDCu and TDFe were filtered through 0.45 μm MCE filter units (Titan, China) and the filtrate was immediately mixed 1:1 by volume with 4% ultrapure nitric acid (Aladdin, China). Samples for TCu and TFe were immediately mixed 5:1 by volume with 70% ultrapure nitric acid (Aladdin, China). Concentrations of TDCu, TCu, TDFe and TFe were analyzed by ICP-MS

(Inductively Coupled Plasma Mass Spectrometry, NexION300, PerkinElmer, USA).

Analytical quality assurance/quality control (QA/QC) for ICP-MS analysis was performed according to US EPA guidelines (US EPA, 1998), including analysis of a certified reference material (CRM, GBW10020 from Beijing Wanjiashouhua Biological Technology Co., Ltd). For total metals (TM), 30 samples were selected for digestion (according to US EPA, 2007) and analysis to verify that the average concentration of TM in mesocosms, $C_{\mathrm{meas}}^{\mathrm{TM}}$, at any particular time, *t*, is conserved to within accepted figures of merit (US EPA, 2007), according to

$$\text{Recovery} = \frac{C_{\mathrm{meas},\,t}^{\mathrm{TM}}}{C_{\mathrm{pred}}^{\mathrm{TM}}} \times 100\%, \tag{3-1a}$$

where the predicted TM, $C_{\mathrm{pred}}^{\mathrm{TM}}$, is the sum of individual contributions to the TM present initially, according to

$$C_{\mathrm{pred}}^{\mathrm{TM}} = C_{\mathrm{water,\,t0}}^{\mathrm{TDM}} + C_{\mathrm{spike,\,t0}}^{\mathrm{TDM}} + C_{\mathrm{algae,\,t0}}^{\mathrm{TM}}. \tag{3-1b}$$

In equation (3-1b), $C_{\mathrm{water,\,t0}}^{\mathrm{TDM}}$, $C_{\mathrm{spike,\,t0}}^{\mathrm{TDM}}$, and $C_{\mathrm{algae,\,t0}}^{\mathrm{TM}}$ are, respectively, the concentration of total dissolved metals (TDM) in filtered water used for mesocosms, the concentration of TDM resulting from spiking a blank (ultra-pure water) mesocosm, and the TM in algae at t0 (for *Microcystis* spp. or *Desmodesmus* spp., with the concentration for the mixture taken as an average of the two).

3.3 CALCULATIONS AND STATISTICAL AND MULTIVARIATE DATA ANALYSIS

Total effective spherical volume (ESV, 25,000 events) was calculated from d.avg according to Li and Dickie (2011). Some data results are reported as normalized or as area under curve (AUC) to obtain an understanding of integrated variations in individual parameters over time (Lucius et al., 2019). For multi-pairwise comparison, Tukey's Honest Significant Difference (HSD) Q_{sample} was calculated using Microsoft Excel. Values for Q_{crit} were obtained from Gleason's Q-value table (Gleason, 1999). The criterion of $p < 0.05$ was used for rejection of the null hypothesis, H_0; individual p-values were calculated using Lane's p-value calculator (Lane, 2015). Additional data analysis utilized the corrplot, factoextra, plot3D, smacof and vegclust packages in R (de Leeuw and Mair, 2009; De Cáceres et al., 2010; Alboukadel and Fabian, 2017; Wei and Simko, 2017; Karline, 2017; R Core Team, 2019) for pair-wise correlation analysis (using Spearman's ρ), CTA and principal component analysis (PCA).

The approach taken here, involving the use of time-series data, is very common in environmental and many other areas of science. For the work that I report, the simplest approach that I take is to compare results from different amendments at a discrete sampling time using multiple pairwise comparison. In this case, I use Tukey's HSD, which is a very conservative approach to avoid Type I error (Wilkinson, 1999; Lane, 2010 and 2015), however, for my data it is potentially overly conservative inasmuch as, for many comparisons that I make, I am not actually trying to compare all trials to each other, but often my focus is to compare two, in which case using a t-test would be valid and would be far

more likely to lead to statistically discernible differences.

Often, condensing time-series data down to a summary statistic or value is used to simplify analysis of time-series data by removing the temporal element (Matthews et al., 1990). Common summary values that are simplest units in common use include peak (maximum), time-to-peak, and area under curve (AUC) (Fedra, 1983; Matthews et al., 1990). Peak holds the advantage of simplicity and a number of disadvantages including the issue that, for the time intervals used in these experiments, it is likely that the true peaks are in between sampling intervals, thus inter-comparison across a single time interval (as I do here with Tukey's HSD) is more likely than not to under-estimate differences (Narang et al., 2020). Time-to-peak is a useful unit, as with peak, for simplicity, and additionally may be useful when early-phase response to stimulus is a focus (Narang et al., 2020). Even more than peak, time-to-peak is susceptible to inaccuracy when the peak centroid is not determinable with confidence. As such, for some data I use instead AUC (Hasenbrink et al., 2005). AUC holds the advantage of reflecting that time-series data are actually two-dimensional (2-D, magnitude of variation of parameter measured and duration of response, Matthews et al., 1990; Narang et al., 2020), and additionally, since data is integrated, there is ensemble averaging of random errors across time points (e.g. as in Thomas, 2016).

Data normalization, in some fields referred to as scaling, is also frequently used. Common methods for time-series/growth related data include fold-change normalization (as I do here, normalizing to t0), normalizing to minimum or maximum (also done for this work), scaling to a 0-1 interval, and Z-scoring

(Goedhart, 2019). Many of these approaches involve ratio calculations, which are performed in order to better visualize changes on the same scale or according to a common benchmark. This has been the major purpose of normalization when used in this work, however, normalization (scaling, ranging) is also sometimes used for different reasons in numerical/multivariate analysis and can alleviate or induce effects that are not fully reflective of the underlying data structure (Rietjens, 1995; Brauner and Shacham, 1998; Nordgård et al., 2006).

All of the approaches above have a history of long-standing use, in some cases because they reduce uncertainty associated with raw data, i.e. as ensemble averaging in AUC. Contrawise, much has been written as well concerning problems with each, in some cases contributing to uncertainty. Normalization is a case in point with reference to my work. Consider a simple quotient or ratio, and the standard approach to propagation of error for same (Ku, 1966):

$$xN = \frac{x}{y}, \tag{3-2a}$$

where xN is x normalized (to y), and then

$$s_{xN} = \sqrt[2]{\left(\left(\frac{1}{y}\right)^2 \cdot s_x^2 + \left(\frac{x}{y^2}\right)^2 \cdot s_y^2\right)}, \tag{3-2b}$$

where s_{xN} is the propagated error of xN given the uncertainties in x (s_x) and y (s_y), respectively. The details concerning the magnitude of uncertainty and form of the distribution of data in y may have a considerable effect on s_{xN}, in plain terms this is to say, rendering xN effectively incorrect, even misleading (Curran-Everett, 2013). In the manner in which I use ratio normalization, the issue is effectively moot. For example, because Chl-a at t0 is derived from replicates of

the “authentic sample” in each case, and said replicates have very low variance, normalizing all Chl-a values to the average value at t0 closely approximates normalizing to a discrete, constant scalar quantity. In this case, the uncertainty in the normalized quantity is simply that of the uncertainty in Chl-a at any time point, t2–t6. Where the issue becomes problematic however is in the case of normalizing *x* to some value *y*, when *y* is a variable with its own peculiarities in the magnitude, structure, and variation in uncertainty, the common example for which is when *y* is some metric representing changes in growth (OD, Cts.m/Cts.ef, etc.). Returning to the simple propagation of error in eq. 3-2b, for chalkophore, consider a value of chalkophore = 6 μeq·L^{-1} EDTA, with an RSD of 15% (i.e. s_x = 0.9) for a sample that has an OD of 0.035 ODU, and an RSD of 10% (s_y = 0.0035). In this case, the propagated error, s_{xN}, amounts to a RSD of 23%, however, the error structure typically magnifies further for larger uncertainties in *x* and *y*, and more problematically, differences in the distribution of the numerator and the denominator can lead to substantial distortions in the resulting normalized data (Curran-Everett, 2013). The issue is that the numerator and denominator represent inherently different kinds of unit. Though normalizing various results to indicators of biomass is quite common for results from the type of experiments that I report here, likewise the points that I make about the dangers of doing this appear to be largely unappreciated, or at least I am not aware of any works that use this normalization that also discuss the need for caution in interpretation of results. My approach for work in this chapter, when dealing with parameters whose changes might be correlated with growth indicators (importantly siderophore, chalkophore, and microcystin) has been as follows: 1) I have scrutinized data for possible

correlations and provided readers with metrics, and in some cases commentary, and 2) I report some results in terms of derived data, according to the summary values chosen as most appropriate, while also including comparative data (*vide infra*), such that readers are equipped with the information needed to make their own conclusions. For all the data that I report, I have taken a conservative approach to uncertainty, i.e., there may be more significant differences in different data that I analyze than I actually report.

3.4 Mesocosm Initial Conditions and Correlation Matrix Plot

Table 3-2 shows t0 water quality results, which agree with prior research on Taihu (Zhang et al., 2019). The Secchi-disk transparency followed St 3 < St 13 < St 28, as expected, reflecting the pattern of HAB formation and the predominant drainage (from northwest to southeast), and consistent with higher particulates in St 3/St 13. TDFe is higher in St 3/St 13, perhaps because some colloidal Fe passes the 0.45 μm filter that is operationally used for TD measurement. TDCu for all stations was < 6.7 $\mu g \cdot L^{-1}$, well below levels causing toxic effects to algae (Wu et al., 2017). Temperature and pH of the water in three stations were similar at the time of sampling.

The high pH of Taihu during the time of sampling should be mentioned as this is a key indicator of the degree of anthropogenic perturbation (Zhang et al., 2019) that results from inorganic carbon scavenging of phytoplankton by HABs (Fang et al., 2018). The high pH indicates an unusually low hydronium ion activity (from carbon scavenging, Section 3.5), compared to the range that is considered normal. TDN was not highly variable between the three stations (relative

standard deviation, RSD, of 16%), while TDP was more variable (RSD 53%), with the TDP value being a factor of two or higher at St 3 than for St 13 and St 28. Both TDN and TDP were dominated by organic forms, (dissolved organic nitrogen (DON) and dissolved organic phosphorus (DOP) (55 to 80%). DOC is similar for these three stations with a RSD of 5%. The initial TDFe were similar for St 3 and St 13, which is double that of St 28 and consistent with findings in my colleague Dr. Zhang's previous work (Zhang et al., 2019).

Table 3-2: Water quality of three sampling stations.[a]

	Parameter	**Station 3**	**Station 13**	**Station 28**
Physical	Secchi Depth (m)	0.25	0.52	> 1.8
	WT (°C)	33.0	32.3	31.2
	pH	9.70	9.26	9.86
Chemical	TDN ($mg \cdot L^{-1}$)	0.70	0.52	0.70
	DON ($mg \cdot L^{-1}$)	0.51 (72)	0.34 (65)	0.56 (80)
	NH4 ($mg \cdot L^{-1}$)	0.17	0.16	0.09
	NO3 ($mg \cdot L^{-1}$)	0.019	0.023	0.049
	NO2 ($mg \cdot L^{-1}$)	0.003	0.002	0.001
	TDP ($mg \cdot L^{-1}$)	0.033	0.012	0.017
	DOP ($mg \cdot L^{-1}$)	0.024 (73)	0.006 (55)	0.013 (78)
	PO4 ($mg \cdot L^{-1}$)	0.009	0.005	0.004
	DOC ($mg \cdot L^{-1}$)	3.88	4.05	3.72
	TDFe ($\mu g \cdot L^{-1}$)	190	200	90
	TDCu ($\mu g \cdot L^{-1}$)	6.7	5.8	6.0
	Na ($mg \cdot L^{-1}$)	46.8	51.0	46.2
	K ($mg \cdot L^{-1}$)	5.62	5.96	4.34
	Mg ($mg \cdot L^{-1}$)	8.57	9.24	8.81
	Ca ($mg \cdot L^{-1}$)	30.1	31.7	21.6
	Cl ($mg \cdot L^{-1}$)	56.9	58.0	54.4
	SO4 ($mg \cdot L^{-1}$)	64.9	66.4	62.4
t0 NP amended	NO3 ($mg \cdot L^{-1}$)	2.019	2.023	2.049
	PO4 ($mg \cdot L^{-1}$)	0.209	0.205	0.204

[a] Values in parentheses are percentages of dissolved organic nitrogen (DON) and dissolved organic phosphorous (DOP) for N and P species.

Concentrations of ions are similar for all three stations except in St 28, where Ca is lower than for the other two stations. Shi et al. (2013) have found that Ca plays an important role in the growth of *Microcystis* spp. and that enhancement in polysaccharide synthesis in response to increases in Ca concentration is a

mechanism that would promote bloom formation. At face value, this would seem to be a potential contributing reason for the absence of HABs in St 28, however, in my work and others, the Ca concentration is variable, sometimes being low compared to, for instance, Meiliang Bay/St 3, sometimes not (Li et al., unpublished data, also see Tao et al., 2013). As there does not seem to be a correspondence between Ca concentrations in St 28 and occurrence of BG, this explanation for why St 28 is "different" seems less likely.

Figure 3-2 is a bivariate correlation matrix plot that gives an overview of inter-parameter associations. Time is listed first, followed by parameters associated with algal growth, including OD, pH, Cts.ef, Cts.m, ESV and d.avg. The counts for different algal species groups (determined from Cts.m) are next, followed by biomolecules (chalkophore, siderophore and microcystin). NP species and Cu/Fe results TDCu, TDFe, TCu and TFe ("N" in Figure 3-2 denotes all normalized to maxima), are shown at the bottom. The growth indicators OD, pH, Cts.ef and Cts.m all have strong correlations with each other. Chl-a is not as strongly correlated with Cts.ef, Cts.m and ESV as OD, a consequence of Chl-a's not being solely related to cell number or volume (Ignatiades et al., 1985) and that different algae have different rates of Chl-a synthesis, according to growth state and conditions. Chl-a alone is not sufficient to make correlation with different type of algae. In addition to Chl a, different algal groups contain additional pigments, which were not quantified in this study. Chl-a correlates most with Alg_{is} (UG, Dia, Rest, i.e. those absent at t0), since temporal Alg_{is} increases contribute to Chl-a. Chalkophore and siderophore correlate positively with OD, pH and Cts.ef, and chalkophore specifically correlates with BG.

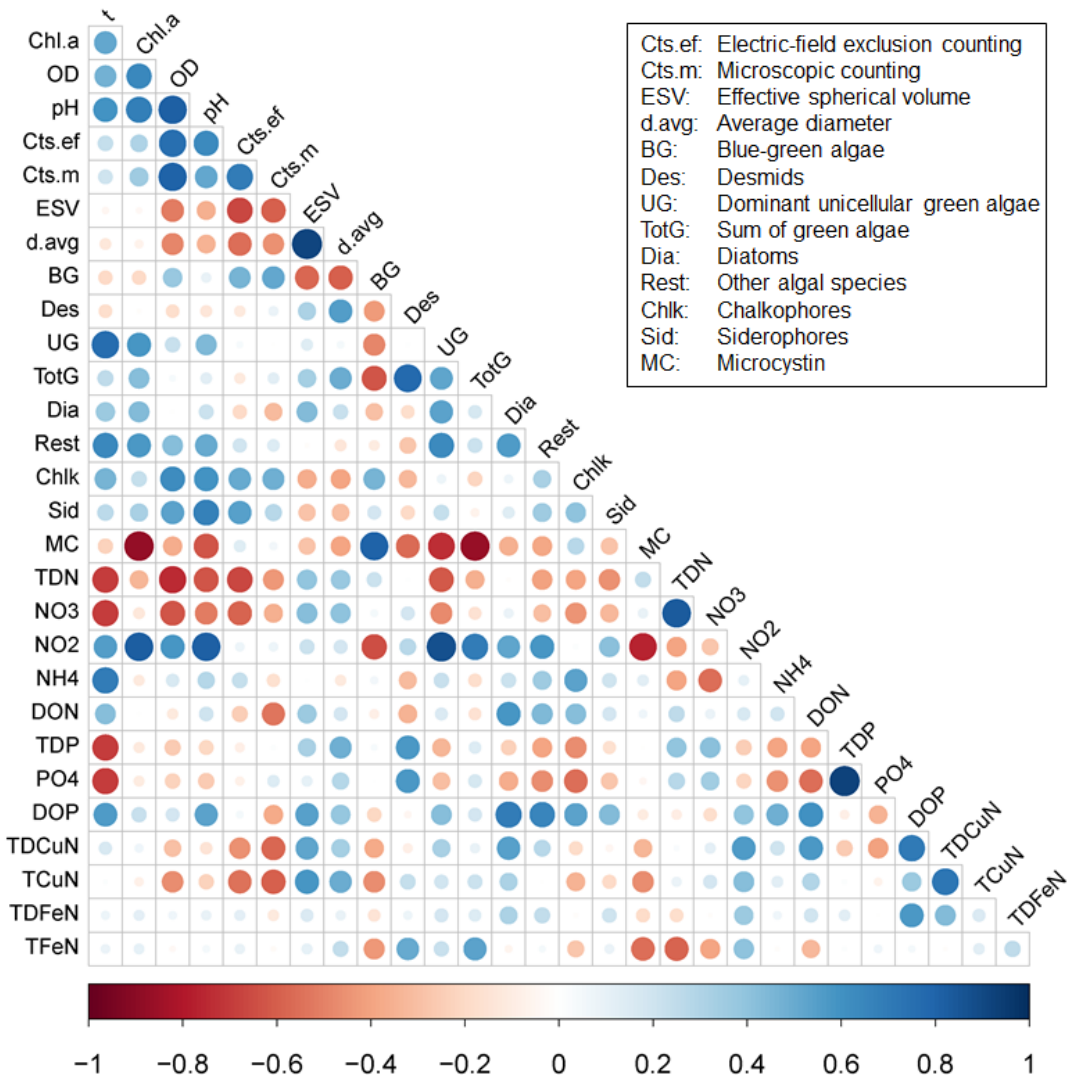

Figure 3-2. Correlation matrix plot showing pairwise-correlation analysis for results from mesocosm experments in the year of 2018. The size and degree of coloration of each circle in the matrix is proportional to Spearman's ρ, according to the color legend at the bottom of the figure. For $|\rho| \geq 0.4$, the associated p-values are all ≤ 0.05.

As expected, TDN/NO3 correlate negatively with growth indicators (OD, pH, Cts.ef and Cts.m), and the strong positive NO2-UG correlation suggests more nitrification in samples with UG. TCu and TDCu negatively correlate with BG, accompanied by reduction in growth indicators and concomitant increases in ESV/d.avg (BG cells being small), reflecting differential BG sensitivity to the level of Cu amended. Interestingly, microcystin correlates negatively with TFe, discussed in more detail in Section 3.7. For individual station data, correlations

are comparatively stronger for St 13 than for St 3/St 28, however St 3/St 13 patterns in pair-wise correlation are more similar compared to St 28. Such differences are discussed where relevant in subsequent sections.

3.5 Changes in Algal Growth Indicators

Figure 3-3 shows OD and pH versus time for all stations and amendments. There is a strong OD-pH correlation (ρ = 0.78, p < 0.001, Figure 3-2) as OD and pH are both primary consequences of growth (pH increases due to inorganic carbon scavenging, Wang et al., 2017). For M_{meso} Ctl/Fe, both parameters increase, then decrease, indicating onset of stationary phase by ~ t2. Where differences exist, M_{meso} OD and pH are higher for Fe than Ctl (p < 0.05) during growth (t2) for St 3, whereas post-stationary Fe > Ctl differences are for St 13 and St 28, much more so for St 28 by t6, indicating that St 28 Ctl growth has started to taper, with an ameliorating affect for Fe. Considering that St 28 t0 TDFe is half of the other stations and that Fe can limit *Microcystis* growth (Fujii et al., 2016), the St 28 difference between Ctl and Fe may be caused by Fe-limitation. Cu for M_{meso} caused inhibition with or without Fe. OD for M_{meso} Cu showed a decrease t0–t2, while pH showed no increase; from microscopic examination, I know that this is from a Cu-induced diminution in BG/*Microcystis*. For M_{meso} Cu, OD slowly recovered with simultaneous pH increases t2–t6. Per results in Section 3.6, this results from Alg_{is} increases. Also with Cu, there are indications that Fe exerts a positive effect, notably pH has risen for CuFe much more than for Cu by t4.

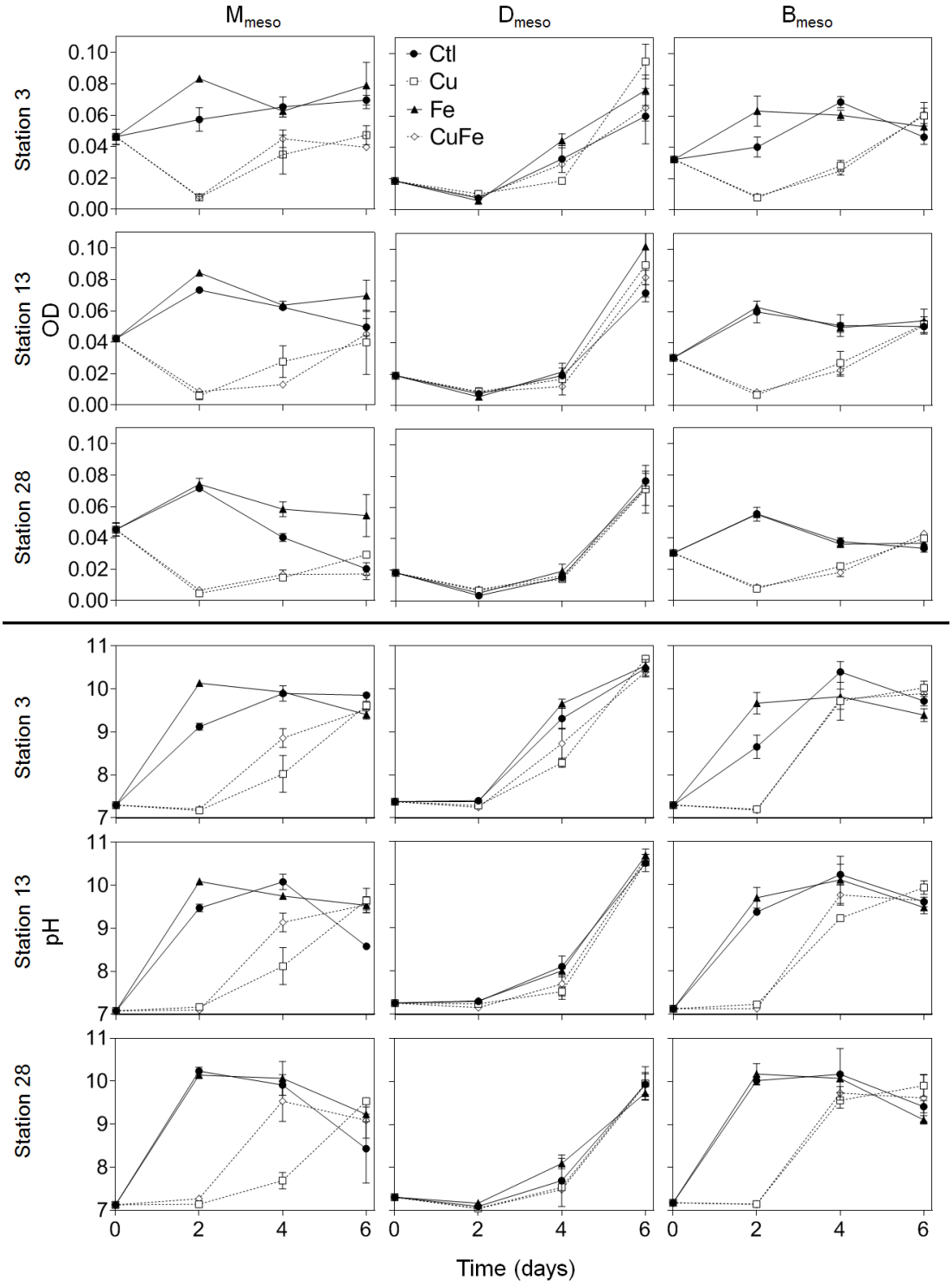

Figure 3-3. Changes in OD and pH with time for mesocosm experments in the year of 2018. Results for OD (750 nm) are in the top three rows and for pH are in the bottom three rows. Results are plotted for three stations as a function of mesocosm type and amendment.

For D_{meso}, OD drops t0–t2, likely a result of incomplete acclimation. After a longer induction than M_{meso}, D_{meso} OD for all amendments entered logarithmic

growth-phase, with substantive increase of OD/pH by t6. There were no differences by amendment, except that St 3 Fe had higher pH compared to Cu/CuFe ($p < 0.01$) at t4; by t6 the benefit of Fe disappeared. Comparing OD/pH results for M_{meso} and D_{meso}, D_{meso} had a greater ability to cope with the amended level of 50 $\mu g \cdot L^{-1}$ Cu, consistent with other research on green algae (Buayam et al., 2019; Wu et al., 2017).

Other metrics used as growth indicators include counts and Chl-a. There are various reasons why strong correlation/linearity between OD and counts/Chl-a might not exist, e.g. differential effects from pH, other environmental factors, that counts represent different species with different growth behavior (Francois et al., 2005; Griffiths et al., 2011)—in effect, OD is a bulk solution measurement and counts are not. Per Figure 3-2, OD strongly correlates with both Cts.ef and Cts.m. (respectively, ρ is 0.76 and 0.79, $p < 0.0001$); I also find a generally linear relationship (Pearson's r of 0.74 and 0.79 respectively, for Cts.ef and Cts.m), shown in Figure 3-4, however with substantial scatter around the trend.

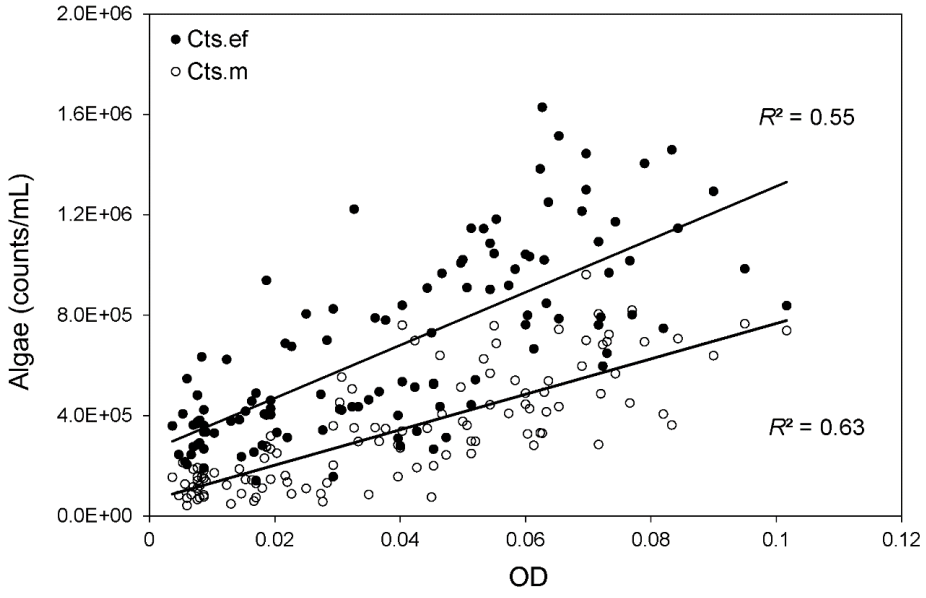

Figure 3-4. Linear relationships between OD (750 nm) with Cts.m and Cts.ef. Cts.m are shown in hollow symbols and Cts.ef in solid fill.

A diminished correlation between OD and Cts.m/Cts.ef might be expected given assemblage diversification (Section 3.6). Consistent with this logic, I find that linearity between counts and OD is strongest for single species mesocosms when pHs < 8 and weakest for mixed species at pHs >10.

In Figure 3-2, the correlation between OD and Chl-a is not as strong (ρ = 0.64, p < 0.001) as for counts, which I find is due, at least in part, to the changing percentages of algal assemblages over time and the proclivity of different groups to produce more or less Chl-a. Figure 3-5 shows Chl-a versus time, normalized to t0 by mesocosm to show relative changes (t0 Chl-a values are given in the figure caption).

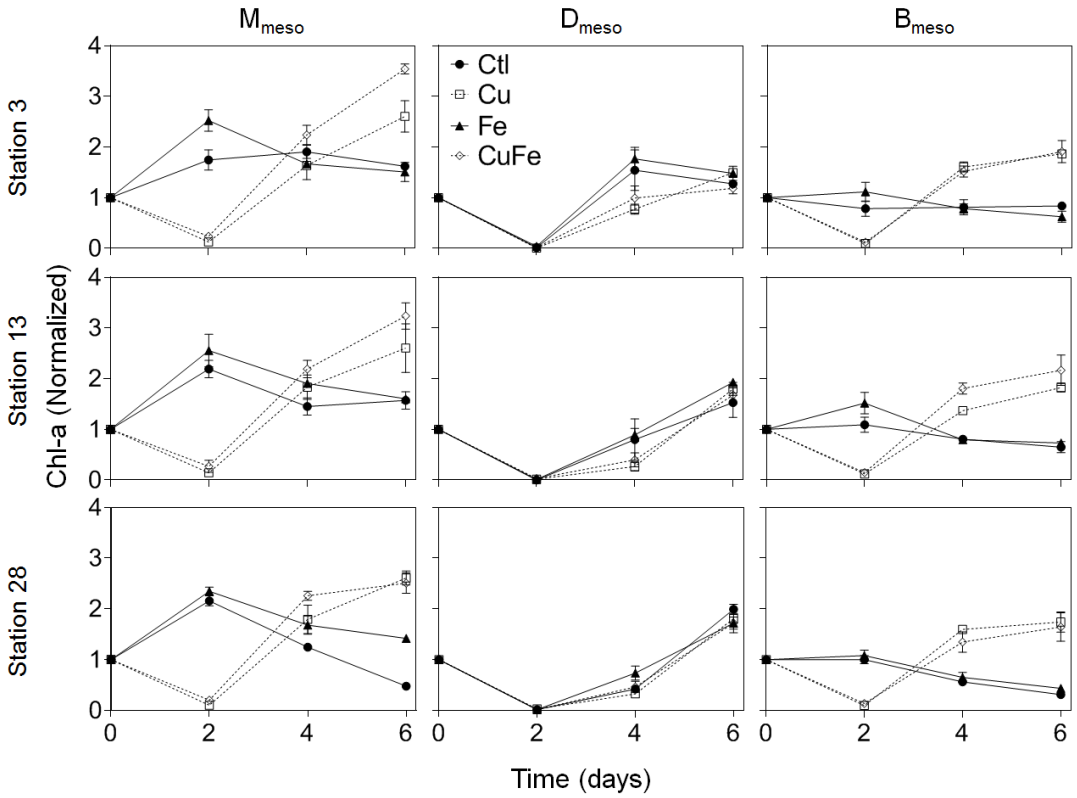

Figure 3-5. Changes in Chl-a with time for three stations as a function of mesocosm type and amendment. For each plot, Chl-a values were normalized to t0 to show relative changes on the same scale. Values of Chl-a at t0 are as follows: St 3 M_{meso}=73 µg·L^{-1}; D_{meso}=207 µg·L^{-1}; B_{meso}=138 µg·L^{-1}. St 13 M_{meso}=78 µg·L^{-1}; D_{meso}=207 µg·L^{-1}; B_{meso}=133 µg·L^{-1}. St 28 M_{meso}=85 µg·L^{-1}; D_{meso}=207 µg·L^{-1}; B_{meso}=153 µg·L^{-1}.

Figure 3-5 shows that Fe results in increases in Chl-a production in M_{meso}, with or without Cu, and shows higher Chl-a compared to Ctl by t2 (St 3 and St 28, $p < 0.05$). Chl-a in St 28 M_{meso} Ctl is less than half of M_{meso} Fe by t6 ($p < 0.05$), which agrees with OD results. That Cu at 50 $\mu g \cdot L^{-1}$ severely impairs M_{meso} Chl-a fully agrees with OD and pH results, however, the M_{meso} OD results for Cu/CuFe are still lower than for Ctl and Fe by t6, and the reverse is true for Chl-a ($p < 0.05$). This corresponds to algal assemblage changes for Cu/CuFe after t2.

Like OD, D_{meso} Chl-a dropped substantively by t2 (Figure 3-5). Compared to Ctl/Fe, Cu/CuFe negatively impacted Chl-a production in D_{meso} at t4 (Cu < Fe, St 3–St 28; CuFe < Fe, St 3/St 28, $p < 0.05$), consistent with Küpper et al.'s (2003), results showing a Cu-induced temporary drop in Chl-a for the Desmid *Scenedesmus quadricauda*. This might be explained by the negative effect Mg^{2+} substitution by Cu^{2+} in the Chl-a complex has been documented to have on Chl-a synthesis at first (Küpper et al., 2003), until Cu-detoxification mechanisms in the green algae overcome this sub-lethal Cu-toxicity and Chl-a synthesis is restored to control levels, as observed at t6 (Figure 3-5). As with OD and pH, Chl-a of green-algae dominated samples (Figure 3-5 and 3-6) increased with time. Though M_{meso} Cu/CuFe contain predominantly green algae from t2, grouping with D_{meso} in Figure 3-6, unlike D_{meso} there are some differences between Cu and CuFe, noted above. For M_{meso} Chl-a levels show CuFe > Cu during t2–t6, though this is not observed by t6 for St 28. The difference in Chl-a results for St 28 may reflect Fe-limitation (Fujii et al., 2016), per OD/pH results, and for St 28 relating to other observations below. Differentiating St 28, Chl-a correlation with TotG is comparatively stronger in St 3 and St 13.

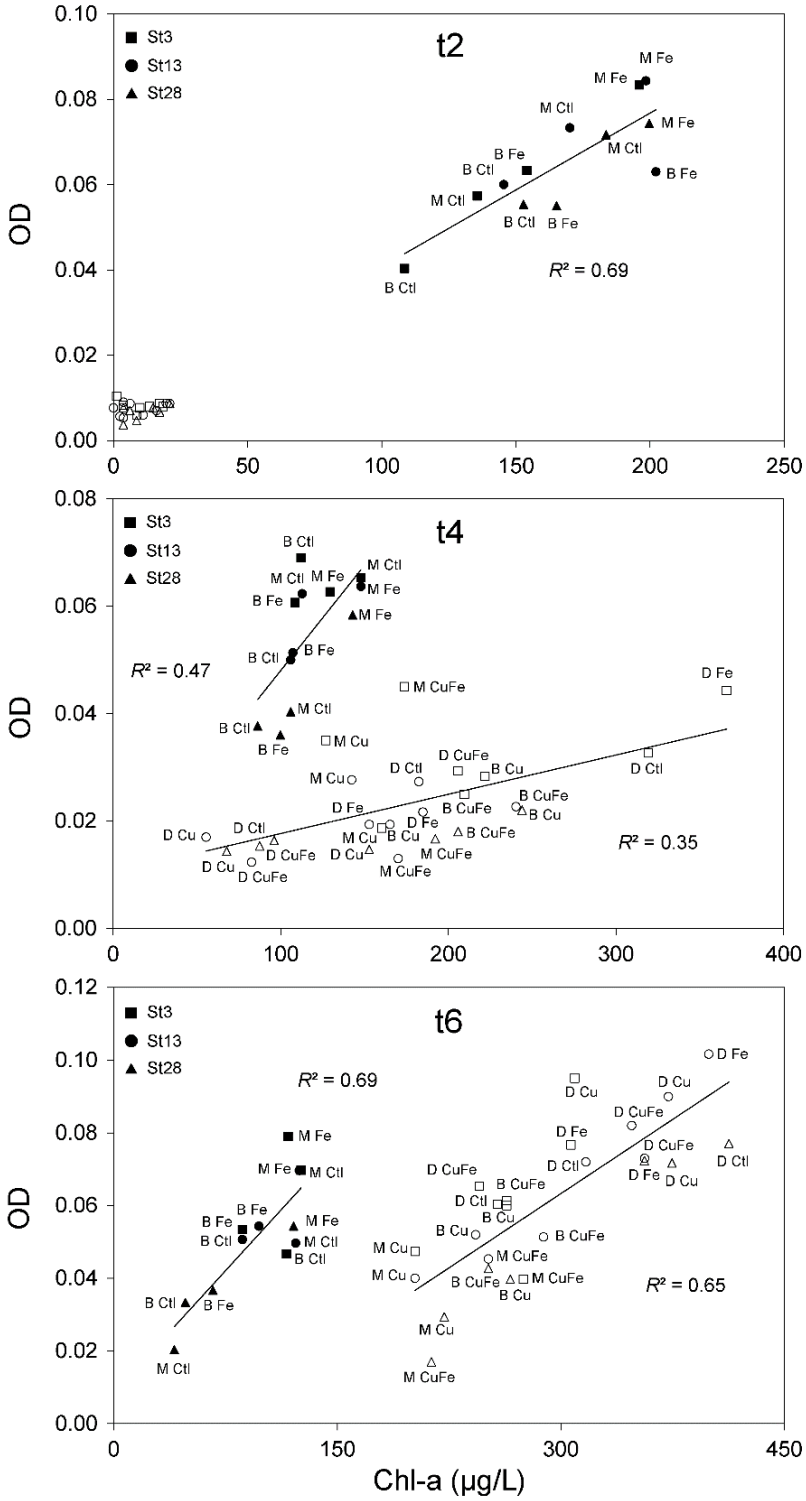

Figure 3-6. Linear relationships between OD (750 nm) and Chl-a. Results for mesocosms are grouped according to dominant algal assemblages (BG versus green algae) with different amendments and for three stations. Panels A, B and C show results for t2, t4 and t6, respectively. Filled symbols are for M_{meso} and B_{meso} Ctl and Fe amendments (i.e. without Cu); hollow symbols are M_{meso} and B_{meso} with Cu/CuFe amendment and D_{meso} for all amendments. Different axis scales are used for visual clarity.

The OD versus Chl-a plot in Figure 3-6 illustrates how different algal assemblages (details in Section 3.6) contribute to Chl-a. The slopes for D_{meso} and samples becoming green-algae dominated (M_{meso} and B_{meso} Cu/CuFe) are less than corresponding slopes for *Microcystis*-dominated samples (M_{meso} and B_{meso} Ctl/Fe), such that for any given increase in OD, the corresponding increase in Chl-a is less for the latter. In my work on Taihu, I have found that *Microcystis* consistently have relatively lower Chl-a than green algae, which has also been observed by others (Ghadouani and Ralph, 2005). For *Microcystis*-dominated samples, Chl-a is consistent with OD and pH, increasing to t2, then diminishing on entering stationary phase, with Fe > Ctl for Chl-a (St 3/St 28, $p < 0.05$) during the period of growth up to t2 (similar to OD). Fe increases Chl-a in M_{meso}, with or without Cu. Chl-a in St 28 M_{meso} Ctl is less than half of M_{meso} Fe by t6 ($p < 0.05$), which also agrees with OD results. Though M_{meso} Cu/CuFe OD are still lower than for Ctl/Fe by t6, the reverse is true for Chl-a ($p < 0.05$). This reflects algal assemblage changes for Cu/CuFe after t2.

3.6 How Amendments Affect Algal Assemblages

Cts.m remain unsurpassed for simple determination of species density/assemblage changes and cell condition (Butterwick et al., 1982). Transition from blue-green to green algae from varying NP/carbon sources has been long-known (Shapiro, 1973), and my colleague Dr. Zhang and I previously found that MN also mediate algal assemblage changes (Zhang et al., 2019). Because of my experimental design, I anticipated that Alg_{is} might cause algal assemblage changes over the course of my field experiments and that changes might reflect initial conditions or Cu/Fe amendment. Figure 3-7 shows time-

dependent changes in Cts.m of algae groups by amendment. At t0, algal species and Cts.m are as expected. Since the mixture in B_{meso} was effected according to OD, Des in D_{meso} constitute larger, but fewer, individuals, and thus t0 BG/*Microcystis* Cts.m is greater than Des in B_{meso}.

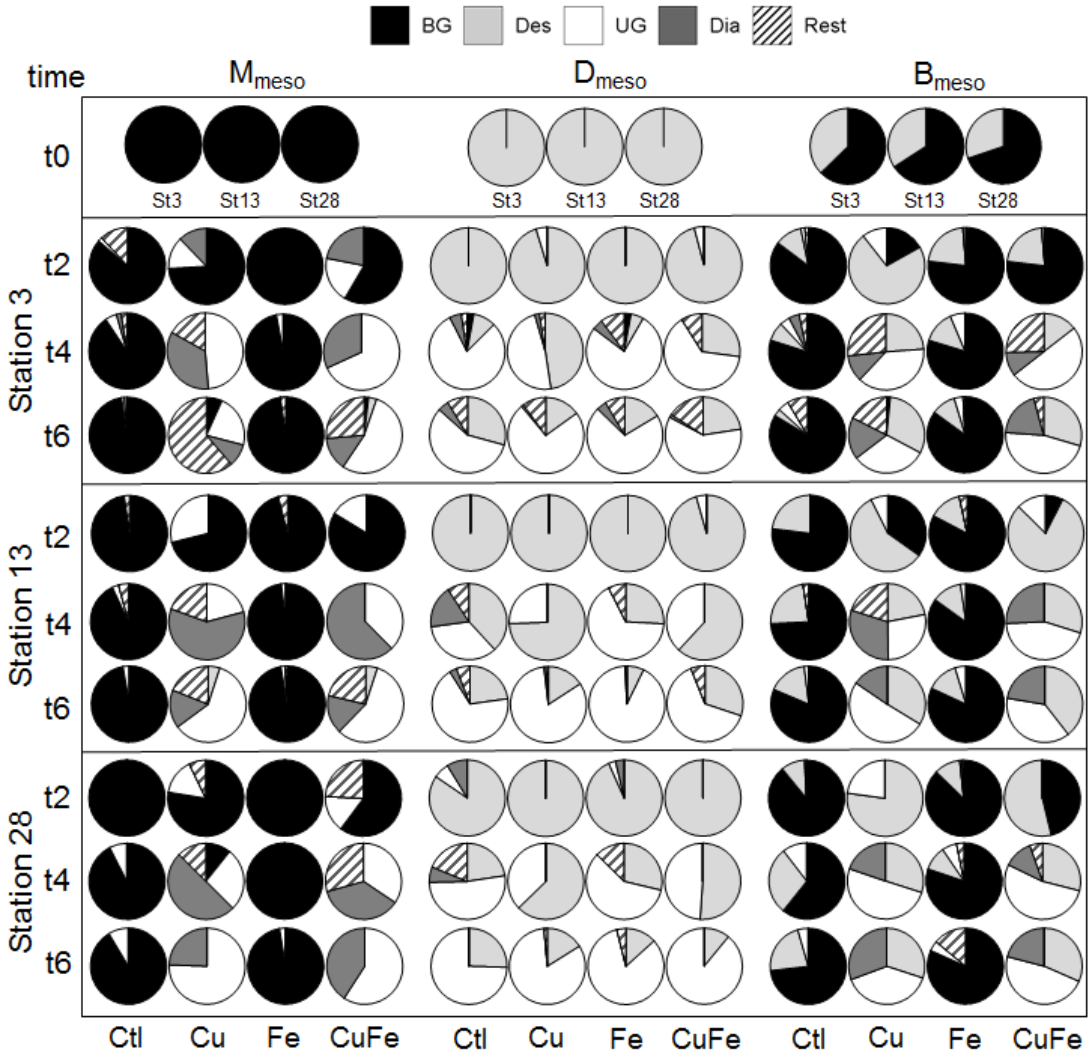

Figure 3-7. Pie charts showing changes in algal assemblages mesocosm experiments in the year of 2018. The percentages of algae for different amendments for three stations are given by group (BG = Blue-green algae; Des = Desmids; UG = Unicellular green algae; Dia = Diatoms; Rest = remaining, less common algae).

For t2–t6, the compositions of the five algal groups were as follows: BG were 97+% *Microcystis* with smaller amounts of *Chroococcus* and *Pseudoanabaena*; Des were primarily *Desmodesmus* with occasional occurrences of *Scenedesmus*;

UG included mixtures of *Carteria* and *Chlorella* (81+%, not always easily differentiable), with lesser amounts of *Chlamydomonas*; Dia were mixtures of *Navicula* and *Nitzschia*, with minor amounts of *Asterionella*, *Cyclotella*, and *Fragilaria* (each never exceeding 12%); and Rest constituted low, highly variable, counts of *Chlosteriopsis*, *Coelastrum*, *Dichtyospaerium*, *Eudorina*, *Haematococcus*, *Kirchneriella*, *Micractinium*, *Monoraphidium*, *Oocystis*, *Pediastrum*, *Planktosphaeria*, *Radiococcus*, *Schrodeiria*, *Tetraedron*, *Mallomonas*, *Chroomonas*, *Chryptomonas* and *Trachelomonas*.

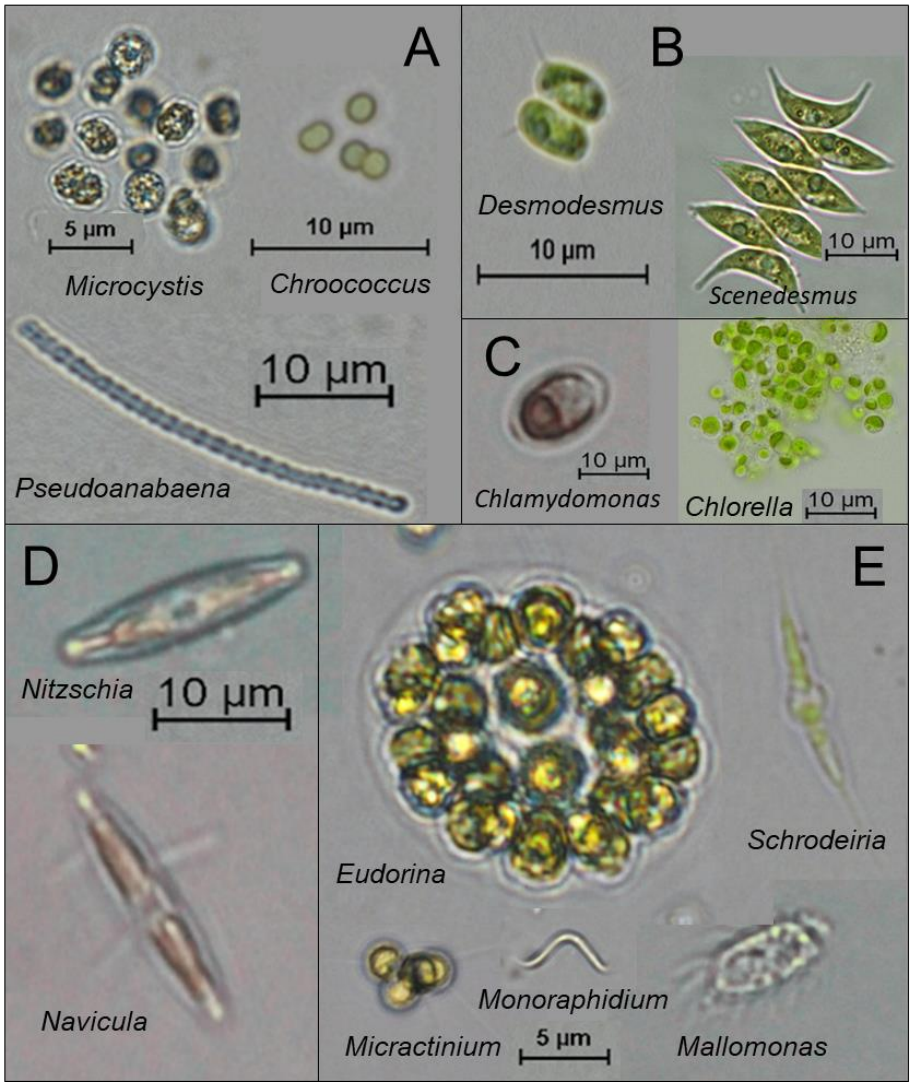

Figure 3-8. Algal species representing different groups observed under the microscope. Blue-green algae (BG, panel A); Desmids (Des, panel B); Dominant unicellular green algae (UG, panel C); Diatoms (Dia, panel D); and the remainder (Rest, panel E).

A striking feature in Figure 3-7 is, by t2, M_{meso} Cu/CuFe amendment resulted in replacement of *Microcystis* by other groups through to t6, i.e., *Microcystis* is more sensitive to the Cu concentrations that I use compared to other freshwater algae, consistent with Zeng et al.'s (2010) report of an IC_{50} of 25.5 $\mu g \cdot L^{-1}$ for *Microcystis*, whereas Buayam et al. (2019) and Wan et al. (2018) reported that *Desmodesmus* and *Chlorella* can tolerate higher Cu concentrations. Figure 3-7 suggests that excretion of Cu-protective compounds (e.g., Nicolaisen et al., 2010) is non-operative or non-effective for M_{meso} Cu/CuFe. Also apparent in Figure 3-7 is that when *Microcystis* is not impacted, it retains its place (M_{meso}) or gains ground (B_{meso}) over other species, which may partially result from more efficient BG CO_2 uptake at high pH (King, 1970; Shapiro, 1973). The proportionate increase of Des in D_{meso} was slower than UG growth, and UG consistently dominated D_{meso} by t6. Des may have been less competitive due to incomplete acclimation. Changes in B_{meso} Ctl/Fe assemblages followed those for M_{meso}, albeit not as dramatically; *Microcystis* was the major species (t0–t6 average ≥ 77%, minimum 61%), while Des averaged 34% at t0, decreasing 17% on average (maximum 37%) in B_{meso} by t6.

Since different algae grow at different rates, results may be considered in terms of AUC to obtain comparative information on integrated growth, growth inhibition (documented for *Microcystis*, Dong et al., 2019; Omidi et al., 2019) or stimulation (i.e. mono- versus mixed-cultures, Stockenreiter et al., 2012; Smith and Crews, 2014). Figure 3-9 shows AUC for the four main algal groups (BG, Des, UG, Dia, in panels A–D, respectively; AUC is normalized to the station maximum to show relative scale). Cts.m for BG of M_{meso} and Des of D_{meso} are divided by two for comparison with B_{meso}-proportionate t0 conditions (Cts.m for BG/Des in

B_{meso} were half those of BG in M_{meso} and Des in D_{meso}, respectively; $p < 0.05$). Results in Figure 3-9A and 3-8B imply that BG and Des grow better in mixed-culture. On average, AUC for BG in B_{meso} Ctl (Figure 7A) is higher by 35%, than BG in M_{meso} Ctl ($p < 0.05$). With Fe, BG in B_{meso} AUC is 27% higher than for M_{meso} (though $p \sim 0.15$), the difference being least for St 13 (not significant) and most for St 28 ($p \sim 0.007$). Looking at Des (Figure 3-9B), for Ctl, B_{meso} is 30% greater than D_{meso}, however, this is not statistically significant on average or station-to-station. For Fe, Des counts in B_{meso} average 25% greater than for D_{meso}; for St 3 and St 13 significantly ($p < 0.05$). For Des Cu/CuFe, there is no apparent difference in in D_{meso} versus B_{meso}.

UG and Dia are Alg_{is}, with comparable small t0 amounts by station, hence are plotted differently than BG/Des. No consistent station-to-station differences were observed, thus plots show station averages. UG AUC (Figure 3-9C) is consistently most variable and highest in D_{meso}, on average, by more than a factor of two compared to M_{meso}/B_{meso} Cu/CuFe. For M_{meso} and B_{meso}, AUC for Cu ~ CuFe > Ctl ~ Fe ($p < 0.05$), except for M_{meso} Cu > Ctl and CuFe > Ctl ($p \sim 0.07$ and 0.08, respectively).

My data show, as others find (Chen et al., 2016; Wan et al., 2018), that UG copes with Cu (comparing D_{meso} Ctl/Fe to Cu/CuFe), however, *Microcystis* is inhibiting (Dong et al., 2019; Omidi et al., 2019), which effect persists even when the original *Microcystis* population is diminished. Logically, lysis and release of microcystin is expected with BG/*Microcystis* diminution in Cu/CuFe (Shen et al., 2019). That microcystin is labile in field surface-water (Welker and Steinberg, 2000; Chen et al., 2008), possibly accounts for higher UG AUC with Cu/CuFe in M_{meso} and B_{meso} While lysing cells may transiently increase solution microcystin,

live cells can provide continuous flux of microcystin/toxic secondary metabolites, flux being in some ways more relevant than load (Tecon et al., 2006; Omidi et al., 2019).

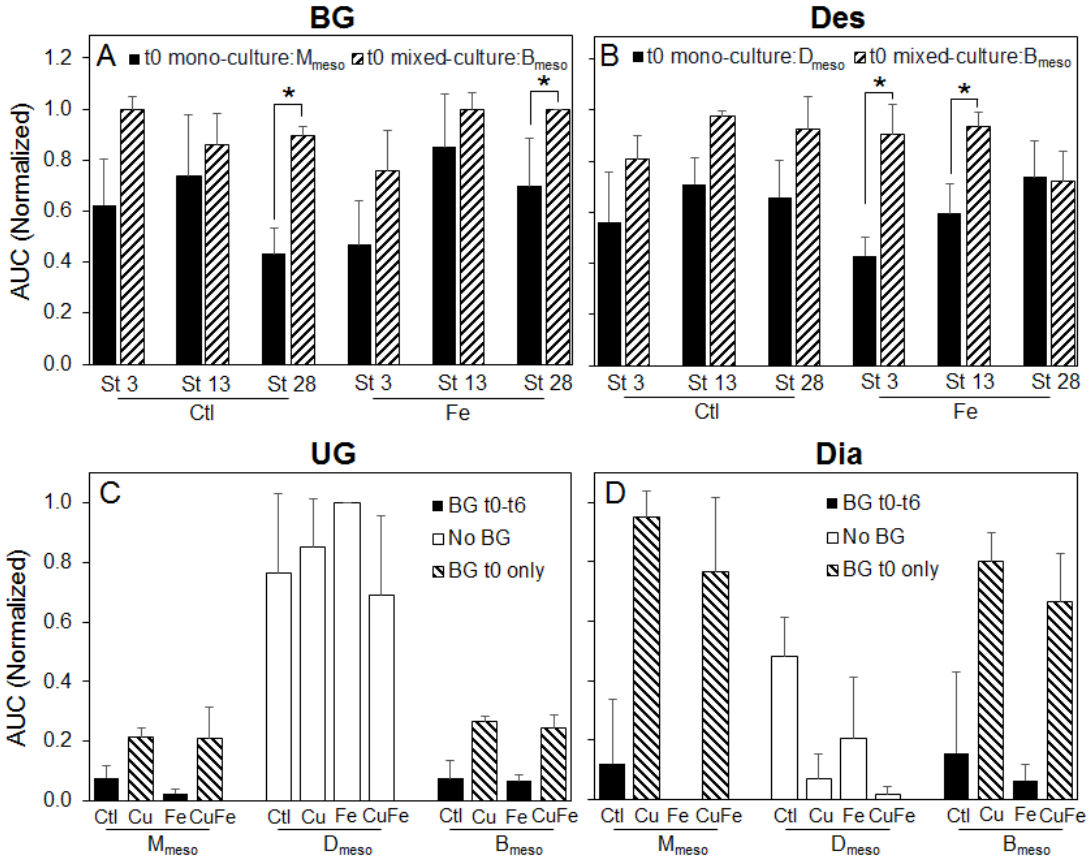

Figure 3-9. Bar plots of AUC for the four main algal groups: (A) BG, (B) Des, (C) UG and (D) Dia. AUC was calculated from the Cts.m results of different algal group over time (t0–t6) and plotted as normalized to station maximum.

For Dia, Cts.m are low and variability high; averaging stations does not increase this. The Dia AUC is higher for Cu/CuFe versus Ctl/Fe in M_{meso} and B_{meso} ($p < 0.05$). In contrast, D_{meso} Dia is higher in Ctl compared to Cu/CuFe ($p < 0.05$) on an average and station-to-station basis. Uncertainty is higher for Fe; D_{meso} Dia Fe > Cu/CuFe, though not significantly ($p \sim 0.21$). Unlike Figures 3-8A–C, which, respectively, show growth favored or inhibited in mixed-culture, M_{meso} and B_{meso} are not different. Dia for M_{meso} Cu/CuFe suggest growth despite this Cu level. Perhaps Dia grow better in these mesocosms because of increased DON (Bronk

et al., 2007) or because the additional DON/DOP in these mesocosms complex Cu in a protective manner (Zeng et al., 2010), however I am cautious about such inferences due to low Cts.m.

3.7 TEMPORAL CHANGES IN AMENDED N AND P

Here I summarize NP results. Three NP changes are most interesting/relevant to other results. First, DON/DOP is higher in Cu/CuFe BG-containing mesocosms, consistent with Cu-induced algal death and subsequent cycling into dissolved organic matter. Second, NO2 increases in mesocosms having active in growth of UG; I postulate that this likely results from different bacterial assemblages in these. Third, all M_{meso}, irrespective of amendment, are steady-state for P, i.e. the rate of P-production from organic matter cycling is equal to the rate of P-uptake by algae and/or bacteria. I posit that this is also an effect of bacterial assemblages, however, as the effect is not a function of amendment, it is less relevant to my focus. As important limiting factors to algal growth, NP species were measured at t0 and t6 as described in Section 3.2. The results are expressed in terms of uptake (deltas, Δ, being negative for net uptake and positive for net release).

Figure 3-10 is a schematic showing major known NP cycles in the water column, and for each measured component of the cycle, relevant Δs are shown. The average of three stations (Δ_{avg}) is given in cases where the relative standard deviation associated with Δ_{avg} is less than 20% or when the results are low (around the LOQ and lower, wherein constant and proportionate error contribute to greater variability).

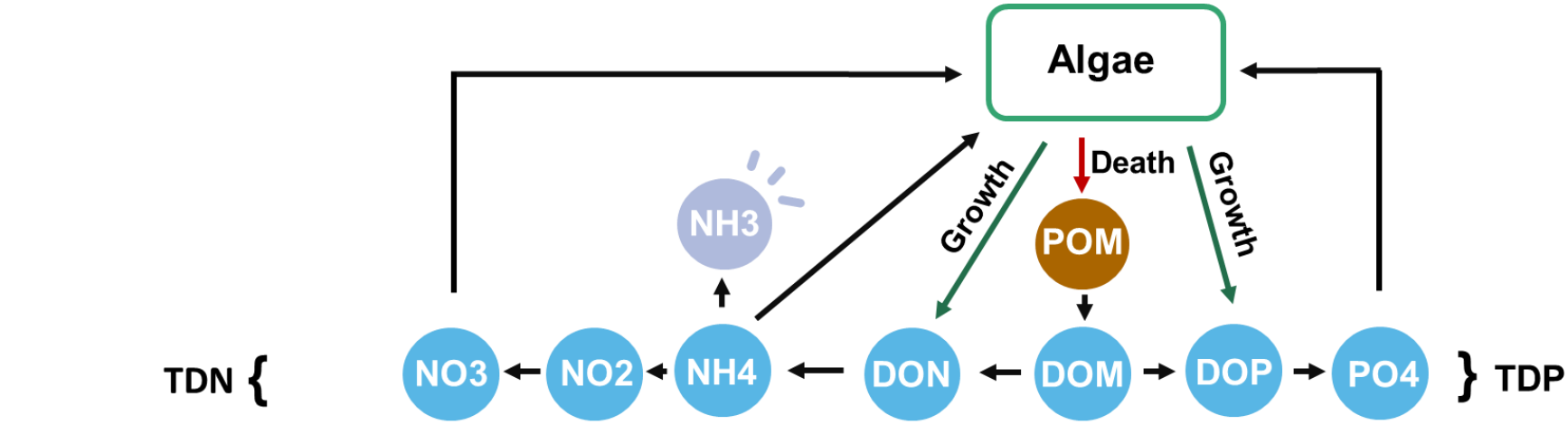

M Ctl	-1.34	-1.43	-0.82	-1.96	0.000	0.41	0.46	0.28	0.32	0.008	-0.19	-0.18
M Cu	-1.17	-1.24	-1.02	-1.87	0.026	0.18	0.55	0.50	0.50	0.025	-0.20	-0.17
M Fe	-1.58	-1.77	-1.62	-1.98	0.000	0.24	0.26	0.00	-0.01	0.003	-0.20	-0.20
M CuFe	-1.15	-1.10	-0.83	-1.88	0.024	0.14	0.60	0.63	0.83	0.018	-0.20	-0.18
D Ctl	-1.66	-1.66	-1.92	-1.97	0.049	0.20	0.01	0.04	-0.13	0.014	-0.15	-0.14
D Cu	-1.63	-1.55	-1.64	-1.95	0.056	0.22	0.16	0.25	-0.20	0.010	-0.16	-0.15
D Fe	-1.81	-1.79	-1.95	-1.98	0.034	0.12	0.06	0.04	-0.14	0.006	-0.16	-0.15
D CuFe	-1.50	-1.57	-2.03	-1.96	0.060	0.14	0.28	0.13	-0.23	0.010	-0.16	-0.15
B Ctl	-1.61	-1.71	-1.44	-1.97	0.000	0.29	0.16	0.01	0.12	0.020	-0.15	-0.13
B Cu	-1.31	-1.26	-1.12	-1.92	0.027	0.25	0.45	0.49	0.30	0.025	-0.15	-0.13
B Fe	-1.72	-1.68	-1.76	-1.98	0.000	0.40	-0.05	-0.27	-0.08	0.009	-0.16	-0.15
B CuFe	-1.37	-1.41	-1.49	-1.92	0.031	0.19	0.35	0.27	-0.19	0.014	-0.18	-0.16
	St 3	St 13	St 28	avg	avg	avg	St 3	St 13	St 28	avg	avg	avg

Figure 3-10. NP cycles with results expressed as deltas. Values of delta (Δ=t6-t0) are negative for net uptake and positive for net release. Numbers are the average delta for three stations, unless otherwise indicated.

A prominent and expected motif in Figure 3-10 is that ΔTDN is dominated by changes in NO3, due to the addition of N in this form, and is always negative, consistent with uptake and conversion to biomass and negative correlations in Figure 3-2 with growth indicators OD, pH, Cts.m, Cts.ef, and to a lesser extent Chl-a. While TDN and Chl-a did not correlate across all mesocosms, perhaps due to changing assemblages (Section 3.6), there was a correlation for St 28 (ρ = -0.54; $p < 0.05$) and a stronger negative correlation between TDN and pH (ρ = -0.80; $p < 0.0005$) for this station. In Figure 3-2, correlations for TDN resemble those of NO3. There are weak positive correlations between TDN, ESV, and d.avg, as the latter two would, on average, increase with TDN uptake. Here again, the correlation between NO3 with ESV/d.avg is stronger for St 28. On average, the largest magnitude ΔTDN is for D_{meso}, and among D_{meso}, the largest changes are for St 28, which in three of four cases appears to approach steady-state, assuming the initial DON-dominated N is refractory. For M_{meso}, save for St 28 Ctl, Cu/CuFe have smaller uptake than for Ctl and Fe. For St 3 and St 13, uptake for Fe is 20% higher than for Ctl, and for St 28 the difference is a factor of 2. This is in excellent agreement with OD results, for which Fe is larger than Ctl by 14%, 40%, and a factor of 2.5, for St 3, St 13, and St 28, respectively. In general, ΔTDN for B_{meso} are similar for three stations among amendments and follow the trend of ΔTDN Fe > Ctl > Cu ~ CuFe, though notably, like M_{meso}, uptake of Ctl in B_{meso} is smaller in St 28. For individual stations, there is strong correlation between TDN and DON, however, for St 28 there is also a correlation with NH4, i.e., the TDN fraction has a somewhat higher component of NH4 for this station.

Subsequent to uptake and conversion to biomass, N is removed from the

dissolved nutrient pool unless ΔDON increases as a result of DOM release by algae or increased particulate organic matter (POM, i.e., from dead algae) decomposition into the dissolved phase (DOM ⇨ DON/DOP). ΔDON is highest in M_{meso} with Cu/CuFe, which is consistent with lysing effects of Cu on BG. For all stations, ΔDON for M_{meso} is positive or ~ zero and follows the trend CuFe > Cu > Ctl > Fe, where the magnitude of CuFe > Cu, Cu > Ctl, and Ctl > Fe is, respectively, 34, 51, and 77+% (large as Δs are very low for Fe St 13 and St 28). For B_{meso} the distinction between Cu/CuFe and Ctl/Fe is not so distinct and ΔDON follows the trend CuFe ~ Cu > Ctl ~ Fe. That ΔDON is higher in M_{meso} and B_{meso} cultures for Cu/CuFe is consistent with recycling of POM from dying *Microcystis* (indicated by changes in OD and counts by t2), and according to ODs, M_{meso} and B_{meso} Ctl/Fe are in various stages of stationary phase, more so Ctl than Fe, suggesting again that Fe amendment increases the resiliency of *Microcystis*. ΔDON in D_{meso} samples overall exhibit lower levels of DON accumulation for St 3 and St 13, consistent with D_{meso} samples still being in exponential growth phase and having high pHs, however, ΔDON is again higher for Cu/CuFe than for Ctl/Fe, suggesting that Cu has a mildly negative effect. For St 28 D_{meso}, ΔDON is negative, with Cu/CuFe having higher uptake than Ctl/Fe. Among other things, this suggests that the mildly negative effect of Cu/CuFe seen in St 3 and St 13 is not happening in St 28, consistent with Chl-a results, where I also see that Chl-a of D_{meso} for Cu/CuFe is lower than for Ctl and Fe in St 3 and St 13 at t4, while examination of the Chl-a trends in Figure 3-6 shows how these differences at t4 are relatively diminished for St 28. Certainly, bacteria may play a major role in organic matter cycling, and as Fan et al. (2018) have shown, the assemblages and their associated activities in different parts of Taihu vary greatly. This also

relates to the positive effect that DON may play on stimulating bacterial production (Seitzinger et al., 1999). Generally, DON does not exhibit strong correlations in Figure 3-2, likely indicative of different states of organic matter cycling in different mesocosms, and hence largely variable/complex behavior in B_{meso}. There is a strong correlation between DON and Dia, as discussed in Section 3.6.

In surface waters, nitrification converts DON to NO3 via NH4 and NO2. NH4 behavior is complicated since, while it is taken up by algae as a N-source, at the high pHs that are reached in these experiments (all my pH samples reached pH 9 by t6), it is also lost via volatilization of ammonia in the form of NH3. I report ΔNH4 for reference in Figure 3-10 and primarily focus my discussion on changes in purely aqueous nutrient forms. In Figure 3-2, the proximal oxidation product of NH4, NO2, correlates with OD, pH, and Chl-a, with strong positive correlations with UG and other Alg_{is} groups, and strong negative correlations with BG and the BG-produced microcystin. Correlations with Cts.m and Cts.ef are absent, as would be expected since all other indicators are consistent with NO2 increases being associated with green algae. In Figure 3-10, when comparing samples dominated by BG (M_{meso} and B_{meso} Ctl/Fe) to the remainder that are dominated by green algae, by the one-half LOD statistical method (Hornung and Reed, 1990), the ΔNO2 of the latter is a minimum of ~ 75-fold that of the former. Production of NO2 as a nitrification intermediate is only observed in samples with more UG; of these, ΔNO2 for D_{meso}, all amendments, average twice that of M_{meso} and B_{meso} Cu/CuFe. All mesocosms with positive ΔNO2 are samples associated with being in an early or exponential growth phase at t6 (as indicated by ODs), and microscopic examination of D_{meso} show a

profusion of aplano- and zoospores. Within the D_{meso} group, values for ΔNO2 are slightly higher for Cu/CuFe than for Ctl/Fe, and the highest values occur for St 28 (data not shown), consistent with this station's having negative ΔDON and the idea that there is a high rate of N cycling and associated bacterial nitrification for this station. Stronger negative correlations were also found in St 28 for NO2 with TDN, DON, and NH4.

ΔNO3 is negative (uptake) and varies less than 2% for all mesocosms, but lowest ΔNO3 values occur for M_{meso} Cu/CuFe followed by B_{meso} Cu/CuFe. These samples are where I saw the Cu effect in diminution of OD and counts for BG. Subsequent to growth inhibition of BG, uptake of source (NO3) by green algae occurs later, and the growth of green algae in these samples is still less than for Ctl and Fe based on OD, pH and counts results.

Regarding P species, PO4 uptake is highest and effectively at steady-state for $M_{meso,}$ and, most conspicuously, is the same across amendments. The algal assemblages and appearance under the microscope are very different for Cu/CuFe and Ctl/Fe, therefore, there does not seem to be a common denominator that would explain this with the purview of algal effects. I considered chemical effects, and can find no explanation from that standpoint. I thus hypothesize that the PO4 uptake for $M_{meso,}$ may relate to bacterial assemblages present at t0 and the more active cycling of biomass based on the growth-phase of M_{meso} Ctl/Fe and injection of DON/DOP into M_{meso} Cu/CuFe. This idea is supported by some literature. In a survey of 15 low-latitude lakes, They et al. (2017) found a dramatic linear decrease in bacterial N : P ratio, consistent with increased P uptake, with increasing bacterial production

(magnitude of slope ~ 100). In contrast to TDN/NO3, PO4 uptake is consistently lowest for D_{meso}, and I posit that this is an outcome of the as-yet exponential growth in these mesocosms, such that PO4 is not at steady-state. For M_{meso}, ΔDOP is always higher for Cu/CuFe, which agrees with the previous discussion on the toxicity effect from Cu addition, but the difference in the average ΔDOP between M_{meso} and D_{meso} is minor. The pool of DOP depends on both degrading algal POM and rate of PO4 release by DOP.

3.8 Temporal Changes in Dissolved versus Total Cu and Fe

For trace metals analysis QA/QC is especially important, and I first review those results. For TM (TCu/TFe) results, QA/QC metrics are within acceptable limits according to the US EPA (2007). Recoveries for TM QA/QC spike checks were 104 and 108% and for the CRM were 104% and 102% for TCu and TFe, respectively. The average respective recoveries (equation 3-1a) for TCu and TFe were 101% and 107%, with an RSD of 15% in each case. Values of $C^{TCu}_{algae,\,t0}$ were 14 μg·L^{-1}, 16 μg·L^{-1} and 15 μg·L^{-1}, respectively, for M_{meso}, D_{meso} and B_{meso}, and values of $C^{TFe}_{algae,\,t0}$ were 400 μg·L^{-1}, 650 μg·L^{-1} and 520 μg·L^{-1}, respectively, for M_{meso}, D_{meso} and B_{meso}. For dissolved metals, the concentration of $C^{TDCu}_{spike,\,t0}$ in Cu and CuFe amendments were 50 and 51 μg·L^{-1}, respectively (100 and 102% recovery), and the concentration of $C^{TDFe}_{spike,\,t0}$ in Fe and CuFe amendments were 213 and 214 μg·L^{-1}, respectively (107% recovery). For TDCu and TDFe sample analysis, QA/QC results were also within acceptable limits, with the average spike recovery being ≥ 97% and the average RSD being 7%.

Given the acceptable QA/QC outcome, I confirmed that TCu/TFe were

conserved for t0–t6, to within analytical uncertainty, and therefore the primary changes that I wanted to look at involved TDM, results for which over time are shown in Figure 3-11. For Cu/CuFe, TDCu results show that the low, ambient concentrations of TDCu at t0 (Table 3-2) did not change over time for Ctl/Fe. For Cu/CuFe, TDCu decreased t0–t2, then stabilized, in most cases by t2. According to speciation calculations, $CuSO_4$ used in amendment should be entirely dissolved, hence the change in TDM from initial conditions for Cu is likely to reflect algal uptake, either intracellular or via adsorption to algal cell walls. The TDCu uptake for Cu/CuFe amendments averaged 27 $\mu g \cdot L^{-1}$ for D_{meso}, or ~ 50% greater than that of 18 $\mu g \cdot L^{-1}$ for M_{meso} ($p < 0.001$). This corresponds to an average TDCu uptake of 47% and 31%, respectively, of t0 TDCu for M_{meso} and D_{meso}. B_{meso} TDCu are not differentiable from predicted based on averaging M_{meso} and D_{meso} ($p > 0.05$). For some Cu mesocosms in Figure 3-11, there appears to be a slight TDCu increase toward t6. I speculate that this may be related to organic matter cycling during the growth phase and/or growth induced changes in pH, which are known to have a significant impact on trace metal speciation and solubility. In several cases, it appears that TDCu uptake for Cu is less than for CuFe (statistically different for St 28 M_{meso} at t2; St 13 B_{meso} at t4 with $p < 0.05$), which could be a small effect of Fe scavenging Cu (Hem and Skougstad, 1960; Hem and Cropper, 1962), however, when present, the effect is not great. A report by Hadjoudja et al. (2010), found that Cu cell surface zeta potential attraction was greater for *Microcystis* than for the green algae *Chlorella* and speculated that this might relate to the differential sensitivity of *Microcystis* to Cu that many authors have found. As others have reported that extracellular Fe crusts are capable of scavenging Cu and thus reducing Cu toxicity, this

toxicity effect could be reduced or offset by Fe. I see no evidence of such an effect here. This may be a question of kinetics. Some investigators have found that uptake rates for soluble metals are reasonably rapid (Zeng et al., 2010; Sutak et al., 2012), in which case, as for my experiments here, the negative zeta potential of *Microcystis* might result in rapid uptake before amended Fe has time to form extracellular adhered oxyhydroxides.

For TDFe, results were not as expected, the main finding of note being the unanticipated differentiation of bioavailable/biounavailable forms. I used different forms of Fe by design (Section 3.2), and I anticipated that FeCitrate used for Fe amendment would exhibit a greater or longer-term bioavailability than for the $FeCl_3 \cdot 6H_2O$ used for CuFe amendment. The most striking feature of TDFe results is that, by t2, Fe in both types of amendment had become TFe of some form. On average, the TDFe uptake from t2 to t6 is the same for M_{meso} versus D_{meso}. Differences in TDFe as a function of amendment are generally not large, though for St 3 and St 13, by t4 the TDFe averages ~ 30% less for Ctl/Fe than for Cu/CuFe ($p < 0.05$ for St 13, $p < 0.07$ to 0.10 for St 3). In some cases, there appears to be a slight TDFe release into solution over time, most noticeable for St 3 M_{meso} Cu/CuFe. As the NP results indicate a considerable reworking of organic matter in the Cu/CuFe amended mesocosms with *Microcystis* spp., it would be reasonable to see Fe released into solution, however, due to oxyhydroxide formation, it is also reasonable that such changes would be low.

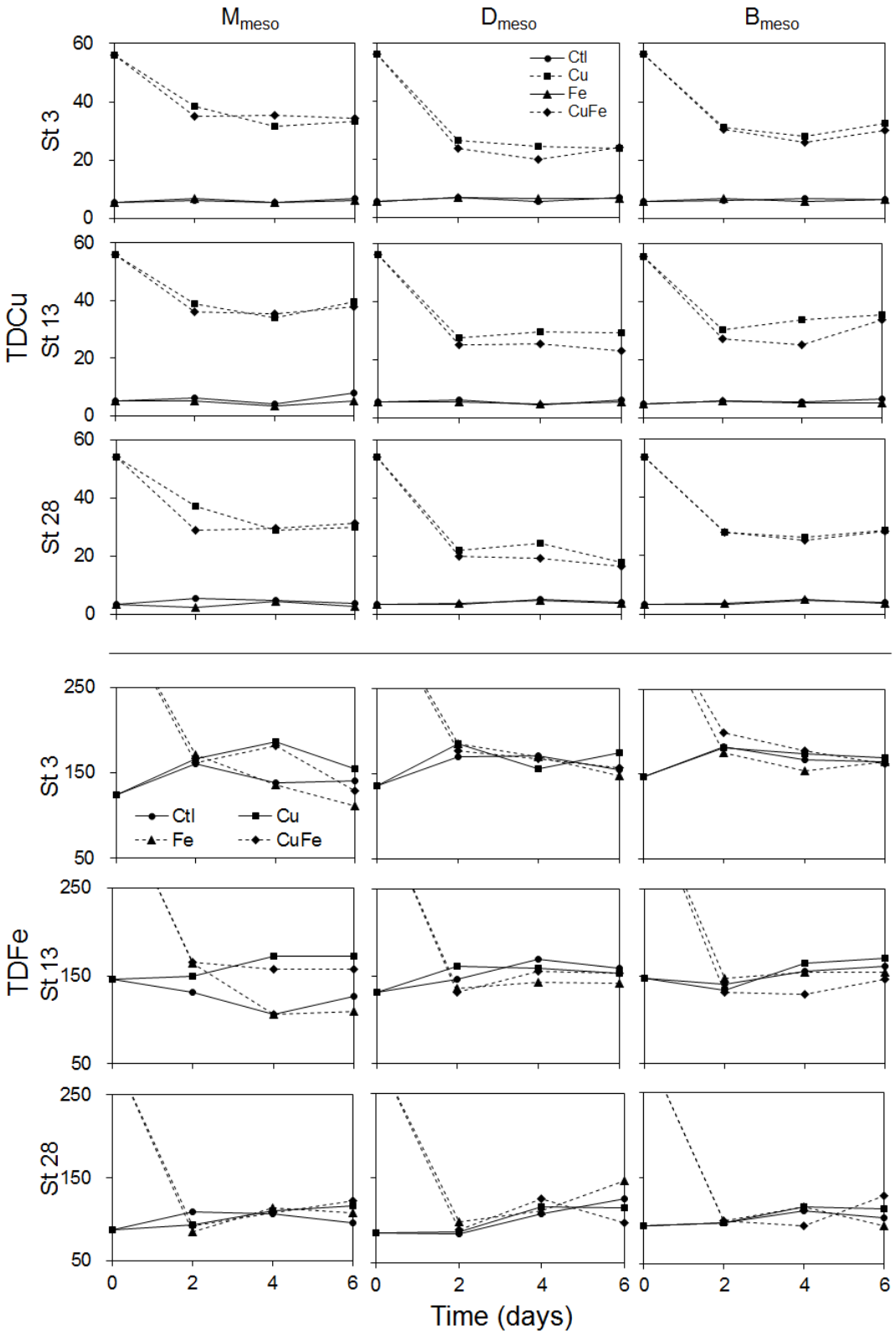

Figure 3-11. Changes in TDCu and TDFe as a function of time for mesocosm experiments in the year of 2018. Results are plotted as a function of mesocosms type for different MN amendments and for three stations. TDFe results at t0 for Fe/CuFe amended mesocosms are plotted off-scale in order to better visualize t2 to t6 changes in TDFe.

Common to both TDCu and TDFe, levels are consistently lower for St 28, though the differences between St 28 and St 3/St 13 are not always pronounced. Another difference for St 28 is that for this station there are stronger negative correlations between TDFe and TDP/PO4 (ρ = -0.65/-0.52 for St 28, ρ = 0.07/0.02, whereas for St 3 and St 13, $-0.2 < \rho < 0$). This is likely related to biogeochemical cycling regimes in Taihu. Fan et al. (2018) used qPCR to study bacterial communities in sediments underlying areas of the lake subject to intense cyanobacteria HABs in comparison to macrophyte-dominated areas such as St 28. These investigators found that bacterial communities in these different areas resulted in much different Fe:P ratios and rates of Fe and P cycling that are conceptually consistent with the inverse TDFe and TDP/PO4 relationships in overlying water that I observe at St 28.

Correlations between TCu/TFe/TDCu/TDFe in Figure 3-2 are in alignment with reasonable expectation. For Cu, TCu and TDCu correlations with other parameters are very similar, in keeping with my expectations based on Cu speciation/solubility. There are some weak to moderate negative correlations with growth indicators, BG, and microcystin, in line with the predominantly toxic effects of Cu in mesocosms containing BG/*Microcystis*. These are the same mesocosms for which I see positive correlations between Cu and DON/DOP, increases in which would result from reworking of BG biomass in the aftermath of Cu toxicity. This is also consistent with a small, weak correlation between TDCu and TDFe, i.e., small amounts of which might be reworked/released at the same time. There are positive correlations with ESV and d.avg, representing changes in growth/colony size for cells in mesocosms that do not exhibit strong toxic response to Cu. There are also positive correlations with NO2, which is

disproportionately produced in those mesocosms wherein green algae are able to outcompete BG due to Cu toxicity. Notably, there is a moderate positive correlation with Dia. Regarding Fe, TDFe is the least correlated parameter in Table 3-2, reflecting the circumstance discussed in Section 3.4: even when amended as FeCitrate, Fe complexed to what is normally regarded as a reasonably stable ligand, TDFe is nonetheless predominately transformed into TFe in my environmental setting. While more than for TDFe, there are still relatively few correlations between parameters and TFe. The causation of these relationships is discussed in Section 3.9.

3.9 Relationships Between Cu/Fe Amendments and Biomolecule Production

This field work is first to study chalkophore and siderophore production using assays differentiating the two. Chalkophores are defined as being ligands that have very strong and, as compared to other metals, very high association/complexing constants for Cu-binding (Saha et al., 2016) and analogously siderophores are ligands that have differentially stronger Fe-binding behavior. Prior work that is not able to separate chalkophores from siderophores as operational classes includes, for instance, studies that characterize strong-Cu binding ligands (that could be siderophores), when it is increasingly recognized that siderophores *are* strong-Cu-binding ligands (Jones and Hart, 1989; Baptista et al., 2014; Solioz, 2018), i.e., many methods in use do not explicitly separate chalkophore from siderophore. The method that I use here (Zhang et al., 2020b) specifically distinguishes chalkophore from siderophore, and the present work is the first to use this approach that

specifically differentiates chalkophores from siderophores. I analyzed results using CTA, recently adduced as a fresh perspective on dynamic aspects of population/community changes (De Cáceres et al., 2019).

Trajectory analysis (TA) is a well-accepted class of formalized mathematical approach to study a wide array of problems including diverse topics such as recurrence quantification analysis, used in cognitive and social sciences, structural damage detection in engineering applications, and land cover change in physical geography (Zhou et al., 2008; Majkut, 2012; Wallot and Leonardi, 2018), and many more. A key aspect of TA is that it represents an approach to analyze multiple time-series (per Wallot and Leonardi, 2018, for instance, multiple physiological indicators from within a group) that are often non-stationary, or possess other interesting dynamics. The dynamical aspect of TA has been key to its use in analysis of process dynamics (using multivariate process trajectories), useful for the systematic consideration of dynamics that may be otherwise masked in static consideration of, for instance, single time points or summary values (Section 3.3, Bogomolov, 2011). Because TA considers inherently dynamical processes, it is a method that can readily accommodate phase differences (e.g. Bischof and Zedrosser, 2009, per Section 3.9, Figure 3-15A and B). As such, another common feature of TA is that initial raw data, how a set of given quantities vary over time, is transformed into so-called phase space (Majkut, 2012; Wallot and Leonardi, 2018, i.e., data that are a function of time are translated to a corresponding phase-space depiction), which rendering is sometimes also referred to as a phase portrait. The sort of processes that are highly amenable to a process-dynamics analytical approach such as TA have long been discussed in the area of ecology, notably in the

textbook case of Lotka-Volterra predator-prey dynamics (see for instance phase-space diagrams in Bischof and Zedrosser, 2009), and, therefore, from the equations of state that govern this and other dynamical processes (e.g., Bischof and Zedrosser, 2009; Majkut, 2012; Wallot and Leonardi, 2018), it should also be apparent that phase-space representations may be likened to velocities in many instances. In the last decade, work by De Cáceres, (2010, also see De Cáceres, 2019, and works of other authors citing these) has formalized the mathematical application of TA to ecological studies (De Cáceres et al., 2019), in the form of CTA wherein different measurements that reflect changes in the community over time constitute community space, the ecological equivalent of phase-space. Analysis of community space trajectories provides a way to formally quantify and analyze variation in properties that reflect community dynamics (Bogomolov, 2011, De Cáceres et al., 2010 and 2019).

Before I discuss the biomolecule results in the context of CTA, I first discuss a question that naturally arises, which is, how do chalkophore/siderophore changes relate to growth? As I detail in Section 3-3, while many authors use some normalization process to try and address this question, the distortions that can be introduced by this practice are often unknown by adherents of the practice, but are potentially disastrous to the goal of proper understanding of processes. Yet, clearly, chalkophore and siderophore are to some extent related to growth (moderate correlations with OD/pH in Figure 3-2, also see results from the first report of chalkophore screening in Zhang et al., 2020). Looking at correlations between chalkophore/siderophore and OD/Cts.ef/Cts.m, I find that relationships between the two are not consistent and often not proportionate or simultaneous. Results for chalkophore and siderophore are shown in Figures 3-

11 and 3-12, normalized to t0 in order to discuss scale changes in the context of growth. For instance, while OD and Cts.ef/Cts.m in M_{meso} increase after t0 by as much as a factor of 2 (Figure 3-4), chalkophores increase by factors of > 8 (Figure 3-12). For siderophores, the maximum increase is more proportionate to changes in growth indicators, albeit not always cotemporaneous (Figure 3-13). Comparison of Figures 3-11 and 3-12 with Figure 3-3 underscores the dynamical aspects of results, on which basis I am interested to expand the current exploratory application of CTA to future work.

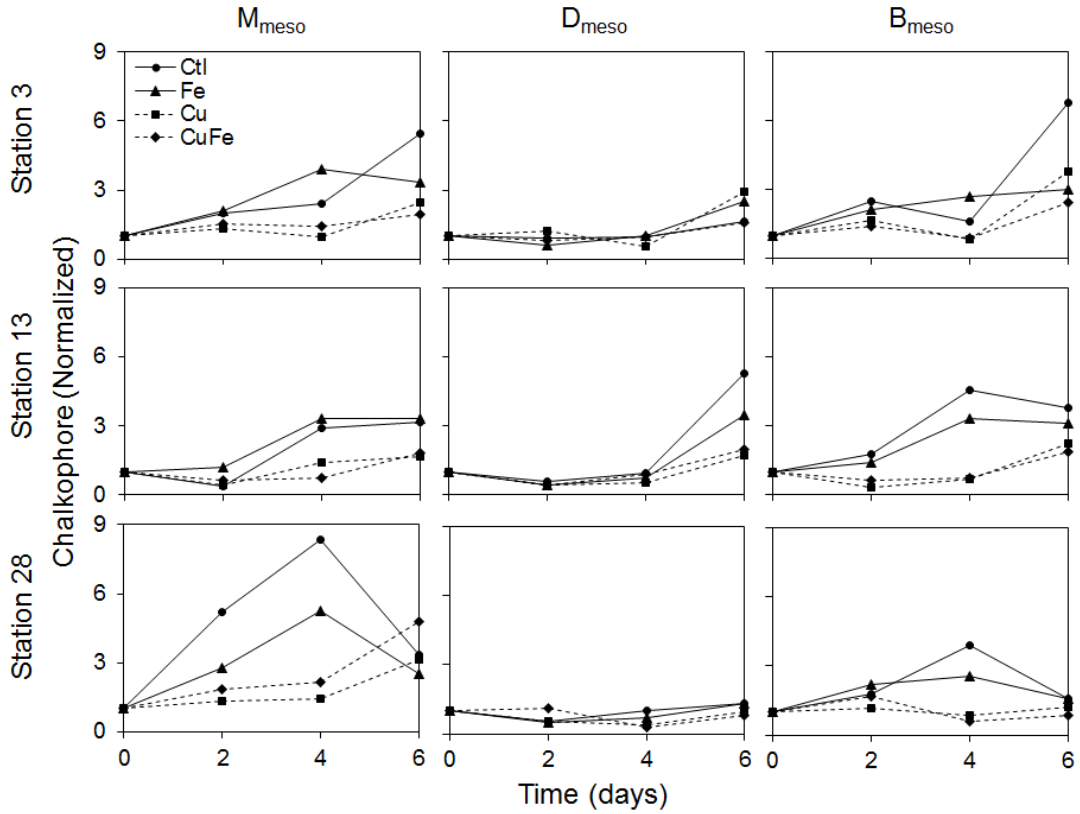

Figure 3-12. Chalkophore values in different mesocosms over time for mesocosm experiments in the year of 2018. All results are normalized to t0 values. Amendment without Cu are present in solid lines and amendment with Cu are present in dash lines.

Figure 3-14A–F illustrates the CTA concept (A–B) and summarizes selected chalkophore/siderophore results (C–G). Figure 3-14A shows time-sequence data for model variables *x* and *y*, similar to results I report (e.g. OD in Figure 3-4; Chl-a in Figure 3-5). Figure 3-14B shows what model *x*-*y* pairs look like as

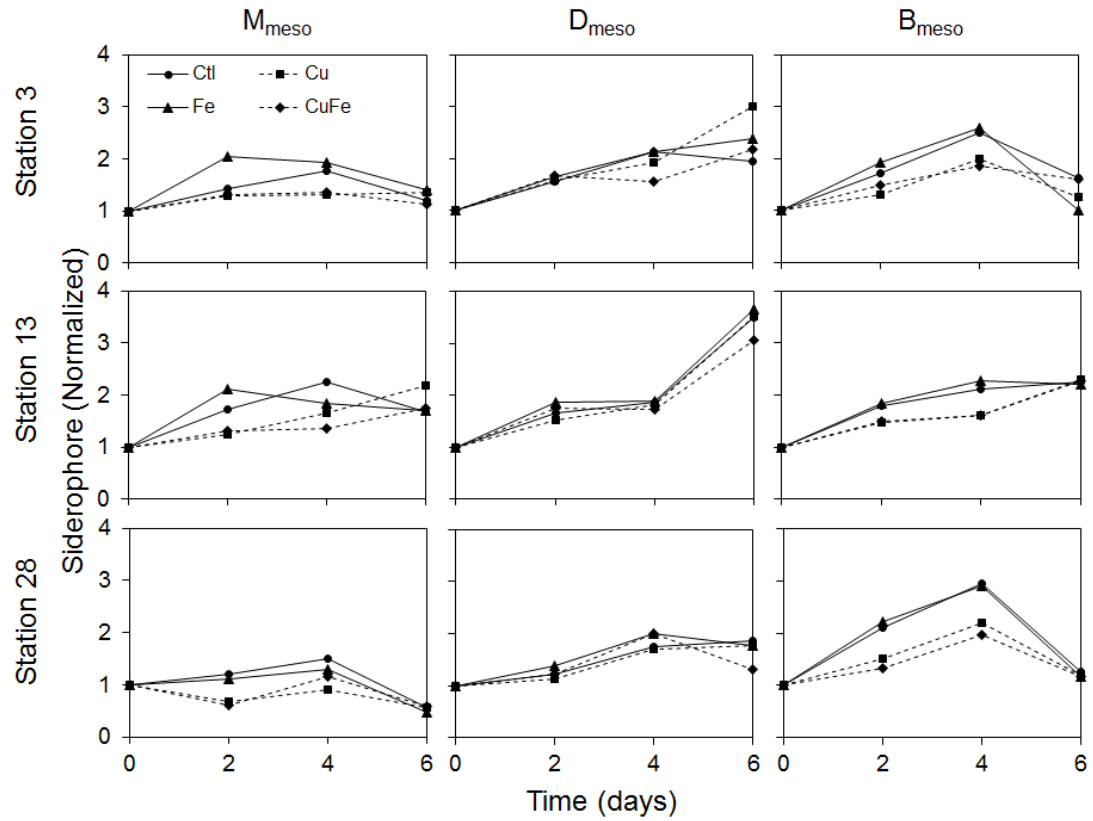

Figure 3-13. Siderophore values in different mesocosms over time for mesocosm experiments in the year of 2018. All results are normalized to t0 values. Amendment without Cu are present in solid lines and amendment with Cu are present in dash lines.

"trajectories in community space". Prominently, without an *x*-*y* phase difference, a trajectory becomes a line, hence subject to correlation analysis (or PCA calculated from a correlation matrix). Phase differences, however, are commonly present between variables in community/ecological data (Bischof and Zedrosser, 2009), and may efface correlation. Though CTA is multivariate, for this first work, I use 2-D community space for data shown in Figure 13-3C–G to simplify understanding of results and eliminate noise from potentially unrelated parameters. Also, I use raw results, not normalized to any growth metric, for reasons discussed above and because the circumstance of potential distortions from such normalization have the potential to be exacerbated in CTA.

Figure 3-14C shows representative chalkophore/siderophore trajectories.

Those trajectories in Figure 3-14C with substantial "shape" (angularity), are counter-clockwise. Angularity results from increase in siderophore relative to chalkophore initially, followed by increasing chalkophores, and in some cases by subsequent decreasing chalkophore/siderophore. The diagonal line shows a chalkophore/siderophore ratio that D_{meso} trajectories never exceed, whereas M_{meso} commonly do by more than threefold. chalkophore/siderophore ratios for B_{meso} vary. I was not able to find any literature that would suggest whether or not this ratio might represent a stoichiometric cellular process. The t0–t2 increase in M_{meso} and B_{meso} siderophore for Ctl/Fe is higher than for other mesocosms by an average factor of ~ 3 (e.g., Figure 3-14C M_{meso} Ctl versus Fe), less pronounced for St 28 M_{meso} (for which, by t2, Fe siderophore is higher than Ctl by 50%, on average). Chalkophore increases following siderophore are more variable in magnitude. For some trajectories chalkophore/siderophore changes are sequential and for some simultaneous, possibly relating to sampling period discussed above.

The trajectories in Figure 3-14C have three segments (S1–S3). The simplest trajectory measurements include total segment length (Figure 3-14D) and angles between segments (two angles, S1/S2 and S2/S3, Figure 3-14E). The former represents the cumulative chalkophore/siderophore bivariate change, a type of velocity, while the latter indicates proportionate change between variables, i.e. angularity is absent when variables change at the same rate. The M_{meso} and B_{meso} Ctl trajectories average more than a factor of two longer than the longest trajectories in green-algae dominated D_{meso} or M_{meso} Cu/CuFe groups. After Ctl, longest trajectories are for M_{meso} Fe, followed by B_{meso} Fe for two of

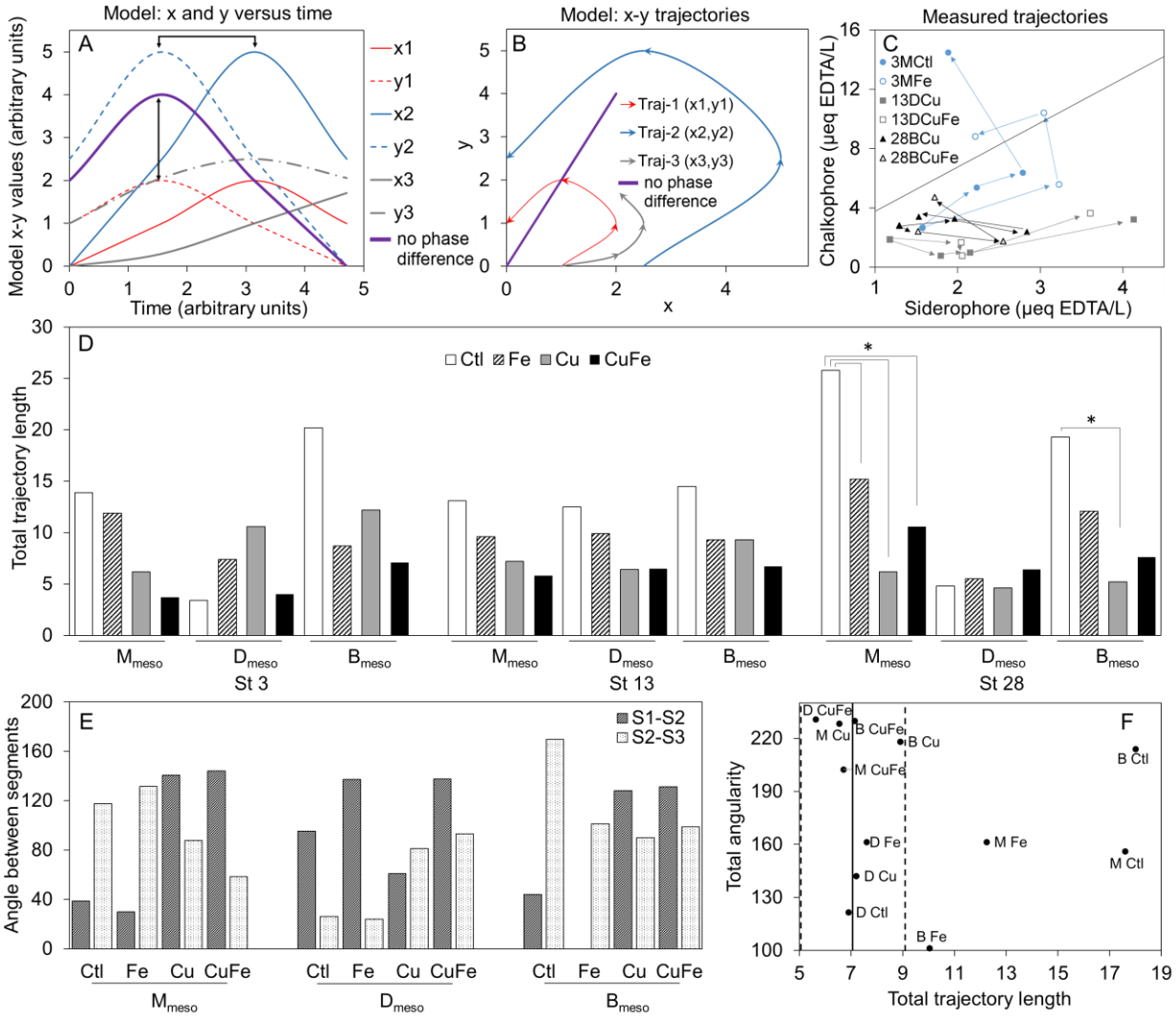

Figure 3-14. Conceptual representation of CTA and summarized results from chalkophore/siderophore analysis. (A) Representation of model time-series data for data pairsin and out of phase. (B) Community-space trajectories of model data in (A). (C) Representative chalkophore/ siderophore bivariate community trajectories that mesocosms in this study follow. (D) Total trajectory lengths. (E) Changes in angles between trajectory segments (two angles, see explanation in text). (F) Total angularity (sum of all angles) plotted versus total trajectory length; the solid and dashed lines are used as in control plots, with the solid line representing the average total length of non-Ctl/Fe M_{meso}/B_{meso} mesocosms, and the dashed line showing two standard deviations.

three stations. M_{meso} and B_{meso} Ctl/Fe also differ from other groups in angularity, for which S2/S3 averages ~360% more than S1/S2, i.e. palpable disproportionate change in the latter growth stages. CTA trajectory length is plotted versus angularity to better understand simultaneous trends in both (Figure 3-14F, angularity plotted as total/sum of all angles). Except for the *Microcystis*-dominated M_{meso} and B_{meso} Ctl/Fe, trajectory lengths are similar, with an average trajectory length of 7 and associated RSD of 13%. In contrast with angularity, there is no obvious pattern in angularity, other than CuFe is high.

While t0–t2 siderophore Fe > Ctl for M_{meso} and B_{meso}, overall, Ctl trajectories are greater. Since this work is the first to screen for chalkophore and siderophore, there is no comparable literature context for results. That t0–t2 siderophore production is higher for Fe versus Ctl may appear counterintuitive, however, Fujii et al. (2016) found that *Microcystis aeruginosa* Fe-uptake rates decreased with increasing Fe-limitation due to lower Fe requirements resulting from adaption to low Fe. This would explain why *Microcystis* in my mesocosms produce more siderophore for Fe. There is another interesting implication—despite conversion of amended TDFe to TFe by t2, Fe bioaccessibility may yet be sensed. With aging (von der Heyden and Roychoudhury, 2015; Jiménez et al., 2019), amorphous oxyhydroxides crystallize, becoming less labile; organisms sensing this, i.e. via reduced flux, could adjust siderophore production accordingly.

Concerning chalkophores, Baptista et al. (2014) found that strong-Cu binding ligand field concentrations were higher during *Microcystis*-dominated HABs,

however, for their analytical method, Cu-binding siderophore are not differentiable from chalkophore. Much as t0–t2 siderophore is higher in *Microcystis*-dominated Fe mesocosms, chalkophore production in these may be differentially increased in Ctl (causing longer trajectories) due to Fe-limitation. It is well-known that, with Fe-limitation, Cu-based plastocyanin becomes important in photosynthetic electron transfer (Quigg et al., 2008), causing Cu requirements to increase up to ten-fold (Schoffman et al., 2016). Unlike McKnight and Morel (1980) and Nicolaisen et al.'s (2010) results for *Anabaena* (discussed in Section 3.1), I find no evidence of chalkophore/siderophore mechanisms to protect from Cu-toxicity in *Microcystis*-dominated mesocosms. Comparing results from M_{meso} to D_{meso}, perhaps even *Microcystis* susceptibility to Cu results from enhanced siderophore and, particularly, chalkophore production, increasing acquisition/uptake of Cu (Hadjoudja et al., 2010).

The meaning of chalkophore and siderophore is explicit—molecules that have, respectively, high association constants for Cu and Fe (Zhang et al., 2020b). The causative basis for *Microcystis* to produce microcystin is as yet unclear (Omidi et al., 2018). Ceballos-Laita et al. (2017) reported microcystin-Fe binding, speculating on microcystin's being a siderophore that conveys competitive advantage to *Microcystis*. I monitored terminal microcystin concentrations to explore this. I find that microcystin produced is higher for Ctl versus Fe for St 3 and St 13 (Figure 3-15A), consistent with Lukač and Aegerter (1993) and Alexova et al. (2011), who found stress-triggered microcystin production induced by Fe-limitation. As with other results here, St 28, which is not subject to HABs, is different. Since other factors in experiments are matched/equal, differences in St 28 may be summarized as "its something in the water"—or not,

as the case may be? One apparent difference for St 28 that relates to Cu- or Fe-binding ligands is TDFe. St 28 t0 TDFe is approximately half that of St 3/St 13. For t2–t6, St 28 TDFe averages 42% that of St 3 and St 13. If microcystin production is suppressed when bioaccessible Fe is sensed, and such is lacking in St 28, microcystin for St 28 Ctl and Fe should be similar.

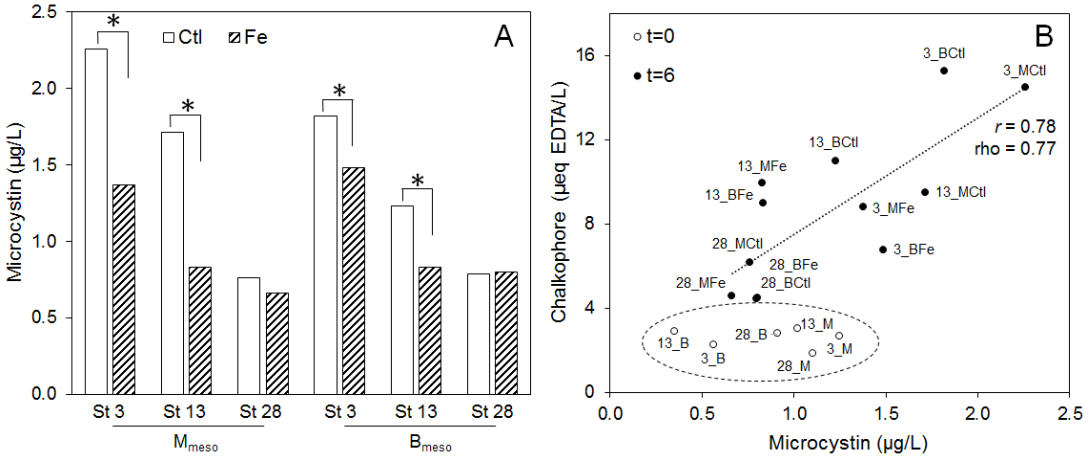

Figure 3-15. Microcystin results for mescosm experiments in the year of 2018. (A) Results from microcystin analysis for those mesocosms having enough *Microcystis* to produce detectable levels of microcystin. (B) Chalkophore versus microcystin relationships at t0 and t6 (t6 Pearson' r = 0.78, p < 0.005, Spearman's ρ = 0.77, p < 0.005).

I find no relationship between microcystin and siderophore production. I do see a possible relationship with chalkophore. Figure 3-15B plots chalkophore versus microcystin. At t0 (dashed ellipse), chalkophore is effectively constant (RSD ~ 18%), and microcystin varies. Specifically, M_{meso} values are all similar and highest, whereas for B_{meso}, in which *Microcystis* Cts.m are approximately half, values are lower and more variable (expected as, for instance, one value is below the LOQ). To within statistical uncertainty, t0 B_{meso} microcystin is half that of M_{meso}. By t6, for the linear chalkophore-microcystin relationship in Figure 3-15, Pearson's r = 0.78 (p < 0.005), with Spearman's ρ being 0.77 (p < 0.005), in close agreement.

As my data for microcystin are a snapshot and not analyzed in phase-space, for comparison I show microcystin results normalized to OD for three stations in Figure 3-16, comparing the difference between Ctl and Fe amendment.

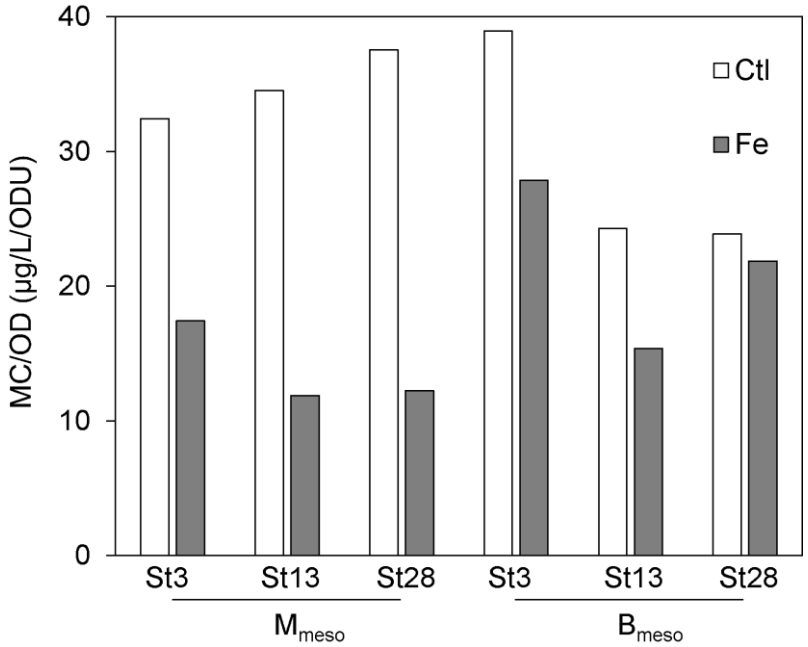

Figure 3-16. Microcystin normalized to OD (750 nm) for three stations from results results of mescosm experiments in the year of 2018.

The overall behavior is the same as seen in Figure 3-15A, wherein production of microcystin is less in Fe than in Ctl, and the differences between Ctl and Fe microcystin production are greater for M_{meso} than B_{meso}. On an OD normalized basis, differences between Ctl and Fe are on average larger. I note again that these normalized results should be viewed with caution, in view of data distortion and uncertainty discussed above herein, and since the rate of change of microcystin production and half-life of microcystin in mesocosms is likely to be much different than the rate of change of OD and half-live of algal individuals in water.

My working hypothesis to explain biomolecule results involves *Microcystis* production of siderophores first, to capture Fe, then shifting to production of

chalkophore as available/accessible Fe depletes. Simultaneously, in Ctl microcystin increases, possibly as a stress reaction or to inhibit other algae/microorganisms that might compete for NP/MN; inhibition is consistent with what I observe for UG and Dia in Figure 3-12C–D. This hypothesis explains why Ctl/Fe trajectories lead with siderophore followed by chalkophore and are longest overall for Ctl (both Cu and Fe low), the greater siderophore initial production for Fe (bioaccessible, less so for St 28 Fe), why microcystin is less for Fe, and why chalkophore-microcystin correlate by t6. St 28 values (Figure 3-15B) are lowest in part because by t6 population crash has begun. My hypothesis concerning Fe-bioavailability in Taihu is consistent with Fan et al. (2018) and a prior finding from work that I did with my colleague Dr. Zhang that organic matter metal-binding affinity/retention of metal solubility is lowest, of 32 monitoring stations across Taihu, at St 28 (Zhang et al., 2020c).

An objective in biomolecule analysis was to see if high Cu causes production of Cu-bioavailability reducing ligands or a Fe-linked effect. I do not see that. Instead, the Cu concentration was toxic to *Microcystis*, and I am not able to see if Cu causes different chalkophore/siderophore/microcystin production than Fe. I do see interesting effects for Fe with the interplay between chalkophore/siderophore production and amendment, and the potential link between microcystin-chalkophore production is very interesting. Emerging literature concerning the importance of Fe and Cu as limiting MNs and the interplay between Cu-Fe (literature cited, references therein) underscores the importance of this topic, however, this is the first work reporting chalkophore/siderophore screening separately as classes. The additional potential interrelationships with microcystin production will be interesting to

pursue in future work. Because these classes of molecule are documented to have short half-lives in environmental conditions[3], the advent of CTA provides a timely and useful new tool for study of both the interplay between time-varying production of these molecules and the ability to treat this interplay in terms of multivariate velocities.

3.10 PCA Analysis of Full Data Set

I chose PCA for multivariate analysis as an approach free from investigator bias and well-known for allowing discrimination of data patterns and indications of which individual parameters most influence same (e.g., see Zhang et al., 2020b). PCA was performed on temporally complete data (t0–t6) as some analytes were measured at t0 and t6 only due to sample volume or other limitations as discussed in Section 3.2. Figure 3-17A shows a PCA scree plot of the percent total variance explained by each PC, and Figures 3-16B–D show the contribution of each variable to PC1–PC3, respectively, calculated to quantify the most important contributing variables to each. In Figure 3-17A, a total of ~ 68 percent of variance in the data is explained by PC1-PC3 (PC1–33.3%, PC2–21.3% and PC3–13.1%), whereas PC4 and larger account for only small amounts of total variance (≤ 6%) with diminishing returns on the amount of variance captured. Thus, PC1–PC3 were chosen for further analysis. PC1 describes how Cu affects indicators of growth, in particular for BG (negative Cu loading associated with positive Cts.ef, Cts.m, OD, and BG (BG being smaller diameter algae). Since BG are smaller diameter algae (individuals) negative d.avg and ESV

[3] Cederocol, a sideophore for gram-negative bacteria and the terminal elimination half-life of cederocol was 1.98 to 2.74 hours (Takayuki et al., 2017) and cefiderocol, a siderophore with reported mean half-life of 0.84 hours (Ghazi et al., 2017). A half-life for microcystin-LR was reproted to be 2.2 days in the water sample taken during HABs (Medvedeva and Kuzikva, 2021)."

loading are likewise observed for this PC. Negative Cu is associated with positive chalkophore in PC1, in accord with the greater length of CTA trajectories (Section 3.9) for mesocosms dominated by BG.

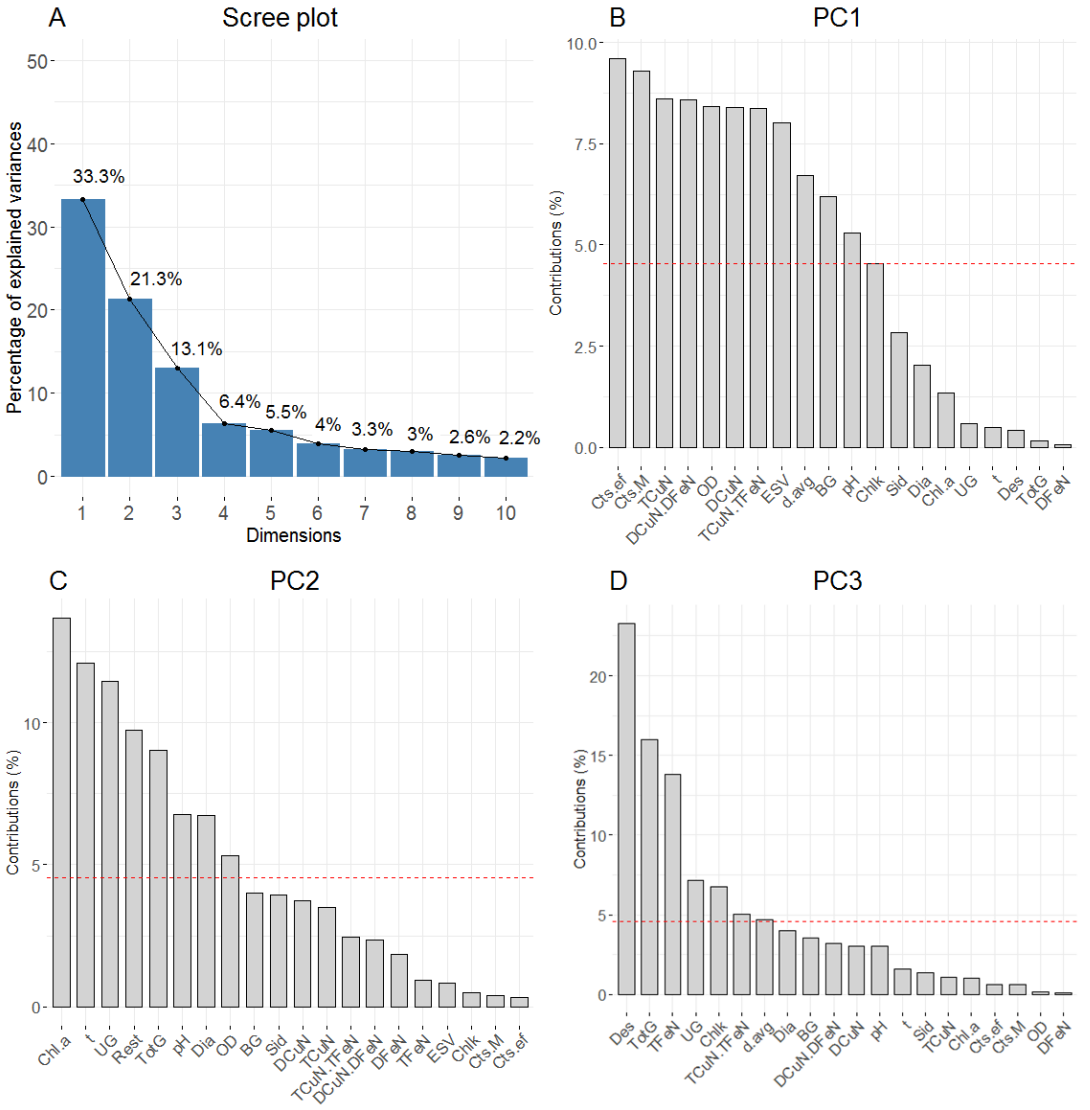

Figure 3-17. Scree plot and variables contributing to PCs from PCA. (A) Scree plot showing total percent explained variance that each PC accounts for in the input data; dimensions 1–10 represent PC1–PC10, respectively. (B–D) Bar plots showing the percent total contribution that each variable makes to PC1 (B), PC2 (C), and PC3 (D). The dashed red reference line corresponds to the expected value if the contribution where uniform; a contribution above the reference line is often considered as important in contributing to the dimensions.

For PC2, there is a concomitant loading of Chl-a, *t*, and Alg_{is}, i.e. representing an

increase of Alg_{is} over time. The TotG loading in PC2 being in part a function of UG Alg_{is} increase and growth-associated increases in pH. PC3 contributions are positive for TFe and dominant green algae (Des and UG, both in turn major contributors to TotG). Des and some UG are larger on average than BG, hence d.avg loading is positive, accompanied by negative loading in chalkophore and TCu/TFe.

Further PCA results in Figure 3-18 include (A) a three-dimensional (3-D) plot of PC1–PC3, (B) a recap listing signed parameters with highest contributions to each PC, and (C–E) 2-D plots of PC1 versus PC2 for St 3–St 28. Figure 3-18A shows that data separate into three clusters: Cluster 1–D_{meso}; Cluster 2–M_{meso} and B_{meso} Ctl/Fe; and Cluster 3–M_{meso} and B_{meso} Cu/CuFe. The "narrative" describing PCs that I construct from Figure 3-18B is as follows: PC1–how Cu affects indicators of growth, particularly for BG; PC2–Alg_{is} increases over time; and PC3–positive TFe-green algae association accompanied by negative chalkophore loading. Figure 3-18A shows clear separation of Cluster 2 (+PC1) and Cluster 3 (-PC1). Cluster 2 PC1 values correspond to M_{meso} and B_{meso} without Cu, whereas Cluster 3 corresponds to M_{meso} and B_{meso} with Cu. As PC1 describes how Cu affects growth (particularly for BG), Cluster 3 has low PC1 values, while Cluster 2 (no Cu) signifies no Cu toxicity, or positive PC1. Also in Figure 3-18A, PC3 = 0 demarcates D_{meso} and M_{meso}, with B_{meso} in between, which is sensible since Des, TotG and TFeN are the biggest contributors to PC3, D_{meso} contains more Des compared to B_{meso}, Des was not added to M_{meso}, and t0 Des contained higher TFe. Though Des has the highest TFe, in PC3 UG and TFe load together, i.e., t0 Des TFe is not the only aspect of Fe concentration providing discrimination. Chalkophore variation by amendment suggests that PC3

chalkophore loads negatively to TFe in consequence of higher chalkophore in BG-dominated mesocosms and as a result of Fe-status in mediating chalkophore production in Ctl (Section 3.9). Separation between Cu and non-Cu amendments in PC2 versus PC1 plots is more complex, per the solid-black diagonal line in Figure 3-18C–E. Temporal shifts parallel to this line relate to growth, since PC1 and PC2 are loaded by growth indicators.

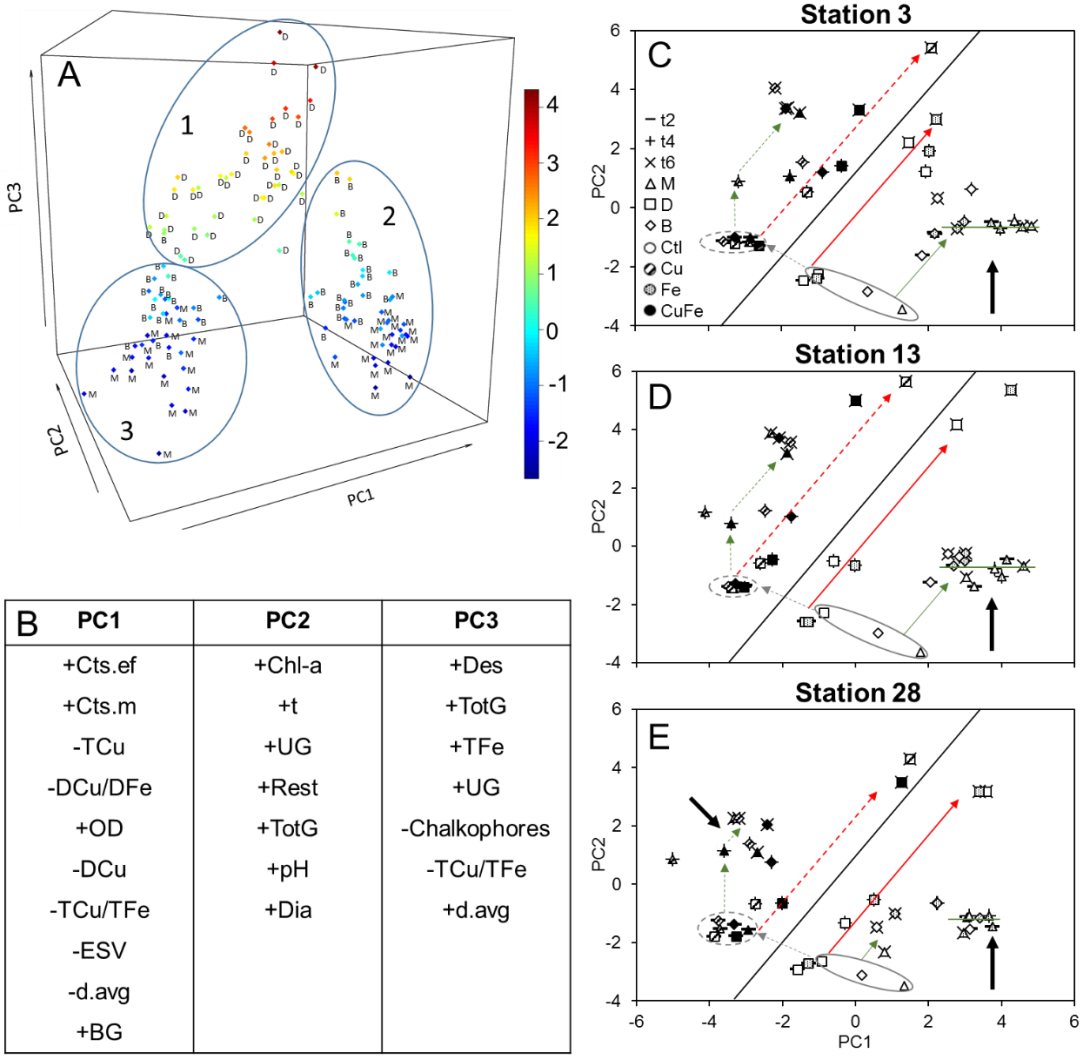

B PC1	PC2	PC3
+Cts.ef	+Chl-a	+Des
+Cts.m	+t	+TotG
-TCu	+UG	+TFe
-DCu/DFe	+Rest	+UG
+OD	+TotG	-Chalkophores
-DCu	+pH	-TCu/TFe
-TCu/TFe	+Dia	+d.avg
-ESV		
-d.avg		
+BG		

Figure 3-18. Analysis of results from PCA. (A) Three-dimensional (3-D) plot of PC1–PC3; ellipses show three separate groupings according to mesocosm algae and amendment. (B) Parameters that have important contributions to each PC (i.e. that are larger than what would be expected if each parameter contributed equally to variance). (C), (D) and (E) show PC1 vs PC2, respectively, for St 3, St 13 and St 28. Ellipses in (A) and markups in (C) through (E) are discussed in the text.

PC1 and PC2 are loaded by BG and Alg_{is}, respectively, which explains the variable rate of change in PC1 versus PC2. In Figure 3-18C–E, t0 is centered at PC1~ 0 and PC2 ~ -3 (solid-grey ellipses), wherein M_{meso} have greater PC1 (more BG) than D_{meso}, D_{meso} has greater PC2 (more green algae/Chl-a), and B_{meso} is in the middle. By t2, PC2 for all mesocosms increases or remains approximately the same. For PC1, in contrast, all Cu decrease substantively (dashed-grey ellipses), while M_{meso} and B_{meso} Ctl/Fe increase similarly in PC1. Thus PC1 separates Cu and non-Cu mesocosms across the black line for the remainder of the experiments. D_{meso} follows the diagonal black line (red solid and dashed arrows) over t2–t6, per comments above regarding PC1/PC2 and growth. For M_{meso} and B_{meso} Cu/CuFe, after the t0–t2 decrease in PC1, subsequent changes are in PC2 only (vertical dashed-green line). After the Cu toxic effect to BG, as the transition to different algal assemblage progresses, growth resumes along PC1/PC2 (diagonal dashed-green line). M_{meso} and B_{meso} Ctl/Fe change in PC1 and PC2/growth over t0–t2 (diagonal solid-green line), after which there is no further change. These mesocosms remain dominated by BG till t6, thus t2–t6 these mesocosms are dominated by BG-loaded PC1 changes (horizontal solid-green line). The graphical change of those mesocosms t2–t6 agrees with OD, Cts.m, Cts.ef, and pH results; as BG growth progressed into stationary phase, PC1 first shifted to higher values, and then later back to lower values by t6.

With PCA, I wanted to know whether variations across the whole data set would discriminate according to initial water used in the otherwise t0-matched mesocosms. In Figure 3-18C–E, notable differences (thick black arrows) involve growth in St 28 versus St 3/St 13 M_{meso} and B_{meso}. Changes in St 28 for M_{meso} and

B_{meso} t2–t6 are all diminished in comparison to St 3 and St 13. This finding is most interesting because it applies to Ctl/Fe *and* Cu/CuFe mesocosms, which have very different algal assemblages. It is as if to say, growth will be diminished for any St 28 mesocosm touched by *Microcystis*, per Figure 3-3 wherein the maximum OD and final OD, compared to t0 for St 28 mesocosms, averages 55% that of St 3/St 13. This echos again the concept of "something in the water"—or not. So what could "something" be? The high (equalizing) t0 NP amended effectively rules out macronutrient-based causation. Other water quality indicators, which have been measured and reported in Table 3-2, are not likely. My discussion herein suggests that microcystin is not the direct cause, however, chalkophore/siderophore trajectories are very different for St 28 and t0 TDFe is half that of St 3/St 13, remaining lower t2–t6 relative to amendment. Why would the TDFe differ by a factor of two in this polymictic, ergo relatively short water-retention time, lake? The most likely explanation that I have seen relates to Fan et al.'s work (2018) demonstrating how different bacterial consortia affect Fe biogeochemistry. Prior work shows MN/Fe-limitation in eastern Taihu (including St 28, Fan et al., 2018; Zhang et al., 2019 and references therein).

Chalkophore/siderophore trajectories clearly concern the reaction of algae/associated bacteria to the mesocosm environments, particularly to the status of Cu-Fe MNs. The evidence that I present here clearly shows 1) the difficulty of keeping Fe bioavailable in more realistic experiments compared to lab studies, 2) the lower TDFe in St 28 water, as collected *and as amended* over time, 3) the increased production of siderophore/chalkophore in *Microcystis*-dominated mesocosms, i.e. strong Cu-Fe chelating ligands that microorganisms

may produce to modulate the bioavailability of Cu-Fe. While the work herein cannot be considered as fully conclusive, it strongly supports a model wherein Fe/Cu-Fe MNs biogeochemistry is a fundamental control on HAB formation in eastern Taihu.

4 Chalkophore is a Predictor of Microcystin Toxin Production by Harmful Cyanobacteria

4.1 Rationale and Experimental Design for Additional Mesocosm Investigations—Focus on Biomolecules

Chapter 3 addressed an important gap in furthering research on the effects of MN bioavailability in natural waters, with particular reference to Cu, Fe and links between the two. Understanding possible links is important in turn to understand how MNs might or might not play a role in environmental management. One innovation in Chapter 3 is that I performed field mesocosm studies to examine the specific production of chalkophores and siderophores, as separate and distinct classes of ligand, in response to Cu and Fe amendment. In particular, my work is the first that I know of to study chalkophores in natural oxygenated freshwater environments using a screening assay that has only recently been reported. This assay, unlike others that have been used, is able to operationally distinguish strong Cu-binding ligands, chalkophores, from siderophores that in some instances might also be able to engage in strong Cu-binding. Two aspects of my work from Chapter 3 that I found most interesting

were 1) that I was able to observe patterns in chalkophores and siderophores indicative of modulated production of these biomolecules in response to MN amendment, and 2) that I observed an unreported link between production of chalkophore and the cyanobacterial toxin microcystin. While I felt that my work in Chapter 3 made an important contribution to filling knowledge gaps that I had identified, it also raised more interesting questions that need further work. There were two important areas of further enquiry that interested me.

One thing that I wanted to investigate further subsequent to Chapter 3 work involves the level of Cu amended. I had wanted to investigate whether high Cu causes production of Cu-bioavailability changing ligands or a Fe-linked effect, and the level that I used previously, 50 $\mu g \cdot L^{-1}$, was chosen based on prior work as a level targeted to be at the lower part of a dose response curve. In hindsight, I decided that the Cu concentration that I amended was too high for what I wanted, and so I was not able to see if Cu causes different chalkophore/siderophore/ microcystin production than Fe. For the work reported here therefore, I decided upon an alternate approach to Cu amendment.

A second area that I wanted to investigate deals with microcystin production. Because it has been proposed that microcystin perhaps serves as a siderophore, especially during extended iron starvation, or acts as an iron storage component (Martin-Luna et al. 2006, Alexova et al. 2011), I was surprised to find in my initial work that there was no apparent microcystin-siderophore correlation, and even more surprised at my discovery of a hitherto unreported discovery microcystin-chalkophore link. The type of experiment that I have been doing is

highly field-relevant, however, with aspects of control. Nonetheless, despite controlled aspects, the water that I use, the algae that I use (particularly *Microcystis*) and the environmental conditions in the field, hence mesocosms, vary year-on-year. Because of this variability, which considerably complicates making generalizations about results, I was greatly interested in designing experiments that would supplement my knowledge from those described in Chapter 3, while at the same time affording an opportunity to see if I would again observe a microcystin-chalkophore link, and how this might or might not relate to Fe-limitation.

With the aims above in mind, for my follow-up work, I designed the MN dosing scheme to include four amendments 1) Control (Ctl), i.e., no MNs added, 2) "Low" Cu (CuLo), 2) low Cu with "high" Fe (CuLoFeHi) and 4) high Cu with high Fe (CuHiFeHi). The Ctl is clearly required for comparative purposes. My rationale for CuLo was that Cu is a MN, and might promote growth, as has been seen previously. Additionally, however, Cu, when at low enough concentrations to be nontoxic, may be involved in the same mechanisms of uptake as Fe to promote algal growth. Therefore, CuLo also serves as a kind of potential control or contrast to CuLoFeHi. It is well known that high Cu will produce toxic effects, however, it has also been hypothesized that Fe might compete with Cu for BL and reduce toxicity from Cu (Kochoni and Fortin, 2019), ergo my choice of the CuHiFeHi amendment. In using CuHiFeHi, I was also interested to see, would the high Fe compete with Cu for BL and reduce toxicity from Cu? For all MN amendments, would there be notable differences in biomolecule formation suggestive of similar and/or different reactions to Cu and Fe? Further details concerning the specific rationale that I followed to decide which concentrations

constituted “high” and “low” for Cu and Fe are given in Section 4-2 below.

For the rationale of which algae to use, *Microcystis* and *Desmodesmus* were selected for the reasons described in Chapter 3, Section 3.2. My primary focus is *Microcystis* as it is the main HAB species and with more interesting biomolecule results found for *Microcystis* in Chapter 3. As *Desmodesmus* populations had crashed in the early phase of experiments reported in Chapter 3, I selected *Chlorella* as another contrasting, non-nuisance green alga, and there is recent interest concerning Cu toxicity to *Chlorella* (Chen et al., 2016; Wan et al., 2018). Ultimately, to include trials on non-nuisance green algae, instead of using one genus as I had previously, I mixed *Desmodesmus* and *Chlorella.* My reasoning was as follows: 1.) There was a possibility that the algal acclimation would again not be sufficient, so mixing *Desmodesmus* and *Chlorella* added insurance for the green algae to survive in the field experiment. 2.) Since the focus is *Microcystis*, whether the contrasting green alga is mono- or mixed-culture is not as important. As previously, I also added mesocosm trials with a 1:1 mixture of *Microcystis* and the non-nuisance green algae. The basis for doing this was, as before, to see if behaviour would be additive or not (one organism potentially affecting others) and as this adds an element to the controlled experiment that more closely reflects the field situation where diversity occurs, at least prior to full HAB development.

The experiments described in previous work of mine and work in which I participated (Zhang et al., 2019, and Li et al., 2021/Chapter 3) involved mesocosms using water from three stations. Our group found that water chemistry from these three sites is different, and therefore the significant

differences found in MN mesocosm experiments for these stations were consistent with this. Considering that the strongest effects for Cu reported in my previous work was for mesocosms using water from Xukou Bay (St 28) (Li et al., 2021/Chapter 3, also see Zhang et al., 2019), and that the experiments are very laborious (Li et al., 2021), I decided to focus my follow-up work on this special station. In focusing work on St 28, I was able to spend more time in crucial preparations, including algal acclimation, which I believe had been at issue in the original work, and my strategy was to try to maximize the chances of obtaining high quality data by performing more focused work on only one station.

In this chapter, I report my follow-up work to that of Chapter 3, based on the rationale and experimental design described above. To implement the experimental design, I chose Taihu as my field area for reasons discussed in detail in Chapter 3, Section 3.2. Additionally, since the CTA approach to analysis that I introduced in Chapter 3 is ideally suited to the results observed, I explored this approach further here, applying more advanced algorithms within the family of techniques used in trajectory analysis. Summarizing major findings, 1) while the exact form of trajectories observed for this work differ from those that I reported in Chapter 3, more so for *Microcystis*, I again see a very similar dynamical phased behavior between chalkophore/siderophore production that show significant trajectories differences under different Cu and Fe amendments. 2) I again observe a microcystin-chalkophore relationship, for this work being much stronger than that reported in Chapter 3, and I find again that microcystin production is lower with Fe.

4.2 Modifications to Experimental Methods for Algal Mesocosm Experiments

The method of collecting and characterizing St 28 water is described in Chapter 3, Section 3.2. *Microcystis* (> 99% *Microcystis* spp. from microscopic examination) were collected from Meiliang Bay during an HAB in August, 2019. In August, 2018, I had collected *Microcystis* from a point off the dock at TLLER, because I found that the algae there were effectively mono-algal *Microcystis* spp.

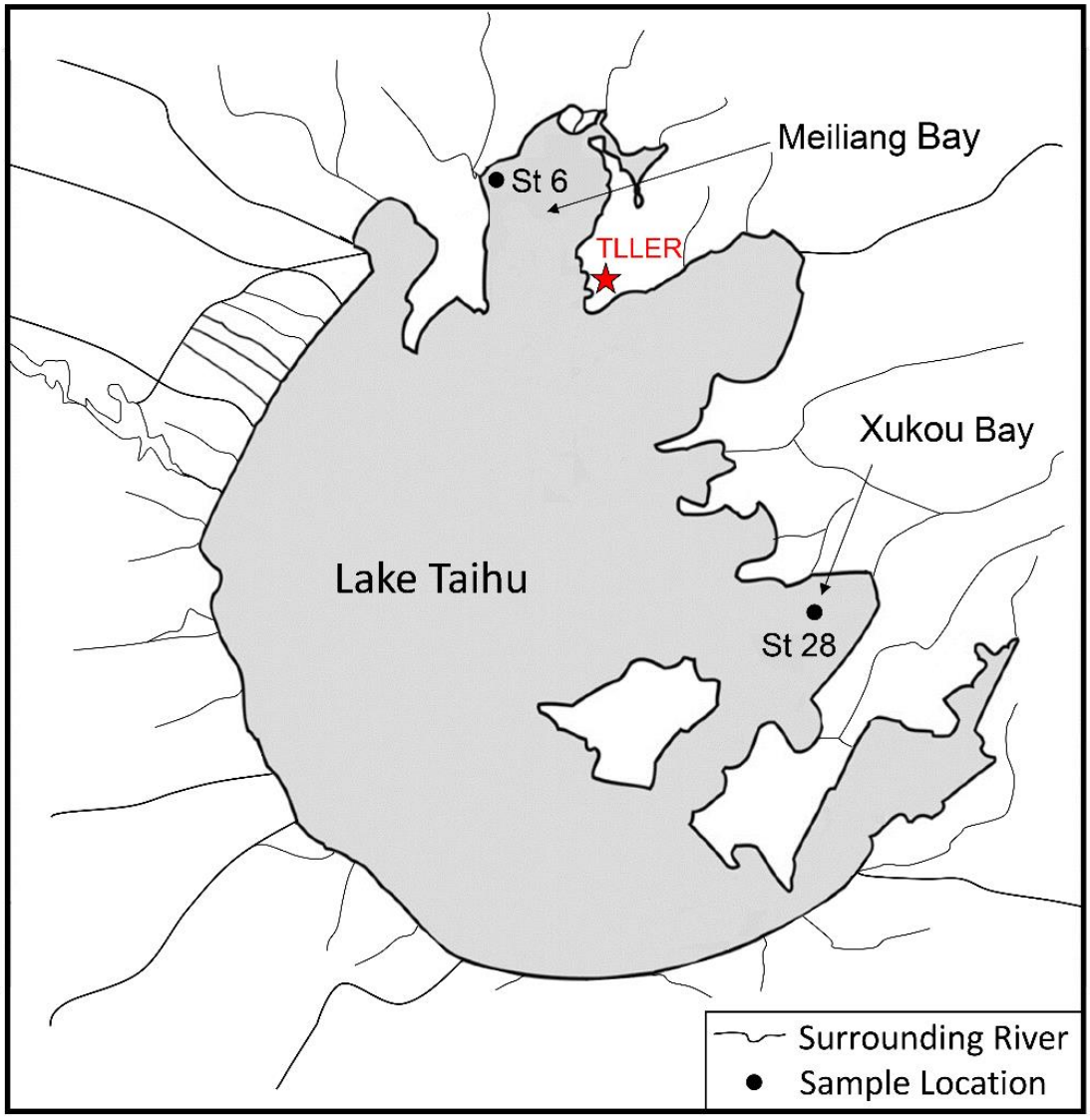

Figure 4-1. Map showing Taihu field sites for mesocosm experiments in the year of 2019. The locations of St 6 (*Microcystis* collection site), St 28 (water collection site), and TLLER, the site of mesocosm experiments.

In August, 2019, as compared to 2018, the situation was different, and while at many sites experiencing an HAB I found > 95% *Microcystis* spp., there were small amounts of other genera of algae (*Chroococcus*, *Pseudoanabaena* and *Nitzschia*). I travelled around the whole of Taihu and found a breathtaking level of HAB development at St 6 in Meiliang Bay. On microscopic examination back at TLLER, this was > 99% *Microcystis* spp., so I changed the location for *Microcystis* collection to Taihu St 6 in 2019. Figure 4-1 shows the stations where I collected algae and water for the work described in this chapter, as well as the location of TLLER where I did some lab work and deployed the mesocosm experiments.

Figure 4-2. Pictures from field sampling work in the year of 2019. These images show what Taihu looked like at Meiliang Bay, St 6, during the HAB in August, 2019.

Figure 4-2 shows some photos that will provide an appreciation of the state of development of the HAB in August, 2019. The other algae that I used, *Desmodesmus* and *Chlorella*, were purchased from Aquatic Biology Services (Wuxi Zhongshun Biotechnology Co., Ltd; > 99% *Desmodesmus* and *Chlorella* from microscopic examination).

I took a much more intensive approach to algal acclimation in 2019, aiming to mimic as much as possible an environment similar with my field site, Taihu, where the sunlight is strong and water temperature is high (an average of 32 °C as reported in Chapter 3, Section 3.3). First, I obtained permission to deploy a series of 160 L buckets with water outside my lab (this violated security protocols, however, I was able to secure permission for the time that I needed). I used the large buckets to mimic the surface environment of Taihu, and the size was workable for me to control the temperature of water in the bucket. Since my lab is not far from Taihu, the sunlight at the top of the water surface in the bucket should have been similar sunlight for the algae as at Taihu. I divided my algae (filtered and in modified COMBO medium, per Chapter 3) into several 3-L transparent capped bottles; I added 1.5 L algal culture to each transparent bottle to make sure there would be enough air in the bottle. Then I placed the 3-L transparent bottles with algae at the water surface inside in the middle of the 160 L buckets. I devised a method to make sure that the 3-L transparent bottles were set and remained in the middle of the water bucket, where the environment was more stable. Daily maintenance of the algal cultures during acclimation included two important operations. The first consisted of opening the 3-L transparent bottles to allow air exchange, agitating the bottles to mix algae with the medium and promote air exchange, then closing and reopening

each bottle to repeat, multiple times with each bottle. The second operation was to ensure temperature control in the bucket. From preliminary experiments with the buckets, I realized that the temperature in the buckets could become too hot, due to their relatively low thermal mass. To control the temperature, I would first mix the water in the bucket, then take the temperature. If the bucket was approaching too high of a temperature (according to records of surface water temperature in Taihu), I would add ice, agitate the water till the ice melted, check the temperature, and then repeat this process as necessary until the temperature of the bucket was to within a degree or two below the target water temperature. I needed to perform the two operations to ensure air exchange and measure and control the temperature in the buckets several times each day, with multiple visits needed during the hottest part of the day. Algae were acclimatized in this way for two weeks before the field experiments.

Table 4-1 lists details concerning the four amendments used for mesocosm experiments in this work. Regarding Cu concentrations, as I summarized in Chapter 3, during my work on Cu-amended mesocosms in Taihu, I observed two very different outcomes between 20 and 50 $\mu g \cdot L^{-1}$ Cu. At 20 $\mu g \cdot L^{-1}$ Cu, this strongly stimulated growth and effected assemblage changes that sometimes favored *Microcystis* spp. (Zhang et al., 2019), whereas 50 $\mu g \cdot L^{-1}$ Cu, with or without Fe, favored an assemblage shift from *Microcystis* spp. to green algae. For CuLo, therefore, I chose 20 $\mu g \cdot L^{-1}$ wherein significant growth promotion was observed at this concentration (per Zhang et al., 2019, also see references therein). For CuHi I decided to increase this by a factor of two over my previous work (Li et al., 2020). Based on my work and that of others (Wu et al., 2017), I predicted that this increase would ensure Cu levels toxic to *Microcystis*. Setting

CuHi to this level is also relevant to observe how this affects mesocosm progression, because this level is reportedly in the starting range of toxicity to green alga, for instance the EC_{50} (growth inhibition) of Cu was found to be in the range of 50 to 500 $\mu g \cdot L^{-1}$ for the green algae *Desmodesmus*, *Scenedesmus* and *Chlorella* spp. in similar water compositions (Shehata and Badr, 1980; Zhang et al., 2001; Lombardi et al., 2007). For Fe, I chose the concentration of 200 $\mu g \cdot L^{-1}$, per my colleague Dr. Zhang's and my previous work (Zhang et al., 2019; Li et al., 2020). I call it FeHi in the sense that it is the concentration that we and others (Xu et al., 2013) have used to enhance growth and the concentration is high compared to CuHi. I used $FeCl_3 \cdot 6H_2O$ for the Fe amendment. It is widely held that this form is less bioavailable due to the formation of insoluble Fe-oxyhydroxides (Lis et al., 2015; von der Heyden and Roychoudhury, 2015; Jiménez et al., 2019), use of which serves to test whether the response of algae to Cu will have an influence on the bioavailability of Fe.

Table 4-1. Amendment schedule used in Taihu NLB for 2019 experiments.

	N [a]	P [b]	Cu [c]	Fe [d]
Control	2.0 $mg \cdot L^{-1}$ N	0.2 $mg \cdot L^{-1}$ P	No added Cu	No added Fe
CuLo	"	"	20 $\mu g \cdot L^{-1}$ Cu	No added Fe
CuLoFeHi	"	"	20 $\mu g \cdot L^{-1}$ Cu	200 $\mu g \cdot L^{-1}$ Fe
CuHiFeHi	"	"	100 $\mu g \cdot L^{-1}$ Cu	200 $\mu g \cdot L^{-1}$ Fe

[a] added as KNO_3; [b] added as $K_2HPO_3 \cdot 3H_2O$; [c] added as $CuSO_4 \cdot 5H_2O$; [d] added as $FeCl_3 \cdot 6H_2O$.

Additionally, however, my work in Chapter 3 suggests that the other form of Fe that I used there rapidly becomes un- or less bioavailable over the time periods and conditions of my mesocosm experiments. As listed in Table 4-1, all mesocosms had NP added to ensure that these are non-limiting and to focus on the effects of the different concentrations of Cu and Fe amended. Concentrations of N and P were the same as used previously (Zhang et al., 2019; Li et al., 2020,

and references therein).

The three different types of mesocosm trial that I performed for this work, with reference to initial algal assemblages, were mesocosms initially dosed with 1.) *Microcystis* spp. to reach an initial OD ~ 0.05 (M_{meso}), 2.) a 1:1 mixture of OD ~ 0.05 *Desmodesmus* and OD ~ 0.05 *Chlorella* spp. (Gmeso) and 3.) a 1:1 mixture, by volume, of the algae used to dose M_{meso} and G_{meso} (B_{meso}, i.e. dosed with "both" types of algae in mesocosm types 1 and 2 above). The NLBs were performed following the method described in Chapter 3, Section 3.2 with an initial OD of ~ 0.05. As before, for each NLB permutation (algae dosed, amendment type), triplicate subsamples were placed into 1-L transparent, chemically inert, cubitainers, which were then spiked to achieve the final concentrations of NP and MN (Table 4-1). The cubitainers were then incubated *in situ* in Taihu near the surface at TLLER. Subsamples for analysis were collected from initial water, initial algal suspensions (t0), and then each cubitainer was subsampled four times, at days 2, 4, 6 and 8 (t2, t4, t6 and t8). Experimental measurements on mesocosm subsamples were as described in detail in Chapter 3, Section 3.2.

4.3 Advances in Approach to Community Trajectory Analysis

Some methods of data analysis were also as described in Chapter 3 (e.g., descriptive statistics), however, for the CTA I took a different approach for this work. For the work in Chapter 3, I used the simplest approach possible to CTA, as this was the first time that I, or others, had applied this to data such as mine. The approach that I used in Chapter 3 had the advantage of being simple, however, the simplest methods are not always the most powerful ones. For the

work here, I wanted to evaluate two different tools. One involves the use of multivariate trajectory distances, and the other is time-lagged cross correlation of trajectories.

Calculating multivariate distances between trajectories is a technique in multivariate analysis to quantify the similarities/differences in trajectories (McCune and Grace, 2002). Among methods for calculating multivariate distance, Euclidian distance is a common, perhaps the simplest and common, form of multivariate distance used. It is well-known, for instance, to calculate the hypotenuse of two sides of a triangle in 2-D Cartesian space, however it is often not that powerful in multivariate space. This is likely for the kind of biological data that I have, for instance, since Euclidian distance is often not the shortest distance between two points in hyperspace and it has no inherent capacity to deal with phase-shifts. There are a large number of distance functions that I could have used for this work, however, after reviewing the literature on time-dependent trajectories, with an emphasis on those used in biological CTA applications, I decided to focus on using the Fréchet distance (FD, for example, Jiang et al., 2008; Cleasby et al., 2019) and a distance metric based on dynamic time warping (DTW, e.g., Bar-Joseph et al., 2003; Yuan et al., 2011; Cleasby et al., 2019). The FD is a measure of similarity between multivariate trajectories that takes into account the location and ordering of the points along the curves. The algorithm is usually described in terms of a person walking a dog on a leash, illustrated schematically in Figure 4-3. The person walks on one path (i.e., multivariate trajectory) while the dog walks on another (Alt and Godau, 1995). The dog and the person will likely vary their speeds, or even stop. While in real life, either has the option to go backwards, in the algorithm, the

mathematical equivalent of this is not tenable. In this analogy, the FD is the minimum leash length required for both the person and dog to complete their individual trajectories.

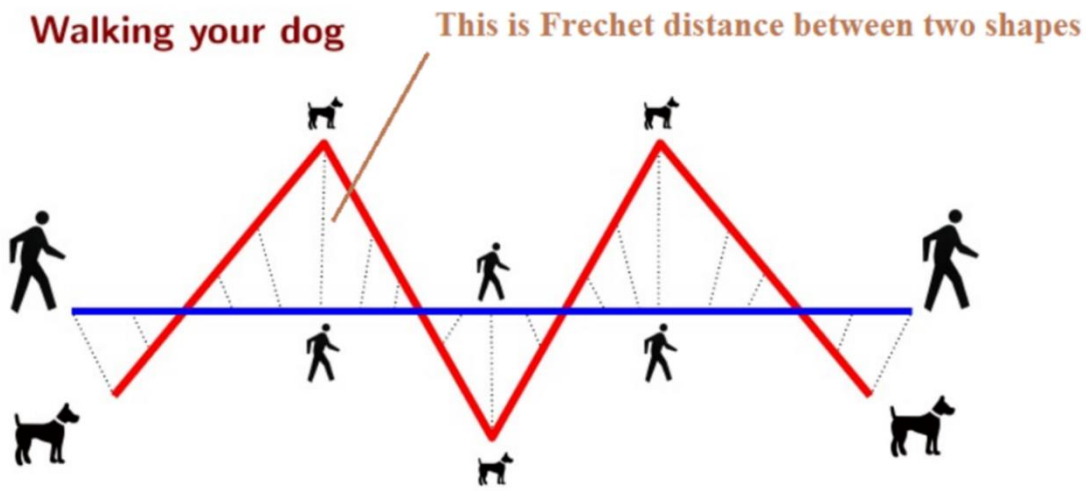

Figure 4-3. Schematic diagram illustrating Fréchet distance. The conceptual basis of uses the analogy of a person walking their dog (uncopyrighted graphic from Shah, 2021).

DTW is its own algorithm, however, for conceptual purposes it has been compared to an outcome that would occur when minimizing Euclidean distance between time series that have a phase difference, under all admissible temporal alignments (Tavenard, 2021). Figure 4-4 is a schematic representation of how DTW distance works according to this conceptualization, i.e., in comparison with Euclidian distance. While the schematic analogies used here oversimplify the actual algorithms, nonetheless, even schematically it is evident that Euclidean distance is the simplest, and, for my application, least powerful. I chose FD because it is able has been used in analysis of biological time-series data such as mine (Fernando and Miriam, 2021), which exhibit evolving characteristics. Because of the synchronization (per Kassidas et al., 1998) inherent in DTW and its past use in analysis of phase-differenced time-series

data, from the outset I thought that DTW seems ideal for my application. I used the SimilarityMeasures package (Kevin, 2015) in R to calculate FD and DTW.

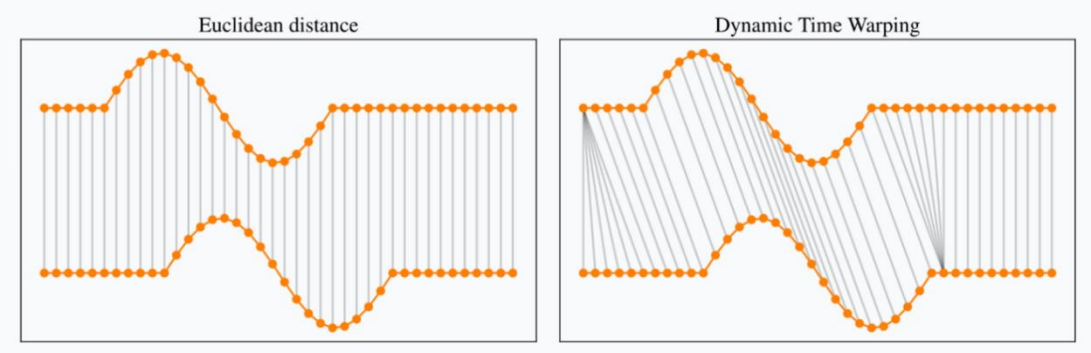

Figure 4-4. Schematic diagram comparing Euclidean and DTW distances. Conceptually, the DTW algorithm achieves temporal matching of features resulting in a smaller DTW distance/higher similarity result for a close feature match and vice versa (uncopyrighted graphic from Tavenard, 2021).

The other technique that I wanted to explore for this work is time-lagged cross correlation of trajectories (Kushkevych and Beno, 2013). Figure 4-5 shows a conceptual example of how this approach works. Panel 4-5A shows two well-known examples of time-dependent functions (i.e., in wave physics), cosine, $y_{cos} = f(t) = A\cos(2\pi ft)$, and sine, $y_{sin} = f(t) = A\sin(2\pi ft)$. While the functions themselves are continuous, the abscissa is plotted in discretized units such as I use here, and, generally, for these types of calculations, some form of indexing is used; in my example, the amplitude, $A = 1$, the initial value is assumed to occur at $t = 0$, and the indices (i.e., corresponding to a product of frequency and time, ft) roughly correspond to radians. The phase shift between the two functions is $\pi/2$, hence if I shift the indices for y_{sin} by an amount that corresponds to this phase shift, and then test the correlation between y_{cos} and y_{sin}, the Pearson's R^2 will be 1.0. Panel B, then, shows the R^2 that I will obtain as a function of the percent phase shift. Figure 4-5 shows how, for some functions/trajectories, one can detect correlations within data that are related to each other via a phase-

shift. From the outset, I thought that there might be a time-lagged cross correlation for my biomolecule data in view of the effects of Cu and Fe in stimulating biomolecule production and that the environmental half-life of some MN-binding ligands and microcystin may be relatively low, as I discussed in Chapter 3, Section 3.1.

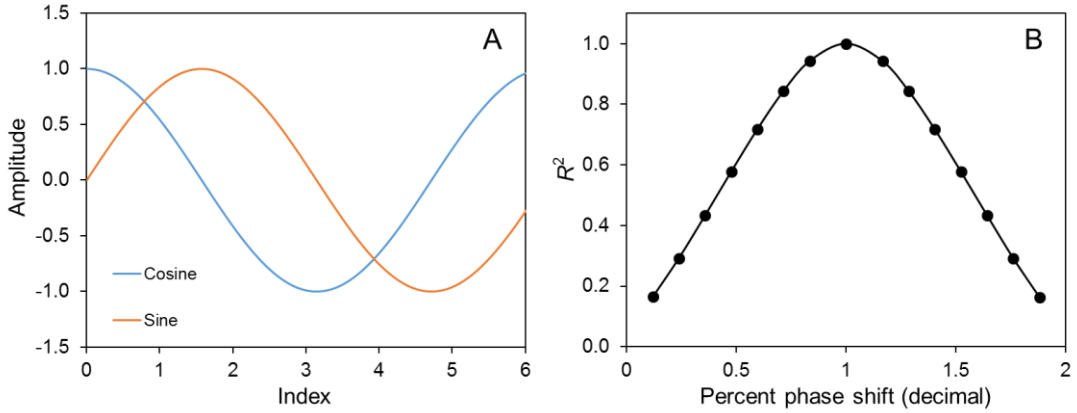

Figure 4-5. Example of the relationship between phase-shift and correlation. (A) Two time-dependent functions that are related through a phase shift, and (B) R^2 as a function of the percent phase shift, i.e., time-lagged cross correlation of the functions in panel A.

In order to conduct the time-lagged cross correlation and discover if indeed there could be optimum lag-adjusted correlations for my biomolecule data, I had a problem. Due to the nature of my experiments, it would be impossible for me to sample at the intervals realistically desirable based on the number of helpers I had available for my experiments and the volume of sample available. This problem of needing to reformat discretization is very common in biological time-series data and is handled using resampling or sample-rate conversion, which in this application refers to changing the frequency of time-series observations (Oppenheim et al., 1999; Sundararajan, 2021). Resampling includes upsampling and downsampling. I needed to first upsample my data, since the sampling time of my field experiments is limited to every two days for a total

time of 8 days. After upsampling, I performed lagged cross-correlation analysis, after which I downsampled again to recover the original discretization of my data.

Upsampling typically consists of two steps, one involves inserting the extra indices desired to produce the desired sample rate, sometimes referred to as zero-stuffing since no information exists in these inserted indices, followed by some form of interpolation to populate the inserted indices with data (Bar-Joseph et al., 2003). In my case, both of these steps were achieved in one step using function calls in R, and I used two commonly used approaches for interpolation, linear and spline. Panels A and B in Figure 4-6 show two examples of data that I made up for illustrative purposes here, for which I plot linear and spline functions that achieve upsampling. As the figure illustrates, linear interpolation results in an upsampled discretization that tacitly accepts the structure of the data collected as being representative of all time points. Because of the relatively long intervals between actual sampling times, however, the lowest or highest measured results measured may not reflect the actual minima or maxima of biomolecule in the mesocosm, and there is also the issue of noise in measurement. For the graph in panel A, a maximum occurs after t2 and before t8. For linear interpolation, this occurs at t6, however, the spline fit effectively uses the time intervals of observation with the relative response observed to project this maximum to a time between t4 and t6, and closer to t6. In this case, the spline fit, when compared to linear interpolation, is likely a better reflection of what the "real" results would be if I had more measurements, and this will be the case much of the time. In contrast, an example where the spline may not perform as well is given in panel B. When I observe the behavior

of the data t6–t8, the spline suggests that there is a small minima just after t6, however, given measurement uncertainty (noise), it may be that the actual response in this interval is flat. In other words, it could be that random experimental uncertainties and the coarse measurement interval result in the appearance of a minima at t6, when in actual fact the measurements at t6 and t8 are slightly low and slightly high, respectively, as a result of random measurement error. If the apparent small minimum is an artefact of noise, this means that linear interpolation is somewhat better in such cases as it does not project values below the measured low at t6.

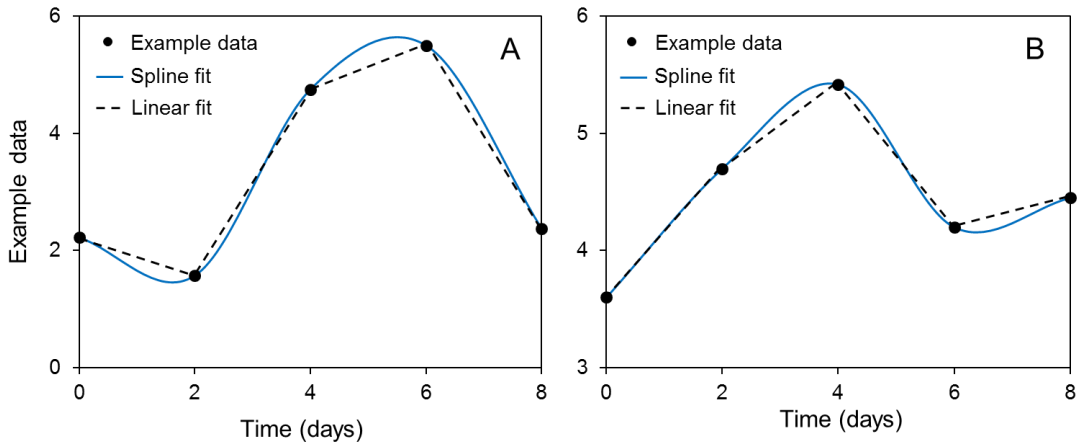

Figure 4-6. Two examples of upsampling. The examples use linear and spline interpolation of artificial example data.

Time-lagged cross correlation for paired trajectories was performed after upsampling via the two methods. The phase-shifted trajectories were then downsampled again to recover the original discretization of my data. Downsampling addresses two considerations. First, the signal frequency inherent in the original structure of my data is recovered, and second, downsampling is performed via averaging across the original indices of measurement, thereby ensemble averaging errors that might have been introduced. To perform the calculations needed for time-lagged cross correlation,

I used the caret, stats, graphics, and grid packages in R (Max, 2021; R Core Team, 2021). The spline algorithm employed the Catmull-Rom option.

4.4 Correlation Matrix Plot Overview of Results from Biomolecule-Focused Experiments

Figure 4-7 is a bivariate correlation matrix plot that gives an overview of inter-parameter associations. Time is plotted as the first variable, followed by the primary indicators of algal growth, including OD, Cts.m, and the counts for the different algal groups at the top of the matrix. The counts for the different algal groups (described in Li et al., 2021/Chapter 3, as determined from Cts.m) include BG, Des, UG, TotG, Dia, and Rest. These are followed by the dissolved metals DCu, and DFe, total metals, TCu and TFe, and the ratios DCu/DFe and TCu/TFe, all normalized to maxima as in Chapter 3. The biomolecules (chalkophore, siderophore and microcystin), are shown at the bottom. As this plot is intended as an overview of the data, I will primarily mention what I consider to be notable or points that relate to discussion later. The size and degree of coloration of each circle in the matrix of Figure 4-7 is proportional to Spearman's ρ, according to the color legend at the bottom of the figure. For $|\rho| \geq 0.3$, the associated p-values are all ≤ 0.05.

The growth indicators OD and Cts.m correlate with each other, and both positively correlate to Des and TotG. Des and TotG both negatively correlate to BG, ergo reflecting the increasing dominance of Des at the relative expense of BG, generally, across the experiments/treatments. The Rest group positively correlates with time, and not much else, which makes sense because Alg_{is} grew in my mesocosms over time and with no clear Cu or Fe effect.

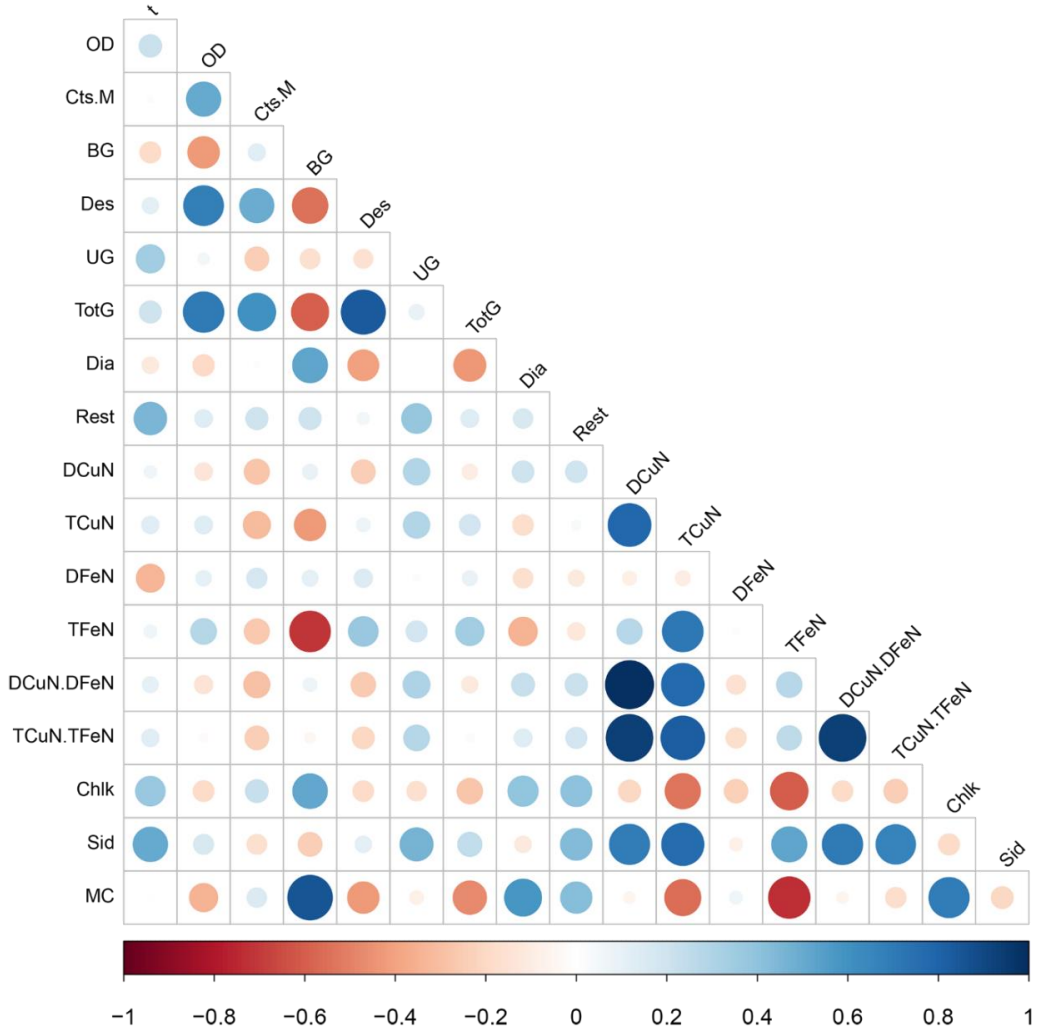

Figure 4-7. Correlation matrix plot showing pairwise-correlation analysis for results from mesocosm experments in the year of 2019. Plot shows the results of pairwise-correlation analysis. The size and degree of coloration of each circle in the matrix is proportional to Spearman's ρ, according to the color legend at the bottom of the figure. For $|\rho| \geq 0.4$, the associated p-values are all ≤ 0.05.

Regarding correlations with metals, TCu negatively correlates with BG, accompanied by a reduction in Cts.m, reflecting the differential BG sensitivity to the level of Cu amended, notably as I discuss below, for high Cu. I find that the 2019 results are nominally consistent with 2018 results; for both, there is a significant negative correlation between BG and TCu, with less or no correlation for DCu. I discuss this in more detail below. A strong negative correlation occurs between TFe and BG, however this is a kind of artificial correlation. It results

because Fe is only amended with Cu (CuLoFeHi and CuHiFeHi), and I observe TCu inhibition of BG is strong with CuHi (discussed below), so this correlation is weighted by the CuHiFeHi results for BG. UG exhibits a weak positive correlation for all metal forms, whereas Des is only weakly correlated with TFe.

The significant correlations between the quantities DCu, TCu, DFe, TFe, DCu/DFe, and TCu/TFe and chalkophore and siderophore are all negative for chalkophore (TCu, TFe) and positive for siderophore (DCu, TCu, TFe, DCu/DFe, TCu/TFe). The negative correlation for chalkophore with TCu is discussed in Section 4.5. The negative correlation for chalkophore with dissolved metals and TFe is also further discussed in Section 4.5, though, the correlation with TFe arises in large part because Fe amendments are always amended with Cu. Siderophore correlations occur because production increased with both Cu and Fe, which I discuss in more detail in Section 4.7. The positive correlation of siderophore with UG is misleading as is arises from a small number of points (see discussion on t6 and t8 M_{meso} CuHiFeHi below).

Interestingly, microcystin correlates negatively with TFe, which is consistent with my findings in Chapter 3, discussed in more detail in Section 3.9. For correlation between the biomolecules, siderophore and microcystin do not correlate significantly (slightly negative, as for Chapter 3), however chalkophore specifically correlates positively with microcystin and BG, consistent with my findings in Chapter 3 and discussed in more detail in Sections 4.6 and 4.7. Chalkophore and siderophore both develop with time as experiments progress, less so for microcystin since microcystin is present in BG/*Microcystis* initially and *Microcystis* is decreasing in some cases.

4.5 Temporal Changes in Mesocosms as a Result of Cu and Fe Amendment

Changes in OD

Examining the raw data in greater detail, Figure 4-8 shows OD versus time for all mesocosm experiments. For M_{meso} Ctl, there is a small but monotonic increase in OD from t0 to t4, with a maximum increase of 24% by t6 at the onset of stationary phase. The remaining M_{meso} amendments all contain Cu and all show a marked drop in OD by t2, with subsequent increases in OD thereafter. Interestingly, concerning the drop in OD at t2, Fe is consistently associated with a larger t2 decrease. Both FeHi amendments, CuLoFeHi and CuHiFeHi, OD decrease by 58% and 61%, respectively, irrespective of Cu level, whereas OD for the CuLo amendment only decreases by 40% at t2 relative to the start of the experiment. While the initial OD drops for metals amended mesocosms were similar, to within ~20%, the M_{meso} OD recovery for CuLo, CuLoFeHi and CuHiFeHi from t2 to t8 followed the order CuLo > CuLoFeHi > CuHiFeHi, with the former two reaching stationary phase by the end of the experiment, whereas CuHiFeHi did not. For G_{meso}, ODs for all four amendments were similar, increasing to stationary phase by t4–t6 and declining in post-stationary by t8, except for the significant decrease in OD for CuHiFeHi by t2 ($p < 0.05$). The trend of OD versus time for B_{meso} is similar as for G_{meso}, except that a relatively flat OD at stationary phase persists to the end of the experiment for all but the Ctl. Comparing the CuHiFeHi amendment across all mesocosms in Figure 4-8, the decreases in OD from t0–t2, are, respectively, 61%, 32%, and 48% for M_{meso}, G_{meso}, and B_{meso}, i.e., while the microscopic counts tell me a detailed story about

how the high Cu amendment is affecting the algal assemblages, I nonetheless see that all mesocosms were affected by the high Cu concentration. I also note that the drop in OD for G_{meso} by t2 is half that of M_{meso}, and that the OD decrease for B_{meso} averages that of M_{meso} and G_{meso}. Though the high Cu did decrease the growth of green algae by t2, the OD recovery for the high Cu amendment is quicker for green algae in G_{meso} compared to *Microcystis* in M_{meso}. That the trend of the OD change with time is similar for G_{meso} and B_{meso} is explainable from microscopic examination, wherein I found that the percentage of BG/*Microcystis* in B_{meso} was overtaken by green algae during the course of the experiment, which I discuss in more detail later in this section.

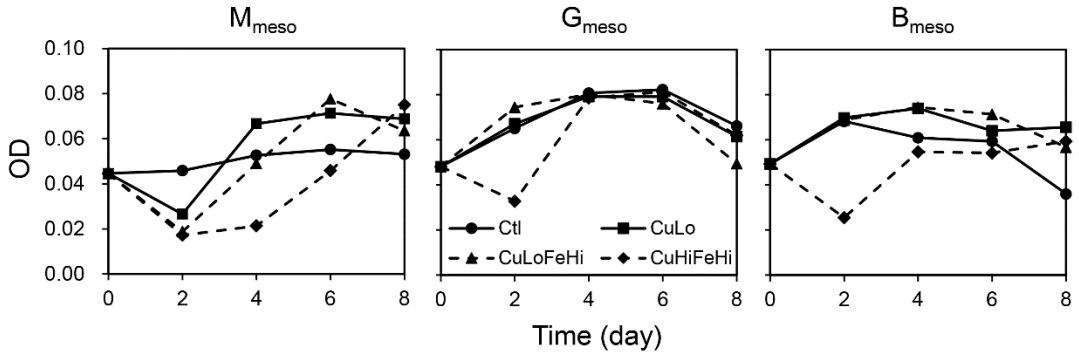

Figure 4-8. Changes in OD (750 nm) with time for mesocosm experiments in the year of 2019. Results are plotted as a function of mesocosm type and amendment (amendment without Fe are present in solid lines and amendment with Fe are present in dash lines).

How Amendments Affect Changes in Algal Assemblages

As I discussed in Chapter 3, Cts.m remain the dependable standard for simple determination of species density/assemblage changes and cell condition (Butterwick et al., 1982), and, also as I discussed in Chapter 3, there was the possibility that Alg_{is} present in very small numbers initially might cause algal assemblage changes over the course of my field experiments and that Alg_{is}

changes might reflect initial conditions or Cu/Fe amendment from my experimental design. Certainly, in my work and the work of my colleague Dr. Zhang in which I participated, I previously found that Cu and Fe mediate algal assemblage changes (Zhang et al., 2019; Li et al., 2021). Figure 4-9 shows time-dependent changes in Cts.m of algae groups by amendment. At t0, algal species and Cts.m are as expected. Since the mixture Des and UG in G_{meso} was effected according to OD, Des in G_{meso} constitute larger, but fewer, individuals, while UG in G_{meso} constitute smaller, but more numerous, individuals. I was therefore reasonably satisfied that the t0 ratio that I found for G_{meso} (41% Des, 59% UG) was reasonably close to 50:50, with the percentage of UG being larger, as expected, since the cells are smaller. Similar comments pertain to B_{meso} given the relatively small size of *Microcystis* cells.

A striking feature in Figure 4-9 is that, by t4, the M_{meso} CuHiFeHi amendment began to demonstrate the replacement of BG/*Microcystis* by UG, which persisted through to t8. This replacement of *Microcystis* by UG for the high Cu amendment (100 $\mu g \cdot L^{-1}$) is consistent with my results from 2018 in Chapter 3, Section 3.6, where I amended 50 $\mu g \cdot L^{-1}$ Cu. The percentage of UG in M_{meso}, on average, follows CuHiFeHi > CuLoFeHi > CuLo > Ctl over time, with only 2% UG in M_{meso} Ctl by t8. The replacement of BG/*Microcystis* by UG is strongly associated with Cu, and secondarily with Fe as well since UG in CuLoFeHi > CuLo. For the three M_{meso} amendments other than CuHiFeHi, Des increases over t4–t8 to become the dominant species by t8, however, the process occurs more slowly for Ctl, and is similar for CuLo versus CuLoFeHi. The percentage of BG remaining in M_{meso} Ctl, CuLo and CuLoFeHi by t8 is 46%, 29% and 21%, respectively. That Des slowly took over the M_{meso} Ctl mesocosms over the course of the experiment suggests

that Cu amendment alone is not responsible for the change, however, the persistence of BG/*Microcystis* being highest in Ctl, followed by CuLo and CuLoFeHi suggests that inhibition of BG/*Microcystis* growth by Cu did happen under my experimental setting with low Cu as well as high. The change for the high Cu amendment is much larger, with only 4.8% *Microcystis* remaining by t8.

For G_{meso}, I started with a 1:1 mixture, by OD, of Des and UG, however, Des rapidly became the major species by t2 for all amendments. Despite the rapid decrease in UG counts in G_{meso}, I do not think that algal acclimation was an issue. I regard algal acclimation in G_{meso} as successful when considering the OD results above in Figure 4-8, as there is not a drop in OD for G_{meso} Ctl, while compared to my results in Chapter 3, Section 3.5, I did observe a large decrease in OD for green algae that, as I discussed there, did appear to result from insufficient algal acclimation.[4] The rapid dominance by Des in G_{meso} is not specific to any of the amendments, it is general. In fact, for G_{meso}, this is the only large change. UG, as compared to Ctl (an average of 1.6% over t2–t8) is somewhat more persistent for all amendments (averaging 4.5% over t2–t8). For G_{meso}, I did not see large UG differences with amendment as I saw I for M_{meso}, however, there is still an order, following CuHiFeHi (7%) > CuLo ~CuLoFeHi 3% > Ctl 2%. The only other differences of note in Figure 4-9 for G_{meso} is that at t8, the percentage of BG increased to 18% for G_{meso} CuHiFeHi. This higher BG count was almost completely comprised of *Pseudoanabaena*.

[4] Considering that I suspected insufficient algal acclimation in Chapter 3, Section 3.5. I added stricter condition control to the algal acclimation to the work here in this chapter including longer algal acclimation time (increased from 3 days in Chapter 3 to 14 days), and stricter temperature control (measuring and adjusting the water temperature used for acclimation several times per day).

The B_{meso} share some commonalities with both M_{meso} and G_{meso}. The persistence of BG/*Microcystis* being highest in Ctl, followed by CuLo, CuLoFeHi and CuHiFeHi reported above in M_{meso} was also found in B_{meso}. Averaging the percentage of BG/*Microcystis* in B_{meso} over t2–t8, it is 17%, 14%, 13% and 12% for Ctl, CuLo, CuLoFeHi and CuHiFeHi, respectively, albeit the difference is small and not statistically significant. Though the differences of the persistence of BG/*Microcystis* for B_{meso} is not obvious as in M_{meso}, however the trend follows, suggesting that inhibition of BG/*Microcystis* growth by Cu also happened in B_{meso} with low Cu, and the inhibition is greater with higher Cu.

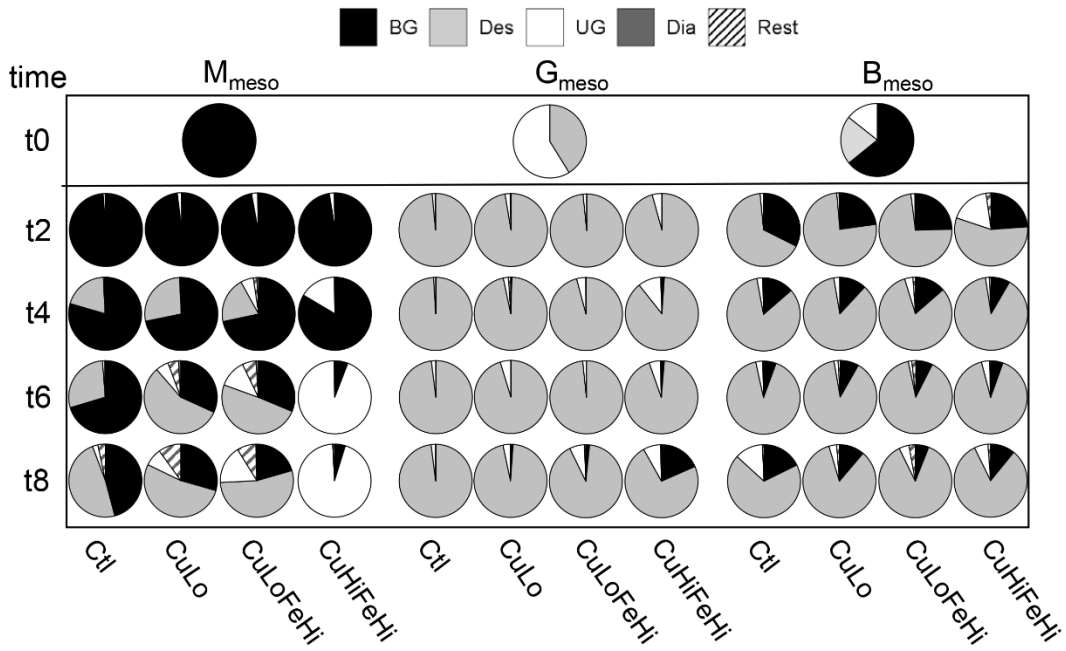

Figure 4-9. Pie charts showing changing algal assemblages in time for mesocosm experiments in the year of 2019. Percentages are plotted for algae by group for different amendments (BG = Blue-green algae; Des = Desmids; UG = Unicellular green algae; Dia = Diatoms; Rest = remaining, less common algae).

Like G_{meso}, Des rapidly displace UG by t2, and the percent of Des by count increases from 21%, at t0, to 66%, 76%, 73%, and 56% by t2 for Ctl, CuLo, CuLoFeHi, and CuHiFeHi, respectively, with the majority of the remainder in all

cases being *Microcystis*. The average amount of UG over t2–t8 in B_{meso} was again higher for CuHiFeHi, though again, not statistically significant. The transition of algal assemblages in B_{meso}, compared M_{meso} and G_{meso}, showed an apparent resurgence of UG in the Ctl by t8. The OD results above in Figure 4-8 indicate that the Ctl culture is crashing at t8, and the UG in B_{meso} Ctl by t8 was constituted of an equal amount of *Carteria* (47%) and *Chlamydomonas* (53%), i.e., not the *Chlorella* that was present at t0, and therefore the apparent resurgence of UG in B_{meso} Ctl by t8 is not comparable to the persistence of t0 UG/*Chlorella* in other mesocosms.

Changes in Amended Metals

Regarding Cu and Fe, as for Chapter 3, I first evaluated QA/QC. Recoveries for TM QA/QC spike checks were 102 and 95% and for the CRM were 97% and 97% for TCu and TFe, respectively. The average respective recoveries (eq. 3-1, Chapter 3) for TCu and TFe were 102% and 107%, with an RSD of 17% in each case. Values of $C_{algae,\,t0}^{TCu}$ were 2 μg·L^{-1}, 6 μg·L^{-1} and 4 μg·L^{-1}, respectively, for M_{meso}, G_{meso} and B_{meso}, and values of $C_{algae,\,t0}^{TFe}$ were 122 μg·L^{-1}, 308 μg·L^{-1} and 236 μg·L^{-1}, respectively, for M_{meso}, G_{meso} and B_{meso}. The concentration of $C_{spike,\,t0}^{TDCu}$ in CuLo and CuHi amendment were 21 μg·L^{-1} and 102 μg·L^{-1}, respectively (105% and 102% recovery, respectively), and the concentration of $C_{spike,\,t0}^{TDFe}$ in FeHi amendment was 182 μg·L^{-1} (91% recovery). For TDCu and TDFe, QA/QC results were also within acceptable limits, with the average spike recovery being ≥ 96% and the average RSD being 9%.

Subsequent to the QA/QC results, I verified that TCu/TFe were conserved for t0–t8. Changes in TDM over time are shown in Figure 4-10. The dissolved forms,

TDCu/TDFe, arrived at or near steady-state by t2, except TDCu for the CuHiFeHi M_{meso}, which exhibits very different behavior, seemingly bi-phasic, in accord with changes in algal assemblages, whereby a "*Microcystis* steady-state" of ~59 $\mu g \cdot L^{-1}$, or 46% uptake, is achieved by t2, persistent to t4, and subsequently as the shift to UG dominance by t6 occurs, these mesocosms arrive at a second TDCu steady-state of 31 $\mu g \cdot L^{-1}$, 74% uptake, by t8. For high Cu amendments, the t8 uptake for M_{meso}, G_{meso} and B_{meso} is similar, being, respectively, 75, 76 and 72 $\mu g \cdot L^{-1}$, averaging 74 $\mu g \cdot L^{-1}$ or 73% uptake. Assuming that 31 $\mu g \cdot L^{-1}$ is the t4 TDCu steady-state for the *Microcystis*-dominated M_{meso} CuHiFeHi and that 74 $\mu g \cdot L^{-1}$ is representative for the CuHiFeHi mesocosms, which are all green-algae dominated by t8, this suggests that *Microcystis* uptake is ~40% that of green algae. This observation agrees with what I reported in Chapter 3 with a significant ~ 50% greater uptake of D_{meso} as compared to M_{meso}.

Regarding the similarity of the dissolved Cu uptake results here in Figure 4-10, and with the results previously reported in Chapter 3, Figure 3-11, the results could be explained in terms of sorption theory. Some research on algal-metal interactions reports that *Microcystis* (even dead cells) apparently sorbs metals quite well due to mucilage (Parker et al., 1998; Tien et al., 2004; Alwaleed et al., 2021). For green algae, high sorption of metals was also reported as a function of the cell wall structure (Kumar et al., 2015; Saavedra et al., 2018; Buayam et al., 2019; Spain et al., 2021). I also notice that the uptake rates for DCu for low Cu amendments (CuLo and CuLoFeHi) are more similar; the maximum uptake of Cu was 58%, 76% and 63% for M_{meso}, G_{meso} and B_{meso}, respectively. Here again, uptake for M_{meso} is lower than that for G_{meso}, with uptake for B_{meso} being the average of the two, approximately. These results, taken together, suggest a

sorption phenomenon wherein sorption of Cu by *Microcystis* is lower than that for green algae. The differential is greater for high Cu comparatively because sorption is a function of metal concentration, and it may be as well that the specific sorption capacity of *Microcystis* in the high Cu M_{meso} is closer to saturation than for the green algae. That B_{meso} should roughly approximate an average of M_{meso} and G_{meso} would also be consistent with sorption.

For TDFe, results were as expected because the experimental design involved using aged forms of Fe (Section 4.2). As I had anticipated, by t2, all amended Fe had become TFe of some form. This could be sorbed, or unsorbed, Fe-oxyhydroxides. Comparing the TDCu results for TDFe results, while I saw differences for DCu behavior for different algae, the DFe is similar in all cases. Chemical equilibria governing oxyhydroxide formation are almost certainly the cause of DFe behavior and the consistent baseline by t2 and after. These values of DFe are well above what chemical equilibria would allow, and instead probably represent the fraction of colloids that pass through the filter that is used for the operational standard for dissolved.

In Chapter 3 I found that correlations between metals and BG were in alignment with reasonable expectation, with smaller values of ρ for correlations between BG and DCu, as compared to TCu, but nonetheless, the negative correlations were all significant. Here, in Figure 4-7, I do not see a DCu-BG correlation. This lack of correlation may be misleading due to process kinetics resulting from what I discussed above. The correlations in Figure 4-7 were analyzed for all mesocosms together, however, the timing of DCu changes is phased in this work and probably there is a phase-shift for some processes as well.

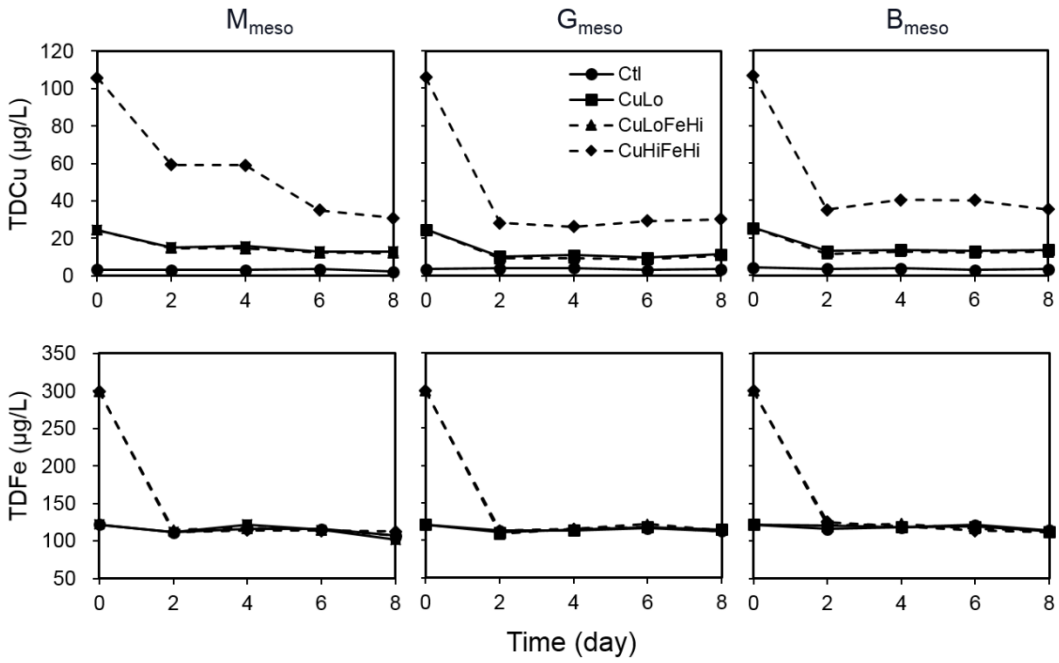

Figure 4-10. Changes in TDCu and TDFe as a function of time for mesocosm experiments in the year of 2019. Results are plotted as a function of mesocosm type and amendment (amendment without Fe are present in solid lines and amendment with Fe are present in dash lines).

I saw strong positive correlation for DCu with TCu, but no correlation between DFe and TFe. This may explained as the form of Fe amended quickly became insoluble, i.e., DFe was invariant for all mesocosms by t2, while changes in DCu/TCu were more variable. Both TCu and TFe negatively correlated to BG, chalkophore and microcystin, but positively correlated to siderophore. Those correlations that I observed in Figure 4-7 are reasonable as the Cu and Fe I amended did relate to the production of biomolecules; the effect of amended metals on the production of those biomolecules I discuss below.

Changes in Biomolecule Production

Figure 4-11 shows changes in chalkophore and siderophore over time. Even more than my prior work, there are distinct patterns resulting from amendments. The changes in chalkophore with time in M_{meso} follow the order

Ctl > CuLo ~ CuLoFeHi > CuHiFeHi (differences indicated by > all significant), resulting in negative correlation. The large decrease in chalkophore production by as early as t2 for CuHiFeHi may relate in part to the decrease of *Microcystis* by t2, however, the decrease in chalkophore production (83%), is substantially greater than the decrease in OD (62%) or Cts.m (31%) by t2. For G_{meso} the order is Ctl ~ CuLo > CuHiFeHi > CuLoFeHi, which is quite different than that of M_{meso}, with additional differences being that the initial level of chalkophore is zero and the maximum level of chalkophore production is around half that of M_{meso} (52%). For G_{meso}, the order Ctl ~ CuLo > CuHiFeHi ~ CuLoFeHi, is significant at t2; by t4, only the difference Ctl > CuLoFeHi is significant. B_{meso} t0 chalkophore is, approximately, the average of that of M_{meso} and G_{meso}, then follows the order of G_{meso} chalkophore production, having higher chalkophore in all cases by t8, presumably because of the persistence of some *Microcystis* in these B_{meso} by that time (Figure 4-9). A common feature of the chalkophore production for all mesocosms is that chalkophore production is always highest in Ctl, i.e., the algae, depleted of Cu and Fe during acclimation, seem to have sensed the low Cu in their environment, thus increased the chalkophore production.

The change in siderophores with time as a function of mesocosm type and amendment was quite different compared to chalkophores. First, the order of siderophore production level, CuHiFeHi > CuLoFeHi > CuLo > Ctl, is the same for all mesocosms. Second, the basal t0 level is the same for all mesocosms. Third, the maximum siderophore production is for G_{meso}, rather than M_{meso}, and for G_{meso}, at t4, when production maximizes and begins to level off, and at the same time the OD for all four amendments is approximately the same (Figure 4-8). By t8, B_{meso} siderophore behavior reflects that of G_{meso}. Siderophore, then, seems to

be very different from chalkophore. Based on these results I think of chalkophore as being a sort of primary domain of *Microcystis*, for which, if there is too much Cu, production stops, and when there is no Cu, production is highest. Siderophore, in contrast, appears to be more subject to the rule of TotG, and in all cases, in agreement with my speculations in Chapter 3, despite the relative biounavailability of Fe in the form in which I amended it, the algae can sense when Fe is present, and modulate their siderophore production in response. In fact, unlike Fe for chalkophore, the non-cognate metal, Cu, seems to stimulate siderophore production as well as the cognate metal, relevant to findings of others that some siderophores can strongly bind to Cu as well as Fe (McKnight and Morel, 1980; Nair et al., 2007; Holden and Bachman, 2015, see Section 4.7 for further discussion).

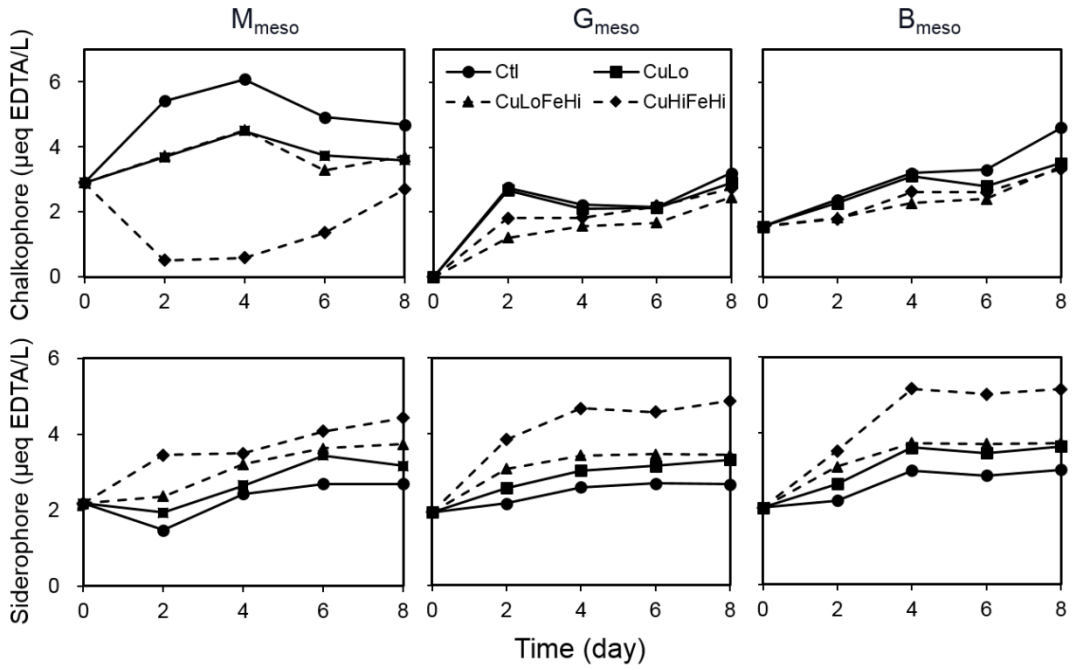

Figure 4-11. Changes in chalkophore and siderophore as a function of time for mesocosm experiments in the year of 2019. Results are plotted as a function of mesocosm type and amendment (amendment without Fe are present in solid lines and amendment with Fe are present in dash lines).

In Chapter 3, Section 3.4, I saw some correlations between chalkophore/ siderophore and OD/Cts.m, however, as I discussed in Section 3.9 relationships between the two are not consistent and often not proportionate or simultaneous. For this work, in Figure 4-7 I did not find any significant correlations between chalkophore/siderophore and OD/Cts.m. I did find positive correlations between chalkophore with BG, and siderophore with UG. As I observed a previously unreported link between chalkophore and microcystin production in Chapter 3, the positive correlation that I see in Figure 4-7 for chalkophore and BG, seems likely to relate to this chalkophore-microcystin link. The positive correlation between siderophore and UG may be misleading, as the greatest increase of UG with time came from the M_{meso} CuHiFeHi discussed above, where high Cu inhibited *Microcystis* simultaneous with UG ingrowth.

Concerning microcystin, as the work in Chapter 3 was highly exploratory, my microcystin data was limited to t0 and the terminal mesocosm subsampling, i.e., I did not have a complete time series. While I tried different techniques for microcystin analysis, I was not able to obtain satisfactory performance from these, and therefore I used the highly reliable/ US EPA-approved commercial ELISA kit, however, each kit cost in excess of 500 £, hence the decision in Chapter 3 work not to collect a full time series. Based on Chapter 3 results, however, I analyzed microcystin for the full time series here. Figure 4-12 shows changes in microcystin over time (G_{meso} results omitted due to being below LOD). Microcystin production has been reported to change with different concentrations of iron (Sevilla et al., 2008; Zakhia et al., 2008), thus it has been proposed that microcystin perhaps serves as a siderophore (Martin-Luna et al.,

2006; Alexova et al., 2011). The Fe-binding stability constant of microcystin reported by Klein et al. (2013), is orders of magnitude lower than the value of $\sim 10^{21}$ regarded by many as the level of high affinity that characterizes Fe-siderophore binding (Zhang et al., 2020a), and thus they proposed that microcystin is unlikely to serve as an extracellular siderophore. Consistent with my results in Chapter 3, I again find no microcystin-siderophore correlation here (see Figure 4-7).

The t0 microcystin results for M_{meso} are almost four times higher than for those in Chapter 3. The t0 result for B_{meso} was as expected, being just under half that of M_{meso}. There were no statistically significant differences between Ctl, CuLo and CuLoFeHi amendments for M_{meso} or B_{meso}. The only significant difference was for CuHiFeHi, versus all other amendments, in both M_{meso} and B_{meso} from t2–t8 (note, for B_{meso} this finding is not apparent from the scale of the graph, which compresses the appearance of B_{meso} results; I plotted the graph on this scale to show the relative differences with M_{meso}). There is no significant correlation between microcystin and OD/Cts.m. While I see some changes in microcystin that appear to mimic those in OD, for instance, the dip at t2 for CuLo, CuLoFeHi, the dip does not occur in OD for the t2 Ctl, however is present for microcystin. Similarly, microcystin production shows a marked decrease between t6 and t8, while OD does not, though this change in microcystin is undoubtedly associated with the algal assemblage shift toward green algae for M_{meso} by t8. The most notable feature of Figure 4-12 could be the remarkable uniformity of Ctl, CuLo and CuLoFeHi results for both M_{meso} and B_{meso}.

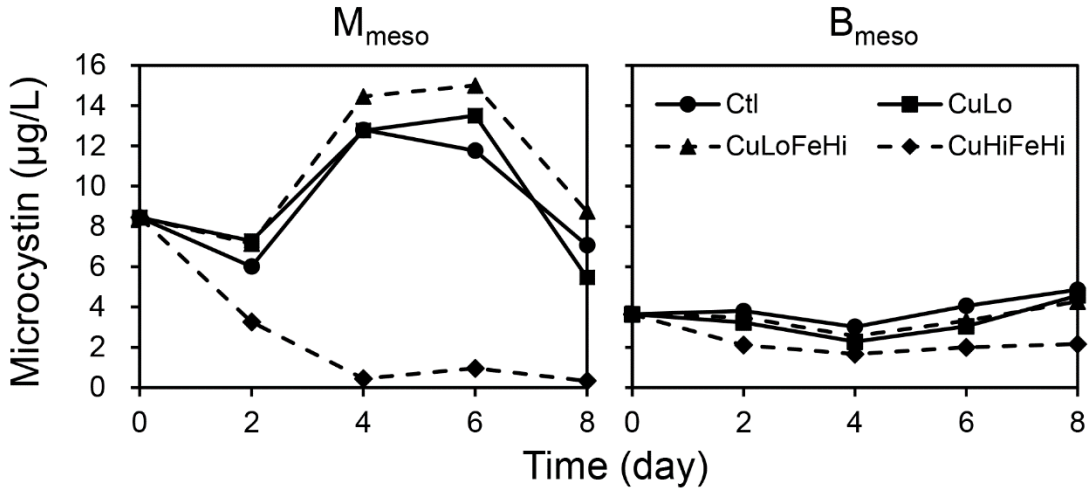

Figure 4-12. Changes in microcystin as a function of time for mesocosm experiments in the year of 2019. Results are plotted as a function of mesocosm type and amendment (amendment without Fe are present in solid lines and amendment with Fe are present in dash lines).

4.6 Results from Extended CTA Analysis of Biomolecules

I began this analysis as for Chapter 3, Section 3.9, by plotting chalkophore versus siderophore trajectories. Figure 4-13 shows community trajectories based on raw results (A–C) and OD/normalized results (D–E). While the latter may be in some way misrepresentative, according to comments in Chapter 3, Section 3.3, I was interested to compare the two types of results to see if they would agree with each other or not. In general, the trajectories of chalkophore/siderophore for M_{meso} are very different than for G_{meso} and B_{meso}. The trajectories are a very different type of data than raw time series, however, I also observe a similar contrast between M_{meso} and G_{meso}/B_{meso} results for raw data such as OD and algal assemblages reported in Section 4.5.

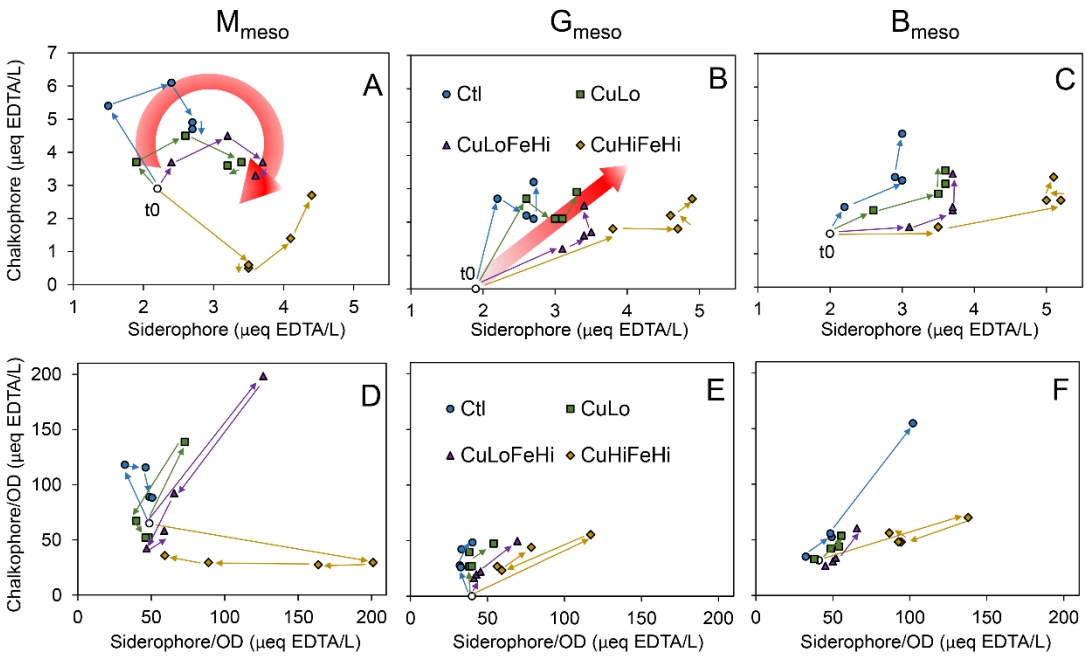

Figure 4-13. Chalkophore/siderophore bivariate community trajectories for mesocosm experiments in the year of 2019. Results are plotted as a function of mesocosm type and amendment for raw results (A–C) and after OD normalization (D–F).

In Figure 4-13A–C, there is an evolution of the trajectories for all mesocosms, from one spatial behavior (Ctl) through the progression to CuLo, then CuLoFeHi, and then CuHiFeHi. For M_{meso}, for all mesocosms the chalkophore/siderophore showed circular trajectories, clockwise for Ctl, CuLo and CuLoFeHi and counter-clockwise for CuHiFeHi, mainly caused by the differences of the decreased chalkophores from t0 to t2 which is only found in CuHiFeHi. The rotation in these trajectories (wide red arc) for M_{meso} reflect an adaptive strategy, whereby there are preferential changes in one direction or another, according to whether Cu or Cu-and-Fe is present. When amended with high Cu, the direction of change in M_{meso} totally changed due to the immediate decrease/cessation of chalkophore production from t0 to t2. When comparing M_{meso} Ctl with CuLo and CuLoFeHi, a differential chalkophore increase from t0 to t2 resulted in a higher initial trajectory along the chalkophore/*y*-axis. In fact, for the Ctl, and to a lesser

extent CuLo, the only other amendment without Fe, the initial chalkophore production is accompanied by a decrease in siderophore; siderophore production only begins as chalkophore production tapers. In contrast, there is no decrease of siderophore from t0 to t2 for Fe-amended mesocosms, which exhibit longer trajectories on the siderophore/*x*-axis.

The trajectories for G_{meso} are all much different than those for M_{meso} in that, rather than being described in terms of rotation, they could all be approximated in polar coordinates as vectors (e.g., wide red arrow), the angle and magnitude of which varies relative to the amounts of Cu or Fe amendment at t0. While I describe M_{meso} as seeming adaptive to me, changing chalkophore/siderophore differentially, in contrast G_{meso} chalkophore/siderophore trajectories could be approximated as vectors in polar coordinates because levels changed simultaneously. For G_{meso}, as no chalkophores were measured for the t0 samples, the trajectories for all mesocosms start from $y = 0$. The major differences in trajectories for G_{meso} correspond to changes, resulting in longer trajectories, on the siderophore/*x*-axis.

For B_{meso}, even t0–t2 when there is still an appreciable amount of *Microcystis* present, I do not see the rotation-type trajectory shape that I see for M_{meso}. When amended with Cu and having a lower amount of *Microcystis* relative to the Ctl, B_{meso} trajectories become more similar to those of G_{meso}, consistent with the changes in algal assemblages. B_{meso} chalkophore increases are most pronounced when greater quantities of *Microcystis* are present, which may relate to the interesting chalkophore-microcystin link discussed in Chapter 3, Section 3.9. For G_{meso} and B_{meso}, siderophore is for the most part increasing (longer *x*-axis

trajectories), with no substantive decrease at any point. The trajectory view of chalkophore/siderophore interactions, is, to my thinking, a more informative way to consider the inter-relationship between the two, as compared to Figure 4-11.

Comparing the chalkophore/siderophore trajectories from work in Chapter 3 to those here in Figure 4-13, clockwise trajectories dominate in Figure 4-13 for M_{meso}, but a counter-clockwise behavior was found for the work in Chapter 3. Though M_{meso} showed different phasing, the trajectories in Chapter 3 versus here are all adaptive/rotational when compared to those trajectories for green algae. Trajectories for green algae of the work in Chapter 3 are even more heavily siderophore dominated. When comparing chalkophore/siderophore trajectories for B_{meso} from the work in Chapter 3 to Figure 4-13, the trajectories of B_{meso} in Figure 4-13 are more similar with trajectories of green algae, however, trajectories of B_{meso} in Chapter 3 were more like M_{meso}, which is sensible to me based on the different changes in algal assemblages. For Chapter 3; some of the B_{meso} were dominated by *Microcystis*, while the progression has instead favored green algae in all cases for B_{meso} in this work.

I described in Chapter 3, Section 3.3, the dangers of conducting the type of analysis that I do here on data normalized to growth indicators such as OD. Caveats aside, whether this is best practice or not, it is certainly common practice, so I decided to try that with the data here. Figure 4-13D–F shows the same results as in panels A–C, only normalized to OD for each axis. After normalization, I still see clear differences between different mesocosms and different amendments within mesocosm type. OD-normalized,

chalkophore/siderophore trajectories for M_{meso} still showed bigger differences in shape/behavior when compared to G_{meso} and B_{meso} trajectories, which are again more similar to each other, as I saw in panels A–C. Compared to Figure 4-13A–C, M_{meso} trajectories are "flattened" and have more the appearance of returning to the point of origin. After normalization, the trajectory distance of M_{meso} CuLoFeHi was more distinct.

OD normalization is probably only really sensible for G_{meso} due to the way the other mesocosm assemblages change, discussed in Section 4.5, No clear differences were found between raw results and the OD normalized results of the chalkophore/siderophore trajectories for G_{meso}, however, if these trajectories would be expressed as vectors, on a normalized basis the slope of the vectors is much higher, i.e., chalkophore production is dominating over siderophore for lower Cu/Fe amendments. For B_{meso} the Ctl trajectory appears magnified relative to the others. This is due in large part to the OD drop for B_{meso} Ctl at t8. Otherwise, for the most part, these trajectories more closely resemble those of G_{meso}, as was also the case for non-normalized B_{meso} trajectories.

The trajectories in Figure 4-13, in contrast to those in Figure 3-14, vary more in behavior than in absolute length, and hence are suited to a more sophisticated measure than those I used in Chapter 3 CTA. I trialed both FD and DTW techniques to test for trajectory similarities or differences. As expected, as compared to the approaches used in Chapter 3, which I also tested, these distance measures were far superior to detect differences in trajectories. Of the two, DTW was more powerful at discriminating differences than FD, as I has suspected it might be for reasons discussed in Section 4.3, so my focus here will

be CTA with DTW. As with the analysis for Figure 4-13 above, I wanted to compare trajectory distances based on non-normalized and OD-normalized input data, and now, since I have a full data set for microcystin, I also compared DTW distances in 2-D (chalkophore and siderophore) and 3-D (2-D plus microcystin) community space. Results are presented in Figure 4-14. The microcystin results for G_{meso} are not reported since they all measure below LOD (0.1 $\mu g \cdot L^{-1}$ according to the Microcystins-ADDA ELISA kit as discussed in Chapter 3, Section 3.2), such that in Figure 4-14, there are no 3-D plots for G_{meso} According to DTW, trajectories for all amendments save two are significantly different from each other ($p < 0.05$, Tukey's HSD).

For simplicity in plotting, the DTW distances in Figure 4-14 have all been normalized to the maximum DTW per mesocosm. In all cases this is the DTW distance between Ctl and CuHiFeHi, so all distances are normalized to this maximum such that the normalized CuHiFeHi is 1.0 in all cases. For the two DTW distances in Figure 4-14 that are not different at $p < 0.05$, the associated p-values, ($p = 0.068$ and 0.056) are shown in red text. Considering the multiplicity of uncertainties and complexity of the environmental field experiments that produced these data, I regard these DTW distances as still being significant.

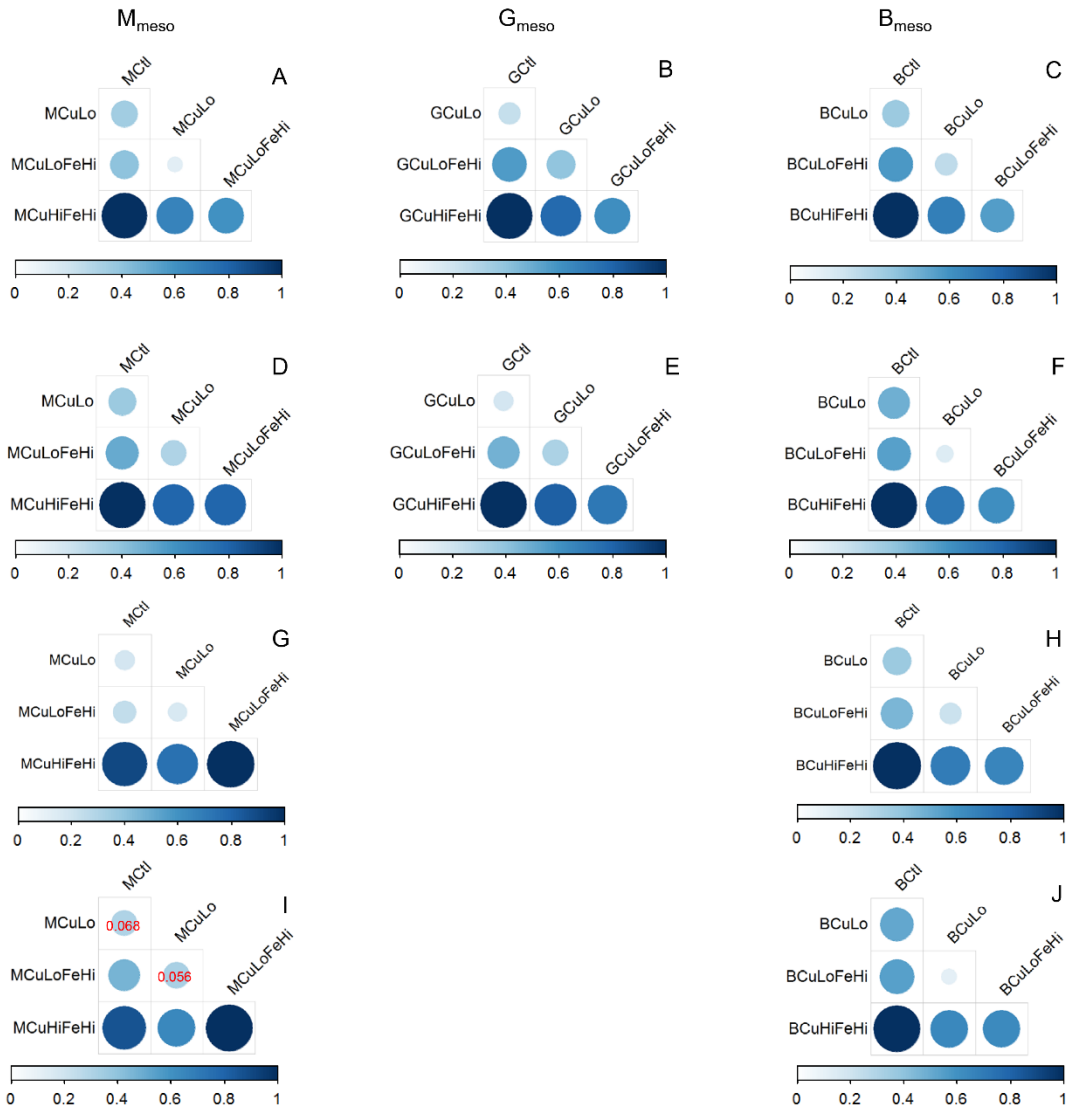

Figure 4-14. DTW distance matrix plots. Plots show the results of pairwise comparisons. DTW for each mesocosm (M_{meso}, G_{meso}, and B_{meso}) is normalized to 1.0 as described in the text. Result are plotted in array form, wherby columns correspond to mesocosm type (column 1 being M_{meso}, column 2 G_{meso}, and column 3 B_{meso}), while rows correspond to different types of calculation input (row 1 is 2-D chalkophore/siderophore data not normalized to OD; row 2 is 2-D chalkophore/siderophore data normalized to OD; row 3 is 3-D chalkophore/siderophore/microcystin data not normalized to OD). The size and degree of coloration of each circle in the matrix is proportional to the normalized DTW distance, according to the color legend at the bottom of the figure. From Tukey's HSD test, *p*-values of all distances are < 0.05, except for those in Panel I where *p*-values are shown in red text.

Figure 4-14 shows how, in all cases, no matter how I analyze the data, CuHiFeHi is always most different from all other trajectories. For M_{meso} and B_{meso} the

greatest similarities/smallest DTW distances occur for CuLo versus CuLoFeHi (Figure 4-14A, C, D, F, G and H). For G_{meso} the greatest similarity is consistently for Ctl versus CuLo (Figure 4-14B, and E). It is remarkable to me that the findings in Figure 4-14 present such differences, and so consistently, whether OD-normalized or not, 2-D or 3-D. This suggests to me that the approach I take here is far more powerful than others I tried. Within the consistency, one interesting point of difference that I observe in is that, when comparing the 3-D DTW distances, the largest distance observed shifts from Ctl versus CuHiFeHi to CuLoFeHi versus CuHiFeHi for M_{meso}, reflecting the largest univariate distance for microcystin.

A major motivation for me in this work was to discover if I would again observe the microcystin-chalkophore link that I had in Chapter 3. In Figure 4-7, there is a Spearman's ρ of 0.68 for the microcystin-chalkophore correlation, and the corresponding Pearson's R^2 was 0.47, greater than what I previously found (see correlation matrix plot in Chapter 3, Figure 3-2) of Spearman's ρ of 0.28 and a corresponding Pearson's R^2 of 0.27. Looking only at M_{meso} and B_{meso} mesocosms (those with *Microcystis*), I had found a R^2 = 0.61 in Chapter 3, Figure 3-15, for the correlation between microcystin and chalkophore at t6. Clearly timing should be relevant to the relationship, and of course, I had already anticipated that year-on-year differences would occur. The matter is further complicated by what I now know to be the inherent (and likely varying) phase-dependencies in the data. As a result of these considerations, I decided to try time-lagged cross correlation to examine a possible microcystin-chalkophore link. The results from my analysis of time-lagged cross correlations for M_{meso} and B_{meso} chalkophore and microcystin using the spline interpolation method are shown

in Figure 4-15; the optimum time-lagged Pearson's R^2 is plotted for each amendment, as noted on the plots.

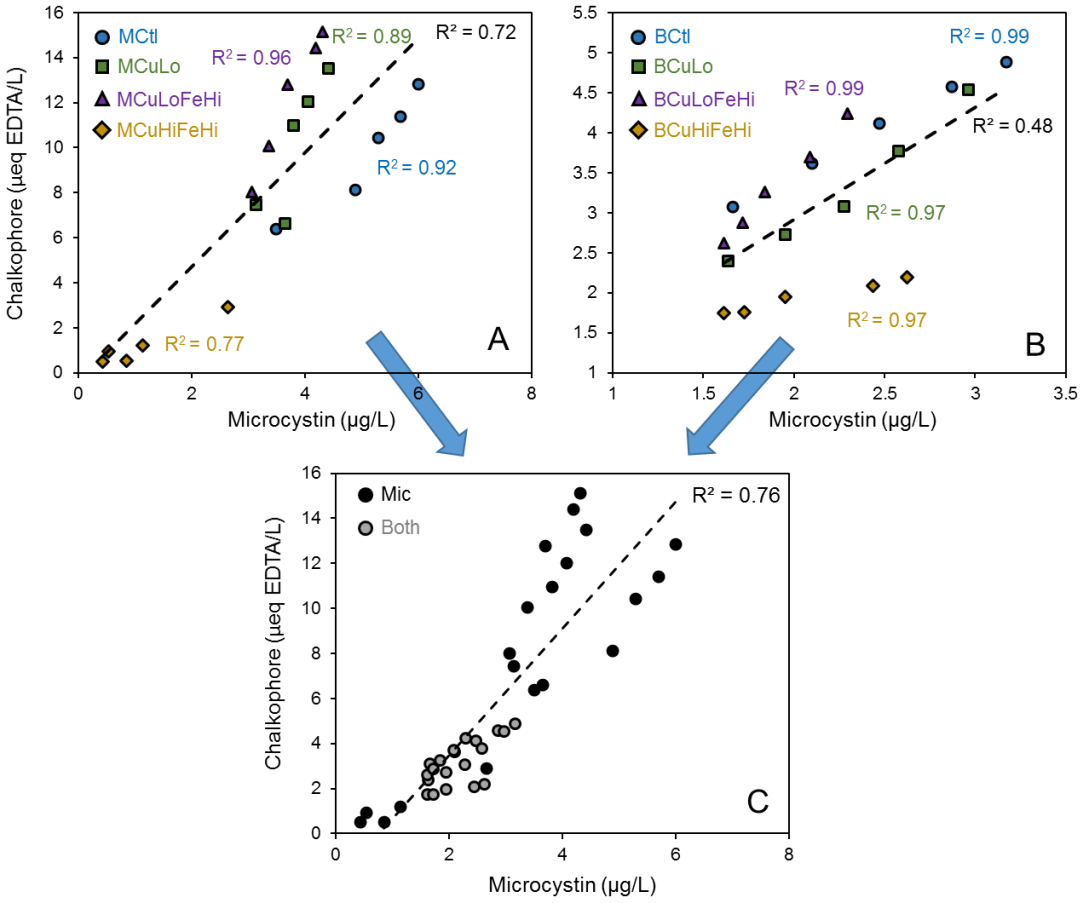

Figure 4-15. Time-lagged cross correlation for chalkophore and microcystin. Results are given for (A) M_{meso}, (B) B_{meso}, and (C) and combining M_{meso} and B_{meso} together. The R^2 value is reported for each amendment in the same color as the corresponding symbol (see legend). The dashed line in each panel indicates the trend line for all the data in the panel, with R^2 given in black.

Combining data from different amendments, the correlation between chalkophore and microcystin is R^2 = 0.72 for M_{meso}, R^2 = 0.48 for B_{meso}, and R^2 = 0.76 for all the data from the two mesocosm types together. The time-lagged cross correlations of chalkophore and microcystin in each amendment were quite strong, ~ 0.9 or above, except for M_{meso} CuHiFeHi. As discussed in Section 4.3, I used two common approaches for interpolation, linear and spline, for upsampling. I find slightly higher correlations using the spline approach (e.g., I

obtain an R^2 = 0.70 with linear interpolation compared to R^2 = 0.72 for spline in Figure 4-15A), consistent with literature commentary on the advantage of spline methods to better reflect "real" results (Bar-Joseph et al., 2003). The important point is that I obtain the same results either way, i.e., any distortions in data that might occur from sample-rate conversion are minor enough as to lead to a consistent conclusion.

Table 4-2. Slopes for optimum time-lagged correlation of chalkophore and microcystin.

Mesocosm	Amendments	Slope	Mesocosm	Amendments	Slope
M_{meso}	Ctl	2.53	B_{meso}	Ctl	1.21
	CuLo	5.42		CuLo	1.63
	CuLoFeHi	5.56		CuLoFeHi	2.32
	CuHiFeHi	1.15		CuHiFeHi	0.44

Aside from the strong correlations, another interesting trend was the progression in the slopes, reported in Table 4-2, where we see that, for slope, CuLoFeHi > CuLo > Ctl > CuHiFeHi for both M_{meso} and B_{meso}. As discussed in Section 4.1, the design of this experiment was, in part, to see if any chalkophore-microcystin link observed is related to Fe limitation. For the slopes of the chalkophore-microcystin correlations reported in Table 4-2, a higher slope reflects a smaller microcystin production for a given increment of chalkophore production (or vice versa). Tukey's HSD was performed to check the differences of those slopes between amendments were significant or not, and the results showed all the slopes are significantly different ($p < 0.05$) for M_{meso} and B_{meso} between amendments, except the differences between M_{meso} CuLo / CuLoFeHi (where slopes differ by only ~3%) and M_{meso} Ctl / CuHiFeHi (though with the slope for M_{meso} Ctl being greater than that of M_{meso} CuHiFeHi by a factor of more

than two, and at $p < 0.26$, it might not be appropriate to term this as an insignificant difference).

That the slope of CuHiFeHi is lowest for both M_{meso} and B_{meos} is because of inhibition of chalkophore production in both cases, as shown in Figure 4-11. For both M_{meso} and B_{meso}, when comparing CuLoFeHi with CuHiFeHi, i.e., the amount of Cu is variable, and much more chalkophore is produced when the amount of Cu is low. When comparing CuLo with CuLoFeHi, where the amount of Fe is variable, the Fe results in a higher chalkophore production per unit microcystin in B_{meso}, albeit the difference is effectively negligible for M_{meso}. Taking further into account the significant slope difference whereby the CuLo is greater than that for the Ctl is suggestive that *Microcystis* increased chalkophore production to capture Cu when the amended Cu is low, but decreased chalkophore production when the amended Cu is too high.

4.7 Discussion of Possible Controls on Biomolecule Production

With respect to chalkophore and siderophore production, the acclimation strategy that I used for this work was not just more stringent with respect to duration and duplicating as much as possible the irradiance and temperature of the field site. Because I used a type of minimal media without Cu or Fe, and I used high purity reagents to make the media, the algae would have been much more Cu and Fe starved at the outset of experiments for this work as compared to the work I report in Chapter 3. Revisiting comments from Chapter 3, under MN-limited conditions, cellular Cu requirements for microalgae may increase up to ten-fold (Quigg, 2008; Schoffman et al., 2016). After being in placed in St 28

water, which did have some Cu and Fe (3 and 128 μg·L^{-1}, respectively), the M_{meso} slope for chalkophore production between t0 and t2 suggests that it began rapidly, consistent with specific production to capture Cu; with low Cu amended, chalkophore production relative to the Ctl decreased, and the striking agreement between M_{meso} CuLo and CuLoFeHi indicates that chalkophore production is not related to Fe. The Pearson's R^2 for chalkophore versus the amount of Cu amended varies from 0.97 to > 0.99 (plotted at t2, t4, or using the extrema in the interval from t2 to t4). For siderophores, there is a direct proportionality between siderophore production and the sum of Cu and Fe amended. Testing all time points for correlation between siderophore and the sum of Cu and Fe amended, the largest Pearson's R^2 are as follows: 0.98 for M_{meso} at t4 (*Microcystis* dominated); 0.93 for M_{meso} at t8 (UG dominated); 0.92 for G_{meso} at t2; and 0.92 for B_{meso} at t2.

Considering these points relating to MN starvation, I reviewed my data for $C^{\mathrm{TCu}}_{\mathrm{algae,\,t0}}$ and $C^{\mathrm{TFe}}_{\mathrm{algae,\,t0}}$ from Chapter 3/2018 as compared to Section 4.5/2019 above. I find that, on average, $C^{\mathrm{TM}}_{\mathrm{algae,\,t0}}$ for all algae in 2018 are ~380% higher than for 2019. For M_{meso} $C^{\mathrm{TFe}}_{\mathrm{algae,\,t0}}$ and G_{meso} $C^{\mathrm{TCu}}_{\mathrm{algae,\,t0}}$ and $C^{\mathrm{TFe}}_{\mathrm{algae,\,t0}}$, the average is 270% with a relatively modest RSD of 22%, whereas, for M_{meso} $C^{\mathrm{TCu}}_{\mathrm{algae,\,t0}}$ was 700% times higher in 2018 than in 2019. The M_{meso} relative Cu starvation is exceptional, i.e., one could say that algae are ~270% more MN starved in 2019 compared to 2018, *except for M_{meso} Cu*, where the differential between G_{meso} Cu / G_{meso} Fe / M_{meso} Fe versus M_{meso} Cu, at 270%, is almost a factor of three, and *Microcystis* Cu-starvation is in turn a factor of 2.6 greater than this 270% average. The relative MN depletion of *Microcystis* itself may be differentially

higher than for green algae. The 2018 ratio of $C^{TCu}_{algae,\ t0}$ in G_{meso} compared to M_{meso} was 1.1, and the corresponding ratio for $C^{TFe}_{algae,\ t0}$ was 1.6, i.e., the Cu content of the *Microcystis* and green algae at t0 were similar in 2018, while the Fe content of green algae was higher, by approximately 60%. In contrast, for 2019, these two ratios for Cu and Fe are, respectively, 3 and 2.5, i.e., as compared to 2018, green algae have 300% more Cu and 250% more Fe than do *Microcystis*. Viewed from this perspective, the initial Cu and Fe status of algae is easily sufficient to explain the differences in trajectories that I observed in 2018 versus 2019. Since both *Microcystis* and the green algae started their acclimation in the same media, this is also an indication of the relatively higher copper needs of *Microcystis.*

Based on literature, and in accord with my results, it seems reasonable that chalkophore and siderophore, while both binding with very high affinity for their respective cognate metals of Cu and Fe, have nonetheless somewhat different purposes. Much has been written concerning how bacteria (including cyanobacteria) navigate the divide between nutrition and toxicity for Cu. In a review by Porcheron et al. (2013), the authors note that bacteria need highly sensitive regulatory factors responding to metal concentration to allow rapid and sufficient metal uptake, ensuring that physiological needs for MNs are met, however, these authors also note a general trend whereby intracellular concentrations of metals (Fe, Cu, zinc, and manganese specifically mentioned) are higher, sometimes much higher than extracellular concentrations. In gram-negative bacteria, including examples of cyanobacteria, Badarau and Dennison (2011) have noted that production of chalkophores is one Cu uptake mechanism, and Andrei et al. (2020) have described toxicity management via Cu-binding,

commenting "*the virtual absence of free Cu in the bacterial cytosol is achieved by Cu-chaperones, Cu-storage proteins and low-molecular weight thiol-containing molecules*". A thermodynamic study of very high affinity (chalkophoric) intracellular cognate binding with Cu for one cyanobacteria demonstrated how it is managed to protect the bacterium from Cu toxicity, while also facilitating rapid and efficient relocation to plastocyanin and cytochrome *c* oxidase as needed (Badarau and Dennison, 2011). The behaviour that I observe for M_{meso} chalkophore in this work is entirely consistent with a process of Cu uptake for Cu-starved cells, and discontinuation of production of Cu uptake/storage biomolecules when there is an excess of Cu.

Comparing chalkophore binding with siderophore, Porcheron et al. (2013) note that bacterial regulators, including the copper-dependent regulator CueR, have very strong binding with Cu, ensuring that all cytoplasmic copper is bound/buffered to achieve very low intracellular concentrations. In contrast, the Fe-uptake regulator Fur binds Fe much less tightly, leaving much more Fe free-ion in the cytoplasm to bind with other weaker metal-binding proteins. They go on to say that the Fur family of regulatory proteins is implicated in the regulation network of several metals (also see details in Kaushik et al., 2016). These points, taken together with reports that siderophores in some instances can also bind Cu strongly (Nicolaisen et al., 2010; Hofmann et al., 2020), cause me to hypothesize that the chalkophores are being produced by *Microcystis* as part of a specific cognate response system, whereas siderophores and different parts of the Fe-regulating cellular machinery are more complex and involve numerous metals besides Fe, and including Cu (Chen et al., 2020).

The production of chalkophore in green algae/G_{meso} is quite different than for M_{meso} and does exhibit differences based on Fe. Overall, results suggest, consistent with literature, that the Cu needs of green algae are less, and are ameliorated by the presence of Fe. I do not have an explanation for why G_{meso} CuHiFeHi chalkophore production is generally higher than for CuLoFeHi, however, this apparent difference may be deceiving since it is not statistically significant. Concerning the effect of Fe on G_{meso} chalkophore production, one recent report found that the green alga *C. reinhardtii* requires Cu for high affinity Fe uptake, and it may be that the high Fe amendments therefore reduce Cu requirements to effect Fe uptake (Herbik et al., 2002).

I find that these very different behaviors of *Microcystis* and green algae with respect to chalkophore and siderophore production are very well reflected by the different trajectories. For green algae, it seems indeed that chalkophore production is an ancillary process, with siderophore production being in all cases more prominent, whereas for *Microcystis*, the response, here and in Chapter 3, is much more consistent with high cellular Cu requirements, and, based on the inter-relationship with siderophore production, there does appear to be an active interplay between Cu and Fe management. While the results here in this chapter concerning the relative timing of chalkophore and siderophore production vary from those in Chapter 3, the dynamics and magnitude of effects are similar, despite the quite different initial Cu and Fe status of algae from those used in the work that I describe here.

Despite a vast amount of research, the ecological function behind production of the cyanobacterial toxin microcystin has not been elucidated (Omidi et al., 2019

and references therein). I did not find a microcystin-siderophore link for work in Chapter 3 or here in this chapter, and, despite speculations of some authors, Klein et al. (2013) demonstrated that microcystin is not a siderophore. In any case, Martin-Luna et al. (2006) one of the most highly cited works on the siderophore-microcystin link, state that evidence concerning the link is "*widely discussed, with contradictory results*".

While microcystin is not a siderophore, it is not a chalkophore either (Humble et al., 1997; Yan et al., 2000). The issue of whether microcystin is a siderophore (or chalkophore) has been raised and is of interest because, if it were, this would serve as an important intracellular detoxification mechanism. In their research on Cd toxicity to *Microcystis*, Huang et al. (2015) recently compared a strain producing microcystin to a microcystin-lacking mutant and demonstrated that microcystin cannot affect metal toxicity either by regulating metal accumulation or by altering the detoxification ability of the cyanobacteria. Wang et al. (2012) found that, microcystin did not affect the bioaccumulation of Cd or Cu exposure in *C. reinhardtii*. Since Cu bears some binding similarities with Cd as divalent metals, and since microcystin does not have a high binding affinity for, e.g., Cd, Cu, Fe (Yan et al., 2000; Pochodylo et al., 2017) means that it is unlikely that microcystin's function is to reduce metal toxicity.

Why microcystin *is* produced is harder to say. There are two ways that I can think of to address this, phenomenological and molecular. Phenomenologically, consistent with Chapter 3, but especially as clearly revealed by the time-lagged cross correlation analysis that I did, microcystin production appears to occur at a point where cells could well be becoming stressed. There are reports that

microcystins affect other species by causing photosynthesis inhibition, growth inhibition, and oxidative stress induction (Legrand et al. 2003, Gantar et al. 2008). Omidi et al. (2018) have summarized microcystin's allelopathic function to other phytoplankton and zooplankton, including growth inhibition for algae including *Chlamydomonas, Haematococcus, Navicula, Cryptomonas,* and other cyanobacteria. At a molecular level, Chen et al. (2020) recently published work showing that microcystin synthesis genes were indirectly activated by Cu via Cu's affecting the expression of the Fur-related genes, i.e., Cu affected the expression of Fur-related genes, genes that directly regulate microcystin synthesis (the latter effect has been discussed by other authors, also see Kaushik et al., 2016). Chen et al. observed that copper stress resulted in increased microcystin production, as I see here, after a lag time. Mathematically speaking, I can say with certainty based on the preliminary results in Chapter 3 and results from more detailed study given in Figure 4-15 that chalkophore is a predictor of microcystin production. In result of the recent work from Chen et al. (2020), I now have some insight as to the causative effects as well. Linking molecular results to ecological meaning will no doubt be an interesting area of future research.

5 Conclusions and Further Work

This chapter revisits and draws together the key findings of Chapters 2 to 4, and additionally, I consider further work in my research area that I believe to hold most promise for the future.

5.1 CONCLUSIONS

Chapter 2: From speciation to toxicity: using a "two-in-one" whole-cell bioreporter approach to assess harmful effects of Cd and Pb

This is the first work to use a lights-on bioreporter combining the study of speciation and toxicity simultaneously and within the BLM framework for risk assessment of hazardous materials. Major findings are as follows:

- No reports have been found for detailing the use of a lights-on bioreporter to measure toxicity; these lights-on reporters have thus far been used for speciation measurement. My results showed that the lights-on bioreporter zntA can also be used to measure toxicity, as benchmarked by an independent toxicity assay, thus providing a "two-in-one" functionality for toxic metal risk assessment work.

- The results reported herein are the first for use of a bioreporter to predicted both speciation and toxicity. The predicted speciation and toxicity for the test metals, Cd and Pb, are well within BLM validation guidelines for agreement between predicted and measured results.
- The FAV WQC represents genera in the lowest rank $P_{5\%}$. In comparison, toxicity endpoints for other Cd and Pb BLMs reported in literature average $P_{71\%}$ and $P_{44\%}$ rank percentile sensitivity (i.e., insensitive) for Cd and Pb, respectively, and in consequence could not be regarded in any context as fit-for-purpose for toxic metal environmental risk assessment according to WQCs based on protection of 95% of aquatic species. Since the LODs of Cd and Pb for zntA are below the relevant Cd and Pb CMCs, zntA is able to measure the speciated values of Cd and Pb that correspond to the toxicity endpoints of the most sensitive half of species (from the CMC WQC to the $P_{50\%}$).
- The results reported for zntA as a "two-in-one" bioreporter for Cd and Pb measurements and BLM predictions are theoretically generalizable to any lights-on bioreporter, substantially broadening the use of other lights-on bioreporters for risk assessment and ecotoxicity studies of other toxic elements and hazardous substances.

Chapter 3: A new perspective of copper-iron effects on bloom-forming algae in a highly impacted environment

The results presented in Chapter 3 show the following with respect to Cu-Fe effects on bloom-forming algae in a highly impacted environment:

- The 50 $\mu g \cdot L^{-1}$ levels of Cu used, with or without Fe, favors changes to green algae as dominant species over *Microcystis* spp. This starkly contrasts previous work in which I participated, wherein 20 $\mu g \cdot L^{-1}$ Cu strongly stimulated growth and affected algal assemblages changes that sometimes favored *Microcystis* spp. Given this narrow concentration difference with two very different outcomes, responsible whole-lake management of algae using Cu is untenable.
- I observe neither dramatic Cu-modulation of Fe demand (for algae that can switch from Fe-based Cyt-c6 to Cu-based plastocyanin in electron transfer), nor evidence of an Fe-protective effect from Cu toxicity, as observed in multiple lab studies, underscoring the desirability of relatively more complex field experimentation.
- I report a first example of coupled chalkophore/siderophore production and using CTA. Using CTA represents an important innovation since chalkophore and siderophore production is not cotemporaneous. My results support a concept-model wherein, for *Microcystis*-dominated mesocosms, siderophore production is differentially increased in the presence of bioaccessible Fe and subsequent chalkophore production is Fe-modulated—lower Fe increases Cu demand/chalkophore production.
- Though reports show that microcystin can function as a siderophore, I find no microcystin-siderophore correlation, however I find that microcystin production is lower with Fe and a hitherto unreported discovery of a microcystin-chalkophore link. Microcystin and chalkophore production both accompany Fe-shortage, indicating response to Fe-limitation.

- Despite rapid diminution of amended bioavailable/TDFe, there are multiple significant differences in individual parameters for Fe that are more pronounced for St 28. PCA also shows that St 28 behavior is differentiable from St 3 and St 13 across all mesocosms that are *Microcystis*-dominated by t6. The explanation that is consistent with other literature reports involves the different bacterial communities known to be in this part of the lake and how these affect 1) Fe status—t0 TDFe in St 28 is half that of the other stations and amended TDFe declines more rapidly than for St 3/St 13, and 2) more intense chalkophore/siderophore CTA trajectories in consequence.

The evidence presented in Chapter 3, implicating variable MN bioavailability and demonstrating coupled chalkophore, siderophore and microcystin production in response to varying MN, is a first step and warrants further research, including expression profiles of genes involved in synthesis of chalkophore, siderophore, and microcystin, and how these are activated in response to environmental conditions.

Chapter 4: Chalkophore is a predictor of microcystin toxin production by harmful cyanobacteria

In Chapter 4, I report my follow-up work to that of Chapter 3 with revised Cu/Fe amendments, an increased level of algal acclimation and more advanced algorithms within the family of techniques used in trajectory analysis. From this work, I draw the following conclusions:

- The effect of Cu/Fe amendments on chalkophore and siderophore production is very different, more so for *Microcystis* where chalkophore

production has a very strong correlation with Cu but not with Fe, while siderophore production for all mesocosms with different algal types all showed strong correlation with the sum of Cu and Fe.

- The exact form of trajectories observed for this work differ from those that I reported in Chapter 3, more so for *Microcystis*, and especially the production of chalkophore is higher here, likely caused by a more intense MN starvation during algal acclimation; however, I again see a very similar dynamical phased behavior between chalkophore/siderophore production that shows significant differences in trajectories according to, and in response to, specific differences in Cu and Fe amendments.
- I again observe a microcystin-chalkophore relationship, for this work being much stronger than that reported in Chapter 3. With the additional data to perform analysis of time-lagged cross correlation, I found even stronger evidence of a microcystin-chalkophore relationship. As the optimum time-lagged cross correlation of microcystin-chalkophore entails a time-lag for microcystin, chalkophore is a predictor of microcystin production.
- Recent molecular biological work (Chen et al., 2020) confirms the activation of microcystin synthesis genes indirectly by Cu via a pathway involving a genetic regulatory pathway primarily known for regulating cellular Fe status, confirming my earlier hypotheses (Zhang et al., 2019) regarding a fundamental Cu-Fe link. Contrary to some published speculation, nothing in my work suggests that microcystin acts as a siderophore (or chalkophore), and other published work that I cite shows that it is neither a siderophore nor a chalkophore. While the ecological

function behind the cyanobacterial production of microcystin has not been elucidated, my results are consistent with published results implicating an allelopathic response from stressed cells.

5.2 Further Work

A future direction for the "two-in-one" approach developed in Chapter 2 would include work with other reporters/toxic analytes, and work to test proof-of-principle calibrating lights-on reporters to chronic toxicity endpoints.

Regarding Chapters 3 and 4, this this is the first work to specifically study chalkophore in a freshwater setting. Using HAB-forming algae, I find interesting results, with a confirmed microcystin-chalkophore link and chalkophore as a predictor of microcystin production. Isolating and structurally characterizing chalkophores produced by *Microcystis* spp. and further studies on genetics of chalkophore production would help to understand more regarding this link and would also hold promise to advance our understanding of the ecological function behind production of the cyanobacterial toxin, microcystin.

6 LITERATURE CITED

Abbas, M., Adil, M., Ehtisham-ul-Haque, S., Munir, B., Yameen, M., Ghaffar, A., Shar, G.A., Tahir, M.A., Iqbal, M., 2018. *Vibrio fischeri* bioluminescence inhibition assay for ecotoxicity assessment: A review. Sci. Total Environ. 626, 1295–1309.

Ahmed, I.A., Hamilton-Taylor, J., Bieroza, M., Zhang, H., Davison,W., 2014. Improving and testing geochemical speciation predictions of metal ions in natural waters. Water Res. 67, 276–291.

Al-Anizi, A.A., Hellyer, M.T., Zhang, D., 2014. Toxicity assessment and modelling of *Moringa oleifera* seeds in water purification by whole cell bioreporter. Water Res. 56, 77–87.

Alboukadel, K., Fabian, M., 2017. Factoextra: extract and visualize the results of multivariate data analyses. R package version 1.0.5. https://CRAN.R-project.org/package=factoextra.

Alengebawy, A., Abdelkhalek, S.T., Qureshi, S.R., Wang, M.Q., 2021. Heavy metals and pesticides toxicity in agricultural soil and plants: Ecological risks and human health implications. Toxics 9, 42.

Alexova, R., Fujii, M., Birch, D., Cheng, J., Waite, T.D., Ferrari, B.C., Neilan, B.A., 2011. Iron uptake and toxin synthesis in the bloom-forming *Microcystis aeruginosa* under iron limitation. Environ. Microbiol. 13, 1064–1077.

Alt, H., Godau, M., 1995. Computing the Fréchet distance between two polygonal curves. Int. J. Comput. Geom. Ap. 5, 75–91.

An, J., Jeong, S., Moon, H.S., Jho, E.H., Nam, K., 2012. Prediction of Cd and Pb toxicity to *Vibrio fischeri* using biotic ligand-based models in soil. J. Hazard. Mater. 203, 69–76.

An, J., Jho, E.H., Nam, K., 2015. Effect of dissolved humic acid on the Pb bioavailability in soil solution and its consequence on ecological risk. J. Hazard. Mater. 286, 236–241.

Andersen, R.A., 2005. Algal Culturing Techniques, first ed. Elsevier/Academic Press, Burlington, Massachusetts.

Andreae, M.O., Asami, T., Bertine, K.K., Buat-Ménard, P.E., Duce, R.A., Filip, Z., Förstner, U., Goldberg, E.D., Heinrichs, H., Jernelöv, A.B., Pacyna, J.M., Thornton, I., Tobschall, H.J., Zoller, W.H., 1984. Changing biogeochemical cycles. In Changing Metal Cycles and Human Health, J.O. Nriagu, ed. Springer, Berlin, Heidelberg.

Andrei, A., Öztürk, Y., Khalfaoui-Hassani, B., Rauch, J., Marckmann, D., Trasnea, P. I., ... & Koch, H.G., 2020. Cu homeostasis in bacteria: The ins and outs. Membranes 10, 242.

APHA, 1995. Standard Methods for the Examination of Water and Wastewater, nineteenth ed. American Public Health Association American Water Works Association Water Environment Federation, Washington, DC.

Badarau, A., Dennison, C., 2011. Thermodynamics of copper and zinc distribution in the cyanobacterium *Synechocystis* PCC 6803. P. Natl. A. Sci. 108, 13007–13012.

Bagherifam, S., Lakzian, A., Fotovat, A., Khorasani, R., Komarneni, S., 2014. *In situ* stabilization of As and Sb with naturally occurring Mn, Al and Fe oxides in a calcareous soil: Bioaccessibility, bioavailability and speciation studies. J. Hazard. Mater. 273, 247–252.

Baptista, M.S., Vasconcelos, V.M., Vasconcelos, M.T.S., 2014. Trace metal concentration in a temperate freshwater reservoir seasonally subjected to blooms of toxin-producing cyanobacteria. Microb. Ecol. 68, 671–678.

Bar-Joseph, Z., Gerber, G.K., Gifford, D.K., Jaakkola, T.S., Simon, I., 2003. Continuous representations of time-series gene expression data. J. Comput. Biol. 10, 341–356.

Batley, G.E., Apte, S.C., Stauber, J.L., 2004. Speciation and bioavailability of trace metals in water: Progress since 1982. Aust. J. Chem. 57, 903–919.

Belkin, S., 2003. Microbial whole-cell sensing systems of environmental pollutants. Curr. Opin. Microbiol. 6, 206–212.

Bertani, G., 2004. Lysogeny at mid-twentieth century: P1, P2, and other experimental systems. J. Bacteriol. 186, 595–600.

Best, J., 2019. Anthropogenic stresses on the world's big rivers. Nature Geosci. 12, 7–21.

Bischof, R., Zedrosser, A., 2009. The educated prey: consequences for exploitation and control. Behav. Ecol. 20, 1228–1235.

Bogomolov, A., 2011. Multivariate process trajectories: capture, resolution and analysis. Chemometr. Intell. Lab. 108, 49–63.

Boyd, P.W., Jickells, T., Law, C.S., Blain, S., Boyle, E.A., Buesseler, K.O., Coale, K.H., Cullen, J.J., de Baar, H.J.W., Follows, M., Harvey, M., Lancelot, C., Levasseur, M., Owens, N.P.J., Pollard, R., Rivkin, R.B., Sarmiento, J., Schoemann, V., Smetacek, V., Takeda, S., Tsuda, A., Turner, S., Waston, A.J., 2007. Mesoscale iron enrichment experiments 1993–2005: Synthesis and future directions. Science 315, 612–617.

Brand, L.E., 1991. Minimum iron requirements of marine phytoplankton and the implications for the biogeochemical control of new production. Limnol. Oceanogr. 36, 1756–1771.

Braud, A., Geoffroy, V., Hoegy, F., Mislin, G.L.A., Schalk, I.J., 2010. Presence of the siderophores pyoverdine and pyochelin in the extracellular medium reduces toxic metal accumulation in *Pseudomonas aeruginosa* and increases bacterial metal tolerance. Environ. Microbiol. Rep. 2, 419–425.

Brauner, N., Shacham, M., 1998. Role of range and precision of the independent variable in regression of data. AIChE J. 44, 603–611.

Bronk, D.A., See, J.H., Bradley, P., Killberg, L., 2007. DON as a source of bioavailable nitrogen for phytoplankton. Biogeosci. 2007, 4, 283–296.

Brooks, B.W., Lazorchak, J.M., Howard, M.D., Johnson, M.V.V., Morton, S.L., Perkins, D.A., Reavie, E.D., Scott, G.I., Smith, S.A., Steevens, J.A., 2016. Are harmful algal blooms becoming the greatest inland water quality threat to public health and aquatic ecosystems? Environ. Toxicol. Chem. 35, 6–13.

Brown, P.L., Markich, S.J., 2000. Evaluation of the free ion activity model of metal organism-interaction: Extension of the conceptual model. Aquat. Toxicol. 51, 177–194.

Buayam, N., Davey, M.P., Smith, A.G., Pumas, C., 2019. Effects of copper and pH on the growth and physiology of *Desmodesmus* sp. AARLG074. Metabolites 9, 84.

Buffi, N., Merulla, D., Beutier, J., Barbaud, F., Beggah, S., van Lintel, H., Renaud, P., van der Meer, J.R., 2011. Development of a microfluidics biosensor for agarose-bead immobilized *Escherichia coli* bioreporter cells for arsenite detection in aqueous samples. Lab Chip 11, 2369–2377.

Butterwick, C., Heaney, S.I., Talling, J.F., 1982. A comparison of eight methods for estimating the biomass and growth of planktonic algae. British Phycol. J. 17, 69–79.

Campbell, P.G.C., 1995. In Metal speciation and bioavailability in aquatic systems. Tessier. A and Turner, D.R, eds. John Wiley, New York.

Ceballos-Laita, L., Marcuello, C., Lostao, A., Calvo-Begueria, L., Velazquez-Campoy, A., Bes, M.T., Peleato, M.L., 2017. Microcystin-LR binds iron, and iron promotes self-assembly. Environ. Sci. Technol. 51, 4841–4850.

CERCLA (Comprehensive Environmental Response Compensation and Liability Act), 2005. Top 20 Hazardous Substances. CERCLA 275. https://www.fixr.com/info/toxic_substances.html.

Chakraborty, P., Babu, P.V.R., Acharyya, T., Bandyopadhyay, D., 2010. Stress and toxicity of biologically important transition metals (Co, Ni, Cu and Zn) on phytoplankton in a tropical freshwater system: An investigation with pigment analysis by HPLC. Chemosphere 80, 548–553.

Chang, X., Eigemann, F., Hilt, S., 2012. Do macrophytes support harmful cyanobacteria? Interactions with a green alga reverse the inhibiting effects of macrophyte allelochemicals on *Microcystis aeruginosa*. Harmful Algae 19, 76–84.

Chen, W., Song, L., Peng, L., Wan, N., Zhang, X., Gan, N., 2008. Reduction in microcystin concentrations in large and shallow lakes: Water and sediment-interface contributions. Water Res. 42, 763–773.

Chen, Y., Yin, J., Wei, J., Zhang, X.,2020. FurA-dependent microcystin synthesis under copper stress in *Microcystis aeruginosa*. Microorganisms 8, 832.

Chen, Z., Song, S., Wen, Y., Zou, Y., Liu, H., 2016. Toxicity of Cu (II) to the green alga *Chlorella vulgaris*: a perspective of photosynthesis and oxidant stress. Environ. Sci. and Pollut. Res. 23, 17910–17918.

Cheng, S., 2003. Heavy metal pollution in China: Origin, pattern and control. Environ. Sci. Pollut. Res. 10, 192–198.

Cleasby, I.R., Wakefield, E.D., Morrissey, B.J., Bodey, T.W., Votier, S.C., Bearhop, S., Hamer, K.C., 2019. Using time-series similarity measures to compare

animal movement trajectories in ecology. Behav. Ecol. Sociobiol. 73, 1–19.

Coles, C.A., Yong, R.N., 2006. Humic acid preparation, properties and interactions with metals lead and cadmium. Eng. Geol. 85, 26–32.

Crémazy, A., Wood, C.M., Smith, D.S., Ferreira, M.S., Johannsson, O.E., Giacomin, M., Val, A.L., 2016. Investigating copper toxicity in the tropical fish cardinal tetra (*Paracheirodon axelrodi*) in natural Amazonian waters: Measurements, modeling, and reality. Aquat. Toxicol. 180, 353–363.

Curran-Everett, D., 2013. Explorations in statistics: The analysis of ratios and normalized data. Adv. Physiol. Educ. 37, 213–219.

De Cáceres, M., Font, X., Oliva, F., 2010. The management of vegetation classifications with fuzzy clustering. J. Veg. Sci. 21, 1138–1151.

De Cáceres, M., Coll, L., Legendre, P., Allen, R.B., Wiser, S.K., Fortin, M.-J., Condit, R., Hubbell, S., 2019. Trajectory analysis in community ecology. Ecol. Monogr. 89:e01350.

de Leeuw, J., Mair, P., 2009. Multidimensional scaling using majorization: SMACOF in R. J. Stat. Softw. 31, 1–30.

de Schamphelaere, K.A.C., Janssen, C.R., 2002. A biotic ligand model predicting copper toxicity for *Daphnia magna*: The effects of calcium, magnesium, sodium, potassium, and pH. Environ. Sci. Technol. 36, 48–54.

de Schamphelaere, K.A.C., Nys, C., Janssen, C.R., 2014. Toxicity of lead (Pb) to freshwater green algae development and validation of a bioavailability model and inter-species sensitivity comparison. Aquat. Toxicol. 155, 348–359.

Di Toro, D.M., Allen, H.E., Bergman, H.L., Meyer, J.S., Paquin, P.R., Santore, R.C., 2001. Biotic ligand model of the acute toxicity of metals. 1. Technical basis. Environ. Toxicol. Chem. 20, 2383–2396.

Dong, J., Li, C., Chang, M., Dai, D., Liu, S., Quan, B., Gao, Y., 2019. Effects of toxic cyanobacterium *Microcystis aeruginosa* on the morphology of green alga *Chlorella vulgaris*. Ann. Limnol. - Int. J. Lim. 55, 7.

Ebina, J., Tsutsui, T., Shirai, T., 1983. Simultaneous determination of total nitrogen and total phosphorus in water using peroxodisulfate oxidation. Water Res. 17, 1721–1726.

EC (European Commission), 2010. Nickel and Its Compounds. Environmental Quality Standards Sheet. Danish Environmental Protection Agency, Copenhagen, Denmark.

EC (European Commission), 2013. Directive 2013/39/EC Amending Directives 2000/60/EC and 2008/105/EC as Regards Priority Substances in the Field of Water Policy. 2013/39/EC, European Commission, Brussels.

Elser, J.J., Bracken, M.E.S., Cleland, E.E., Gruner, D.S., Harpole, W.S., Hillebrand, H., Ngai, J.T., Seabloom, E.W., Shurin, J.B., Smith J.E., 2007. Global analysis of nitrogen and phosphorus limitation of primary producers in freshwater, marine and terrestrial ecosystems. Ecol. Lett. 10, 1135–1142.

Facey, J.A., Apte, S.C., Mitrovic, S.M., 2019. A review of the effect of trace metals on freshwater cyanobacterial growth and toxin production. Toxins 11, 643.

Fairbrother, A., Wenstel, R., Sappington, K., Wood, W., 2007. Framework for metals risk assessment. Ecotox. Environ Safe. 68, 145–227.

Fan, X., Ding, S., Gong, M., Chen, M., Gao, S., Jin, Z., Tsang, D.C.W., 2018. Different influences of bacterial communities on Fe (III) reduction and phosphorus availability in sediments of the cyanobacteria- and macrophyte-dominated zones. Front. Microbiol. 9, 2636.

Fang, F., Gao, Y., Gan, L., He, X., Yang, L., 2018. Effects of different initial pH and irradiance levels on cyanobacterial colonies from Lake Taihu, China. J. Appl. Phycol. 30, 1–17.

Fedra, K., 1983. Environmental modeling under uncertainty: Monte Carlo simulation. In IIASA Research Report, 86: International Institute for Applied Systems Analysis, Laxenburg, Austria.

Feng, J., Gao, Y., Chen, M., Xu, X., Huang, M., Yang, T., Chen, N., Zhu, L., 2018. Predicting cadmium and lead toxicities in zebrafish (*Danio rerio*) larvae by using a toxicokinetic–toxicodynamic model that considers the effects of cations. Sci. Total Environ. 625, 1584–1595.

Fernando, P.S., Miriam, R.P., 2021. Clustering time series data with tscR: a R package to cluster time series data, base on slope and Fréchet distance. https://bioconductor.org/packages/devel/bioc/vignettes/tscR/inst/doc/tscR.html.

Finzi, A.C., Cole, J.J., Doney, S.C., Holland, E.A., Jackson, R.B., 2011. Research frontiers in the analysis of coupled biogeochemical cycles. Front. Ecol. Environ. 9, 74–80.

Florence, T.M., 1986. Electrochemical approaches to trace element speciation in waters. A review. Analyst, 111, 489–505.

Francois, K., Devlieghere, F., Standaert, A.R., Geeraerd, A.H., Cools, I., Van Impe, J.F., Debevere, J., 2005. Environmental factors influencing the relationship between optical density and cell count for *Listeria monocytogenes*. J. Appl. Microbiol. 99, 1503–1515.

Fujii, M., Dang, T.C., Bligh, M.W., Waite, T.D., 2016. Cellular characteristics and growth behavior of iron-limited *Microcystis aeruginosa* in nutrient-depleted and nutrient-replete chemostat systems. Limnol. Oceanogr. 61, 2151–2164.

Gantar, M., Berry, J.P., Thomas, S., Wang, M., Perez, R., Rein, K.S., 2008. Allelopathic activity among cyanobacteria and microalgae isolated from Florida freshwater habitats. FEMS Microbiol. Ecol. 64, 55–64.

Gao, Y., Feng, J., Zhu, J., Zhu, L., 2020. Predicting copper toxicity in zebrafish larvae under complex water chemistry conditions by using a toxicokinetic–toxicodynamic model. J. Hazard. Mater. 400, 123205.

Ghadouani, A., Ralph, E.H.S., 2005. Phytoplankton distribution in Lake Erie as assessed by a new *in situ* spectrofluorometric technique. J. Great Lakes Res. 31, 0–167.

Girotti, S., Ferri, E.N., Fumo, M.G., Maiolini, E., 2008. Monitoring of environmental pollutants by bioluminescent bacteria. Anal. Chim. Acta 608, 2–29.

Gleason, J.R., 1999. An accurate, non-iterative approximation for studentized range quantiles. Comput. Stat. Data An. 31, 147–158.

Gobler, C.J., Burkholder, J.M., Davis, T.W., Harke, M.J., Johengen, T., Stow, C.A., Van de Waal, D.B., 2016. The dual role of nitrogen supply in controlling the growth and toxicity of cyanobacterial blooms. Harmful Algae 54, 87–97.

Goedhart, J., 2019. PlotTwist–a web app for plotting and annotating time-series data. bioRxiv, 745612.

Gong, B., He, E., Romero-Freire, A., Ruan, J., Yang, W., Zhang, P., Qiu, H., 2021. Do essential elements (P and Fe) have mitigation roles in the toxicity of individual and binary mixture of yttrium and cerium to *Triticum aestivum*? J. Hazard. Mater. 416, 125761.

Gottesfeld, P., Cherry, C.R., 2011. Lead emissions from solar photovoltaic energy systems in China and India. Energ. Policy 39, 4939–4946.

Grandjean, P., 2010. Even low-dose lead exposure is hazardous. Lancet 376, 855–856.

Grandjean, P., Landrigan, P.J., 2014. Neurobehavioural effects of developmental toxicity. Lancet Neurol. 13, 330–338.

Grandjean, P., Bellange, M., 2017. Calculation of the disease burden associated with environmental chemical exposures: Application of toxicological information in health economic estimation. Environ. Health. 16, 1–13.

Griffiths, M.J., Garcin, C., van Hille, R.P., Harrison, S.T., 2011. Interference by pigment in the estimation of microalgal biomass concentration by optical density. J. Microbiol. Meth. 85, 119–123.

Gustafsson, J.P., 2014. Visual MINTEQ 3.0 user guide. August 2014. pp 73 (vminteq.lwr.kth.se).

Hadjoudja, S., Deluchat, V., Baudu, M., 2010. Cell surface characterisation of *Microcystis aeruginosa* and *Chlorella vulgaris*. J. Colloid. Interf. Sci. 342, 293–299.

Hansen, M.G., Marcussen, H., Holm, P.E., Brandt, K.K., 2019. Evaluation of pH-dependent metal speciation artifacts in whole-cell bioreporter analysis. J. Environ. Qual. 48, 199–204.

Hanson, M.A., Herwig, B.R., Zimmer, K.D., Hansel-Welch, N., 2017. Rehabilitation of shallow lakes: Time to adjust expectations? Hydrobiologia 787, 45–59.

Harms, H.; Wells, M.; van der Meer, J.R., 2006. Whole-cell living biosensors – are they ready for environmental application? Appl. Microbiol. Biotech. 70, 273–280.

Hasenbrink, G., Schwarzer, S., Kolacna, L., Ludwig, J., Sychrova, H., Lichtenberg-Fraté, H., 2005. Analysis of the mKir2.1 channel activity in potassium influx defective *Saccharomyces cerevisiae* strains determined as changes in growth characteristics. FEBS. Lett. 579, 1723–1731.

Heisler, J., Glibert, P.M., Burkholder, J.M., Anderson, D.M., Cochlan, W., Dennison, W.C., Dortch, Q., Gobler, C.J., Heil, C.A., Humphries, E., 2008.

Eutrophication and harmful algal blooms: A scientific consensus. Harmful Algae 8, 3–13.

Hem, J.D., Skougstad, M.W., 1960. Coprecipitation effects in solutions containing ferrous, ferric, and cupric ions. Article 1459 – In Chemistry of Iron in Natural Water. US Geological Survey Water Supply Paper – 1459, US Government Printing Office, Washington DC.

Hem, J.D., Cropper, W.H., 1962. Survey of ferrous-ferric chemical equilibria and redox potentials, Article 1459 – A. In Chemistry of Iron in Natural Water. US Geological Survey Water Supply Paper – 1459, US Government Printing Office, Washington DC.

Herbik, A., Bölling, C., Buckhout, T.J., 2002. The involvement of a multicopper oxidase in iron uptake by the green algae *Chlamydomonas reinhardtii*. Plant Physiol. 130, 2039–2048.

Ho, T.-Y., Quigg, A., Finkel, Z.V., Milligan, A.J., Wyman, K., Falkowski, P.G., Morel, F.M.M., 2003. The elemental composition of some marine phytoplankton. J. Phycol. 39, 1145–1159.

Hofmann, M., Retamal-Morales, G., Tischler, D., 2020. Metal binding ability of microbial natural metal chelators and potential applications. Nat. Prod. Rep. 37, 1262–1283.

Holden, V.I., Bachman, M.A., 2015. Diverging roles of bacterial siderophores during infection. Metallomics 7, 986–995.

Hornung, R.W., Reed, L.D., 1990. Estimation of average concentration in the presence of nondetectable values. Appl. Occup. Environ. Hyg. 5, 46–51.

Hu, B., Shao, S., Ni, H., Fu, Z., Hu, L., Zhou, Y., Min, X., She, S., Chen S., Huang, M., Zhou, L., Li, Y., Shi, Z., 2020. Current status, spatial features, health risks, and potential driving factors of soil heavy metal pollution in China at province level. Environ. Pollut. 266, 114961.

Huang, B., Xu, S., Miao, A.J., Xiao, L., Yang, L.Y., 2015. Cadmium toxicity to *Microcystis aeruginosa* PCC 7806 and its microcystin-lacking mutant. PLoS One 10, e0116659.

Humble, A.V., Gadd, G.M., Codd, G.A., 1997. Binding of copper and zinc to three cyanobacterial microcystins quantified by differential pulse polarography. Water Res. 31, 1679–1686.

Hynninen, A., Virta, M., 2009. Whole-cell bioreporters for the detection of bioavailable metals. In Whole Cell Sensing System II, Belkin, S., Gu, M.B., eds. Springer, Berlin.

Ignatiades, L., Vassiliou, A., Karydis, M., 1985. A comparison of phytoplankton biomass parameters and their interrelation with nutrients in Saronicos Gulf (Greece). Hydrobiologia 128, 201–206.

ISO, 1992. Water quality – Measurement of biochemical parameters – Spectrometric determination of the chlorophyll-a concentration. International Organisation for Standardization, Geneva. ISO10260:1992(E).

Jančula, D., Maršálek, B., 2011. Critical review of actually available chemical compounds for prevention and management of cyanobacterial blooms. Chemosphere 85, 1415–1422.

Jiang, B., Song, Y., Liu, Z., Huang, W.E., Li, G., Deng, S., Xing, Y., Zhang, D., 2021. Whole-cell bioreporters for evaluating petroleum hydrocarbon contamination. Crit. Rev. Env. Sci. Tec. 51, 272–322.

Jiang, M., Xu, Y., Zhu, B., 2008. Protein structure–structure alignment with discrete Fréchet distance. J. Bioinf. Comput. B. 6, 51–64.

Jiménez, A., Hernández, A., Prieto, M., 2019. Crystallization behaviour of iron-hydroxide sulphates by aging under ambient temperature conditions. Miner. 9, 27.

Jones, M.J., Hart, B.T., 1989. Copper complexing capacity in fresh-waters using the catechol-cathodic stripping voltammetric method. Chem. Spec. Bioavailab. 1, 59–63.

Jones, R.P., Bednar, A.J., Inouye, L.S., 2009. Subcellular compartmentalization of lead in the earthworm, *Eisenia fetida*: Relationship to survival and reproduction. Ecotox. Environ. Safe. 72, 1045–1052.

Kan, H., 2009. Environment and health in China: Challenges and opportunities. Environ. Health Persp. 117, 12.

Karline, S., 2017. Plot3D: Plotting multi-dimensional data. R package version 1.1.1. https://CRAN.R-project.org/package=plot3D.

Kassidas, A., MacGregor, J.F., Taylor, P.A., 1998. Synchronization of batch trajectories using dynamic time warping. AICHE J. 44, 864–875.

Kauffer, F.A., Merlin, C., Balan, L., Schneider, R., 2014. Incidence of the core composition on the stability, the ROS production and the toxicity of CdSe quantum dots. J. Hazard. Mater. 268, 246–255.

Kaushal, S.S., McDowell, W.H., Wollheim, W.M., 2014. Tracking evolution of urban biogeochemical cycles: Past, present, and future. Biogeochemistry 121, 1–21.

Kaushik, M.S., Singh, P., Tiwari, B., Mishra, A.K., 2016. Ferric Uptake Regulator (FUR) protein: properties and implications in cyanobacteria. Ann. Microbiol. 66, 61–75.

Kessler, N., Schauer, J.J., Yagur-Kroll, S., Melamed, S., Tirosh, O., Belkin, S., Erel, Y., 2012. A bacterial bioreporter panel to assay the cytotoxicity of atmospheric particulate matter. Atmos. Environ. 63, 94–101.

Kevin, T., 2015. SimilarityMeasures: Trajectory Similarity Measures. R package version 1.4. https://CRAN.R-project.org/package=SimilarityMeasures.

Khan, A.M., Bakar, N.K.A., Bakar, A.F.A., Ashraf, M.A., 2017. Chemical speciation and bioavailability of rare earth elements (REEs) in the ecosystem: A review. Environ. Sci. Pollut. Res. 24, 22764–22789.

Khan, S., Naushad, M., Lima, E.C., Zhang, S., Shaheen, S.M., Rinklebe, J., 2021. Global soil pollution by toxic elements: Current status and future perspectives on the risk assessment and remediation strategies–A review. J. Hazard. Mater. 417, 126039.

Kilham, S.S., Kreeger, D.A., Lynn, S.G., Goulden, C.E., Herrera, L., 1998. COMBO: A defined freshwater culture medium for algae and zooplankton. Hydrobiologia 377, 147–159.

Kim, Y.Y., Yang, Y.Y., Lee, Y., 2002. Pb and Cd uptake in rice roots. Physiol. Plantarum 116, 368–372.

King, D.L., 1970. Role of carbon in eutrophication. Water Pollut. Control Fed. 42, 2035–2051.

Klein, A.R., Baldwin, D.S., Silvester, E., 2013. Proton and iron binding by the cyanobacterial toxin microcystin-LR. Environ. Sci. Tech. 47, 5178–5184. Environ. 139476.

Kochoni, E., Fortin, C., 2019. Iron modulation of copper uptake and toxicity in a green alga (*Chlamydomonas reinhardtii*). Environ Sci. Technol. 53, 6539–6545.

Ku, H.H., 1966. Notes on the use of propagation of error formulas. J. Res. Natl. Bur. Stand. 70, 263–273.

Kumar, V., Sharma, A., Kaur, P., Sidhu, G.P.S., Bali, A.S., Bhardwaj, R., Thukral, A.K., Cerda, A., 2019. Pollution assessment of heavy metals in soils of India and ecological risk assessment: A state-of-the-art. Chemosphere 216, 449–462.

Küpper, H., Šetlík, I., Šetliková, E., Ferimazova, N., Spiller, M., Küpper, F.C., 2003. Copper-induced inhibition of photosynthesis: limiting steps of in vivo copper chlorophyll formation in *Scenedesmus quadricauda*. Funct. Plant Biol. 30, 1187–1196.

Kushkevych, I.V., Beno, Y.J., 2013. Cluster and cross-correlation analysis of some physiological parameters by various *Desulfovibrio* sp. and *Desulfomicrobium* sp. bacterial strains of the human intestine. SOJ Microbiol. Inf. Dis, 1, 1–9.

Lane, D. M., 2010. Tukey's honestly significant difference (HSD). In Encyclopedia of Research Design, Thousand Oaks, N. J. Elkind., ed. Sage Publications.

Lane, D. M., 2015. Online Statbook. http://onlinestatbook.com/2/calculators/studentized_range_dist.html.

Legrand, C., Rengefors, K., Fistarol, G.O., Graneli, E., 2003. Allelopathy in phytoplankton-biochemical, ecological and evolutionary aspects. Phycologia 42, 406–419.

Lévêque, C., 2001. Lake and pond ecosystems. Enc. Biodivers. 3, 633–644.

Li, B., Zhang, X., Deng, J., Cheng, Y., Chen, Z., Qin, B., Tefsen, B., Wells, M., 2021. A new perspective of copper-iron effects on bloom-forming algae in a highly impacted environment. Water Res. 195, 116889.

Li, C., Zheng, C., Fu, H., Zhai, S., Hu, F., Naveed, S., Zhang, C., Ge, Y., 2021. Contrasting detoxification mechanisms of *Chlamydomonas reinhardtii* under Cd and Pb stress. Chemosphere 274, 129771.

Li, L.Z., Zhou, D.M., Luo, X.S., Wang, P., Wang, Q.Y., 2008. Effect of major cations and pH on the acute toxicity of cadmium to the earthworm *Eisenia fetida* Implications for the biotic ligand model approach. Arch. Environ. Con. Tox. 55, 70–77.

Li, L., Zhou, D.M, Wang, P., Peijnenburg, W.J.G.M., 2009. Kinetics of cadmium uptake and subcellular partitioning in the earthworm *Eisenia fetida* exposed to cadmium-contaminated soil. Arch. Environ. Con. Tox. 57, 718–724.

Li, W.K.W., Dickie, P.M., 2001. Monitoring phytoplankton, bacterioplankton and virioplankton in a coastal inlet (Bedford Basin) by flow cytometry, Cytometry, 44, 236–246.

Lis, H., Shaked, Y., Kranzler, C., Keren, N., Morel, F.M., 2015. Iron bioavailability to phytoplankton: an empirical approach. J. ISME, 9, 1003–1013.

Liu, H.J., Zhang, J.L., Zhang, F.S., 2007. Role of iron plaque in Cd uptake by and translation within rice (*Oryza sativa* L.) seedlings grown in solution culture. Environ. Exp. Bot. 59, 314–320.

Lombardi, A.T., Hidalgo, T.M.D.R., Vieira, A.A.H., Sartori, A.L., 2007. Toxicity of ionic copper to the freshwater microalga *Scenedesmus acuminatus* (*Chlorophyceae*, *Chlorococcales*). Phycologia, 46, 74–78.

Lucius, N., Rose, K., Osborn, C., Sweeney, M.E., Chesak, R., Beslow, S., Schenk, T., 2019. Predicting *E. coli* concentrations using limited qPCR deployments at Chicago beaches. Water Res. X 2, 100016.

Lukač, M., Aegerter, R., 1993. Influence of trace metals on growth and toxin production of *Microcystis aeruginosa*. Toxicon 31, 293–305.

Machado, M.D., Soares, E.V., Soares, H.M., 2010. Removal of heavy metals using a brewer's yeast strain of *Saccharomyces cerevisiae*: Chemical speciation as a tool in the prediction and improving of treatment efficiency of real electroplating effluents. J. Hazard. Mater. 180, 347–353.

Magrisso, S., Erel, Y., Belkin, S., 2008. Microbial reporters of metal bioavailability. Microb. Biotechnol. 1, 320–330.

Magrisso, S., Belkin, S., Erel, Y., 2009. Lead bioavailability in soil and soil components. Water Air & Soil Pollut. 202, 315–323.

Maier, K.J., Knight, A.W., 1994. Ecotoxicology of selenium in freshwater systems. In Reviews of Environmental Contamination and Toxicology. Ware, G.W., ed. Springer, New York, NY.

Majkut, L., 2012. Quantitative analysis of phase trajectory as the information about technical condition of the object. Acta Physiol. Pol. 121, A168.

Maldonado, M.T., Strzepek, R.F., Sander, S., Boyd, P.W., 2005. Acquisition of iron bound to strong organic complexes, with different Fe binding groups and photochemical reactivities, by plankton communities in Fe-limited subantarctic waters. Global Biogeochem. Cy. 19, GB4S23.

Marie, D., Rigaut-Jalabert, F., Vaulot, D., 2014. An improved protocol for flow cytometry analysis of phytoplankton cultures and natural samples. Cytom. Part A 85A, 962–968.

Martin-Luna, B., Hernandez, J.A., Bes, M.T., Fillat, M.F., Peleato, M.L., 2006. Identification of a ferric uptake regulator from *Microcystis aeruginosa* PCC7806. FEMS Microbial. Lett. 254, 63–70.

Marx, S.K., Rashid, S., Stromsoe, N., 2016. Global-scale patterns in anthropogenic Pb contamination reconstructed from natural archives. Environ. Pollut. 213, 283–298.

Matthews, J., Altman, D.G., Campbell, M.J., Royston, P., 1990. Analysis of serial measurements in medical research. Brit. Med. J. 300, 230–235.

Max, K., 2021. caret: Classification and Regression Training. R package version

6.0-90. https://CRAN.R-project.org/package=caret.

McCune, B., Grace, J.B., 2002. Analysis of Ecological Communities. MJM Software Design, Gleneden Beach, Oregon, USA.

McGuire, S., 2016. World Cancer Report 2014. In World Health Organization, International Agency for Research on Cancer. Stewart, B.W., Wild, C.P., eds. WHO Press, 2015, Geneva, Switzerland.

McKnight, D.M., Morel, F.M.M., 1980. Copper complexation by siderophores from filamentous blue-green algae. Limnol. Oceanogr. 25, 62–71.

Mergeay, M., Nies, D., Schlegel, H.G., Gerits, J., Charles, P., Van, G.F., 1985. *Alcaligenes eutrophus* CH34 is a facultative chemolithotroph with plasmid-bound resistance to heavy metals. J. Bacteriol. 162, 328–334.

MHPRC, 2016a. Water Quality: Determination of Water Inorganic Anions (F^-, Cl^-, NO_2^-, Br^-, NO^{3-} , PO_4^{3-}, SO_3^{2-}, SO_4^{2-})—Ion Chromatography (HJ-4-2016). Ministry of Health of the People's Republic of China, Beijing.

MHPRC, 2016b. Water Quality: Determination of Water Soluble Cations (Li^+, Na^+, NH_4^+, K^+, Ca^{2+}, Mg^{2+})—Ion Chromatography (HJ812-2016). Ministry of Health of the People's Republic of China, Beijing.

Molot, L.A., Li, G., Findlay, D.L., Watson, S.B., 2010. Iron-mediated suppression of bloom-forming cyanobacteria by oxine in a eutrophic lake. Freshwater Biol. 55, 1102–1117.

Mostofa, K.M.G., Liu, C.Q., Feng, X., Yoshioka, T., Vione, D., Pan, X., Wu, F., 2013. Complexation of Dissolved Organic Matter with Trace Metal Ions in

Natural Waters. In Photobiogeochemistry of Organic Matter. Mostofa, K.M.G.,Yoshioka, T., Mottaleb, A., Vione, D., eds. , Springer, Berlin.

Morel, F.M.M., 1983. Principles of Aquatic Chemistry. John Wiley, New York.

Mudd, G.M., 2013. The limits to growth and 'finite' mineral resources: Re-visiting the assumptions and drinking from that half-capacity glass. Int. J. Sust. Dev. 16, 204–220.

Mushtaq, N., Singh, D.V., Bhat, R.A., Dervash, M.A., Bin Hameed, O., 2020. Freshwater contamination: Sources and hazards to aquatic biota. In Fresh Water Pollution Dynamics and Remediation, Bhat, H.Q.R.A., Mehmood, M.A., Dar, G.H., eds. Springer, Singapore.

Mustoe, G.E., 2018. Biogenic weathering: Solubilization of iron from minerals by epilithic freshwater algae and cyanobacteria. Microorganisms 6, 8.

Nagai, T., Imai, A., Matsushige, K., Yokoi, K., Fukushima, T., 2007. Dissolved iron and its speciation in a shallow eutrophic lake and its inflowing rivers. Water Res. 41, 775–784.

Nair, A., Juwarkar, A.A., Singh, S.K., 2007. Production and characterization of siderophores and its application in arsenic removal from contaminated soil. Water Air Soil Poll. 180, 199–212.

Narang, B.J., Atkinson, G., Gonzalez, J.T., Betts, J.A., 2020. A tool to explore discrete-time data: The time series response analyser. Int. J. Sport Nutr. Exe. 1, 1–8.

Nault, M.E., Netherland, M.D., Mikulyuk, A., Skogerboe, J.G., Asplund, T., Hauxwell, J., Toshner, P., 2014. Efficacy, selectivity, and herbicide concentrations

following a whole-lake 2,4-D application targeting Eurasian watermilfoil in two adjacent northern Wisconsin lakes. Lake Reserv. Manage. 30, 1–10.

Nicolaisen, K., Hahn, A., Valdebenito, M., Moslavac, S., Samborski, A., Maldener, I., Wilken, C., Valladares, A., Flores, E., Hantke, K., Schleiff, E., 2010. The interplay between siderophore secretion and coupled iron and copper transport in the heterocyst-forming cyanobacterium *Anabaena* sp. PCC 7120. BBA Biomembr. 1798, 2131–2140.

Niyogi, S., Wood, C.M., 2004. Biotic ligand model, a flexible tool for developing site-specific water quality guidelines for metals. Environ. Sci. Technol. 38, 6177–6192.

Nordgård, O., Kvaløy, J.T., Farmen, R.K., Heikkilä, R., 2006. Error propagation in relative real-time reverse transcription polymerase chain reaction quantification models: the balance between accuracy and precision. Anal. Biochem. 356, 182–193.

NTP (National Toxicology Program), 2016. Report on Carcinogens, Fourteenth Edition (https://ntp.niehs.nih.gov/go/roc14). U.S. Department of Health and Human Services, Public Health Service, Research Triangle Park, NC.

Nor, Y.M., Cheng, H.H., 1986. Chemical speciation and bioavailability of copper: Uptake and accumulation by *Eichornia*. Environ. Toxicol. Chem. 5, 941–947.

Oldani, M., Fabbri, M., Melchioretto, P., Callegaro, G., Fusi, P., Gribaldo, L., Forcella, M., Urani, C., 2020. *In vitro* and bioinformatics mechanistic-

based approach for cadmium carcinogenicity understanding. Toxicol. in Vitro. 65, 104757.

Omidi, A., Esterhuizen-Londt, M., Pflugmacher, S., 2018. Still challenging: The ecological function of the cyanobacterial toxin microcystin—What we know so far. Toxin Rev. 37, 87–105.

Omidi, A., Esterhuizen-Londt, M., Pflugmacher, S., 2019. *Desmodesmus subspicatus* co-cultured with microcystin producing (PCC 7806) and the non-producing (PCC 7005) strains of *Microcystis aeruginosa*. Ecotoxicology 28**,** 834–842.

O'Neil, J.M., Davis, T.W., Burford, M.A., Gobler, C.J., 2012. The rise of harmful cyanobacteria blooms: The potential roles of eutrophication and climate change. Harmful Algae 14, 313–334.

Oppenheim, A.V., Schafer, R.W., Buck, J.R., 1999. In Discrete-time signal processing. Horton, M, eds. Prentice Hall, New Jersey.

Outridge, P.M., Noller, B.N., 1991. Accumulation of toxic trace elements by freshwater vascular plants. In Reviews of Environmental Contamination and Toxicology. Ware, G.W., ed. Springer, New York, NY.

Paerl, H.W., 2018. Mitigating toxic planktonic cyanobacterial blooms in aquatic ecosystems facing increasing anthropogenic and climatic pressures. Toxins 10, 76.

Paerl, H.W., Xu, H., McCarthy, M.J., Zhu, G., Qin, B., Li, Y., Gardner, W.S., 2011. Controlling harmful cyanobacterial blooms in a hyper-eutrophic lake

(Lake Taihu, China): The need for a dual nutrient (N & P) management strategy. Water Res. 45, 1973–1983.

Paerl, H.W., Xu, H., Hall, N.S., Rossignol, K.L., Joyner, A.R., Zhu, G., Qin, B., 2015. Nutrient limitation dynamics examined on a multi-annual scale in Lake Taihu, China: Implications for controlling eutrophication and harmful algal blooms. J. Freshwater Ecol. 30, 5–24.

Paerl, H.W., Scott, J.T., McCarthy, M.J., Newell, S.E., Gardner, W.S., Havens, K.E., Wurtsbaugh, W.A., 2016. It takes two to tango: When and where dual nutrient (N & P) reductions are needed to protect lakes and downstream ecosystems. Environ. Sci. Technol. 50, 10805–10813.

Plaza, C., Brunetti, G., Senesi, N., Polo, A., 2006. Molecular and quantitative analysis of metal ion binding to humic acids from sewage sludge and sludge-amended soils by fluorescence spectroscopy. Environ. Sci. Technol. 40, 917–923.

Pochodylo, A.L., Klein, A.R., Aristilde, L., 2017. Metal-binding selectivity and coordination dynamics for cyanobacterial microcystins with Zn, Cu, Fe, Mg, and Ca. Environ. Chem. Lett. 15, 695–701.

Porcheron, G., Garénaux, A., Proulx, J., Sabri, M., Dozois, C.M., 2013. Iron, copper, zinc, and manganese transport and regulation in pathogenic Enterobacteria: correlations between strains, site of infection and the relative importance of the different metal transport systems for virulence. Front. Cell. Infect. Mi. 3, 90.

Posch, T., Köster, O., Salcher, M.M., Pernthaler, J., 2012. Harmful filamentous cyanobacteria favoured by reduced water turnover with lake warming. Nat. Clim. Change 2, 809–813.

Pure Earth (Blacksmith Institute) and Green Cross., 2015. World's Worst Pollution Problems: Top Six Toxic Threats. Pure Earth and Green Cross, New York, Zurich.

Qin, B., Xu, P., Wu, Q., Luo, L., Zhang, Y., 2007. Environmental issues of Lake Taihu, China. Hydrobiologia 581, 3–14.

Qin, B., Paerl, H.W., Brookes, J.D., Liu, J., Jeppesen, E., Zhu, G., Zhang, Y., Xu, H., Shi, K., Deng, J., 2019. Why Lake Taihu continues to be plagued with cyanobacterial blooms through 10 years (2007–2017) efforts. Sci. Bull. 64, 354–356.

Qu, R., Wang, X., Liu, Z., Yan, Z., Wang, Z., 2013. Development of a model to predict the effect of water chemistry on the acute toxicity of cadmium to *Photobacterium phosphoreum*. J. Hazard. Mater. 262, 288–296.

Quiblier, C., Wood, S., Echenique-Subiabre, I., Heath, M., Villeneuve, A., Humbert, J.-F., 2013. A review of current knowledge on toxic benthic freshwater cyanobacteria—ecology, toxin production and risk management. Water Res. 47, 5464–5479.

Quigg, A., 2008. Trace Elements. In Ecological Stoichiometry. Vol. 5 of Encyclopedia of Ecology, Jørgensen, S.E., Fath, B.D., eds. Elsevier, Oxford.

Quigg, A., 2016. Micronutrients. In Developments in Applied Phycology, 6: The Physiology of Microalgae. Borowitzka, M.A., Beardall, J., Raven, J.A., eds. Springer, Cham, Switzerland.

R Core Team, 2019. R: A language and environment for statistical computing. R Foundation for Statistical Computing, Vienna, Austria. https://www.R-project.org/.

R Core Team, 2020. R: A language and environment for statistical computing. R Foundation for Statistical Computing, Vienna, Austria. https://www.R-project.org/.

R Core Team, 2021. R: A language and environment for statistical computing. R Foundation for Statistical Computing, Vienna, Austria. https://www.R-project.org/.

Ranjitha, P., Karthy, E.S., 2012. Detection of heavy metal resistance bioluminescence bacteria using microplate bioassay method. J. Environ. Sci. Eng. 54, 43–49.

Riether, K.B., Dollard, M.A., Billard, P., 2001. Assessment of heavy metal bioavailability using *Escherichia coli zntAp::lux* and *copAp::lux*-based biosensors. Appl. Microbiol. Biotechnol. 57, 712–716.

Rietjens, M., 1995. Reduction of error propagation due to normalization: Effect of error propagation and closure on spurious correlations. Anal. Chim. Acta, 316, 205–215.

Ritz, C., 2010. Toward a unified approach to dose–response modeling in ecotoxicology. Environ. Toxicol. Chem. 29, 220–229.

Saha, M., Sarkar, S., Sarkar, B., Sharma, B.K., Bhattacharjee, S., Tribedi, P., 2016. Microbial siderophores and their potential applications: A review. Environ. Sci. Pollut. Res. 23, 3984–3999.

Sander, S., Mosley, L.M., Hunter, K.A., 2004. Investigation of interparticle forces in natural waters: Effects of adsorbed humic acids on iron oxide and alumina surface properties. Environ. Sci. Technol. 38, 4791–4796.

Sander, S.G., Hunter, K.A., Harms, H., Wells, M., 2011. Numerical approach to speciation and estimation of parameters used in modeling trace metal bioavailability. Environ. Sci. Technol. 45, 6388–6395.

SCA, 1990. Methods for the Examination of Waters and Associated Material: The Enumeration of Algae, Estimation of Cell Volume, and Use in Bioassays. Blue Book 139. UK Standing Committee of Analysts/Her Majesty's Stationery Office, London.

Schallenberg, M., de Winton, M.D., Verburg, P., Kelly, D.J., Hamill, K.D., Hamilton, D.P., Dymond, J.R., 2013. Ecosystem services of lakes. In: Dymond, J.R. (Ed.), Ecosystem Services of Lakes. Manaaki Whenua Press, Lincoln, New Zealand.

Schlesinger, W.H., Cole, J.J., Finzi, A.C., Holland, E.A., 2011. Introduction to coupled biogeochemical cycles. Front. Ecol. Environ. 9, 5–8.

Schoffman, H., Lis, H., Shaked, Y., Keren, N., 2016. Iron–nutrient interactions within phytoplankton. Front. Plant Sci. 7, 1223.

Schwarzenbach, R.P., Gschwend, P.M., Imboden, D.M., 2016. Environmental Organic Chemistry. Schwarzenbach, R.P., Gschwend, P.M., Imboden, D.M., eds. John Wiley & Sons, New Jersey.

Sebaugh, J.L., 2011. Guidelines for accurate EC50/IC50 estimation. Pharm. Stat. 10, 128–134.

Seitzinger, S.P., Sanders, R.W., 1999. Atmospheric inputs of dissolved organic nitrogen stimulate estuarine bacteria and phytoplankton. Limnol. Oceanogr. 44, 721–730.

Semple, K.T., Doick, K.J., Jones, K.C., Burauel, P., Craven, A., Harms, H., 2004. Defining bioavailability and bioaccessibility of contaminated soil and sediment is complicated. Environ. Sci. Technol. 38, 228A–231A.

Senevirathna, W., Kiro, R., Rosen, R., Popov, I., Belkin, S., Wells, M., 2009. CdSe quantum dots induce superoxide stress in engineered biosensor bacteria. Nanotoxicology 3, 98–108.

Shah, R., 2021. Analyzing Trajectories in SportVu Data. https://rpubs.com/rshah4/Traj_NBA_SportVu.

Shahid, M., Pinelli, E., Dumat, C., 2012. Review of Pb availability and toxicity to plants in relation with metal speciation; role of synthetic and natural organic ligands. J. Hazard. Mater. 219, 1–12.

Shapiro, J., 1973. Blue-green algae: Why they become dominant. Science 179, 382–384.

Shehata, S.A., Badr, S.A., 1980. Growth response of *Scenedesmus* to different concentrations of copper, cadmium, nickel, zinc, and lead. Environ. Int. 4,

431–434.

Shemer, B., Palevsky, N., Yagur-Kroll, S., Belkin, S., 2015. Genetically engineered microorganisms for the detection of explosives' residues. Front. Microbiol. 6, 1175.

Shen, X., Zhang, H., He, X., Shi, H., Stephan, C., Jiang, H., Wan, C., Eichholz, T., 2019. Evaluating the treatment effectiveness of copper-based algaecides on toxic algae *Microcystis aeruginosa* using single cell-inductively coupled plasma-mass spectrometry. Anal. Bioanal. Chem. 411, 5531–5543.

Shi, J.Q., Wu, Z.X., Song, L.R., 2013. Physiological and molecular responses to calcium supplementation in *Microcystis aeruginosa* (Cyanobacteria). New Zeal. J. Mar. Freshwater Res. 47, 51–61.

Shi, Q., Wang, J., Zou, J., Jiang, Z., Wang, J., Wu, H., Jiang, W., Liu, D., 2016. Cd subcellular localization in root tips of *Hordeum vulgare*. Pol. J. Environ. Stud. 25, 903–908.

Shrivastava, A., 2011. Methods for the determination of limit of detection and limit of quantitation of the analytical methods. Chron. Young Sci. 2, 21–25.

Smith, V.H., Crews, T., 2014. Applying ecological principles of crop cultivation in large-scale algal biomass production. Algal Res. 4, 23–34.

Solioz, M., 2018. Copper and bacteria. Evolution, homeostasis and toxicity. Springer Briefs in Molecular Science Series—Biometals. Springer, Cham, Switzerland.

Song, W.E., Chen, S.B., Liu, J.F., Chen, L., Song, N.N., Ning, L., Bin, L., 2015. Variation of Cd concentration in various rice cultivars and derivation of cadmium toxicity thresholds for paddy soil by species-sensitivity distribution. J. Integr. Agr. 14, 1845–1854.

Spivak, A.C., Vanni, M.J., Mette, E., 2011. Moving on up: Can results from simple aquatic mesocosm experiments be applied across broad spatial scales? Freshwater Biol. 56, 279–291.

Stauber, J.L., Florence, T.M., 1987. Mechanism of toxicity of ionic copper and copper complexes to algae. Mar. Biol. 94, 511–519.

Stockenreiter, M., Graber, A.-K., Haupt, F., Stibor, H., 2012. The effect of species diversity on lipid production by micro-algal communities. J. Appl. Phycol. 24, 45–54.

Stocks, S.M., 2004. Mechanism and use of the commercially available viability stain, *Bac*Light. Cytometry A 61, 189–195.

Sundararajan, D., 2021, Multirate Digital Signal Processing. In: Digital Signal Processing. Springer, Cham, Switzerland.

Sundaray, S.K., Nayak, B.B., Lin, S., Bhatta, D., 2011. Geochemical speciation and risk assessment of heavy metals in the river estuarine sediments—a case study: Mahanadi basin, India. J. Hazard. Mater. 186, 1837–1846.

Sutak, R., Botebol, H., Blaiseau, P.-L., Léger, T., Bouget, F.-Y., Camadro, J.-M., Lesuisse, E., 2012. A comparative study of iron uptake mechanisms in marine microalgae: Iron binding at the cell surface is a critical step. Plant Physiol. 160, 2271–2284.

Tao, Y., Yuan, Z., Fengchang, W., Wei, M., 2013. Six-decade change in water chemistry of large freshwater Lake Taihu, China. Environ. Sci. Technol. 47, 9093–9101.

Tavenard, R., 2021. An Introduction to Dynamic Time Warping. https://rtavenar.github.io/blog/dtw.html.

Tecon, R., Wells, M., van der Meer, J.R., 2006. A new green fluorescent protein-based bacterial biosensor for analysing phenanthrene fluxes. Environ. Microbiol. 8, 697–708.

Tellez-Plaza, M., Jones, M.R., Dominguez-Lucas, A., Guallar, E., Navas-Acien, A., 2013. Cadmium exposure and clinical cardiovascular disease: A systematic review. Curr. Atheroscler. Rep. 15, 356.

Teodorovic, I., Planojevic, I., Knezevic, P., Radak, S., Nemet, I., 2009. Sensitivity of bacterial vs. acute *Daphnia magna* toxicity tests to metals. Cent. Eur. J. Biol. 4, 482–492.

Tessier, A., Turner, D.R. (eds.)., 1995. Metal Speciation and Bioavailability in Aquatic Systems. John Wiley, Chichester.

They, N.H., Amado, A.M., Cotner, J.B., 2017. Redfield ratios in inland waters: Higher biological control of C:N:P ratios in tropical semi-arid high water residence time lakes. Front. Microbiol. 8, 1505.

Thomas, M., 2016. Ensemble averaging filter for noise reduction. Int. J. Adv. Res. Comput. Communication Eng. 5, 2278–1021.

Tierbach, A., Groh, K.J., Schönenberger, R., Schirmer, K., Suter, M.J.F., 2018. Glutathione S-transferase protein expression in different life stages of zebrafish (*Danio rerio*). Toxicol. Sci. 162, 702–712.

Tong, S., Schirnding, Y.E.V., Prapamontol, T., 2000. Environmental lead exposure: A public health problem of global dimensions. B. World Health Organ. 78, 1068–1077.

Tripathy, S.C., Jena, B., 2019. Iron-stimulated phytoplankton blooms in the Southern Ocean: A brief review. Remote Sens. Earth Syst. Sci. 2, 64–77.

US EPA (United States Environmental Protection Agency), 1979. Methods for Chemical Analysis of Water and Wastes. EPA 600/4-79-020. US Environmental Protection Agency, Washington DC.

US EPA (United States Environmental Protection Agency), 1984. Ambient Water Quality Criteria for Lead. EPA-440/5-84-027. US Environmental Protection Agency, Washington, DC.

US EPA (United States Environmental Protection Agency), 1998. Method 6020A (SW846): Inductively Coupled Plasma-Mass Spectrometry. Revision 1. US Environmental Protection Agency, Washington DC.

US EPA (United States Environmental Protection Agency), 2002. Review of Metals Action Plan: An EPA Science Advisory Board Report, EPA-SAB-EC-LTR-03-001. US Environmental Protection Agency, Washington, DC.

US EPA (United States Environmental Protection Agency), 2003. The Biotic Ligand Model: Technical Support Document for Its Application of the

Evaluation of Water Quality Criteria for Copper. EPA-822-R-03-027. US Environmental Protection Agency, Washington, DC.

US EPA (United States Environmental Protection Agency), 2007a. Update of Ambient Water Quality Criteria for Copper. EPA-822-F-07-001. US Environmental Protection Agency, Washington, DC.

US EPA (United States Environmental Protection Agency), 2007b. Method 3015A (SW846): Microwave Assisted Acid Digestion of Aqueous Samples and Extracts. Revision 1. US Environmental Protection Agency, Washington DC.

US EPA (United States Environmental Protection Agency), 2015. Recommendations for Public Water Systems to Manage Cyanotoxins in Drinking Water. EPA 815-R-15-010. US Environmental Protection Agency, Office of Water (4606M), Washington DC.

US EPA (United States Environmental Protection Agency), 2016a. Water Quality Standards Academy: Biotic Ligand Model and Copper Criteria. EPA-820-Q-16-001. US Environmental Protection Agency, Washington, DC.

US EPA (United States Environmental Protection Agency), 2016b. Ambient Water Quality Criteria for Cadmium. EPA-820-R-16-002. US Environmental Protection Agency, Washington, DC.

US EPA (United States Environmental Protection Agency), 2021. National Recommended Water Quality Criteria—Aquatic Life Criteria Table. https://www.epa.gov/wqc/national-recommended-water-quality-criteria-aquatic-life-criteria-table#table

van der Meer, J.R., Belkin, S., 2010. Where microbiology meets microengineering: Design and applications of reporter bacteria. Nat. Rev. Microbiol. 8, 511–522.

von der Heyden, B.P., Roychoudhury, A.N., 2015. Application, chemical interaction and fate of iron minerals in polluted sediment and soils. Curr. Pollut. Rep. 1, 265–279.

Wallot, S., Leonardi, G., 2018. Analyzing multivariate dynamics using cross-recurrence quantification analysis (CRQA), diagonal-cross-recurrence profiles (DCRP), and multidimensional recurrence quantification analysis (MdRQA)–a tutorial in R. Front. Psychol. 9, 2232.

Wan, J.-K., Chu, W.-L., Kok, Y.-Y., Cheong, K.-W., 2018. Assessing the toxicity of copper oxide nanoparticles and copper sulfate in a tropical *Chlorella*. J. Appl. Phycol. 30, 3153–3165.

Wang, C., Bi, J., Fath, B.D., 2017. Effects of abiotic factors on ecosystem health of Taihu Lake, China based on eco-exergy theory. Sci. Rep. 7, 42872.

Wang, L., Cai, Y., Fang, L., 2009. Pollution in Taihu Lake China: causal chain and policy options analyses. Front. Earth SCI-PRC. 3(4), 437.

Wang, N.X., Zhang, X.Y., Wu, J., Xiao, L., Yin, Y., Miao, A.J., Ji, R., Yang, L.Y., 2012. Effects of microcystin-LR on the metal bioaccumulation and toxicity in *Chlamydomonas reinhardtii*. Water Res. 46, 369–377.

Wang, X., Wu, M., Ma, J., Chen, X., Hua, L., 2016. Modeling of acute cadmium toxicity in solution to barley root elongation using biotic ligand model theory. J. Environ. Sci. 42, 112–118.

Wei, T., Simko, V., 2017. R package “corrplot”: Visualization of a correlation matrix (Version 0.84). Available from: https://github.com/taiyun/corrplot.

Welker, M., Steinberg, C., 2000. Rates of humic substance photosensitized degradation of microcystin-LR in natural waters. Environ. Sci. Technol. 34, 3415–3419.

Wells, M., 2012. Polycyclic Aromatic Hydrocarbon (PAH) Sensitive Bacterial Biosensors in Environmental Health. In Biosensors and Environment Health. Hunter, R.J., Preedy, V.R. (eds.), CRC Environmental Health Series, Enfield, New Hampshire.

Wells, M., Wick, L.Y., Harms, H., 2004. Perspectives on modeling the release of hydrophobic organic contaminants drawn from Model Polymer Release Systems. J. Mater. Chem. 14, 2461–2472.

Wilkinson, L. and the Task Force on Statistical Inference, APA Board of Scientific Affairs., 1999. Statistical methods in psychology journals: Guidelines and explanations. Am. Psychol. 54, 594–604.

Woelkerling, W.J., Kowal, R.R., Gough, S.B., 1976. Sedgwick-Rafter cell counts: a procedural analysis. Hydrobiologia 48, 95–107.

World Health Organization, 2013. Guidelines for Drinking-water Quality, World Health Organization. https://www.who.int/publications/i/item/9789241547611.

Wu, H., Wei, G., Tan, X., Li, L., Li, M., 2017. Species-dependent variation in sensitivity of *Microcystis* species to copper sulfate: Implication in algal toxicity of copper and controls of blooms. Sci. Rep. 7, 40393.

Xu, H., Zhu, G., Qin, B., Paerl, H.W., 2013. Growth response of *Microcystis* spp. to iron enrichment in different regions of Lake Taihu, China. Hydrobiologia 700, 187–202.

Xu, T., Perry, N., Chuahan, A., Sayler, G., Ripp, S., 2014. Microbial indicators for monitoring pollution and bioremediation. In Microbial Biodegradation and Bioremediation. Das, S., ed. Elsevier, USA.

Yan, F., Ozsoz, M., Sadik, O.A., 2000. Electrochemical and conformational studies of microcystin–LR. Anal. Chim. Acta 409, 247–255.

Yan, K., Dong, Z., Naidu, R., Liu, Y., Li, Y., Wijayawardena, A., Sanderson, P., Li, H., Ma, L.Q., 2020. Comparison of *in vitro* models in a mice model and investigation of the changes in Pb speciation during Pb bioavailability assessments. J. Hazard. Mater. 388, 121744.

Yuan, Y., Chen, Y.P.P., Ni, S., Xu, A.G., Tang, L., Vingron, M., Somel, M., Khaitovich, P., 2011. Development and application of a modified dynamic time warping algorithm (DTW-S) to analyses of primate brain expression time series. BMC Bioinformatics 12, 1–13.

Zeng, J., Yang, L., Wang, W.-X., 2010. High sensitivity of cyanobacterium *Microcystis aeruginosa* to copper and the prediction of copper toxicity. Environ. Toxicol. Chem. 29, 2260–2268.

Zhang, W., Yan, H., Wu, Z.L., 2001. Toxic effects of copper on inhibition of the

growths of unicellular green algae. J. Environ. Sci. (China) 21, 4–7.

Zhang, X., Chen, Q., 2011. Spatial-temporal characteristic of water quality in Lake Taihu and its relationship with algal bloom. J. Lake Sci. 23, 339–347 (in Chinese).

Zhang, X., Qin, B., Deng, J., Wells, M., 2017. Whole-cell bioreporters and risk assessment of environmental pollution: A proof-of-concept study using lead. Environ. Pollut. 229, 902–910.

Zhang, X., Li, B., Xu, H., Wells, M., Tefsen, B., Qin, B., 2019. Effect of micronutrients on algae in different regions of Taihu, a large, spatially diverse, hypereutrophic lake. Water Res. 151, 500–514.

Zhang, X., Li, B., Deng, J., Qin, B., Wells, M., Tefsen, B., 2020a. Advances in freshwater risk assessment: Improved accuracy of dissolved organic matter-metal speciation prediction and rapid biological validation. Ecotox. Environ. Safe. 202, 110848.

Zhang, X., Li, B., Deng, J., Qin, B., Wells, M., Tefsen, B., 2020b. Quantitative high-throughput approach to chalkophore screening in freshwaters. Sci. Total Environ. 139476.

Zhang, X., Li, B., Deng, J., Qin, B., Wells, M., Tefsen, B., 2020c. Regional-scale investigation of dissolved organic matter and lead binding in a large impacted lake with a focus on environmental risk assessment. Water Res. 172, 115478.

Zhang, Z., Huang, K., Tan, T., 2006. *Comparison of similarity measures for trajectory clustering in outdoor surveillance scenes*. 18th International Conference on Pattern Recognition, August 20–24, IEEE, Hong Kong.

Zhou, Q., Li, B., Kurban, A., 2008. Trajectory analysis of land cover change in arid environment of China. Int. J. Remote Sens. 29, 1093–1107.